REPORT DOCUMENTATION PAGE	Form Approved OMB No. 0704-0188

Public reporting burden for this collection of information is estimated to average 1 hour per response, including the time for reviewing instructions, searching existing data sources, gathering and maintaining the data needed, and completing and reviewing the collection of information. Send comments regarding this burden estimate or any other aspect of this collection of information, including suggestions for reducing this burden, to Washington Headquarters Services, Directorate for Information Operations and Reports, 1215 Jefferson Davis Highway, Suite 1204, Arlington, VA 22202-4302, and to the Office of Management and Budget, Paperwork Reduction Project (0704-0188), Washington, DC 20503.

1. AGENCY USE ONLY (Leave blank)	2. REPORT DATE 13 Feb 98	3. REPORT TYPE AND DATES COVERED

4. TITLE AND SUBTITLE
Wall Effects Observed in Tissue-Equivalent Proportional Counters

5. FUNDING NUMBERS

6. AUTHOR(S)
Steven Edward Rademacher

7. PERFORMING ORGANIZATION NAME(S) AND ADDRESS(ES)
Colorado State University

8. PERFORMING ORGANIZATION REPORT NUMBER

97-041D

9. SPONSORING/MONITORING AGENCY NAME(S) AND ADDRESS(ES)
THE DEPARTMENT OF THE AIR FORCE
AFIT/CIA, BLDG 125
2950 P STREET
WPAFB OH 45433

10. SPONSORING/MONITORING AGENCY REPORT NUMBER

11. SUPPLEMENTARY NOTES

12b. DISTRIBUTION CODE

13. ABSTRACT (Maximum 200 words)

19980310 117

DTIC QUALITY INSPECTED

14. SUBJECT TERMS

15. NUMBER OF PAGES
183

16. PRICE CODE

17. SECURITY CLASSIFICATION OF REPORT	18. SECURITY CLASSIFICATION OF THIS PAGE	19. SECURITY CLASSIFICATION OF ABSTRACT	20. LIMITATION OF ABSTRACT

Standard Form 298 (Rev. 2-89) (EG)
Prescribed by ANSI Std. 239.18
Designed using Perform Pro, WHS/DIOR, Oct 94

DISSERTATION

Wall Effects Observed in Tissue-Equivalent Proportional Counters

Submitted by

Steven Edward Rademacher

Department of Radiological Health Sciences

In partial fulfillment of the requirements

for the Degree of Doctor of Philosophy

Colorado State University

Fort Collins, Colorado

Fall 1997

Colorado State University

October 15, 1997

We hereby recommend that the Dissertation prepared under our supervision by Steven Edward Rademacher entitled "Wall Effects Observed in Tissue Equivalent Proportional Counters" be accepted as fulfilling in part the requirements for the Degree of Doctor of Philosophy.

<u>Committee on Graduate Work</u>

_____

_____

_____

_____
Advisor

_____
Department Head

Abstract of Dissertation

Wall Effects Observed in Tissue Equivalent Proportional Counters

Tissue-equivalent proportional counters (TEPC) have been used to measure energy deposition in simulated volumes of tissue ranging in diameter from 0.1 to 10 μm. There has been some concern that the wall used to define the volume of interest could influence energy deposition within the sensitive volume. These "wall effects" occur because the wall has a density significantly greater than the cavity gas. Energy deposition measurements were made for 1 GeV/nucleon Fe ions in a TEPC simulating 1, 2, and 3 μm diameter spheres of tissue. The detector was nested within a particle spectrometer that provided identification and flight path of individual particles. Energy deposition was studied as a function of pathlength through the detector. Approximately 25 % of the energy transfer along trajectories through the center of the detector escapes the sensitive volume. The response of the detector, for trajectories through the detector, is always larger than calculations for energy loss in a homogenous medium. This enhancement is greatest for trajectories near the cavity/wall interface. An integration of the response indicates that charged particle equilibrium is essentially achieved for a wall thickness of 2.54 mm. However, estimates of LET and quality factor are influenced by these wall effects.

Detector response for fragment particles through the detector was found to scale closely to Z^2 for ions of $18 < Z < 26$, as expected by theory for ions of high velocity.

The mean detector response to particle trajectories where a charge-changing nuclear interaction occurred in the detector wall was lower than that of the response to particle trajectories not involved in charge-changing nuclear interactions.

Steven Edward Rademacher
Radiological Health Sciences
Colorado State University
Fort Collins, CO 80523
Fall 1997

TABLE OF CONTENTS

Acknowledgments

Many have had an influence in my life and the success in completing my graduate studies. First, I must thank God for providing me with life, everything I have needed, the gift of strong mind and desire, and loving and supporting people in my life. My parents have always been very supportive, loving, and giving to me and are directly responsible for setting me on a good course in life. My wife has been very supportive and understanding of the necessity to spend many long hours at school, the weeks away from home on travels supporting my studies, and many long hours on the computer.

Dr Borak has been a very patient mentor and friend to me. I appreciate his ability to determine when assistance was necessary and when it was important to allow me to struggle through a problem. In the long run, the struggles were of greater benefit to me. The US Air Force provided me three years to complete my work - a proposition that is difficult for most advisors to work within. I appreciate Dr Borak giving me the opportunity to work on a NASA project that was very conducive to completion within 3 years.

I have had an exciting and interesting career in the US Air Force. I have had the benefit of working with many intelligent and highly professional people. The Air Force has been quite generous in allowing me the opportunity to receive two degrees while on active duty. This would have been nearly impossible without this assistance.

The National Aeronautics and Space Administration Specialized Center for Research and Training in Radiation Health has provided me with the opportunity for involvement with accelerator experiment s at Brookhaven National Laboratory. The funding provided by NASA for the accelerator beam time, laboratory equipment and supplies, financial support of the teaching faculty, and travel monies has been indispensable in the collection of my data and successful completion of my project. A special thanks is due to Dr Walter Schimmerling for his work in keeping research and training alive in space radiation health.

LIST OF TABLES

LIST OF FIGURES

Chapter 1: Introduction

Zirkle *et al.* (1952) first introduced the concept of linear energy transfer (LET) to explain specific variations in biological response from different radiation types. In part, the physical basis of relative biological effectiveness (RBE) is believed to be due to differences in the spatial distribution of ionization along the track of charged particles (Katz *et al.* 1972). Rossi and Rosenzweig (1955) developed the first device to measure energy deposition in simulated volumes of tissue with diameters on the order of 1 micron (μm). These devices are referred to as tissue-equivalent proportional counters (TEPC). Microdosimetric techniques have been used in radiation protection, radiobiology, medical radiotherapy, and microelectronics . The technique has been used by the National Aeronautics and Space Administration (NASA) for characterizing radiation exposure to personnel on manned space flights (Badhwar *et al.* 1992) where the radiation environment is a complex combination of electrons, γ-rays, neutrons, protons, helium and heavier ions.

Of these, particular attention has been given to the high-energy particles with Z greater than 2 (HZE) (NCRP 1989).

The concept of quality factor, Q, has been introduced to modify the absorbed dose and define an equivalent dose that is related to risk associated with the incident radiation. The International Commission on Radiological Protection (ICRP) defines Q as a function of the unrestricted linear energy transfer, L (ICRP 1977). The International Commission on Radiation Units and Measurements (ICRU) has defined Q in terms of lineal energy $\left(\frac{\varepsilon}{\bar{l}} \right)$, where ε is the energy deposited to the matter in a volume by a single energy deposition-event and $\bar{l}$ is the mean chord length in that volume (ICRU 1983). Because lineal energy is directly related to discrete energy deposition, from a biological standpoint it may be more

meaningful than L. One objective of this study is to determine how energy deposition in a TEPC by HZE particles with known L is influenced by the composition of the detector.

A conventional TEPC consists of a solid wall surrounding a gas-filled cavity (sensitive volume). Wall effects caused by the difference in density between the two media were first described by Failla and Failla (1960) and later by Rossi (1968). Oldenburg and Booz (1970) classified these effect into different categories. Kellerer (1971a and b) provided a detailed theoretical analysis for heavy charged particles, where the V-effect and δ-ray effect are most important. The V-effect is the distortion created by the exaggeration in number of nuclear collisions that occur in the wall as compared to the homogenous case (when the cavity has the same density as the wall).

The δ-ray effect is divided into one of two cases: *direct events* for when the primary charged particle trajectory crosses the cavity and *indirect events* for when the primary trajectory passes outside of the cavity. For direct events, energy deposition in the TEPC is enhanced by the wall because energetic δ-rays created in the wall can deposit energy in the cavity. For indirect events that penetrate the wall, event size is enhanced provided the trajectory of the primary is sufficiently close to the cavity/wall interface. For trajectories distant from the interface, δ-rays are stopped in the high density wall before reaching the cavity. Indirect events from particles that pass outside of the wall will have energy deposition that is suppressed due to absorption of δ-rays in the wall of the detector. If the wall is thicker than the penetration range of the maximum energy δ-ray, deposition of energy in the cavity by electrons will not occur.

Experimental measurements have been performed to characterize wall effects of HZE particles. Rodgers *et al.* (1973) compared the response of walled and nearly wall-less TEPCs in the field of 279 MeV/nucleon nitrogen ions, $\beta(v/c) = 0.64$. Data with minimum absorber material upstream of the detectors indicated that the dose mean lineal energy of the

walled detector was about 30 % higher than that of the nearly wall-less one. The difference in dose mean lineal energy between the two detectors decreased when the velocity of the beam was reduced by slowing the incident particles in absorber material. This observation would be expected because for secondary electrons from low velocity ion interactions, the site of energy transfer and deposition are in close spatial proximity. However, for high velocity incident ions, energetic secondary electrons can deposit energy at large distances from the location of initial energy transfer.

Dicello *et al.* (1991) found similar results in the comparison of walled and nearly wall-less detectors in beams of Fe, Ar, and Ne with respective energies of 535, 570, and 557 MeV/nucleon (β: 0.772 - 0.784).

The distributions of energy deposition collected with walled and wall-less detectors will differ for high velocity ions. However, because of the Fano Theorem (1954), the mean absorbed dose should remain unchanged, provided the frequency of nuclear interactions in the wall are negligible. This principle must be satisfied for conventional dosimetry using ionization chambers.

Although the mean dose measured by the two types of TEPC will remain the same, estimates of $\overline{Q}$ based on frequency distributions of y can be significantly different because of wall effects, differences among the recommendations of scientific commissions, and the assumptions that must be made in the calculations.

NASA has assumed that y is equivalent to L for energy deposition events measured during manned space flights. Because energy deposition is influenced by the pathlength of the ion through the detector, clearly this is not true on an event by event basis. The implications of this assumption for determining $\overline{Q}$ for microdosimetric single event spectra has not been studied.

In this study, microdosimetric measurements were collected with two spherical walled TEPCs using 1 GeV/nucleon ^{56}Fe ions. The wall thicknesses were 1.27 and 2.54 mm.

The TEPCs were placed within a particle spectrometer system that provided identity and trajectory through the TEPC for each incident particle. TEPC response was characterized for Fe particles through the TEPC, fragments of Fe through the TEPC, and for events where the Fe was involved in a charge-changing nuclear interaction in the detector wall.

This study of the wall effect for heavy ions is original and different in comparison to earlier work in many respects. This study identified the particle trajectory through the TEPC for each event. This work was for ions of energy 1 GeV/nucleon, while the highest energy ions used previously were 600 MeV/nucleon. Because particle spectrometer systems were not used in earlier work, the beams were comprised of primary particles as well as fragmentation products and assumptions were made concerning the spatial uniformity of the beam. Characterization of the δ-ray effect and calculations of $\overline{Q}$ were not made. In previous work, very high energy deposition events in the spectra collected with walled TEPCs were absent in the spectra of walless TEPCs. Authors could only speculate as to the cause. Because a particle spectrometer system was used in this work, the following tasks could be accomplished:

1. characterization of the δ-ray effect to a monoenergetic beam of Fe particles,

2. calculations of $\overline{Q}$ for Fe particles (based on a known value of L for each event and the relationships between Q and L of ICRP), and

3. more concrete evidence as to mechanism for production of very high energy deposition events.

Also, in addition to analysis of detector response to ^{56}Fe ions, preliminary evaluations are provided for detector response to:

4. ions of lower Z than Fe (with the same velocity as Fe particles) and

5. incident Fe particles where the particle is involved in a charge-reducing nuclear interaction in the wall of the detector.

4

Both of these evaluations are considered preliminary because of the limited number of events available for analysis.

Chapter 2:   Literature Search and Background

Ionizing Radiation and Relevance to Biological Systems

Ionizing radiation transfers energy to materials through ionizations and excitations of electrons, and nuclear interactions. Biological effects from exposure to ionizing radiation are determined in part by several characteristics of the radiation field. Among the characteristics, absorbed dose is perhaps the most important. Absorbed dose (D), as defined by the ICRU (1980), is the quotient of $d\bar{\varepsilon}$ by dm, where $d\bar{\varepsilon}$ is the mean energy imparted by ionizing radiation to matter of mass dm. Secondly, deposition rate is important due to the ability of living organisms to repair damage. Repair capability may be limited in part by dose rate and the type of ionizing radiation. The spatial distribution of energy deposition at the microscopic level is another important characteristic that will be discussed later.

Space Radiation Environment

The space radiation environment is different from that encountered on earth in both intensity and types of radiation. The earth has the protective magnetic field that shields the surface from charged particle radiations as well as the attenuation provided by the atmosphere. Space radiation consists of three components: trapped particle, solar particle, and galactic cosmic radiations (GCR).

The electron belts surrounding the earth contain particles trapped in the earth's magnetic field. The belts consists of two distinct regions: an inner region that extends out to about 1.8×10^4 kilometers (km) and an outer region beyond that of the inner to 7.6×10^4 km (NCRP 1989). Electron intensities in the outer region are typically about 10 times those in

the inner region, and within both regions intensities can vary drastically over short periods of time (NCRP 1989). For the inner region, exposure to protons is of greater importance than electrons for manned space missions (NCRP 1989). At 450 km altitude (28.5° inclination), the majority of the proton fluence has energies between 5 and 100 MeV (NCRP 1989). There can be considerable variation in proton fluence with inclination angle to the earth's axis; the most intense region being the South Atlantic Anomaly that is located between Africa and South America.

Outside the protection of the earth's magnetic field, the environment consists of solar and galactic particles. The galactic cosmic spectrum is present isotropically in space and is from source(s) outside the solar system. Ninety-eight percent of total galactic particle fluence is protons and heavier ions, with 2 % electrons and positrons (NCRP 1989). For the barions, the bulk of the particle fluence have energies between 0.1 to 10 GeV/nucleon and among these the majority is between 0.1 to 1 GeV/nucleon (NCRP 1989). Table 2-1 lists the fractional abundance (FA) of the most important ions and their FA multiplied by the Z^2 of the ion (NCRP 1989). For galactic cosmic rays, FA • Z^2 is a good indicator of the relative dose among the various ions as collisional stopping power is closely proportional to Z^2 and the energy spectra among the ions is similar in except for scaling factors. Thus, though the FA of Fe is 2300 times lower than that of protons and one-tenth that of C and O, its contribution to dose is greater than that of both O and C, and about

Table 2-1. Fluence Weighted Relative Fractional Abundance (FA)
of Galactic Cosmic Barions and FA • Z^2 (NCRP 1989).

Barion	Fractional Abundance	FA • Z^2
Hydrogen	0.87	0.87
Helium	0.12	0.48
Carbon	0.004	0.13
Oxygen	0.004	0.20
Iron	0.0004	0.26

30 % of that from protons. Ions that are heavier than helium are referred to as HZE particles (high Z and energy). The influence of the sun to the radiation environment outside the earth's magnetosphere is highly dependent on the activity of the sun. Solar winds are created by ionized gas emissions from the sun and carry magnetic fields. These magnetic fields decrease the intensity of the GCR in interplanetary space. Thus in years of lower solar activity (solar minimum), the GCR reaches a maximum, while GCR minimums are achieved during periods higher solar activity. In addition to the influence of solar winds, the sun has large emissions of charged particles in solar particle events (SPE) that occur during solar flare activity. The emissions consist of protons, helium, and heavier nuclei, but have energy spectra lower than that of the GCR. Solar particle events can be grouped into two categories: ordinary and anomalously large events. One anomalously large event occurred from 4 - 7 August, 1972 and had a one-week integrated fluence many orders of magnitude greater than that of the galactic fluence. These events are rare (NCRP 1989).

In addition to the primary particles described, secondary particles are produced through interactions with spacecraft materials and personnel. Secondary particles consist primarily of charged fragmentation and spallation products, and neutrons from nuclear interactions .

Spatial Patterns of Energy Deposition

Introduction

For different types of radiations that provide similar dose and dose rates to biological systems, the primary difference among the radiations in reaching many biological outcomes is related to the spatial pattern of energy deposition.

In 1952, Zirkle *et al.* (1952) introduced the concept of linear energy transfer (LET) which referred to the linear density of all forms of energy transfers from ionizing radiation. Zirkle introduced the concept to explain differences in survival of spores exposed to α-particles and x-radiations. In his experiment, the high-LET α-particles exposed spores had a lower survival than those exposed to the x-radiation (low-LET) at the same dose. In

8

1962, the ICRU (1962) defined linear energy transfer (LET) for charged particles in a medium as the quotient of dE_L/dl, where dE_L is the average energy locally imparted to the medium by a charged particle of specified energy in traversing a distance of dl. Within this definition, it was recognized that primary charged particles could transfer significant energy to secondary electrons such that the energy carried by these secondaries would impart the majority of their kinetic energy outside of the location of the primary particle track. The term "locally imparted" referred either to a maximum radial distance from the particle track or a maximum discrete kinetic energy transfer to a secondary electron beyond which are not included in LET. Secondaries with high kinetic energy are generally referred to as δ-rays and are created by hard or "knock-on" collisions with the primary where the classical impact parameter (of the primary and atom that possesses the secondary electron) is on the order of atomic dimensions. Subsequent ICRU Reports (1970,1980) defined LET (restricted linear collision stopping power - L_Δ) of charged particles in a medium as the quotient of dE_Δ by dl, where dE_Δ is the mean energy loss due to collisions, with kinetic energy transfers less than some specified value Δ, and dl is the distance transversed by the particle. For the remainder of this document, LET (and LET_∞) will interchangeably refer to the total (or unrestricted) LET that accounts for all collisional losses regardless of energy. For simplicity an L will be used in place of LET.

Many researchers over the years have investigated the spatial patterns of energy deposition for protons, α-particles, and heavy ions. The work was prompted primarily by concern over radiation hazards from neutrons encountered in the commercial nuclear power industry, α-particles from natural and man-made sources, ions encountered in space operations, and ions used in medicine. The investigations have consisted of:

a) measurements of radial dose distributions and formulation of empirically based models,

9

b) Monte Carlo simulations of energy deposition, and

c) microdosimetric measurements.

Track Structure Models

Katz Model

Katz and co-workers (Butts and Katz 1967, Katz e al. 1971) provided one of the first track structure models for heavy ions based on a δ-ray distribution formula and an extrapolated range-energy relation for electrons. The radial distribution of dose, calculated from these relations, follows an approximate $(1/r^2)$ relationship, where r is the radial distance from the primary track. In biological studies with dry enzymes and viruses, Katz found their response to heavy ions irradiation to be predicted solely on the distance from the primary track.

Chunxiang et al. (1985) compared the Katz model of radial distribution of dose to four sets of experimental data collected by Varma et al. (1975, 1976, 1980a, and 1980b) and another model of radial dose distribution proposed by Fain et al. (1974). Comparison of the model to experimental data provided close agreement for helium (Z = 2), oxygen (Z = 8), neon (Z = 10), and bromine (Z = 35) ions over a velocity range of: $0.072 < \beta < 0.7$. For comparison with the Fain model, there was close agreement for carbon (Z = 6 and $\beta = 0.065$) and iron (Z = 26 and $\beta = 0.41$) ions.

The Katz model was used by NASA (Cucinotta 1991) to predict biological damage to mammalian cell cultures from galactic cosmic rays. Cucinotta et al. (1995) have modified input parameters to the Katz model to improve accuracy of the model both near and far from the ion trajectory where the model had the greatest uncertainties.

Chatterjee Model

Chatterjee and co-workers (Chatterjee *et al.*, 1973; Chatterjee and Shaefer, 1976; and Chatterjee, 1993) developed a model similar to Katz's in the $(1/r^2)$ relationship of dose to radial distance from the primary track. The model is simpler than Katz's model having only three input parameters: L, penumbra radius, and core radius. The model divides radial dose in two distinct regions: an inner region of very dense ionization called the core that arises primarily from deposition of energy from electrons created from soft collisions, and an outer region that encompasses the range of δ-rays produced along the track that is called the penumbra. Energy deposition is assumed not to occur outside the penumbra. The model is independent of particle charge. The penumbra and core radii are the same for particles of the same total kinetic energy per nucleon and are dependent only on velocity. Like the Katz's model, Chatterjee's model closely agreed with microdosimetric measurements of 600 MeV/amu Fe ions that were stripped of their electrons (Metting *et al.* 1986). Toburen *et al.* (1990) provided microdosimetric measurement of partially stripped U and Ge ions that had a maximum velocity of $\beta = 0.189$. The mean energy deposited was in close agreement with the Chatterjee model, but had energy deposition beyond the penumbra radius of the model. One advantage of the Chatterjee model over the Katz's model is that it incorporates energy conservation and can be used to calculate the fraction of L absorbed in volumes surrounding the particle track. For this reason, this model will be used for calculations in this report. Though some researchers measured energy deposition beyond the penumbra radii specified in the model, this inaccuracy of the model should have no influence on the calculations used in this report because they were made for radii well within the penumbra. Appendix A summarizes the calculations performed with this model.

Monte Carlo Simulations

Several computer codes based on the Monte Carlo method are currently used to simulate the transport of charged particles through media (Kraft *et al.*, 1992 and Wilson *et al.*, 1994). The codes generally accomplish the same task, but may be subtly different in the extent to which tracks are followed (Rossi and Zaider, 1996). Ottolenghi *et al.* (1995) have adapted a Monte Carlo track structure code to simulate strand breaks produced in DNA from α-particles and protons.

The Monte Carlo method, being based on the stochastic characteristics of energy deposition, more closely approximate physical reality than track structure models that provide only mean energy deposition. Under some conditions, mean values may be sufficient in describing energy deposition. For large sites in and near the track of charged particles, or for multiply charged ions with high ionization, the variance in energy deposition may be small. But, for sensitive volumes distant from the track, small volume sites, or singly charged ions, the stochastic nature of energy deposition becomes more important, making mean values less meaningful.

Microdosimetry

1. Micrometer Measurements. Rossi and coworkers (1955a, 1955b) developed the first device to measure energy deposition in simulated volumes of tissue with diameters on the order of 1 μm. These devices are referred to as tissue-equivalent proportional counters (TEPC). Microdosimetric techniques have been used in radiation protection, radiobiology, medical therapy, and microelectronics. Volume size is chosen relevent to structure of biological interest, for example, cell nuclei of diameters typically between 1 and 10 μm. The technique has been used for characterizing radiation exposure to NASA personnel on manned space flights, with simulated diameters in the micron range (Badhwar *et al.* 1992).

2. Conventional TEPCs. A conventional TEPC consists of a solid wall surrounding a gas-filled cavity (sensitive volume). The most commonly utilized shape of the sensitive volume has been the sphere since it possesses complete symmetry with respect

12

to isotropic and directional radiation sources (ICRU 1983). Another shape commonly implemented is the cylinder and is the type used for dosimetry on manned space flights. Cylindrical devices are easier to construct and generally are structurally more rugged, which makes them more attractive for use on spacecraft. Detectors constructed of solid tissue-equivalent plastic walls to define the sensitive volume are easy to construct and rugged. But, wall-less detectors (where the medium surrounding the sensitive volume is of the same density and composition), are the most desirable because radiation equilibrium is preserved as generally is the case in tissue. Distortions created by the solid wall, termed "wall effects," are the primary focus of this research.

3. <u>Limitations of Microdosimetry</u>. The measurement of energy deposition on the micrometer scale has been useful for predicting a wide range of biological experimental data (Kellerer and Rossi, 1972). Limitations in the predictive ability of microdosimetry was apparent for very low-energy X-rays (Cox *et al.* 1977, Goodhead *et al.* 1978). For very low-energy X-rays, ionizations are closely spaced and resultant biological effects could not be predicted by energy deposition on the micrometer scale. Experiments of this type stress the importance of energy deposition on the nanometer scale (in addition to that on the micrometer scale) in predicting biological effects (Kliauga 1994).

4. <u>Nanodosimeters</u>. Kliauga (1990) evaluated the response of a ultraminiature walled cylindrical TEPC to photons and neutrons down to site sizes of 10 nm. More recently Kliauga (1994) evaluated the response of a nearly wall-less miniature cylindrical TEPC to heavy ions. Acceptable performance was achieved for simulated site sizes down to 20 nm.

5. <u>Dosimetry on NASA Missions</u>. Based on the above discussion, the ideal TEPCs would be of nearly wall-less designs and incorporate devices that simulated nanometer and micrometer site sizes. For many reasons this has yet to occur. Wall-less devices are not as rugged as walled devices and may not be able to withstand G-stresses encountered during lift-off. To properly create radiation equilibrium with a wall-less detector, the detector

13

container would have to be orders of magnitude larger than detector sensitive volume (Metting *et al.* 1988). This is not practical for spacecraft. Miniature detectors that are necessary to simulate nanometer site sizes are difficult to construct and not as rugged as devices that simulate micrometer site sizes. Distortions created by the wall effect (to be discussed in detail later in this Chapter) will be more pronounced for nanodosimeters than microdosimeters in the field of high velocity ions.

6. <u>Quantities and Units</u>. The measured ionization produced in a TEPC is proportional to the energy deposited in the cavity, ε. In the field of microdosimetry, the concept of lineal energy (y) is more commonly used. ICRU (1983) defined lineal energy as the quotient of ε by $\bar{l}$, where $\bar{l}$ is the mean chord length of μ-random particle traversals through that volume. Lineal energy is a random or stochastic quantity and is normally expressed in units of keV μm^{-1}. By recording the number of events within event size (energy) bins of some defined value and dividing each by the total number of events among all bins, a discrete probability density function (pdf), f(y), in lineal energy can be defined. These distributions or functions are called single event spectra. The first moment of f(y), $\bar{y}_F$, is called the frequency mean lineal energy, is a nonstochastic property of f(y), and is defined as:

$$\bar{y}_F = \int_0^\infty y\, f(y)\, dy. \tag{2-1}$$

The second moment of f(y), $\bar{y}_D$, is called the dose mean lineal energy, is a nonstochastic property of f(y), and is defined as:

$$\bar{y}_D = \frac{\int_0^\infty y^2\, f(y)\, dy}{\bar{y}_F} = \int_0^\infty y\, d(y)\, dy, \tag{2-2}$$

where $d(y) = \dfrac{y}{\bar{y}_F}\, f(y)$.

14

Radiation Dosimetry and Radiation Protection

Relative biological effectiveness (RBE) is a concept used in radiobiology to compare the dose of a test radiation with the dose of 250 kVp x-rays required to achieve a similar biological outcome. RBE is defined as the quotient of the absorbed dose of the test radiation by that of 250 kVp x-rays. While the concept of RBE may appear to be straightforward, it is difficult to apply directly to radiation protection because RBE changes with dose, dose rate, mixed radiation fields, and specific biological outcomes.

For the purpose of radiation protection, quality factor (Q), has been assigned to radiations of different types to account for the varying ability to cause detrimental radiation effects. Risks for detrimental effects from radiation exposure are related to the dose of radiation received modified by the Q of the radiation. The International Commission on Radiological Protection in Publication 26 (ICRP 1977) provided a recommended relationship between L and Q. The recommendation was changed in Publication 60 (ICRP 1990) where Q was replaced by w_r, the radiation weighting factor. In this report, Q will be used interchangeably for both set of recommendations. The recommendations of both publications is given in Fig. 2-1.

For charged particles of similar L, but with different charge and velocity, there can be large differences is the spatial pattern of energy deposition and therefore biological effects. Also, L is a quantity that is difficult to measure. ICRU (1986) has recommended a relationship between Q and y. The relationship is provided in Fig. 2-2 for 1 μm diameter spheres. Because lineal energy represents discrete energy deposition, from a biological standpoint it may be more meaningful than L. A TEPC can be designed to measure y directly and therefore provide direct measurements of Q.

NCRP (1989) recommended dose equivalent limits for space travel. In the document, it was recognized that the ICRU (1986) recommended Q values for neutrons should be implemented for radiation exposures in space. But, the report did not specifically recommend determination of $\overline{Q}$ directly from measured microdosimetric spectra. NASA is

15

Figure 2-1. ICRP 26 and 60 Quality Factor Relationships to L
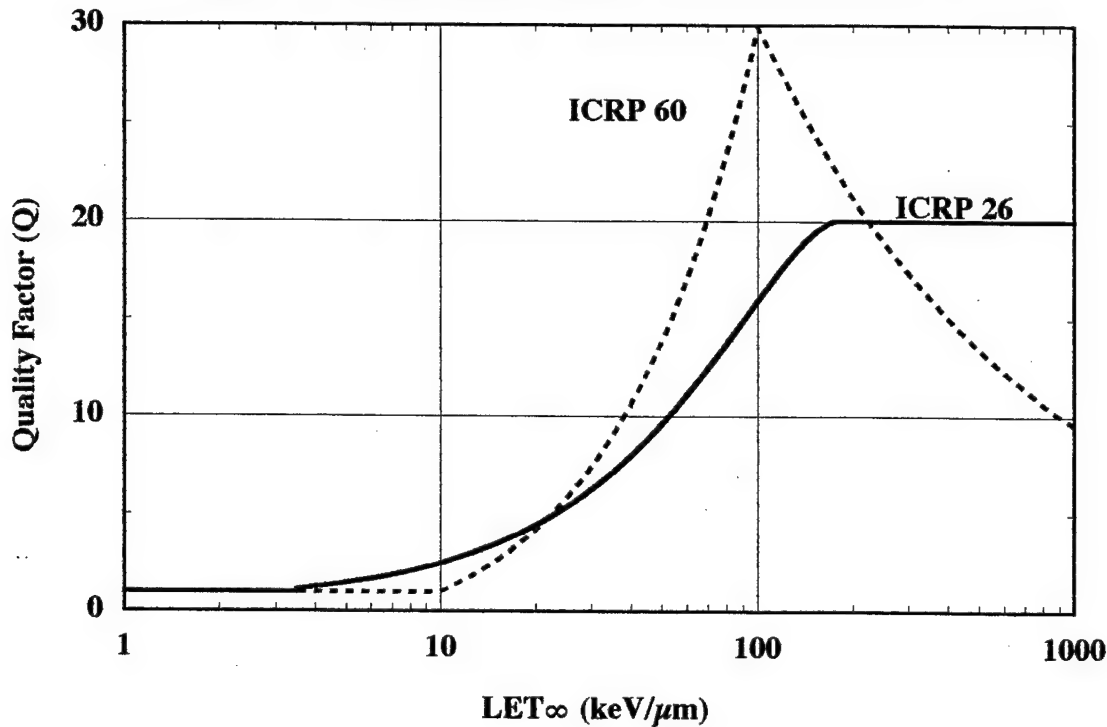
Figure 2-2. ICRU 40 Quality Factor Relationship to y.
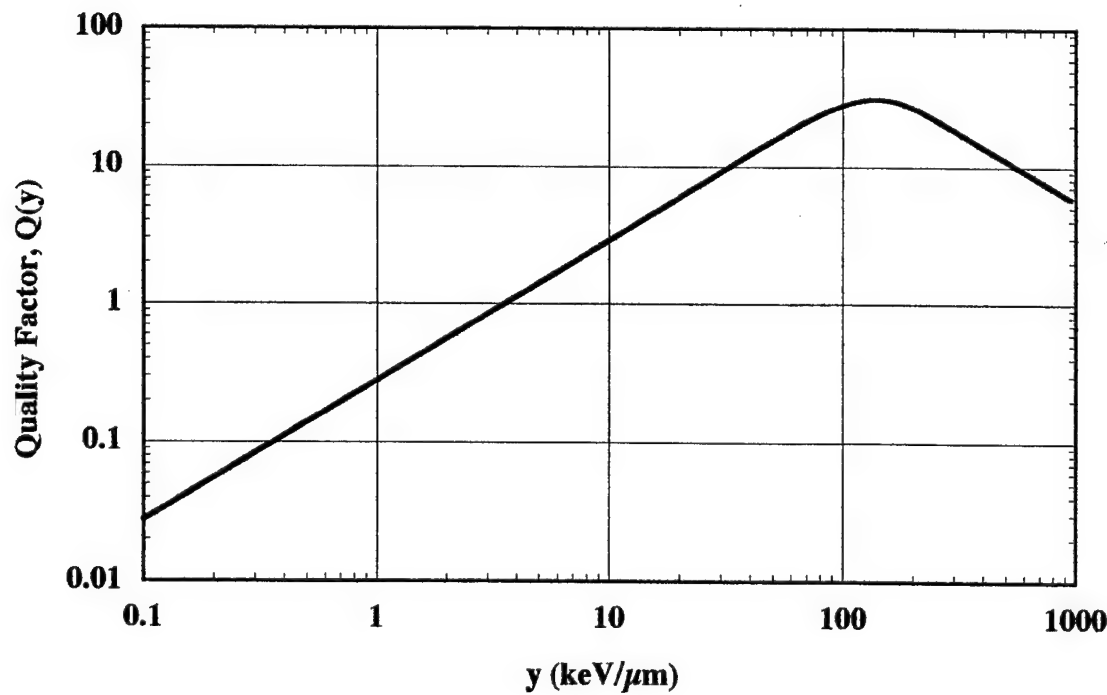
currently determining $\overline{Q}$ under the assumption that $y = L$ and with the ICRP recommended relationship between Q and L. Plastic detectors CR-39, cellulose nitrate, and Lexan polycarbonate have been used by NASA on past missions to measure L (NCRP 1989). NASA has collected microdosimetric spectra with walled cylindrical TEPCs on manned space flights. Calculations of $\overline{Q}$ have been made from these spectra under the assumption that y is equivalent to L for discrete energy deposition events. Because energy deposition is influenced by the pathlength of the ion through the detector, clearly the equivalence is not true on an individual event basis. NASA has been criticized for this practice (Dicello *et al.* 1991). However, it has not been determined whether calculations of $\overline{Q}$ are significantly different from the known values for high velocity ions because the wall effects for these detectors have not been firmly established.

Ricourt *et al.* (1981) recommended that dose equivalent, H, be determined from measurements of D(y) using the following relationship:

$$H = \int Q(L = \tfrac{8}{9}y)\, D(y)\, dy \qquad (2\text{-}3)$$

"The substitution of 8/9 y for L is derived from the moments analysis of y in the limit when the simulated tissue diameter approaches zero," according to Borak and Stinchcomb (1982). Borak and Stinchcomb (1982) found that the substitution provided an almost exact estimate of the actual $\overline{Q}$ for neutrons of energy from thermal to 4 MeV if the simulated diameter of the tissue is zero. But, as the simulated diameter increased, calculated values of $\overline{Q}$ decreased.

Radiation risk coefficients based on a fluence based system were first discussed by Curtis, Dye, and Sheldon (Wilson *et al.* 1990). The system used risk coefficients for a particular endpoint based on the fluence of individual particles in the radiation field. Dosimetry under this system would require particle identification and velocity. Practically, this could be accomplished with a particle telescope that contained a series of silicon

detectors. Unfortunately, a system of this type could not record dose from indirectly ionizing radiations that are present in the space environment.

The purpose of this work is to characterize the wall effects from ^{56}Fe incident on walled TEPCs. This data can be used to determine an appropriate method for calculation of $\overline{Q}$.

Wall Effects

General

Wall effects caused by the difference in density between two media were first described by Failla and Failla (1960) and later by Rossi (1968). Oldenburg and Booz (1970) classified these effects into different categories. Kellerer (1971a, 1971b) provided detailed theoretical analysis for heavy charged particles, where the V-effect and δ-ray effect are most important.

δ-Ray Effect

The effect is most important for high velocity charged particles where δ-ray secondaries can have significant energy and range. The effect is dependent on the trajectory of the charged particle with respect to the cavity of the detector. Three types of trajectories will be described.

Figure 2-3 illustrates the δ-ray effect for a walled cavity as compared to energy deposition in homogenous media. For both cases, the primary charged particle traverses the sensitive volume (cavity). These are referred to as "direct events." In the case of the walled cavity, the energy deposited will be the sum of that from the primary particle and from the δ-ray(s) created in the wall. However, in homogenous media, the distance between the location of δ-ray creation and the entrance point of the detector may be sufficiently large such that only one of the particles may traverse the sensitive volume. As shown in the figure for homogenous media, the equivalent amount of energy that was deposited in the walled cavity, is represented by two discrete energy deposition events.

18

For highly charged particles, a single event in a walled cavity may be represented by the sum of numerous discrete energy deposition events.

Figure 2-3. Diagram Illustrating the δ-Ray Effect in a Walled Cavity as Compared to Equivalent Energy Deposition in Homogenous Media. [In the walled cavity, energy deposition is represented by a single event, but for homogenous media the same energy deposition is represented by two discrete events.] [Adapted from Kellerer (1971b)].

a) walled cavity   b) homogenous media
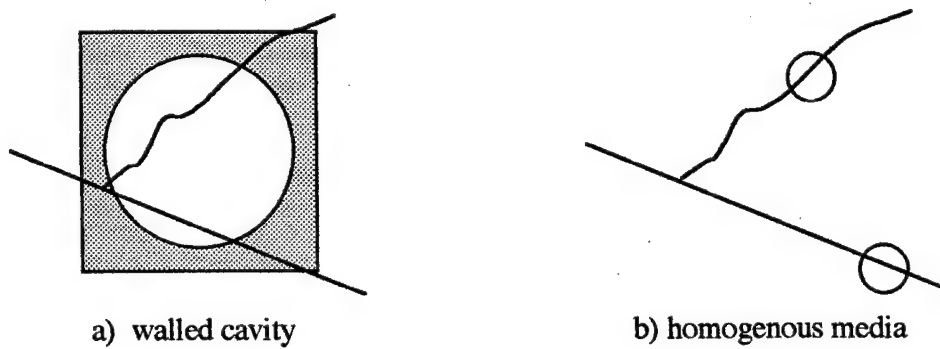
Figure 2-4 provides another illustration of this effect for a primary charged particle traversing a spherical cavity along the longest chord length. Evaluation of the difference in energy deposition between a walled cavity and homogenous media for these types of trajectories have not been accomplished.

Figure 2-4. Diagram Illustrating the Difference in Energy Deposition in a Walled Cavity and Homogenous Media for Direct Events [Adapted from Kellerer (1971a)].

a) walled cavity   b) homogenous media
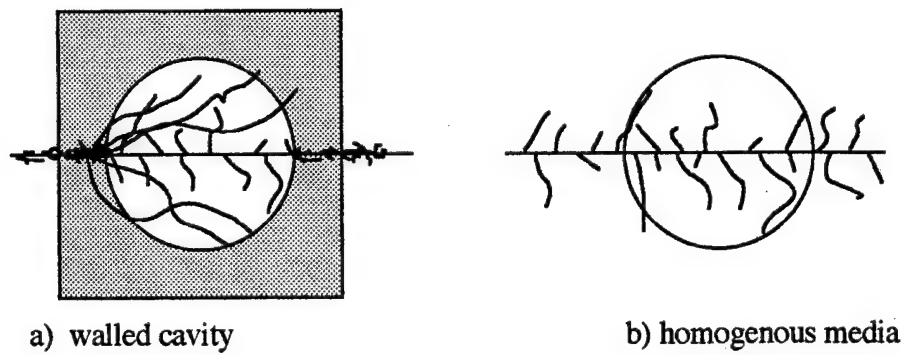
Indirect events are those where the primary charged particle passes outside of the sensitive volume. Indirect events for the walled cavity can either enhance or suppress

energy deposition as compared to that in homogenous media dependent on the location of the particle trajectory.

Figure 2-5a illustrates an indirect event where the trajectory of the primary particle traverses outside of the cavity but in the wall of the detector. Energy deposition for these events will be much greater as compared to that in homogenous media (Fig. 2-5b).

Figure 2-5. Diagram Illustrating Energy Deposition in a Walled Cavity and Homogenous Media for Indirect Events Traversing Outside the Sensitive Volume.

a) walled cavity   b) homogenous media
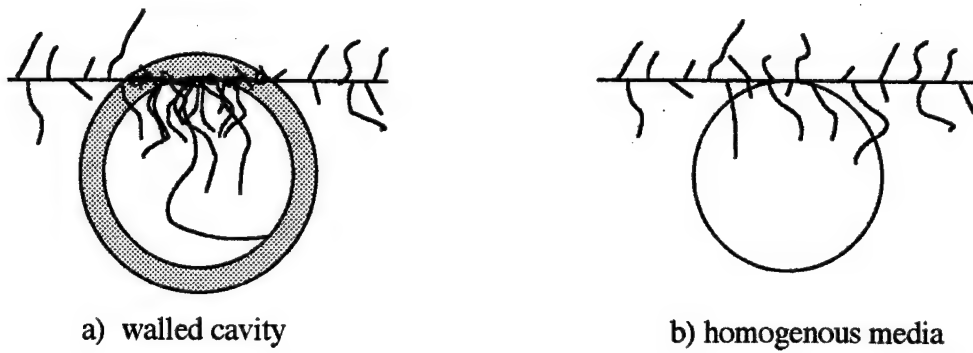
The frequency and magnitude of these events depends on the range of the δ-rays, proximity of the primary particle to the cavity/wall interface, simulated site volume, and the Z of the primary particle. The range of the δ-rays is directly related to the velocity of the primary particle. Kellerer (1971a) calculated the absorbed dose in homogenous media for proton recoils and heavy charged particle (HCP) of initial energies: 1 to 30 MeV/nucleon in spherical sites of diameter from 0.01 to 10 μm. Absorbed dose was determined separately for direct and indirect events. For a 30 MeV/nucleon HCP, the fraction of absorbed dose from indirect events was as high as 0.35 for 0.01 μm diameter sites and lower than 0.09 for 10 μm diameter sites. Theoretical calculations haven't been published for 1 GeV/ nucleon HCP.

Figure 2-6a illustrates an indirect event where the trajectory of the primary is outside of the cavity wall. If the wall is thicker than the range of the maximum energy δ-ray, then

20

there will be no deposition of energy in the cavity from this events, neglecting x-rays from Bremsstrahlung. If the cavity wall is thinner than the penetration range of the maximum energy δ-ray, then there is the potential for energy deposition in the cavity from this event, but the net result of this type of indirect event is a suppression of energy deposition as compared to that in homogenous media (Fig. 2-6b).

Figure 2-6. Diagram Illustrating Energy Deposition in a Walled Cavity and Homogenous Media for Indirect Events with Trajectories Outside the Wall of the Walled Cavity.

a) walled cavity   b) homogenous media
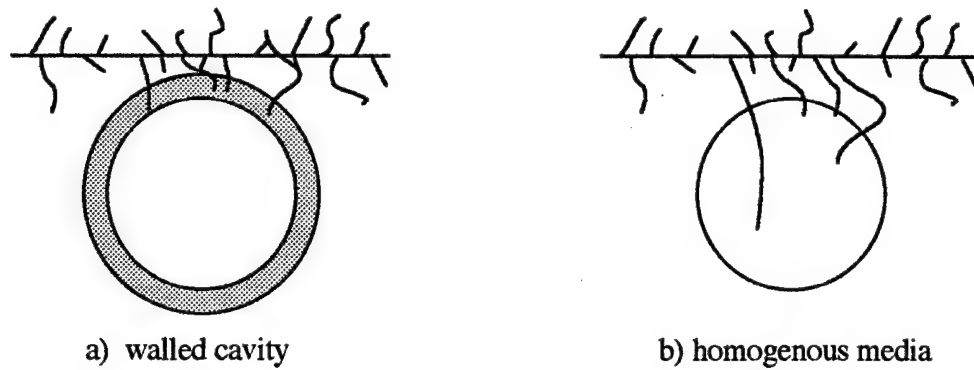
A description of three trajectories have been given to characterize the δ-ray effect for charged particles. For two of the descriptions, energy deposition was enhanced over the homogenous case, while for the other it was suppressed. For a uniformly irradiated walled cavity TEPC, the net result in single event spectra is an increase in $\bar{y}_F$ and $\bar{y}_D$ as compared to homogenous media.

Reentry Effect

Figure 2-7a illustrates the reentry effect for an electron in a walled cavity. From the diagram, the electron traverses the cavity, enters the wall, and reenters the cavity a second time. For homogenous media (Fig. 2-7b), the electron will traverse the cavity only once. For the event depicted, the net effect in the walled cavity is an increase in energy deposition compared to that of homogenous media. The reentry effect is only significant for electrons because they are the only charged particle with significant curvature of path. Because

21

photons deposit energy through transfer of energy to electrons, it is applicable to photons as well.

Figure 2-7. Diagram Illustrating the Reentry Effect in a Walled Cavity. [Energy deposition in a walled cavity is represented by the electron traversing the walled cavity twice, while in homogenous media it is represented as two discrete energy deposition events.] [Adapted from Kellerer (1971a)].
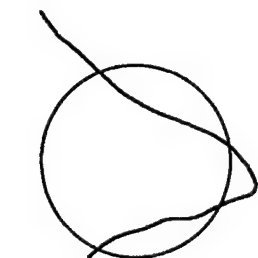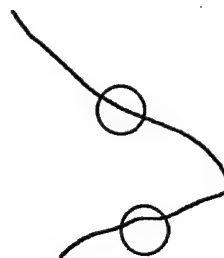
a) walled cavity   b) homogenous media

Scattering Effect

The third category of wall effect is called the scattering effect. The effect is applicable to indirect ionizing radiations (i.e. neutrons and photons). The effect is illustrated for a walled cavity in Fig. 2-8a, where two scattering events occur within close proximity of each other and the scattered charged particles both deposit energy in the cavity.

Figure 2-8. Diagram Illustrating the Scattering Effect in a Walled Cavity. [Energy deposition in the walled cavity is represented by the sum of energy deposited by the two charged particle recoils, but in homogenous media it would be represented by two discrete energy deposition events.] [Adapted from Kellerer (1971a)].
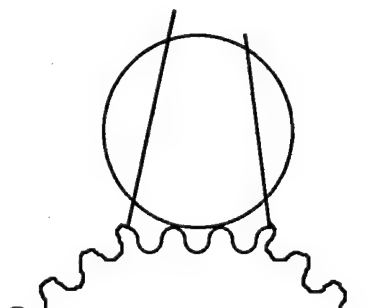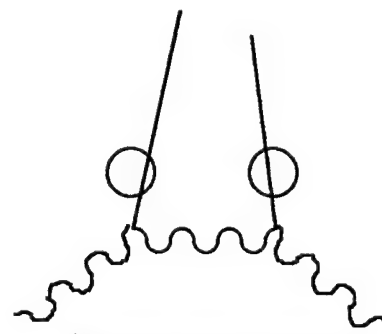
a) walled cavity   b) homogenous media

In homogenous media however, deposition of energy by both secondaries in the same active volume is extremely improbable. The effect is dependent on the relative densities of the cavity and wall materials, thickness of cavity wall, and interaction cross-sections of the primaries. The net result of this effect is enhanced energy deposition as compared to that in homogenous media.

V-Effect

The fourth type of wall effect is the V-effect and can occur in both elastic and inelastic (absorption) nuclear interactions. The effect for a walled cavity is illustrated in Fig. 2-9a

Figure 2-9. Diagram Illustrating the V-Effect Effect in a Walled Cavity. [Energy deposition in the walled cavity is the sum of that from both charged particles trajectories, but in homogenous media it would be represented by two discrete energy deposition events.] [Adapted from Kellerer (1971a)].

a) walled cavity   b) homogenous media
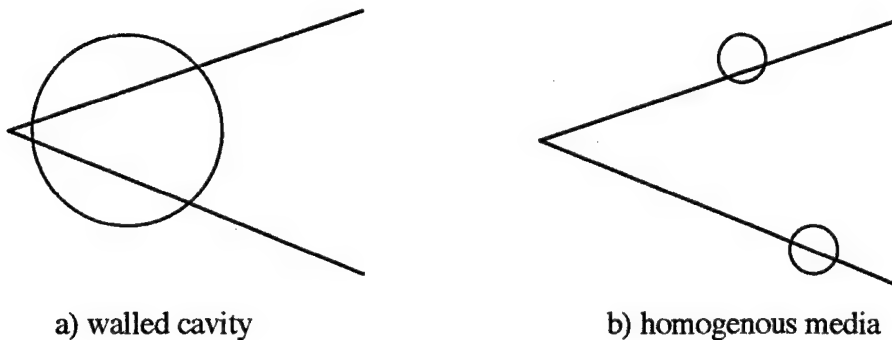
where the nuclear interaction occurs in close proximity of the cavity. The "V" formed illustrates the trajectory of both the primary and a secondary nuclei where both particles contribute to energy deposition in the cavity. In homogenous media (Fig. 2-9b), the two events would not likely deposit energy in the same site. The net effect in a walled cavity is enhanced energy deposition compared to homogenous media where the energy deposition would be represented by to discrete energy deposition events. The example provided here is the simplest case with only one secondary nucleus produced. In violent nuclear collisions, especially seen in HZE particle collisions, there can be many secondary nuclei produced. Appendix C provides details of nuclear interactions for HZE particles with specific data for ^{56}Fe ions.

Wall Effects Characterized by Experimental Measurements

General

A number of investigators experimentally evaluated the difference in response of walled and wall-less TEPC designs. The bulk of the data was collected in the 1970s. Because the focus of this thesis is on the wall effects of HZE particles a more complete summary of relevant work will be provided, while for other radiation types, only a small fraction of the relevant work will be summarized.

Photons

Photons were the primary source of radiation in radiation biology and medical therapy during the early years of these disciplines. As a consequence, a considerable amount of experimental microdosimetry was accomplished on these fields. Braby and Ellett (1971) compared single event spectra from spherical solid- and grid-walled TEPCs in the field of 250 kVp x-rays and a ^{60}Co source. The devices simulated volumes of tissue with diameters from 1 to 6 μm. The result of the work is summarized in Fig. 2-10 in terms of the mean event size of the single event spectra. From the plot, mean event size decreases as the simulated site diameter increases for both radiation and detector types. The difference in the mean event size for the two detectors in the field of the 250 kVp x-rays is considerable with the maximum ratio of 1.52 at 2 μm and minimum ratio of 1.36 at 6 μm. For the irradiations with ^{60}Co, the difference between the two detectors was considerably less, with the maximum ratio being 1.2. The authors attributed the majority of the wall effects to the reentry effect, but noted that for the ^{60}Co γ-rays, a significant fraction of the effect may be due to the δ-ray effect.

Figure 2-10. Frequency Mean Event Size from Single Event Spectra of ^{60}Co and Filtered 250 kVp X-Rays Collected with Solid- and Grid-Walled TEPCs (Braby and Ellett 1971).
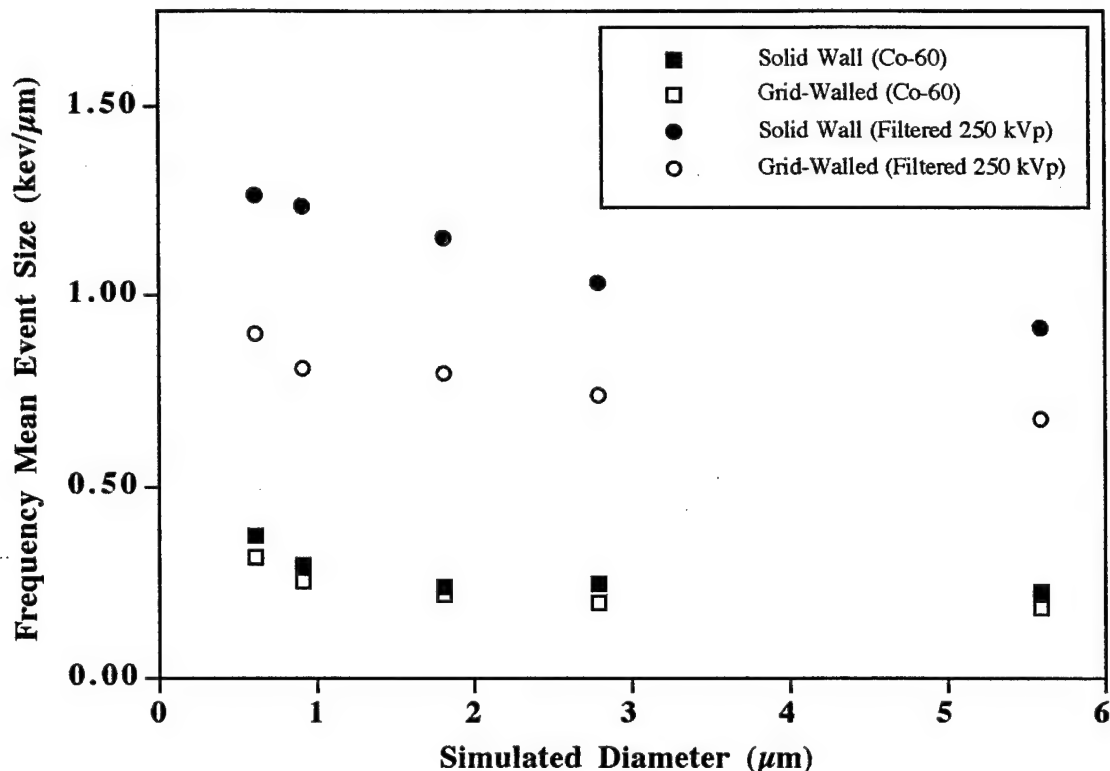
Neutrons

Oldenburg and Booz (1970) provided theoretical calculations and measurements of 6 MeV neutrons for simulated spherical volumes 6.5 μm in diameter. For events with energy deposition below 20 keV, the calculated spectrum for a walled cavity decreased with decreasing neutron energy, while the measured spectrum increased. This difference was believed to be due to the neglect of δ-ray production. For events with medium energy deposition, the measured and calculated spectrums were nearly equivalent. But for events with high energy deposition, event frequency in the calculated spectrum was higher than that of the measured spectrum. The calculated single event spectra for the walled and wall-less TEPCs were in close agreement. For events with energy deposition from 20 to 55 keV (y: 4.6 - 12.7 keV/μm), there was a 2 % difference in event frequency, whereas for those with energy deposition from 55 to 370 keV (y: 12.7 - 85.4 keV/μm) there was no measurable difference. For events with energy deposition greater than 370 keV, the walled

TEPC had an event frequency 9 % greater than the walless TEPC. Since theoretical calculations had produced only 17 V-effect events out of 237,000 runs (0.007 %), the authors assumed that most of the observed wall effects must be from multiple scattering. Since the single event spectrum for the walled TEPC had exaggerated the frequency of high energy deposition events in comparison to that measured, it was concluded that the calculated response for high energy events was biased high and therefore, the expected response of walled and wall-less detectors would be nearly equivalent. Kellerer (1971b) concluded that the fraction of energy deposition involved in wall effects was small and would have an insignificant effect on the frequency, f(y), and dose, D(y), single event spectra for neutron energies below 10 MeV.

Heavy Charged Particles

Theoretical microdosimetric spectra from high velocity charged particles are not well established because: 1) distributions of highly energetic δ-rays are not known to a high degree of certainty (ICRU 1995) and 2) energy deposition from recoil nuclei from nuclear interactions have not been characterized. There is limited experimental work on the wall effects from HZE particles because of limited access to and the expense of operating particle accelerators.

Glass and Braby (1969) measured a broad beam of 5.3 MeV α-particles with a wall-less spherical counter. Theoretical calculations were made under the assumption that all energy transfers were locally deposited. Comparison of the two spectra clearly demonstrated the importance of δ-ray contributions to the single event spectra and the need for wall-less detectors in the fields of heavy charged particles.

Gross $et al.$ (1970) measured a broad beam of α-particles from an ^{241}Am source with a spherical wall-less TEPC simulating sites 0.5, 1, and 2 μm in diameter. In comparison of the single event spectra, the authors noted that the most probable value decreased as the

simulated site diameter became smaller. The most probable value of the spectra corresponds to α-particles traversals with the longest pathlength through the sensitive volume. The decrease in the most probable value is due to a decrease in the amount of energy deposited by δ-rays. Similarly, as the simulated site diameter decreased, the fraction of absorbed dose from indirect events increased. The authors compared the detector response from 5.44 (β = 0.053) to 8.8 MeV (β = 0.069) α-particles and found the relative contribution to absorbed dose from δ-rays created by indirect events to be higher for the α-particles of higher energy.

Rodgers *et al.* (1973) compared the response of spherical walled and wall-less (92 % transparent) TEPCs simulating sites 2 μm in diameter in the field of 279 MeV/nucleon ^{14}N ions (β = 0.638). The theoretical maximum δ-ray energy is 700 keV, significantly higher than that of 5.44 MeV α-particles (2.9 keV). The authors collected spectra for the two detectors at various depths in a phantom. Data with minimum absorber material upstream of the detectors indicated that the mean lineal energy of the walled detector was about 30 % higher than the wall-less detector. The difference between the response of the two detectors became less apparent when the velocity of the particles was reduced through additional absorber material. Near the Bragg peak, the difference in the dose mean lineal energy between the two spectra was less than 10 %. ICRU (1983) discussed the findings of this work and compared the single event dose distributions for each detector without absorber material. The most probable value of each distribution was nearly the same. The walled counter was deplete in low-energy deposition events that were present for the wall-less detector. But, the walled detector had a significantly higher number of high-energy deposition events as compared to the wall-less. High-energy deposition events were

attributed to "spallation and a contribution from δ-rays at low lineal energies" (ICRU 1983).

Dicello *et al*. (1991) found similar results in the comparison of spectra collected with walled and wall-less detectors in beams of bare Fe, Ar, and Ne with respective energies of 535, 570, and 557 MeV/nucleon (β: 0.772 - 0.784). In this work, direct comparisons of frequency and dose mean lineal energy values were not made because the geometry of the detectors was different.

Kliauga *et al*. (1978) measured the response of two spherical wall-less TEPCs in the field of 450 MeV/nucleon ($\beta = 0.738$) ^{40}Ar and 400 MeV/nucleon ($\beta = 0.715$) ^{12}C. One detector had a diameter of 2.54 cm and was 92 % transparent while the other had a diameter of 0.64 cm and was 88 % transparent. Both detectors were enclosed in a 10.15 cm diameter container. The ratio of container to cavity diameters for the two detectors were 4 and 16, respectively. For the experiments, 0.25, 1, and 4 μm diameter sites were simulated in both detectors. For the ^{40}Ar ions evaluated at the plateau, the ratio of the dose mean lineal energy of the physically larger diameter cavity to smaller was 1.45 when both detectors were simulating 1 μm. At the plateau, particle kinetic energy was 429 MeV/nucleon ($\beta = 0.73$), L was about 95 keV/μm, and maximum δ-ray energy was 1.15 MeV. Under similar conditions, measurements made with 10.5 cm of water absorber yielded a ratio in dose mean lineal energy between the detectors of 0.88. Under these conditions, L was about 210 keV/μm, $\beta = 0.46$, the maximum δ-ray energy was 0.27 MeV, and the wall effect was considerably less. The data collected with absorber material is difficult to interpret because the particle fluence had a significant contribution from fragment products and had considerable variance in particle velocity.

Contributions from this Work

This study of the wall effects from heavy ions extends the work done previously. An original and novel method of evaluating the wall effects of heavy ions in walled TEPCs was developed. The method involved the use of a particle spectrometer system that tagged every particle with identification of the charge and trajectory through the experimental set-up. Having knowledge of particle trajectory, the analysis could be tailored to evaluation of the response of the detector to a spatially uniform particle fluence. In previous work, beam spreaders (filters) were used to provide a more spatially uniform particle fluence than that of an unfiltered beam. Because the earlier work used beam spreaders, assumptions were made concerning the spatial uniformity of the beam. Furthermore, filters provided additional fragmentation and increased the variance in velocity of the primary beam. Both of these characteristics are undesirable because they diminish the validity of the assumption of a homogenous beam of particles. Thus, conclusions from these works were concerning qualitative in nature because the beams were not homogenous. The spectrometer system use in this work allowed evaluation of particles that had similar velocity and the same charge by selection on the energy deposition in a series of silicon detectors.

This work evaluated the wall effects for 1 GeV/nucleon Fe particles, higher energy than previous work. The highest energy/nucleon ions used in earlier work was 600 MeV/nucleon. The energy spectra of galactic cosmic HZE particles extends from about 0.1 to 10 GeV/nucleon, with the majority of the fluence between 0.1 and 1 GeV/nucleon. Thus, the wall effects characterized in this work represents a practical upper bound, as the distortions created by the δ-ray effect increase for increases in ion velocity.

The primary focus of this work was the:

1. characterization of the δ-ray effect to a monoenergetic beam of Fe particles based on particle trajectory through the detector,

2. calculation of $\overline{Q}$ for Fe particles based on measured energy deposition in a TEPC and under assumptions that $y = L$ and $8/9y = L$, and

3. comparison of known Q factors for Fe to those calculated.

This work was possible because a particle spectrometer system was used. These details were absent from earlier work on heavy ions.

In the work by Rodgers *et al.* (1973), the ICRU (1983) speculated on the cause of the very high energy deposition events observed in the single event spectra collected by a walled TEPC. Because a particle spectrometer system was used in this work, evidence as to the mechanism responsible for these events could be provided.

Also, in addition to analysis of detector response to Fe ions, preliminary evaluations are provided for detector response to:

1. ions with Z lower than Fe (with the same velocity as Fe particles) and

2. events where the incident Fe particle is involved in a charge-reducing nuclear interaction in the wall of the detector.

Both of these evaluations are considered preliminary because the number of events analyzed was limited. More complete evaluations would require significantly longer beam time. For these experiments, a 6.35 mm thick copper target was used. Increased fragmentation could be produced through use of thicker targets, but increased variance in the velocity of primary and secondary particles will be introduced.

Chapter 3: Materials and Methods

Beam-Line Experimental Set-Up and Equipment Description

Experiments were conducted at the Alternating Gradient Synchrotron (AGS) at Brookhaven National Laboratory (BNL) using ^{56}Fe ions with an on-target energy of 1.053 ± 0.005 GeV/nucleon ($\beta = 0.883$). Figure 3-1 shows a schematic diagram of the experimental arrangement. The TEPC was about 30 cm from each PSD pair.

Figure 3-1. Experimental Arrangement (Not to Scale).
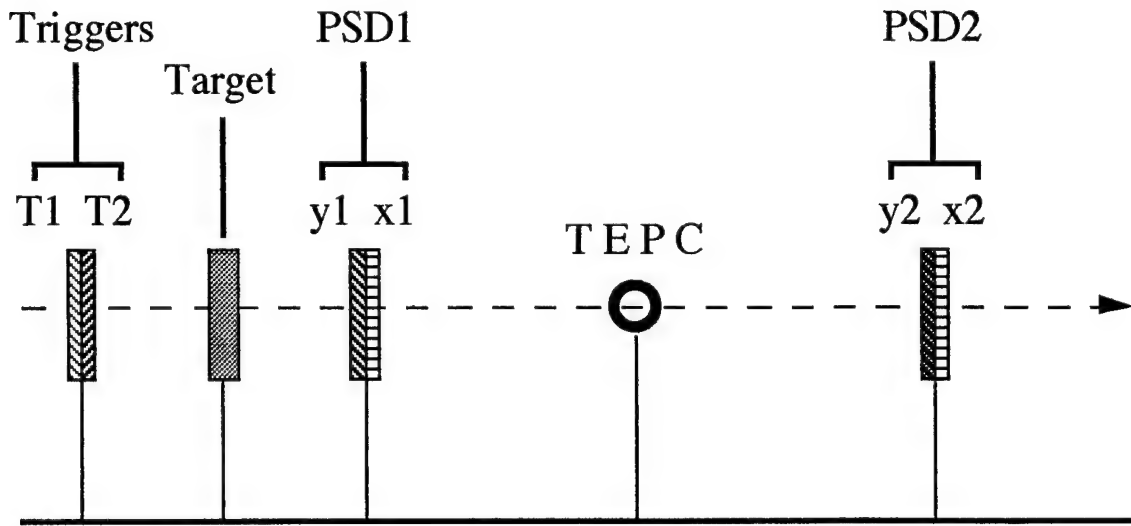
The two trigger detectors, T_1 and T_2, were 330 μm thick silicon detectors with active areas of 300 mm^2. The output signal from each was sent to a locally-mounted charge -sensitive preamplifier, a variable-gain shaping amplifier, and a peak-voltage sensing analog-to-digital converter (ADC). Coincidence between T_1 and T_2 defined the trigger and gates for the experiment. A pair of position-sensitive detectors (PSD1) was placed between the triggers and TEPC, while another pair (PSD2) was placed downstream of the TEPC. Each pair was oriented to provide horizontal and vertical information, designated as (x_1, y_1) and (x_2,

y_2) in Fig. 3-1. Each position-sensitive detector also provided a signal that was proportional to the total energy deposited (i.e., $\Delta E\, y_1$, $\Delta E\, x_1$, . . .). In context, ΔE is a measure of stopping power, dE/dx, without normalizing the signal by the thickness of the silicon detector. A complete description of the PSDs is provided by Wong *et al* . (1990). One experiment was conducted with a 6.35 mm copper target while all others were without a target.

Tissue-Equivalent Proportional Counter Spherical proportional counters[1] with internal cavity diameters of 12.7 mm (0.5 in) were used. Figure 3-2 shows cross-sectional diagrams of the thin-walled detector, while Figure 3-3 provides cross-sectional diagrams of the thick-walled one. The left diagram of both figures is a cross-sectional view on the same plane as the experimental set-up given in Fig. 3-1. The right diagram is a cross-sectional view along the beam axis. The A-150 plastic wall had a thicknesses of 1.27 and 2.54 mm, respectively for the two detectors. A stainless steel central anode wire was coaxially surrounded by a stainless steel helix 1 mm in diameter. The potential between the helix and anode was used to create a symmetrical electric field along the length of the anode (ICRU 1983). A hole in the wall was introduced for gas filling. Since this hole was located on the upstream side of the thin-walled detector, particles intersecting this region of the detector were rejected from analysis. The vent hole for the thick-walled detector was on the downstream side of the detector. Each detector was encapsulated within a 0.018 mm shell of aluminum that maintained the desired vacuum. Figure 3-4 shows "pathlengths" through the cavity and wall with respect to impact parameter (distance from the detector center) for the thin and thick-walled detectors.

The proportional counters were filled with propane-based tissue equivalent gas consisting of CO_2, N_2, propane, and a trace amount of isobutane in mass fractions shown in Table C-1. The ideal gas law:

---

[1] Far-West Technologies, Goleta CA

Figure 3-2. Cross-Sectional Diagrams of Thin-Walled TEPC

Cross-Sectional View Along Beam Axis

Cross-Sectional View Perpendicular to Beam Axis

S/N 1373

33
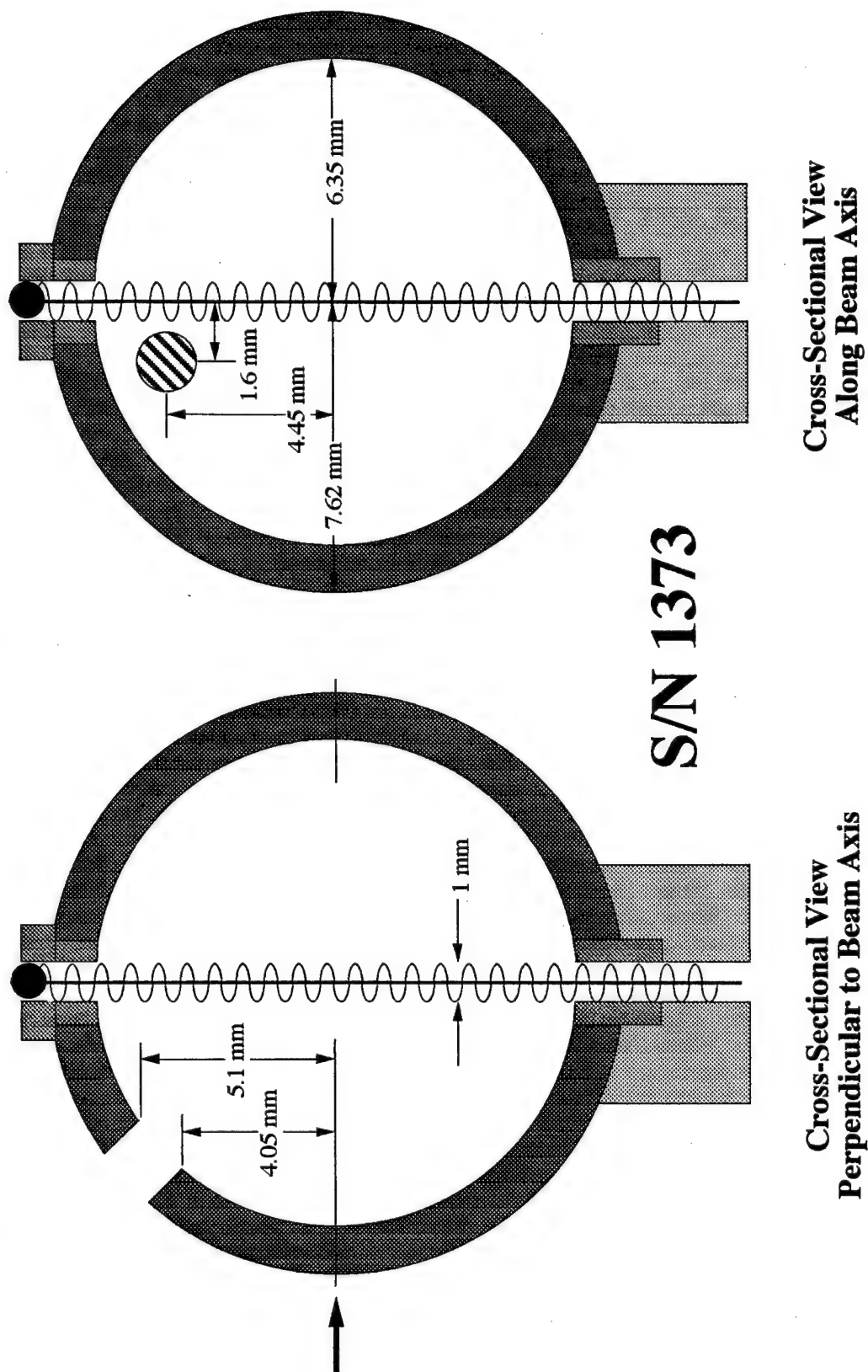
Figure 3-3. Cross-Sectional Diagrams of Thick-Walled TEPC

Cross-Sectional View
Along Beam Axis

Cross-Sectional View
Perpendicular to Beam Axis

S/N 1376

5.35 mm

6.35 mm

8.89 mm

1.6 mm

4.05 mm

5.1 mm

1 mm
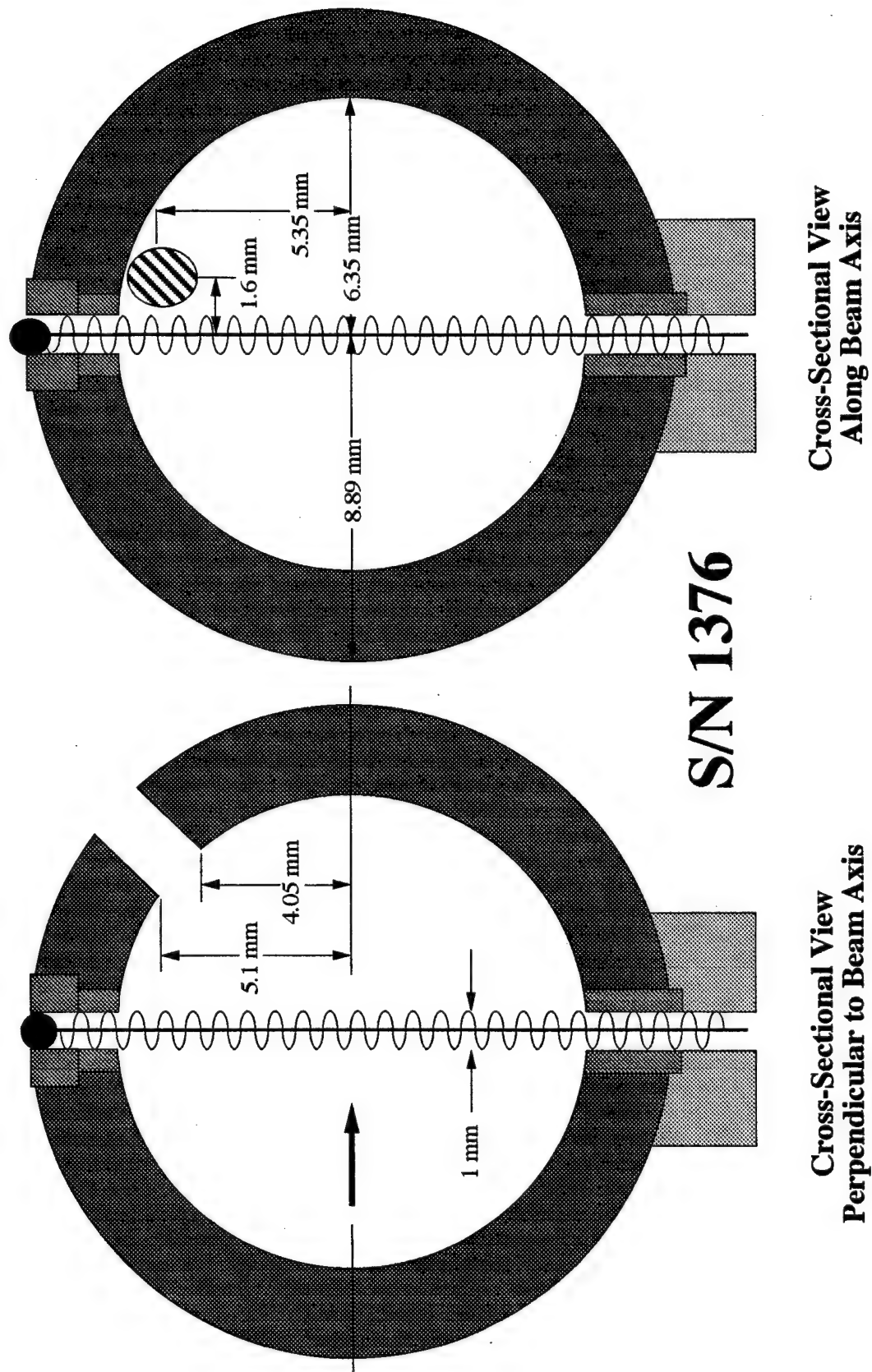
$$P V = n R, \qquad\qquad (3\text{-}1)$$

was used to determine pressure, P, of the gas required to simulate the required diameters where V is detector volume, n is number of moles of the fill gas, and R = 24.1 liter atm mole^{-1} at 21° C.

Figure 3-4. Cavity and Wall Pathlengths for the Thin- and Thick-Walled Detectors.
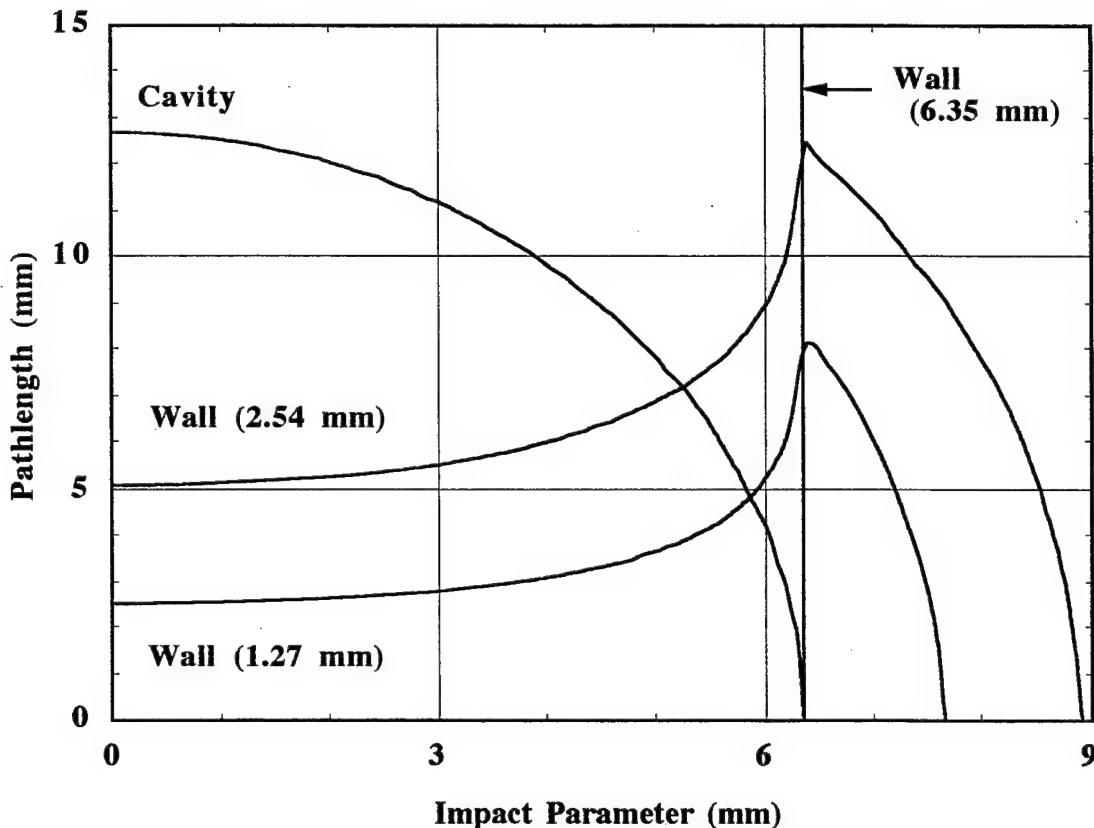
Table C-1 summarizes the calculated parameters for simulation of a 3 μm diameter site at 21°C and pressure of 13,332 Pa (100 mmHg). Other diameters were simulated by directly scaling the pressure. For each use of the detector, a minimum of three flushings of the detector were performed prior to use.

The ratio of densities between the wall and fill gas was about 14,400, 9,600, and 4800, respectively for simulated unit density diameters of 1, 2, and 3 μm.

35

Table 3-1. Calculated Parameters for Propane-Based Tissue-Equivalent Gas at
21 °C, Volume = 1.0725 cm³, Pressure = 13,332 Pa, and Simulated Diameter = 3 μm.

Molecule	Mass Fraction	Moles	Molecular Weight (grams)	Mass (grams)
CO_2	0.3939	2.30×10^{-6}	44.01	1.013×10^{-4}
N_2	0.0564	3.30×10^{-7}	28.02	9.237×10^{-6}
C_3H_8	0.5485	3.21×10^{-6}	44.09	1.414×10^{-4}
C_4H_{10}	0.0012	7.01×10^{-9}	58.12	4.077×10^{-7}
Total	1	5.847×10^{-6}	—	2.523×10^{-4}

Detector bias potentials were selected to provide reasonably high gas amplification with acceptable proportionality. A summary of bias potentials used for each detector and simulated site diameter is listed in Table 3-2.

Table 3-2. TEPC Bias Potentials (Volts).

Detector	1 μm	2 μm	3 μm
Thin (SN 1373)	600	618	658
Thick (SN 1376)	598	606	644

Calibrations were performed using the most probable event size value (unscattered α-particles) from a built-in gravity controlled ^{244}Cm α-radiation source. Using published values of stopping power values (ICRU 1993) and applying a continuous slowing down approximation to account for energy loss in the detector, the mean energy transferred from unscattered α-particles crossing the cavity diameter was 84.1 keV/μm for the thin-walled detector at 1 μm. Calibrations were also performed using the proton edge from an unmoderated $^{239}PuBe$ neutron source and α-edge from the built-in α-source by the technique described by Schrewe *et al.* (1993). When empirical functions of Goodman and

Coyne (1980) for mean energy per ion pair formed (W) were applied, all three methods agreed to within $\pm$ 2.4 %. Details of the calibrations are in Appendix B.

The output signal from the detector was sent to a locally-mounted charge-sensitive preamplifier, split, and sent through two identical variable-gain shaping amplifiers with a ratio of gains equal to 16.

Data Analysis

Particle Identification

The first step in the analysis consisted of evaluating energy deposited in the sequence of trigger detectors and positional devices. Since data were recorded on an event by event basis, the silicon devices could be used to determine particle species along the experimental beamline.

Signals in the trigger detectors were normally distributed about a mean value corresponding to the energy loss, ΔE, of Fe. Events with ΔE beyond $\pm$ 3σ of the mean in either T_1 or T_2 were rejected from the analysis to insure particles entering the target or PSD1 were iron.

Similarly, for the experiments conducted without a target, an event was rejected if ΔE in PSD1 and PSD2 was beyond $\pm$ 2.5σ from the mean corresponding to Fe. For the experiment conducted with the Cu target, individual particles species could be identified and selected for analysis based on the ΔE signal in the PSDs. The relative location of the peaks in the PSD ΔE distributions were roughly proportional to the Z^2 of the particle responsible for each peak.

Particle Trajectories

An analysis of y_1 vs. y_2 and x_1 vs. x_2 indicated that the vertical and horizontal position of individual particles through the two PSD pairs had good correlation indicating that the beam was highly parallel. Events without good correlation were believed to be due to

37

nuclear collisions at some location along the beam axis. Because the purpose of the experiments conducted without the Cu target were to characterize the response of the TEPC to Fe particles not involved in nuclear interactions, events without good correlation were rejected from analysis. The experiment with the Cu target was not screened for trajectory correlation.

The exact location of the TEPC in reference to the PSD's was accomplished using an iterative process that imaged the shape of the detector in each PSD pair. This was done by selecting either very small energy deposition events (i.e., particles that passed outside of the wall) or very high energy deposition events (i.e., particles that passed along the cavity/ wall interface). The final uncertainty in the horizontal and vertical location of the detector center was estimated to be less than 0.1 mm.

After the geometry was established, the trajectory of each particle that satisfied the ΔE selection criteria was reconstructed under the assumption that the particle had a straight trajectory through the system. The impact parameter (i.e. perpendicular distance from the center of the detector) and chord length through the detector were computed and placed in a data file with other information associated with that event. Details of these calculations are provided in Appendix D. Lineal energy was computed for the two TEPC response signals by dividing the energy deposited, ε, by the mean chord length of the simulated sphere. For simulation of a 1 μm diameter sphere, the mean chord length for μ-random particle traversals was $\frac{2}{3}$ μm. The lineal energy from the two amplified TEPC signals overlapped at about 20 keV μm^{-1}. The two signals were combined into one in for data analysis.

TEPC Response vs Impact Parameter for Experiments without Cu Target

Detector response was evaluated in terms of lineal energy as a function of the impact parameter of the trajectory. This was done using two methodologies. The first method sorted events into sequential intervals of impact parameter from 0 to 9.6 mm. There were

about 1000 events in each interval and the mean value of energy deposition associated with that impact parameter was determined by fitting the data to a normal distribution.

Uncertainties in positional information can have a large effect on observed energy deposition for impact parameters near the cavity/wall interface where the TEPC response varied rapidly with small changes in impact parameter. For these regions of the detector, the selection process was reversed. Events were sorted into sequential intervals of energy deposition and an analysis of the impact parameter was performed each interval. Both methods converged to the same result for intermediate regions.

Experiment with CU Target

The data from this experiment was split into three separate data files based on the particle identified in PSD1 and PSD2.

1. **Fe in PSD1 and PSD2** Events in this data file had a ΔE signal in all four PSD devices that was within $\pm 2.5\sigma$ of the mean corresponding to Fe.

2. **Fe in PSD1, but Fragment in PSD2** Events in this data file had a ΔE signal in both PSD1 detectors, but had a ΔE signal at least 2.5σ less that the mean corresponding to Fe in both PSD2 detectors. These events were believed to be involved in charge-changing nuclear interactions somewhere between the two PSD pairs, with the likeliest location being in the wall of the TEPC. Because the Fe particles were involved in a nuclear interaction, the assumption that particle had a straight trajectory between the two PSD pairs is invalid. The impact parameter for these particles was based only on the position data in PSD1 and will have greater uncertainties than determination of impact parameter using both pair of PSDs. Appendix D provides estimates of the uncertainties in impact parameter. Since the response of unfragmented Fe particles (above) are compared to this data, impact parameter was calculated for the Fe events in this manner as well so bias is not introduced.

3. **Fragment in PSD1 and PSD2** Events in this data file had a ΔE signal at least 2.5σ less than the mean corresponding to Fe in all four PSD detectors. These events were believed to be involved in charge-changing nuclear interactions between T_2 and PSD y_1, with the likeliest location being in the copper target. Due to the low number of fragments produced in the copper target, the analysis was restricted to evaluation of energy deposition of fragments with impact parameter less than 3 mm.

Model for Energy Deposition

The Chatterjee model was used to calculate energy deposition in a 1 μm diameter sphere for a range of impact parameters using an LET of 149 keV/μm in propane-based TE gas (ICRU 1993). Details of the calculations are provided in Appendix A.

Chapter 4: Results

Energy Deposition Measurements in the Position Sensitive Devices

Figure 4-1 is a plot of energy deposition in PSD y_2 for the experiment with the thin-walled detector and copper target in place. The prominent peak near 270 MeV corresponds to Fe particles and the peaks with lower values of ΔE correspond to fragments. The plot is truncated to display the peaks for energy deposition of fragments of $Z = 17$ (Cl) to unfragmented Fe. For charge-changing interactions at this velocity, the fragments have velocities close to the velocity of unfragmented Fe. Accordingly, ΔE values for individual peaks scaled closely to the Z^2 of the ion as expected from the Bethe-Bloch stopping power formula (Attix 1986).

Normal distributions were fit to the Fe peaks in the energy spectra of the four PSDs. The coefficients of variation (CV) (σ/μ) were less than 2 %. Discrimination of Fe events from fragments using paired PSD ΔE signals (i.e. $\Delta E\, y_1$ & $\Delta E\, x_1$) was accomplished with less than 1 % probability of falsely selecting a fragment, based on the mean energy deposition for Fe, Mn, and the CV of the data in each peak.

Figs. 4-2a and b are ΔE distributions for PSDs x_1 and y_1 after Fe was selected in T_1, T_2, and PSD1. The CVs for the two distributions were 1.575 $\pm$ 0.004 % and 1.454 $\pm$ 0.004, respectively, based on normal distribution fits to the data. Variance in the distributions is caused by many factors including: 1) energy straggling, 2) variance in energy deposition due to non-uniformity's in detector thickness, 3) random errors in signal

41

Figure 4-1. ΔE in PSD Y2 for Experiment with Copper Target (Labels Correspond to the ΔE of Individual Ions)
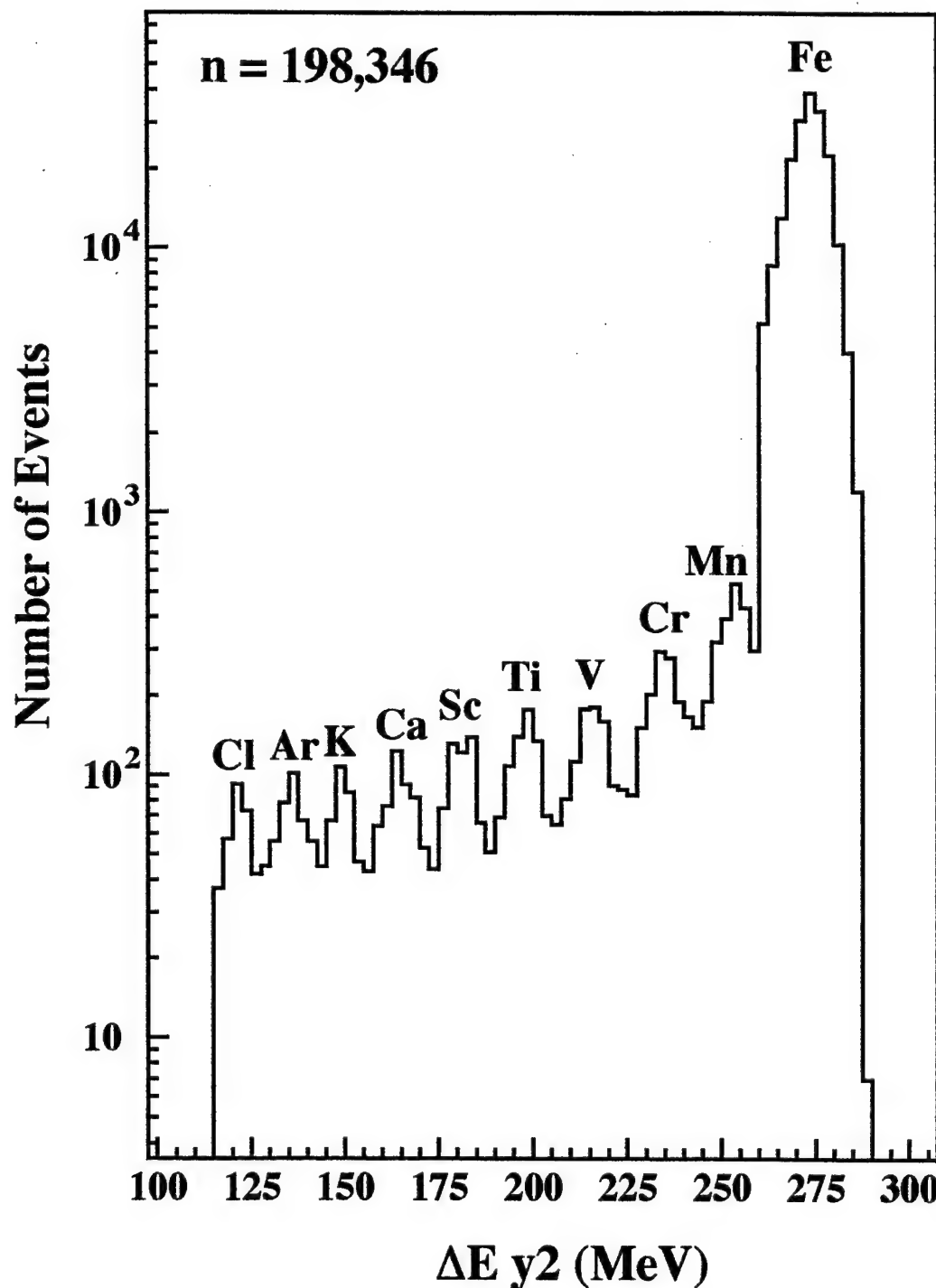
Figure 4-2. Energy Deposition Distributions of Fe Peaks in PSD X1 and Y1

a

n = 131,383
μ = 279.3
σ = 4.40
CV = 1.58 %

ΔE x1 (MeV)

Number of Events

b

n = 131,383
μ = 258.2
σ = 3.75
CV = 1.45 %

ΔE y1 (MeV)

43
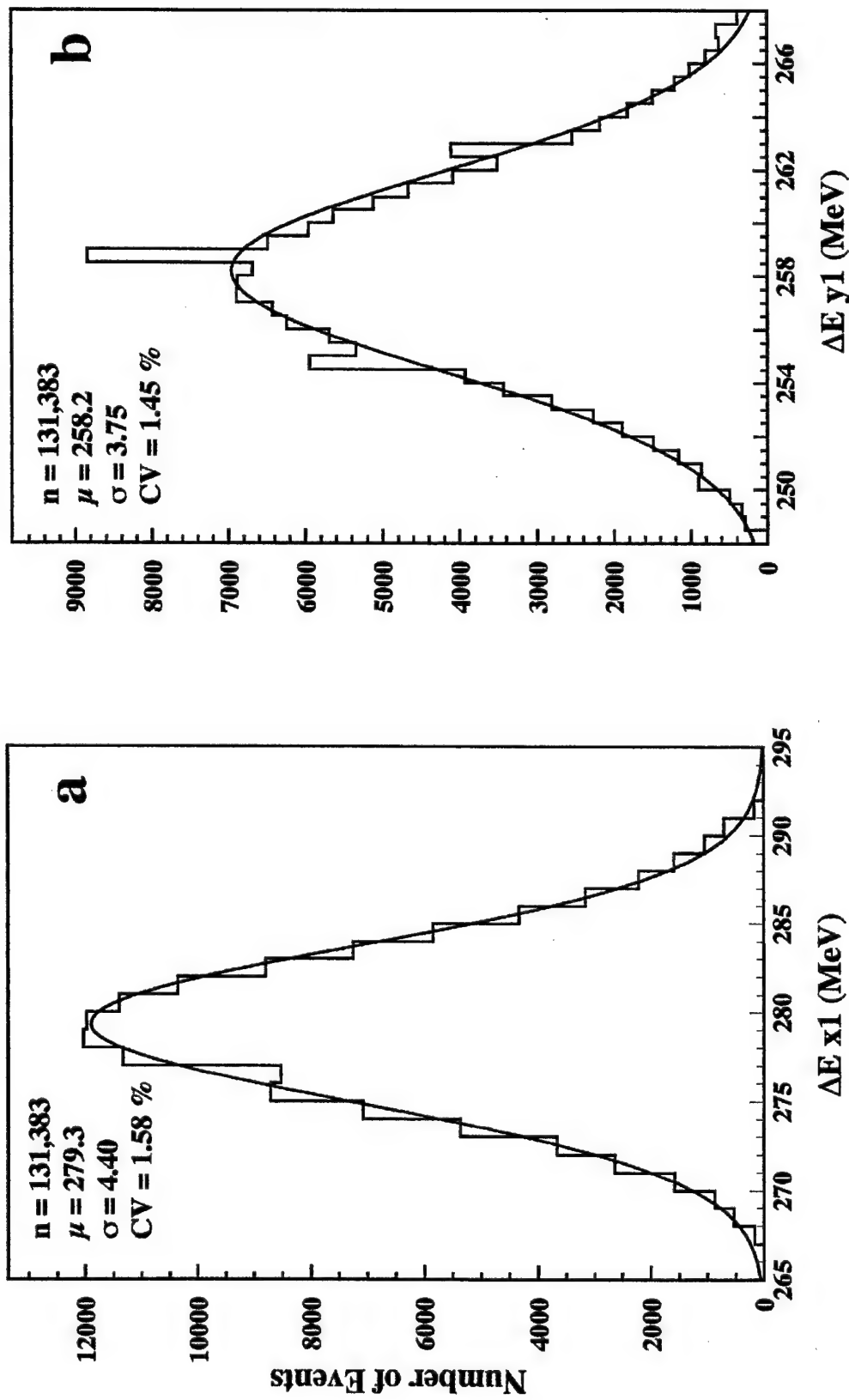
processing, 4) variance in the stopping power of the particles, and 5) variance in energy deposition due to pathlength variations through the PSDs.

All of the factors are stochastic in nature and independently affect the energy deposition in a single PSD. Additionally, the first three factors independently affect energy deposition between each detector in a PSD pair. However, the last two factors are covariant and will affect the energy deposition in each detector in a PSD pair in the same manner.

Per discussions with Dr Zeitlin (1997), the CV introduced by each of the first two factors was about 1 % and jointly account for the majority of the variance in the distributions of Fig. 4-2. To assess the relative contribution of the last factor on the variance in energy deposition, an evaluation of particles trajectory was performed. From distributions of $x_2 - x_1$ and $y_2 - y_1$ for Fe particles that traverse through PSD1 and 2 without charge-reduction fragmentation, distributions of pathlength through the PSDs could be calculated. The CV of pathlength through the PSDs was estimated at 8×10^{-4} %. This value is very small compared to the total CV of energy deposition in the PSDs.

A distribution of $\left[\dfrac{\Delta E\, y_1}{\Delta E\, x_1} \right]$ for the events of Fig. 4-2 is plotted in Fig. 4-3. The data agrees well to a normal distribution. The CV for this distribution is 1.936 ± 0.004 %. Appendix E contains an analysis of variance of the data given here. The estimated covariance between $\Delta E\, y_1$ and $\Delta E\, x_1$ was 3.1 MeV^2 and represents about 22 % and 16 %

of the total variance in $\Delta E\, y_1$ and $\Delta E\, x_1$, respectively. All factors contributing to the covariance between the energy deposition in the two detectors is not known. Variance in stopping power of the Fe particles is one factor. Without knowledge of the contribution of all factors, however, it can be concluded that the covariance introduced by the variance in stopping power is limited by the total covariance. Therefore, because the covariance between the two distributions is low, it can be concluded that the Fe particles used for analysis were very homogenous in stopping power.

Figure 4-3. Distribution of (ΔE y1 / ΔE x1) for Fe Particles in PSD1

n = 131,383
μ = 0.925
σ = 0.0179
CV = 1.94 %

Number of Events

(ΔE y1) / (ΔE x1)
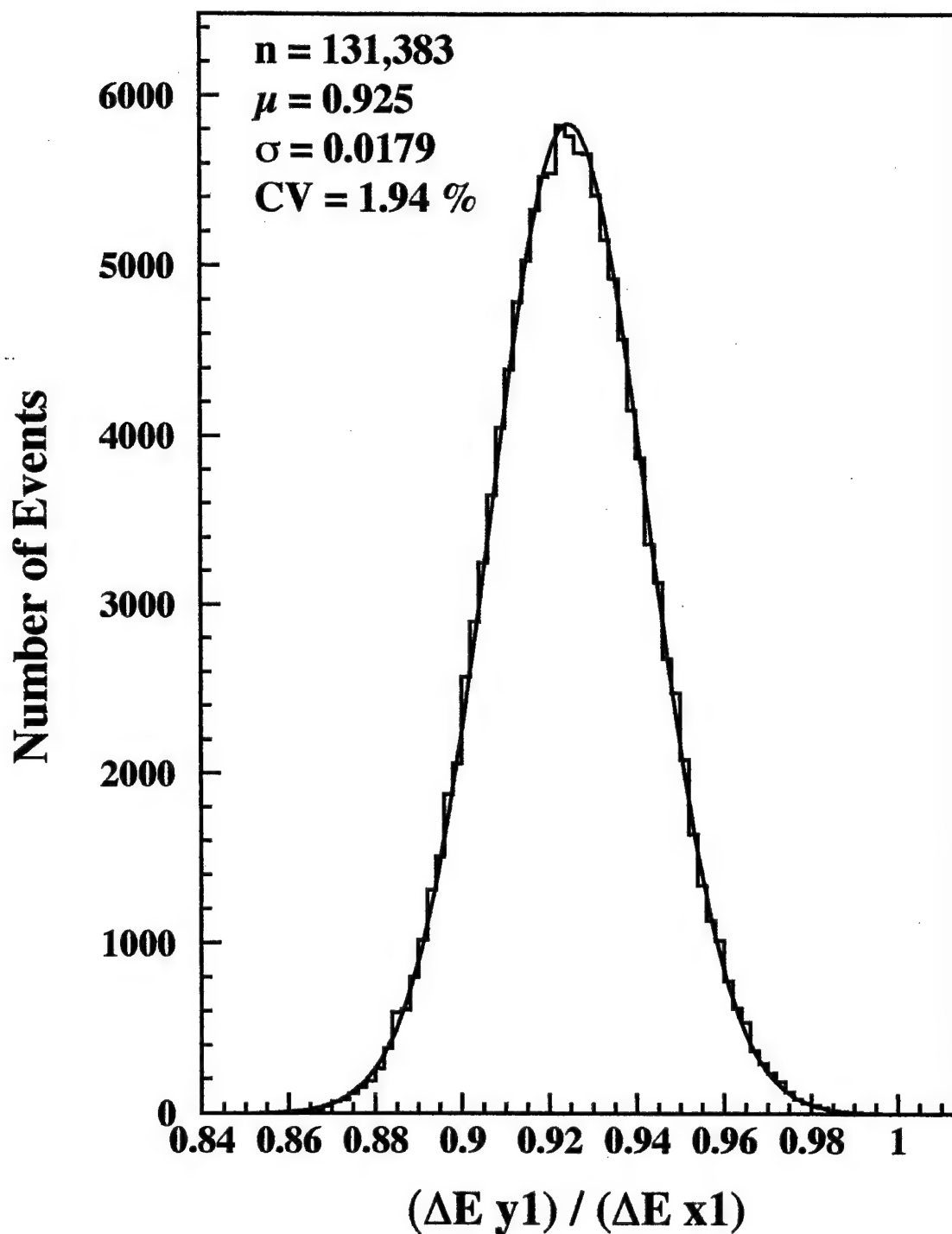
Positioning of the TEPC

The location of the TEPC in the z-dimension was known based on measured distances between the PSDs and TEPC. However, fine positioning of the device in the x-y plane was based on evaluation of the TEPC response. Fig. 4-4 is a plot of detector response for Fe particles in the thin-walled TEPC. A 1 μm diameter site was simulated without the copper target .

Fig. 4.5a is a scatter plot of x_1 vs. y_1 for events that have lineal energy distinctly greater than those in the peak of the distribution ($y \geq 210$ keV μm^{-1}). About one-third of these events are located in proximity to the anode and helix wires and are assumed to have hit a wire. The enhanced energy deposition is likely due to energetic δ-rays produced in the wire. The other events are located in proximity to the cavity/wall interface.

By selection of events with lineal energy much higher than 210 keV μm^{-1}, wire hits events could be eliminated . The distribution of events with $y \geq 255$ keV μm^{-1} were located primarily in proximity to the cavity/wall interface. For position determinations, these events were assumed to arise from trajectories at the cavity/wall interface (impact parameter = 6.35 mm). After many iterations of estimating scaling and position offset factors for each PSD pair, coordinates of a line through the TEPC center and the PSD pairs was made. Fig. 4-6 contains a histogram of impact parameter for events with $y > 255$ keV μm^{-1}. For events in the peak of the distribution, the mean was estimated at 6.356 $\pm$ 0.019 mm. The percent fractional error of the this value with the specified detector radius of 6.35 mm was (- 0.2, + 0.4 %).

Figure 4-5b is a scatter plot of x vs. y in the detector plane for events with lineal energy between 25 and 35 keV μm^{-1}. The scatter plot was generated for corrected position parameters and is reflected by (0, 0) coordinates of the detector center and circular symmetry of the particles with respect to center. The deviation of the particles from a perfect circular pattern arises from uncertainties in the positional devices and variance in the actual location of interaction. Particles distant from the circular pattern were assumed to be

Figure 4-4. **Detector Response to Fe Particles with a Simulated Diameter of 1 μm (No Target)**

n = 110168

Number of Events

y (keV/μm)

47
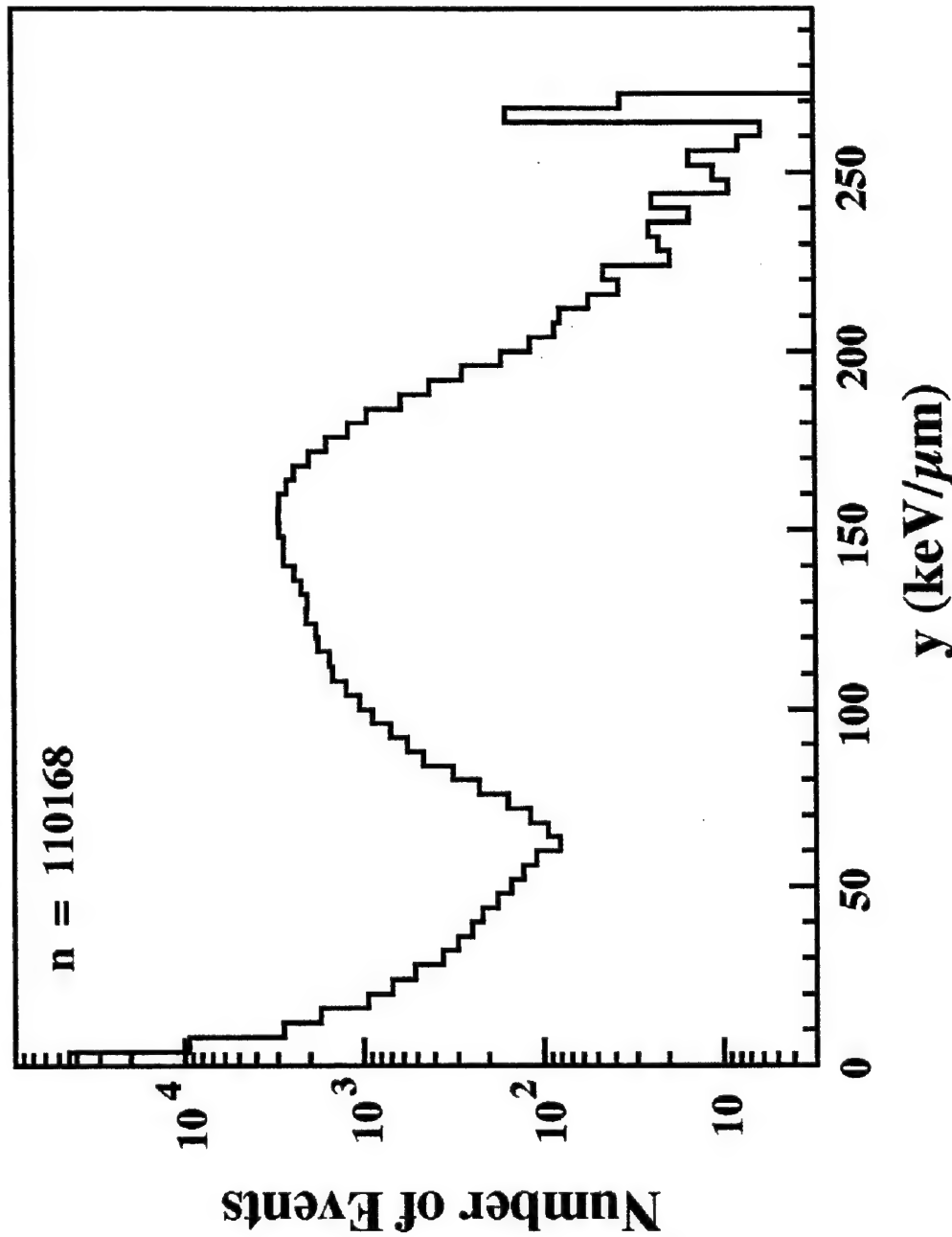
Figure 4-5. Scatter Plots in Position for Detector Response to Fe Particles in Two Selected Intervals of Lineal Energy [Simulated Diameter = 1 μm, a) uncorrected position signals, b) corrected signal positions]
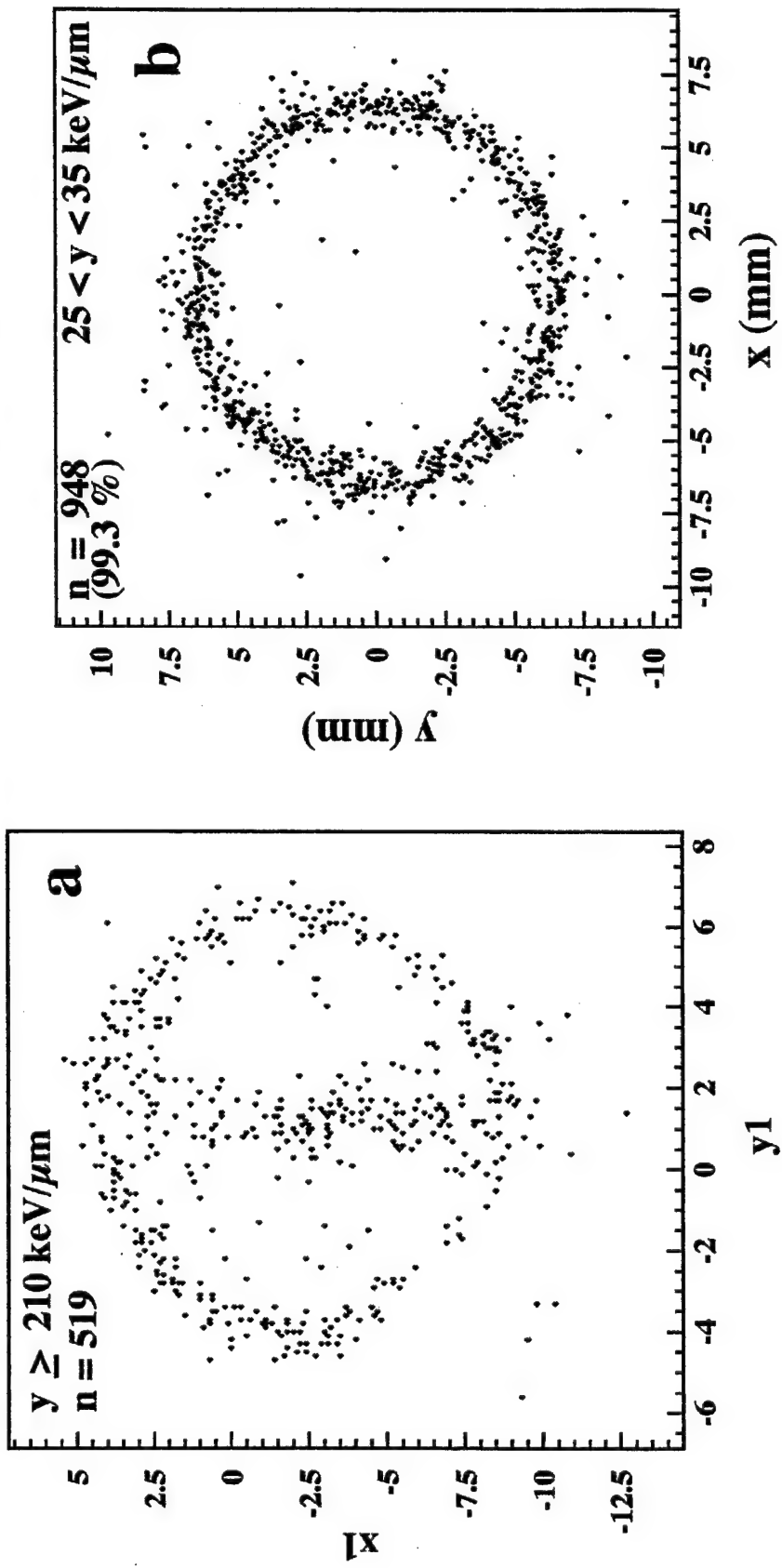
the result of nuclear scattering. The mean impact parameter of unscattered particles was about 6.6 mm and corresponds to trajectories though the wall but not the cavity. Nuclear scattering will be discussed later in detail.

Impact Parameter Uncertainties and Bias

Uncertainties in impact parameter were estimated based on the distribution of impact parameter for events with $y \geq 255$ keV μm^{-1}. At the cavity/wall interface, the estimated uncertainty in impact parameter was assumed to be approximately equal to the standard deviation of the events contained in the peak. For events between 5.7 and 7.0 mm in Fig. 4-6, the standard deviation was 0.23 mm. Uncertainties in impact parameter were estimated to be close to 0.23 mm for the entire range of impact parameter, based on the assumption that uncertainty in impact parameter was caused by the uncertainty in position signals from the PSDs. Details of the evaluation are in Appendix D.

Uncertainties in position signals from the PSDs will propagate bias in calculated values of impact parameter. Estimations of bias in impact parameter were made with Monte Carlo simulations detailed in Appendix D. The bias was positive and had the greatest values for small impact parameters. The estimated bias was less than 2.6 % for impact parameters greater than 1 mm. The bias was determined to have a negligible effect on this work because: 1) the interval of impact parameters that contained significant bias in impact parameter reflected a small fraction of the total fluence and 2) the detector response in the interval of impact parameter having the greatest bias had the most uniform detector response. A summary of estimated of bias values are in Appendix D.

Detector Response vs. Impact Parameter for Fe

Fig. 4-7 shows the distribution of lineal energy for Fe particles in the thin-walled detector for several selected intervals of impact parameter. Collectively, these distributions were used to construct the detector response vs. impact parameter.

Figure 4-7a Fig. 4-7a corresponds to trajectories through the center of the detector. The solid line represents a fit to the peak using a normal distribution. The CV for the

Figure 4-6. Distribution of Impact Parameter for Fe Events with High Lineal Energy

n = 175

y ≥ 255

impact parameter
interval: 5.7 - 7.0

$\mu = 6.35$

$\sigma = 0.23$
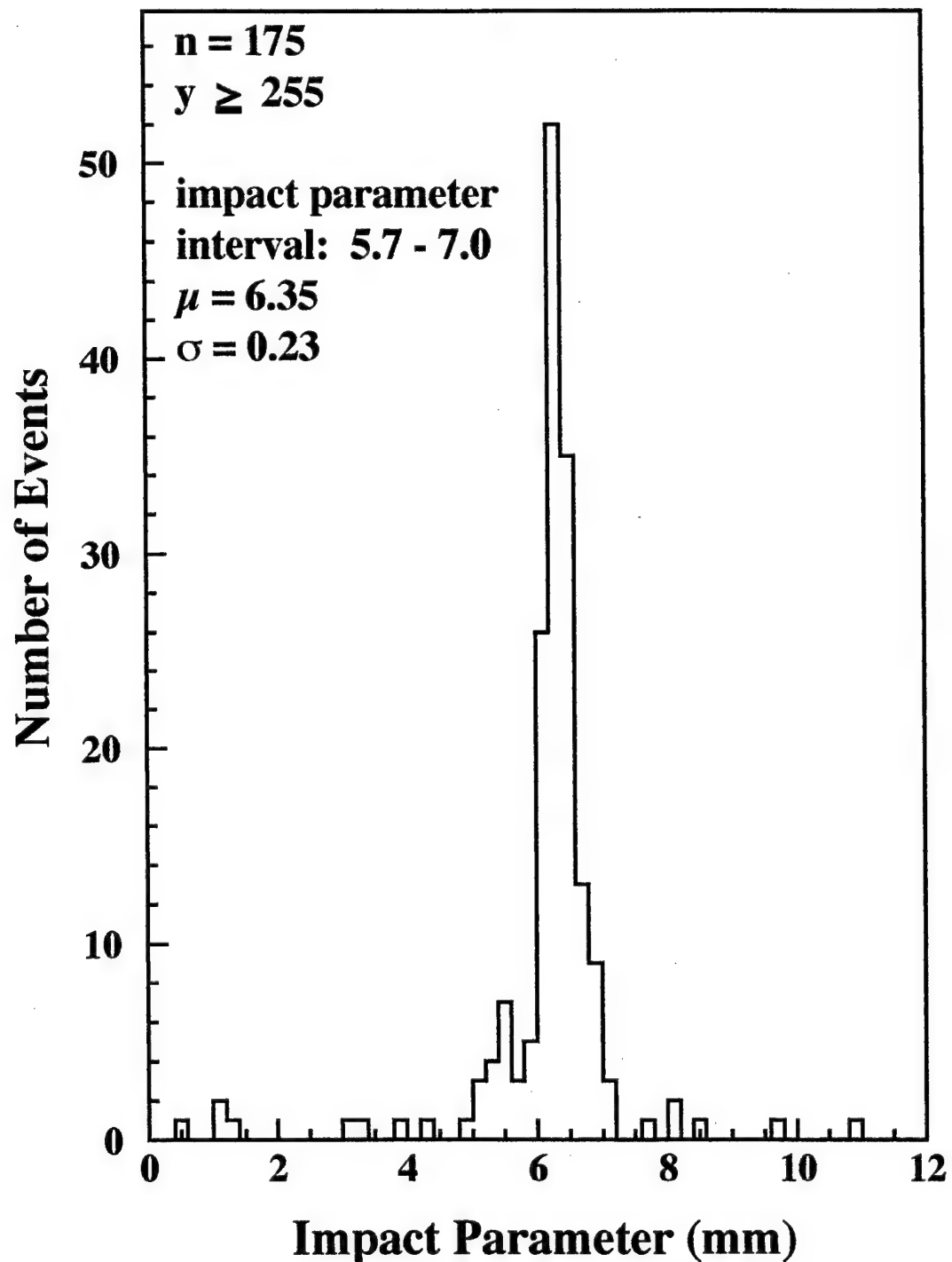
Figure 4-7. Detector Response to Fe for Selected Impact Parameter Intervals [Simulated Diameter = 1 μm]

impact parameter
interval: 4.04 - 4.21 mm

n = 1295
μ = 150.7
σ = 17.5
CV = 12 %

impact parameter
interval: 0 - 0.8 mm

n = 524
μ = 167.8
σ = 13.6
CV = 8.1 %
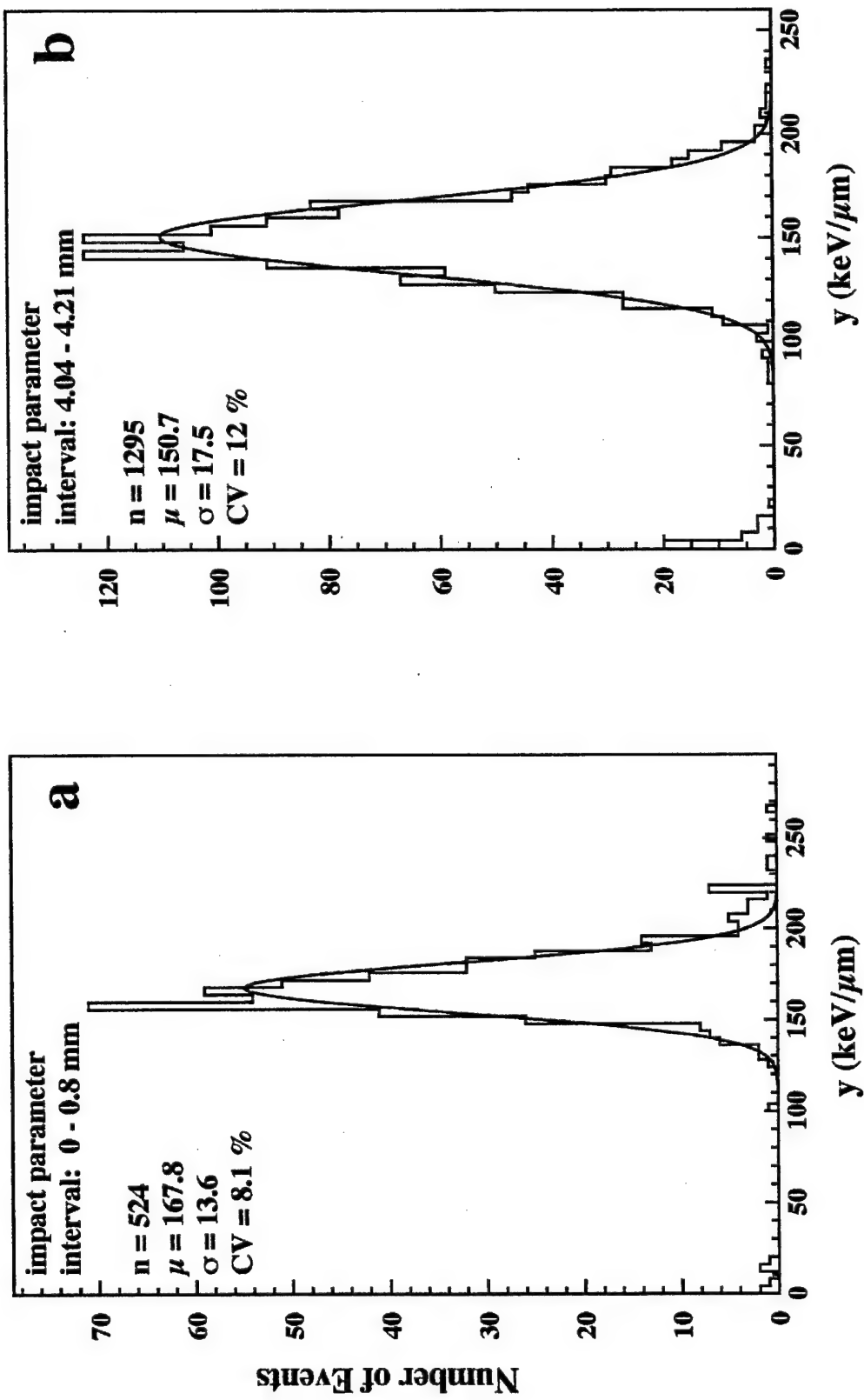
Figure 4-7 cont. Detector Response to Fe for Selected Impact
Parameter Intervals [Simulated Diameter = 1 μm]
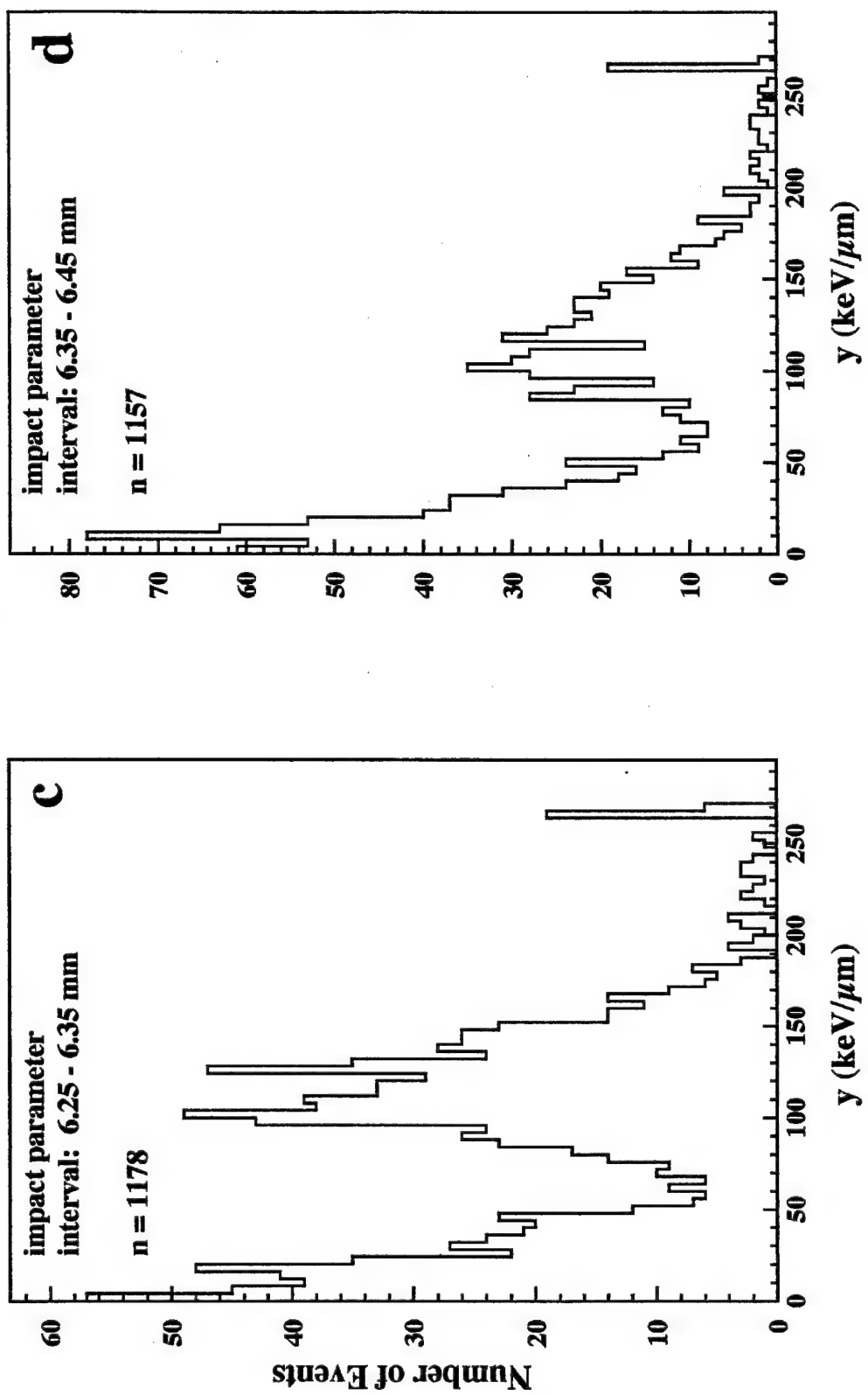
distribution was about 8 %. An analysis of variance indicated that this was primarily due to energy straggling and variations in gas amplification. There were a few events that occurred beyond the tails of the normal distribution. The higher values were attributed to trajectories through the anode and helix wires (wire hits). Very small values of lineal energy were attributed to events with nuclear interactions in the walls of the detector. These particles were believed to have impact parameters near the cavity/wall interface. Scatter of the incident particle caused the calculation of impact parameter to be incorrect.

Trajectory Analysis

All of the distributions of lineal energy had events of lineal energy below the tail of the normal distribution. To determine whether these events were the result of nuclear scattering processes, distributions of $(x_2 - x_1)$ were created using events with impact parameter ≤ 3 mm. Events with impact parameter in this range were selected because it was broad enough to provide a sufficient number of particles for analysis, but sufficiently distant from the wall such that events with incorrect impact parameter would be due primarily to nuclear scattering rather than that caused by PSD uncertainties alone.

Fig 4-8a contains a plot of lineal energy for Fe events in the thin-walled detector simulating 1 μm. The distribution of $(x_2 - x_1)$ for a selection of particles with lineal energy about the mean of the peak is shown in Fig. 4-8b. The mean of this distribution was -3.6 mm with a standard deviation of 0.77 mm. These events were assumed to be unscattered through the TEPC. Similar distributions were collected for events with lineal energy in the intervals: $0 - 50, 50 - 100, \geq 210$ keV μm^{-1}, and repeated for the thick-walled detector. A summary is provided in Table 4-1. From the table, the mean and standard deviations of the events in the intervals: $0 - 50$ and $50 - 100$ keV μm^{-1} are significantly different than that for events in the peak region of the distribution. In particular, the standard deviations of these distributions are considerably higher. As these particles are otherwise identical to the particles assumed to be unscattered, it is logical to conclude that the increase in standard deviation is due to scattering. The events with $y \geq 210$ keV μm^{-1} have distributions of

53

Figure 4-8. Detector Response, and (X2 - X1) for Particles in Peak Region, for Fe Events with Impact Parameter ≤ 3 mm
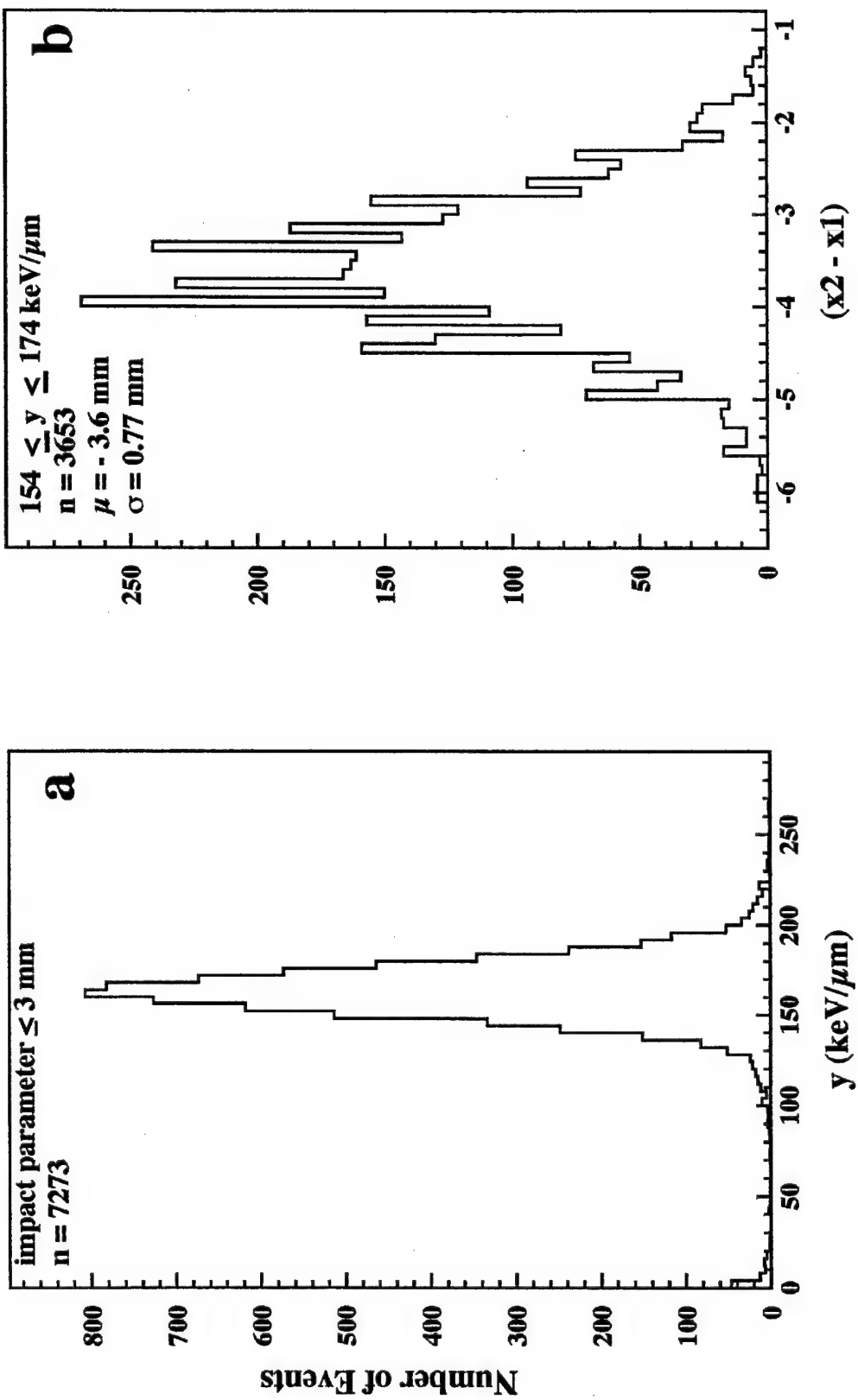
$(x_2 - x_1)$ with mean and standard deviation similar to that of the events in the peak. This indicates that it is unlikely that these events were involved in nuclear scattering.

Table 4-1. $(X_2 - X_1)$ Summary Data for Fe Particles with Impact Parameters ≤ 3 mm in the Thin- and Thick-Walled Detectors [Simulated Diameter $= 1$ μm].

Lineal Energy Interval (keV/μm)	Parameter	Detector	
		Thin-Walled	Thick-Walled
All	n	7273	6813
Peak	n	3653	3174
	$(x_2 - x_1)$ μ (mm)	- 3.6	- 4.0
	$(x_2 - x_1)$ σ (mm)	0.77	0.78
0 - 50	n	88	106
	$(x_2 - x_1)$ μ (mm)	- 3.1	- 3.6
	$(x_2 - x_1)$ σ (mm)	1.2	1.2
50 - 100	n	18	12
	$(x_2 - x_1)$ μ (mm)	- 3.2	- 3.6
	$(x_2 - x_1)$ σ (mm)	0.92	1.3
≥ 210	n	62	148
	$(x_2 - x_1)$ μ (mm)	- 3.5	- 3.9
	$(x_2 - x_1)$ σ (mm)	0.83	0.76

Figure 4-7b Fig. 4-7b shows the data for impact parameters between 4.0 and 4.2 mm. The CV for the fitted distribution was 12 %. The impact parameter interval is for a region of the detector where small changes of impact parameter introduce larger changes of pathlength through the cavity due to the curvature of the spherical wall. Thus, uncertainties in the measured position of the particle are associated with a larger variance in lineal energy compared with particles passing through the center of the detector.

Figure 4-7c and d Fig. 4-7c shows the data for impact parameters between 6.25 and 6.35 mm. These should be trajectories just inside the cavity/wall interface. However,

because of uncertainties in position measurements and nuclear scattering, the data also contains particles that do not traverse the cavity. The central region of the abscissa ($70 < y < 170$ keV μm^{-1}) corresponds to trajectories through the cavity. The region of small y (< 70 keV μm^{-1}) corresponds to trajectories through the wall-only and the large y (> 170 keV μm^{-1}) are from trajectories that graze the cavity/wall interface.

Fig. 4-7d shows the data for impact parameters between 6.35 and 6.45 mm. These should be trajectories just outside the cavity/wall interface. The distribution is similar to that of Fig. 4-7c for large y events, but is enhanced in low y events and suppressed in medium y events.

Figure 4-9 Figure 4-9a shows the detector response for impact parameters between 7.95 and 8.1 mm for Fe particles in the thick-walled detector simulating 1 μm. Distributions of ($x_2 - x_1$) were generated separately for events less than 25 keV μm^{-1} (small y) and those greater than 25 keV μm^{-1}. Figure 4-9b shows the distribution for events greater than 25 keV μm^{-1} with mean and standard deviations of -3.6 and 1.20 mm, respectively. The distribution for the small y events is not displayed, but had a mean and standard deviation of -4.2 and 0.85 mm, respectively. For the large y events, the standard deviation is 41 % higher than the small y events and indicates that these events were likely involved in nuclear interactions. It is reasonable to conclude that these events had trajectories through the cavity, but had incorrect impact parameter due to nuclear scattering. Although, the large y events are few in number, the mean detector response will be biased to higher values for these intervals of impact parameter.

Impact Parameter vs. TEPC Response for Fe

Impact parameter uncertainties and incorrect calculation of impact parameter due to nuclear scattering, made assessment of detector response difficult by the method used above for trajectories near the cavity/wall interface and in the wall-only. An alternate method of analysis was used to overcome these difficulties. Distributions of impact parameter were created based on selected intervals of detector response. Figure 4-10

Figure 4-9. Detector Response, and (X2 - X1) for Particles with y > 25 keV/μm, for Fe Events with Impact Parameter: 7.95 - 8.1 mm

57
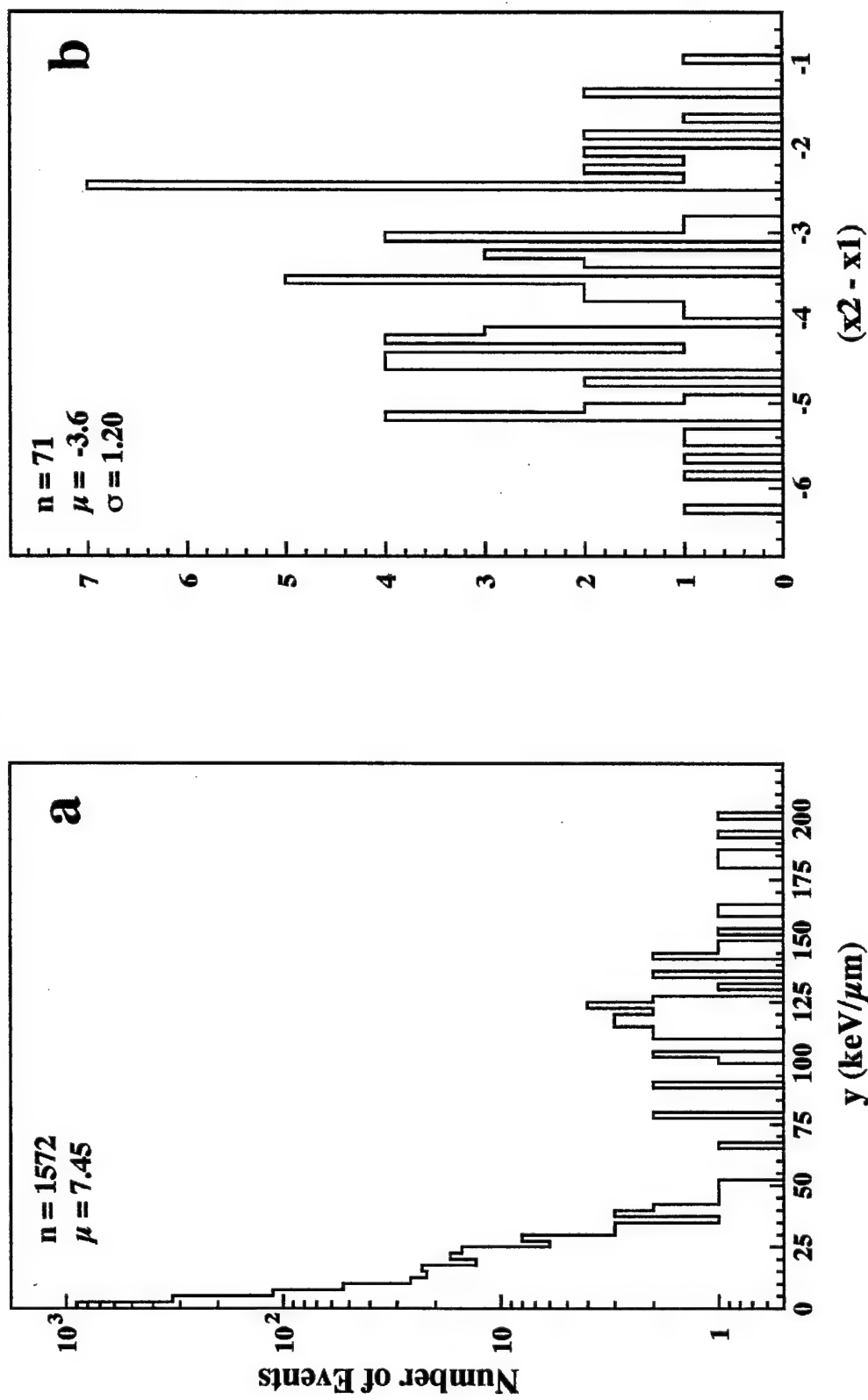
Figure 4-10. Distributions of Impact Parameter for Selected Intervals of Detector Response in the Thin-Walled Detector [Simulated Diameter = 1 μm]

58
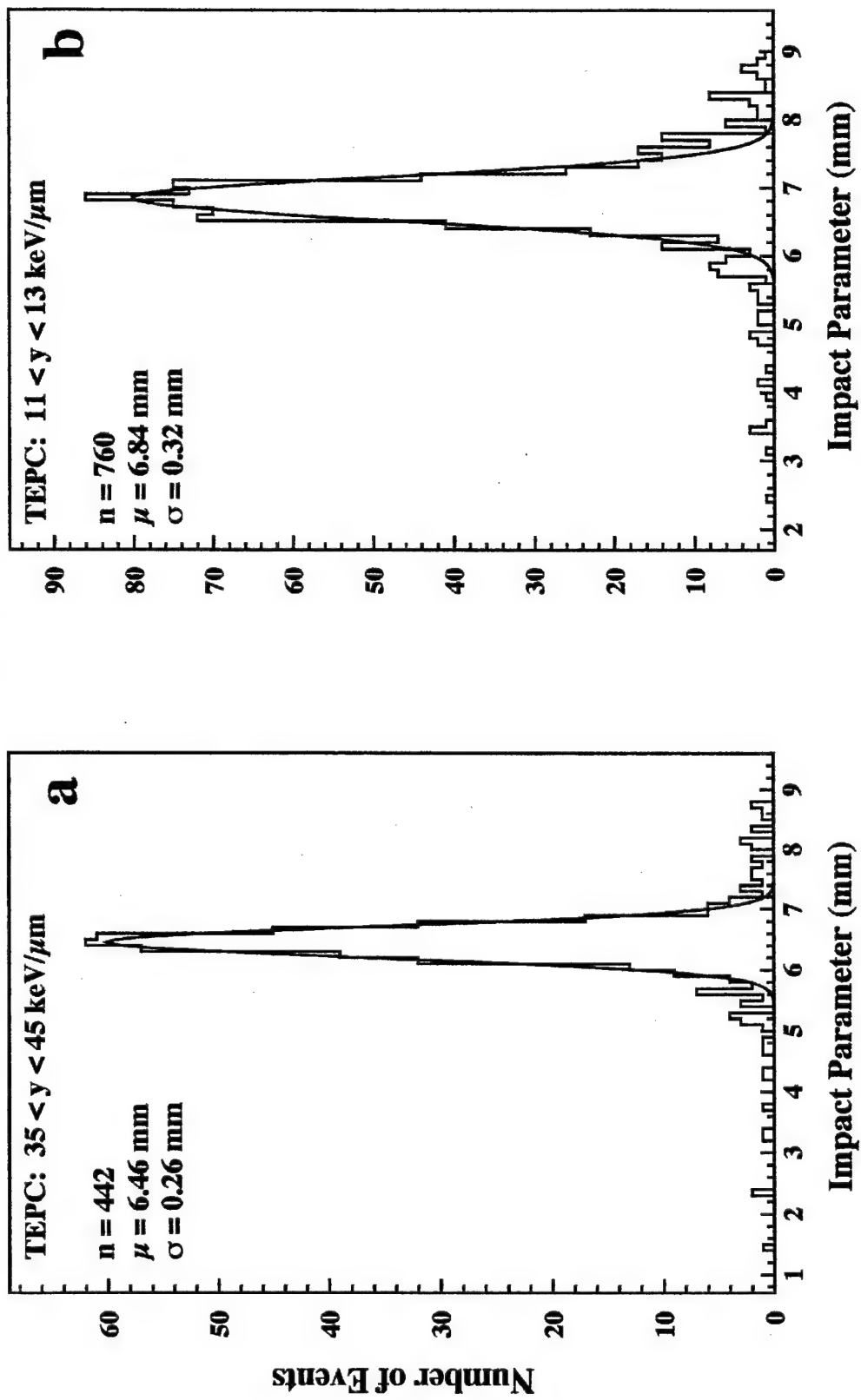
provides two examples of impact parameter distributions for selections of detector response in the thin-walled detector simulating 1 μm. For each distribution, the solid line represents a normal distribution fit to the peak of the data. Based on the mean of the normal distributions, these events were for trajectories through the wall-only. The standard deviation of the normal distributions were 0.26 and 0.32 mm, respectively, for the data of Figs. 4-10a and b. Overall, for distributions created in this manner, the standard deviations of the normal distribution fits to the peak were at a minimum at the cavity/wall interface. This trend in the data is logical since the incremental change in detector response vs. the change in impact parameter was maximum at the cavity/wall interface. This trend was consistent for the two detectors regardless of the simulated diameter.

Composite Plots of TEPC Response vs. Impact Parameter for Fe Events

General

Composite plots of TEPC response vs. impact parameter were generated by combining the data from both of the methods described above. Figure 4-11 shows the overlap in data for in the intermediate region of impact parameter. The data from the two methods overlap well from 4 to 4.7 mm. For the individual experiments, plots of the overlap region were made. The interval of impact parameter with the best overlap in the two data sets was selected qualitatively based on visual inspection. The data of detector response, based on selection of events within intervals of impact parameter, was truncated for impact parameter intervals greater than the overlap region. While, the data of impact parameter, based on selection of events within intervals of detector response, was truncated for impact parameters less than the overlap region.

1 μm Simulated Diameter Experiments - Fe Only

Figure 4-12 is a plot of mean lineal energy vs. impact parameter through the TEPC for the thin-walled detector to Fe particles. The open circles represent the data with a smooth line through the distribution of points. The vertical bars on two of the data points represent the standard deviation of the data at these points. The solid line represents lineal energy in

Figure 4-11. Overlap in Data for Both Analysis Methods in the Intermediate Region of Impact Parameter for the Thick-Walled Detector for Fe Particles [Simulated Diameter = 3 μm, Representative Errors Bars Shown for Solid Circles (●), Vertical Errors Bars for Open Circles (○) were between 0.5 to 0.7 keV μm^{-1} (not shown)]
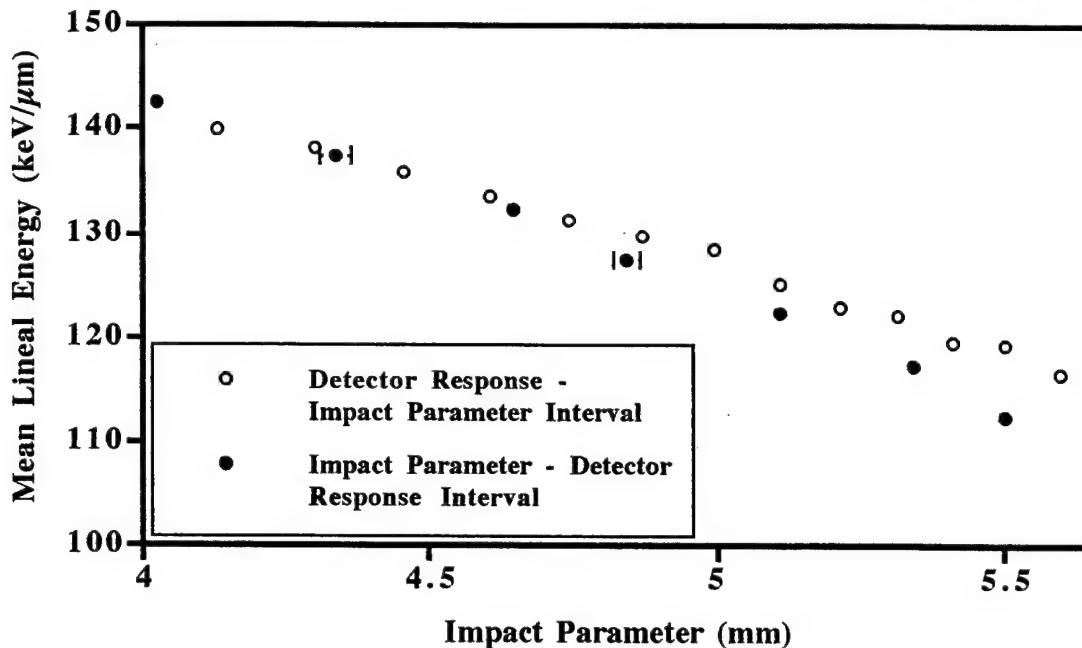
a sphere of tissue that is 1 μm in diameter using the Chatterjee model that includes radial energy loss due to high energy δ-rays. The solid circles correspond to the distribution of lineal energy for particles with L = 149 keV μm^{-1} but assuming that all energy transfer is absorbed locally. Thus, there is no loss of energy radially and ε = L • pathlength through the cavity.

For trajectories through the center of the gas cavity, the mean lineal energy obtained from the model is 70 % of the value for particles with no radial energy loss. However, the data were higher than predicted by the model that only incorporated radial energy loss. This implies that there is a significant reduction in energy deposition due to the escape of δ-rays and that this is only partially compensated by δ-ray production in the front wall of the detector.

Figure 4-12. Data from Experiment with Fe Particles in Thin-Walled Detector Simulating 1 μm [Open Cirles (O) is Data, Solid Line is Chatterjee Model, and Solid Circles (●) is Particles without Radial Loss of Energy]

61
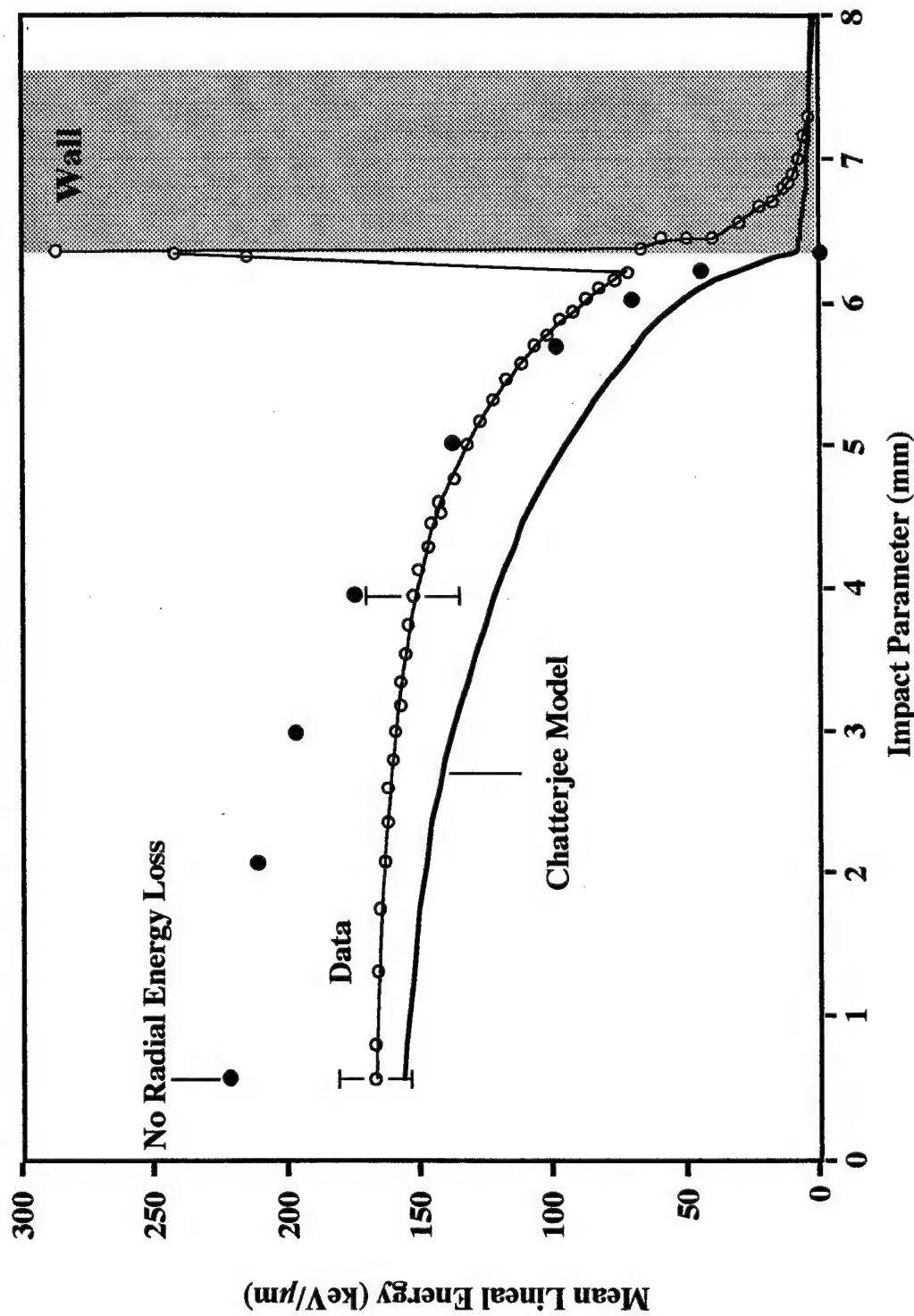
For trajectories near the cavity/wall interface, the data are higher than the model that does not include radial energy loss. Thus, the reduction in energy deposition in the cavity due to the escape of δ-rays created in the cavity is more than compensated by the added energy deposition from δ-rays created in the wall.

Figure 4-13 is a plot of mean lineal energy vs. impact parameter through the TEPC for the thick-walled detector. The open circles represent the data with a smooth line through the distribution of points. The solid line is the distribution of lineal energy using the Chatterjee model as in Fig. 4-12.

1. **Moments of the Distribution of Mean Lineal Energy.** The data in Fig. 4-13 were used to determine $\overline{y}_F$ and $\overline{y}_D$ for μ-random (ICRU 1983) Fe particles at 1 GeV/nucleon. Table 4-2 provides a summary of the results compared with computations assuming that $\varepsilon = L \bullet$ pathlength through the cavity. Calculations were performed according to the method in Appendix F. A marked difference exists in the frequency mean lineal energy, with the data having a value nearly half of that for the particles with no radial energy loss from δ-rays. The dose mean lineal energy values are closer, with the value for the data being 15 % lower than that of the model compared.

Table 4-2. Computed $\overline{y}_F$ and $\overline{y}_D$ Based on Measured Response of Fe Particles in the Thick-Walled Detector Compared to Calculations for Particles with $L = 149$ keV μm^{-1}

	Data (keV μm^{-1})	$\varepsilon = L \bullet$ pathlength (keV μm^{-1})
$\overline{y}_F$	79	150
$\overline{y}_D$	143	169

Figure 4-13. Data from Experiment with Fe Particles in Thick-Walled Detector Simulating 1 μm [Open Cirles (O) is Data, Solid Line is Chatterjee Model]
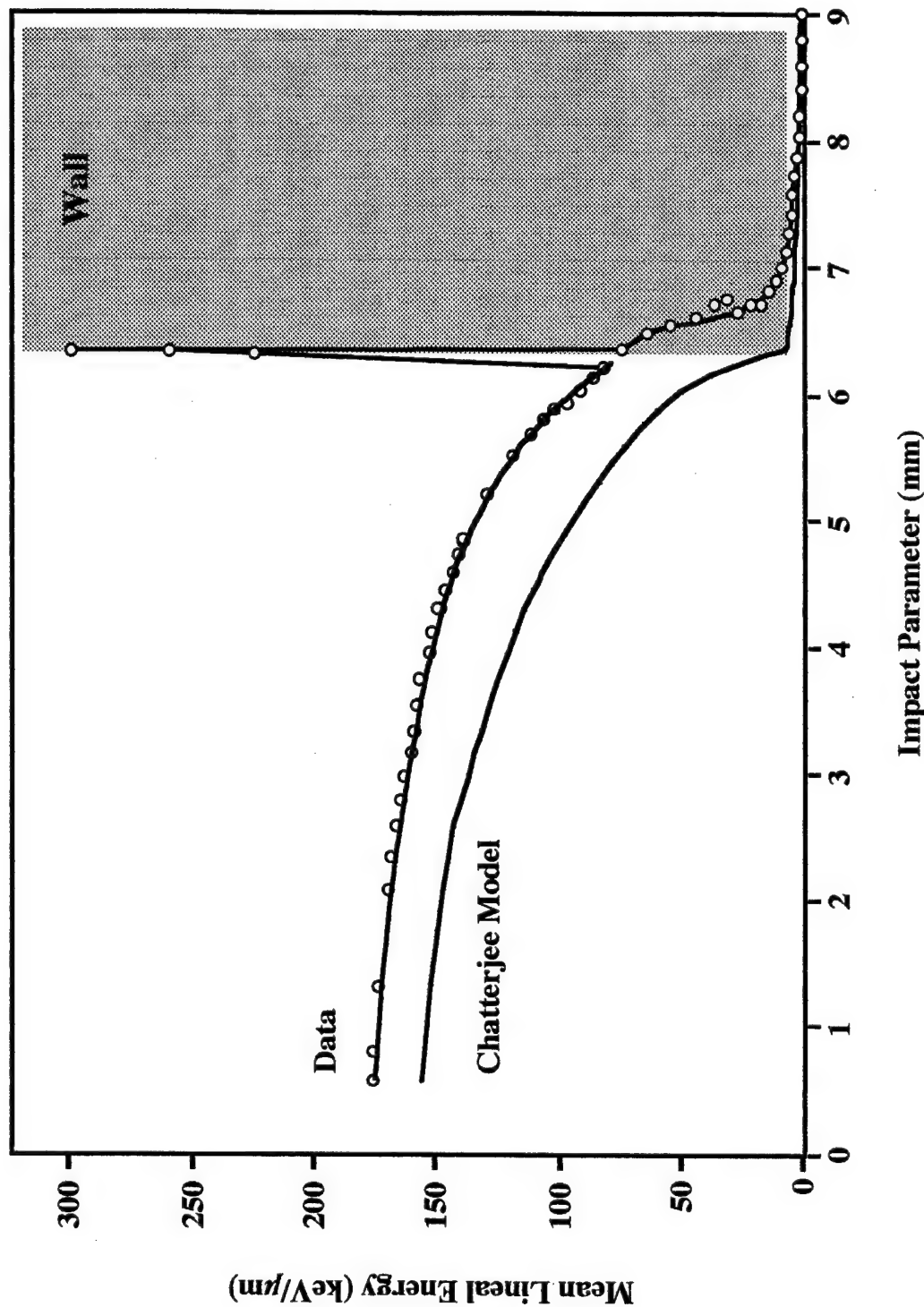
2. Comparison of Data to Homogenous Case (Chatterjee Model)

Figure 4-14 is a plot of the ratio of mean lineal energy measured in the thin- and thick-walled detectors to that of the Chatterjee model. The ordinate of the primary plot is on a logarithmic scale while the abscissa is based on the impact parameter squared, that weighted the data to a μ-random irradiated detector. The abscissa of the small inset plot is on the same scale as the primary plot, but has a truncated linear ordinate scale. The inset plot emphasizes the smaller ratios for impact parameters near the center of the detector.

The ratio of the data to the model is small for intervals of impact parameter through the center of the cavity, with the thick-walled detector being slightly higher. The enhanced response in the thick-walled detector over the thin-walled in this region is likely due to a higher number of δ-rays produced in the front wall of the detector.

The ratio of the data to the model is the greatest at the cavity/wall interface, with the highest ratios due to grazing events. The ratio of the data to the model was high for trajectories through the wall-only, with the response of the thick-walled detector being higher than that of the thin. This result would be expected since the pathlength through wall material is greater for these trajectories in the thick-wall detector as compared to the thin (see Fig. 3-4) and would result in a greater number of δ-rays being produced.

3. Charged Particle Equilibrium (CPE) in the Thick-Walled Detector

"Charged particle equilibrium (CPE) exists for a volume if each charged particle of a given type and energy leaving the volume are replaced by an identical particle of the same energy entering, in terms of the expectation values," according to Attix (1986). For walled cavity detectors, CPE can be approximated if the thickness of the wall is greater than the maximum penetration range of secondary particles produced and the wall material is of approximately the same atomic composition (to provide equivalent mass stopping power in both media). For the detectors used in this work, the wall material and fill gas had very similar atomic composition. For 1 GeV/nucleon particles, the maximum kinetic energy of

Figure 4-14. Ratio of Measured Values of Mean Lineal Energy to Chatterjee Model for the Thin- and Thick-Walled Detectors to Fe [Simulated Diameter = 1 μm]
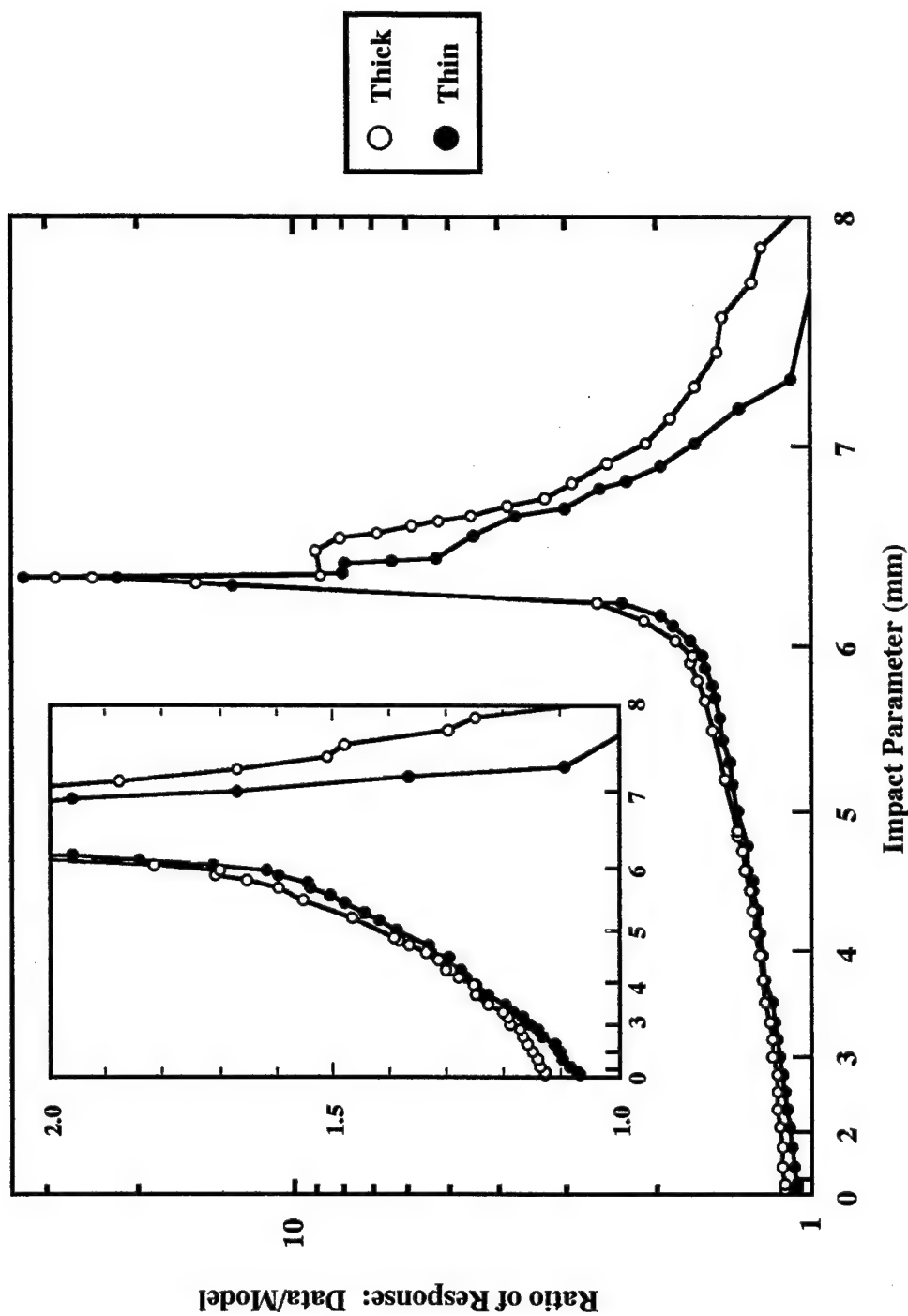
an electron is about 3 MeV and has an approximate CSDA range of 1.5 cm in water. However, the fraction of energy transferred to the medium by electrons of this energy is very small. The thick-walled detector has a wall thickness of 2.54 mm and will completely stop all electrons with energy lower than 0.76 MeV. It is assumed here that approximate CPE can be achieved in the thick-walled detector.

The data in Fig 4-13 can be used to determine if the enhancement in energy deposition by δ-rays created in the wall is sufficient to create CPE for a μ-random fluence of Fe particles. Calculations were performed according to the method described in Appendix F. The mean lineal energy deposited in the cavity for a μ-random fluence corresponded to an effective L of 154 keV μm^{-1}. For CPE, this value should equal L. The value obtained here is 3 % higher than expected for CPE. Possible reasons for the difference are: a) calibration uncertainties, b) position uncertainties, and c) a possible difference between W for the α-particle calibration source and the Fe ions.

4. Calculated Mean Quality Factors Mean quality factors, $\overline{Q}$, for the response of the thick-walled detector to a μ-random Fe particles were calculated using:

      a. ICRU 40 and

      b. ICRP 26 and 60 with:

         (1) L = y

         (2) L = 8/9 y (Stinchcomb and Borak 1982).

Identical calculations were performed for μ-randomly incident particles on the detector, but without radial energy loss (i.e. $\varepsilon = L \cdot$ pathlength through the cavity). Calculations of $\overline{Q}$ for other ions found in the galactic cosmic radiation spectrum were made. The calculations were made for the same velocity of Fe, but with L and detector response scaled according to the Z^2 of the ion compared to that of Fe. This scaling procedure should provide reasonable accuracy because the doubly differential electron spectra of ions of high velocity scales roughly according to Z^2 (ICRU 1996). Details of the method of calculation

are provided in Appendix F. Tables 4-3 and -4 provide a summary of the results of the calculations for the data and model, respectively.

For the experimental data, ICRU 40 provided higher $\overline{Q}$ (for all ions but He) than the two calculations using ICRP 26. For ICRU 40 compared to ICRP 60, some $\overline{Q}$ were higher while some were lower. For the ions without any δ-ray losses, ICRU 40 provided higher $\overline{Q}$ values than either calculation with ICRP 26 and 60, except He.

Figures 4-15 and -16 are bar graphs of the percent discrepancy in the calculated $\overline{Q}$ of the data from Tables 4-3 and -4. For the experimental data, the percent discrepancy was negative or near zero for both ICRP report recommendations. The calculations of $\overline{Q}$ using $y = L$ provided better agreement to the actual Q than using $L = 8/9$ y. For the ions without any δ-ray losses, generally, using $y = 8/9L$ provided a lower absolute percent discrepancy than using $y = L$.

2 and 3 μm Simulated Diameter Experiments - Fe Only - (Thick-Walled)

Figure 4-17 contains the composite distribution of mean lineal energy from Fe for the thick-walled detector for simulated diameters of 2 and 3 μm. The shape of the two distributions are similar to that collected for a 1 μm simulated diameter. Table 4-5 contains summary statistics for the distributions and those from the experiment with a 1 μm simulated diameter. The integrated dose for the experiments with the detector simulating 1 and 2 μm diameter sites were 3 % higher than expected for CPE, while the calculation for the experiment where the detector simulated a 3 μm diameter site was close to that expected for CPE. Also, for the data from the experiments with the detector simulating 1 and 2 μm diameter sites, there is close agreement in the frequency mean and dose mean lineal energy values. The experiment where the detector was simulating 3 μm had frequency mean and dose mean lineal energy values about 3 % lower than those of the other two experiments. Schrewe *et al.* (1988) expected uncertainties in calibrations with internal α- radiation

67

Table 4-3. Calculated Mean and True Quality Factors for Various Ions (μ-Random Incident) on the Thick-Walled Detector for ICRU 40, ICRP 26, and ICRP 60

Species	ICRU 40	ICRP 26			ICRP 60		
		(y = L)	(y = 8/9L)	True Q	(y = L)	(y = 8/9L)	True Q
Fe (26)	28.3	18.1	17.4	19.3	23.8	24.6	24.8
Ca (20)	23.8	13.9	12.8	14.7	24.0	21.4	26.0
Si (14)	12.6	8.1	7.4	8.5	11.1	9.7	11.6
O (8)	3.9	3.2	2.9	3.3	2.3	1.9	2.3
C (6)	2.2	2.0	1.8	2.1	1.0	1.0	1.0
He (2)	0.23	1.0	1.0	1.0	1.0	1.0	1.0

Table 4-4. Calculated Mean and True Quality Factors for
Various Ions (μ-Random Incident) on a 1 μm Site for
ICRU 40, ICRP 26, and ICRP 60 Assuming No δ-Ray Escape

Species	ICRU 40	ICRP 26			ICRP 60		
		(y = L)	(y = 8/9L)	True Q	(y = L)	(y = 8/9L)	True Q
Fe (26)	27.6	18.9	18.5	19.3	23.0	23.9	24.8
Ca (20)	26.4	15.5	14.4	14.7	25.2	24.5	26.0
Si (14)	14.9	9.3	8.4	8.5	13.4	11.6	11.6
O (8)	4.6	3.6	3.3	3.3	3.0	2.4	2.3
C (6)	2.5	2.3	2.1	2.1	1.1	1.0	1.0
He (2)	0.3	1.0	1.0	1.0	1.0	1.0	1.0

69

Figure 4-15. Percent Discrepancy of Calculated Mean Quality Factors from Mean Lineal Energy Distribution of Thick-Walled Detector to Known Quality Factors from ICRP 26 and 60
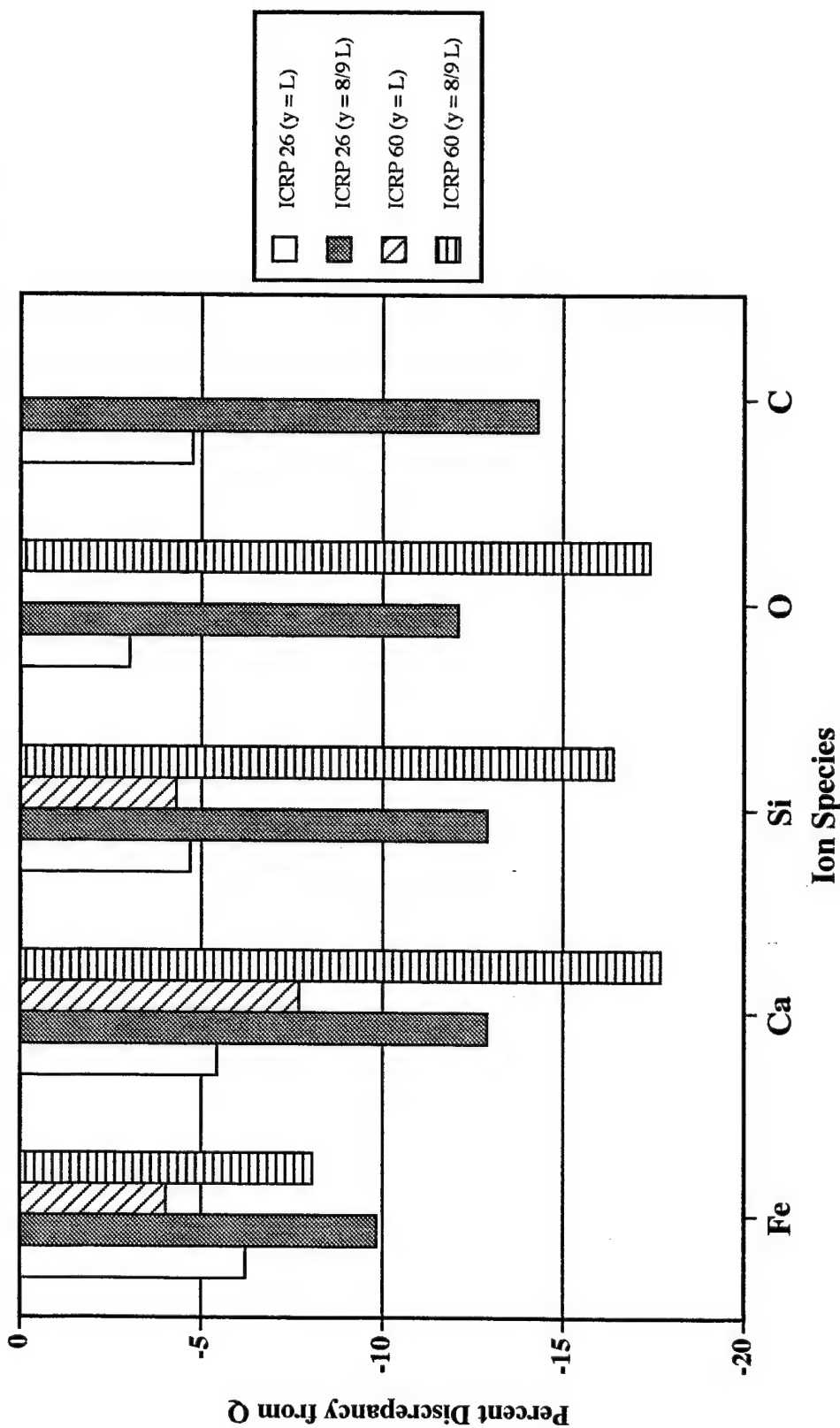
Figure 4-16. Percent Discrepancy of Calculated Mean Quality Factors from Particles Without Radial Energy Loss to Known Quality Factors from ICRP 26 and 60

71
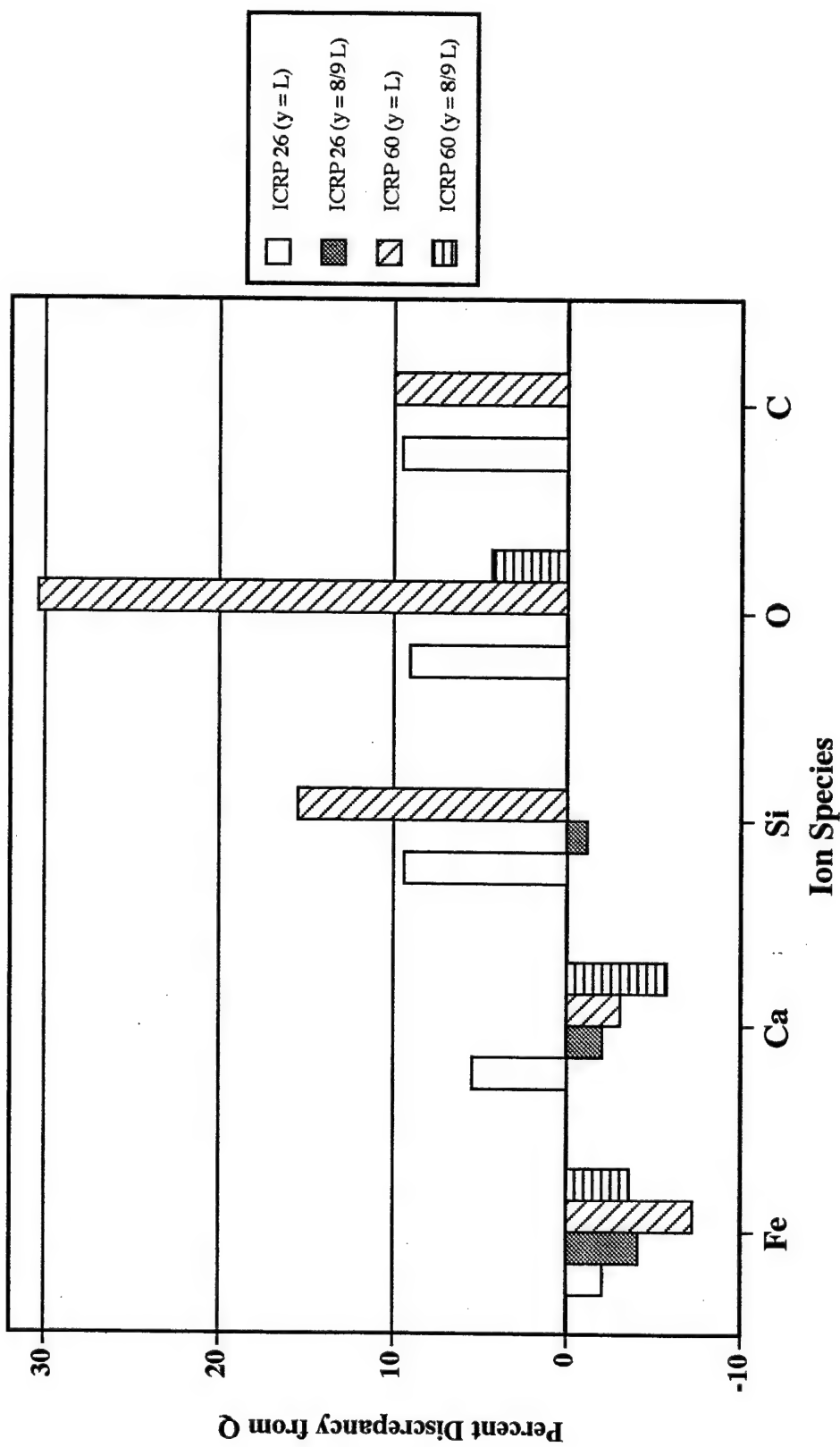
Figure 4-17. Data From Experiment with Fe Particles in the Thick-Walled Detector Simulating: a. 2 μm and b. 3 μm
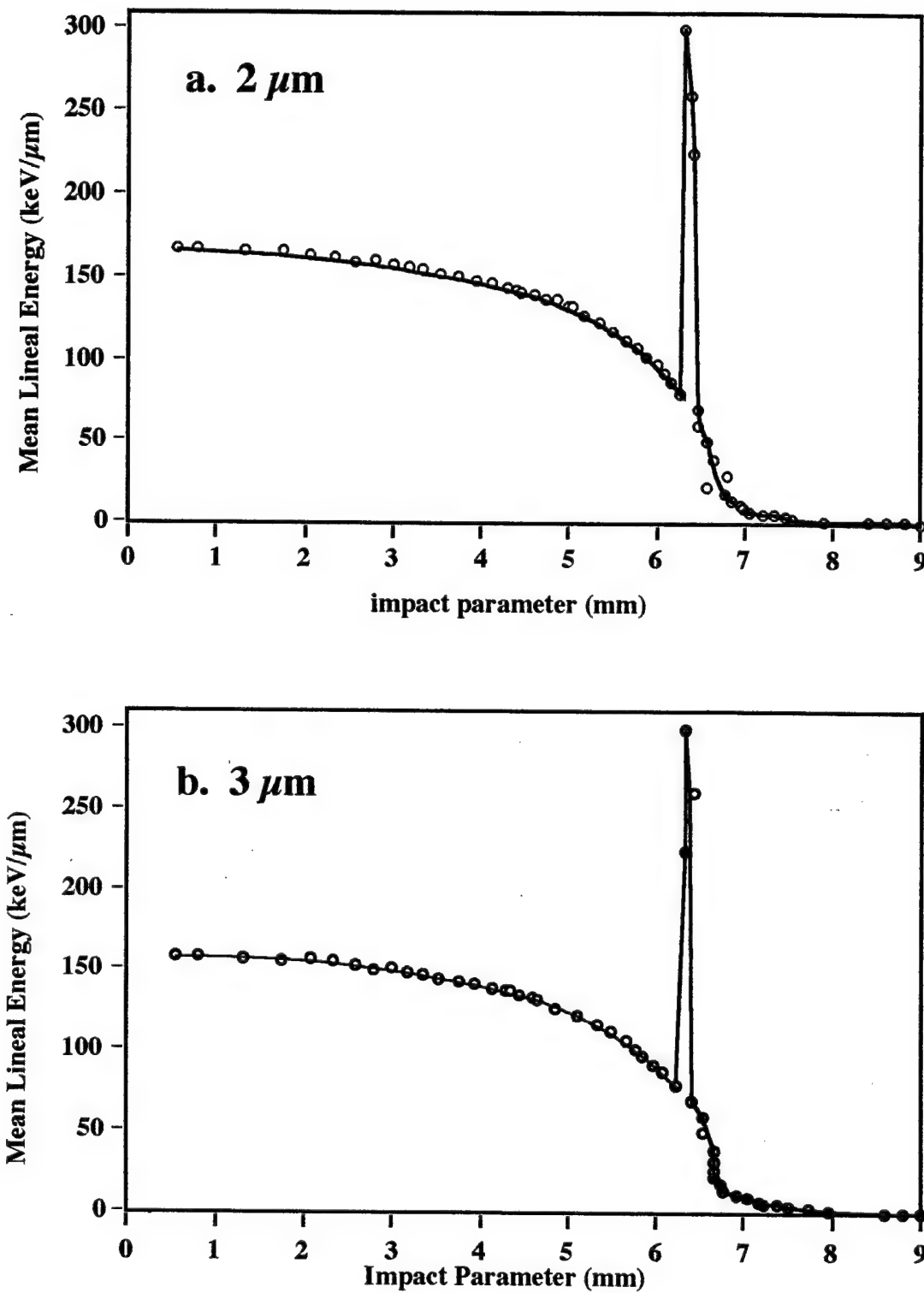
Table 4-5. Computed $\bar{y}_F$ and $\bar{y}_D$ Based on Measured Response to Fe Particles in the Thick-Walled Detector and Integrated Dose Compared to that Expected for CPE

Parameter	Simulated Diameter (μm)		
	1	2	3
$\bar{y}_F$ (keV μm^{-1})	79	79	76
$\bar{y}_D$ (keV μm^{-1})	143	145	140
Ratio: Data/CPE	1.03	1.03	1.00

calibration sources to be on the order of a few percent. Therefore, determination of the differences between the three experiments is beyond the inherent resolution of the calibration technique. It is speculated that there exists a calibration bias between the 3 μm experiment and both the 1 and 2 μm experiments.

Figure 4-18 contains a plot of mean lineal energy vs. impact parameter for Fe trajectories through the cavity for the three simulated diameters. Standard error in estimation of the mean bars for individual data points were typically about 0.5 keV μm^{-1} and were not displayed because they were very small. For trajectories through the center of the detector, higher mean lineal energy was associated with lower simulated site diameter. But, for trajectories closer to the cavity/wall interface, the difference was less apparent.

CV Among Thick-Walled Experiments: 1, 2, and 3 μm

The CV was calculated for distributions of lineal energy for particle trajectories through the center of the detector for the three simulated diameters in the thick-walled detector. CV's were computed for three separate intervals of impact parameter: 0 - 1, 0 - 1.5, and 0 - 1.75 mm with the results in the bar graph of Figure 4-19. The error bars represent 1σ standard error in the estimate of the mean. The CV of the distributions are lower for larger simulated site diameter. This result is expected because the variance in the distribution of lineal energy caused by energy straggling is lower for higher mean energy deposition.

73

Figure 4-18. Mean Lineal Energy vs. Impact Parameter for Fe Trajectories through the Cavity of Thick-Walled Detector [Simulated Diameters of 1, 2, and 3 μm; Standard Error in the Data about 0.5 keV/μm (not shown)]
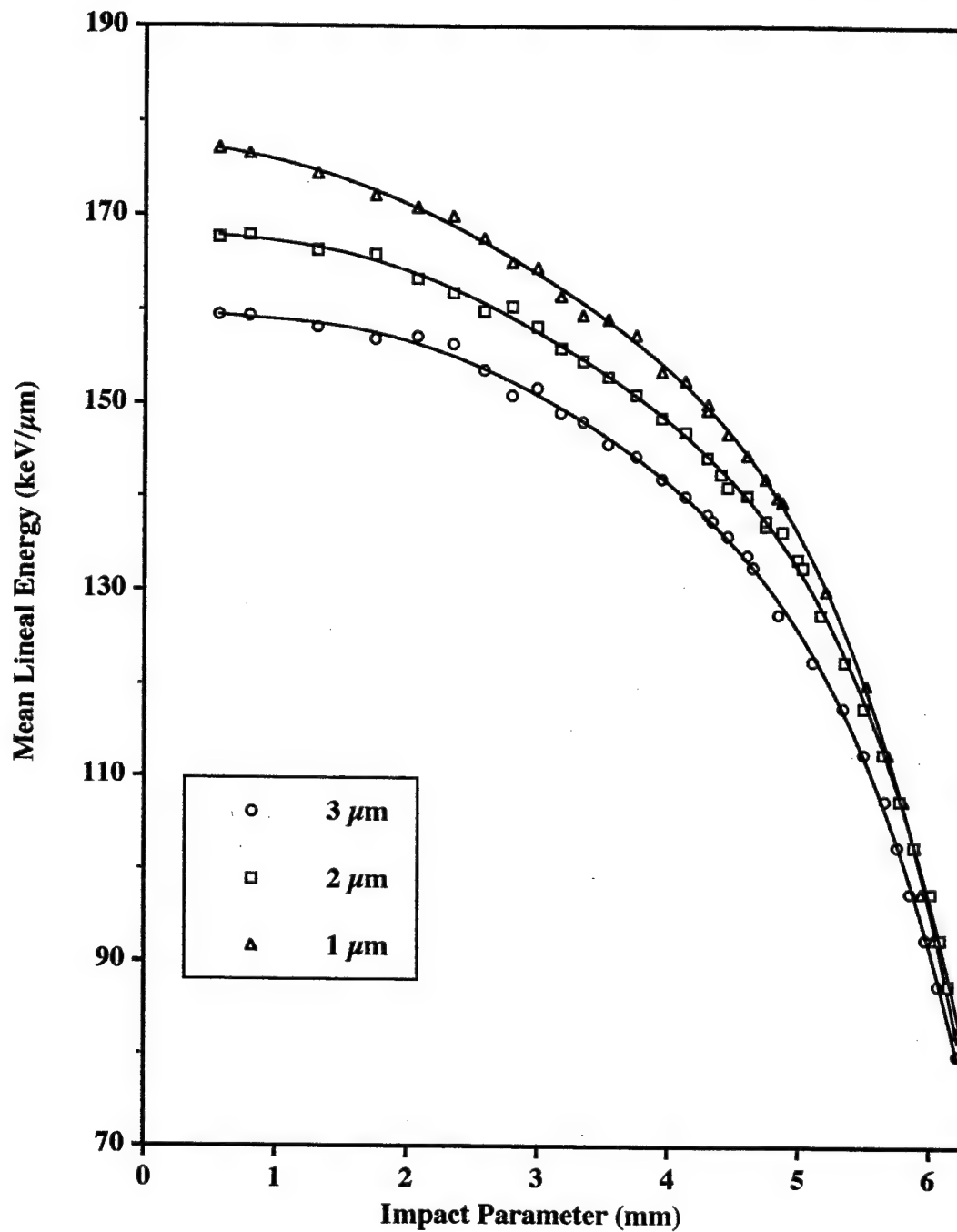
For the experiments where the detector simulated diameters of 2 and 3 μm, the CV increased as the interval of impact parameter increased. This was due to the increasing influence of variance in pathlength for larger intervals of impact parameter.

Figure 4-19. Coefficient of Variation for Distributions of Mean Lineal Energy for Three Impact Parameter Intervals in the Thick-Walled Detector (1, 2, and 3 μm)
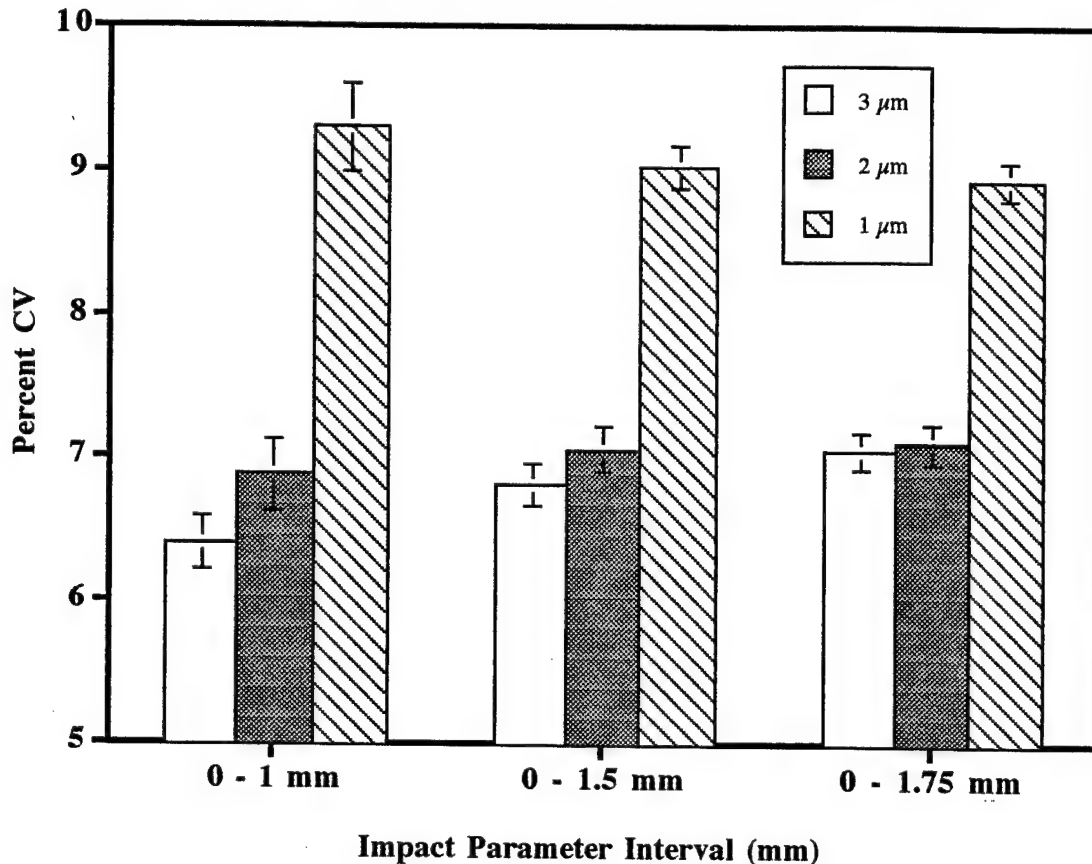
Analysis of Events with Charge-Changing Interactions in the TEPC Wall
General

The results presented to this point have concentrated on the analysis of Fe trajectories through the TEPC. By rejecting events that did not have good correlation between the position values in PSD1 and PSD2, the analysis had a reduced potential of including particles that were involved in nuclear interactions. These interactions include elastic scattering, neutron(s)-only loss in the projectile, and target-only fragmentation. The

analysis provided here is for events involved in charge-changing interactions that occurred between the PSD pairs, with the likeliest location being in the wall of the TEPC.

Because the interactions are assumed to occur in the wall of the TEPC, particle trajectory information determined from the combination of signals from PSD1 and PSD2 would be incorrect. Therefore, impact parameters for this analysis were based solely on PSD1 signals. As such, uncertainties in impact parameter are typically about 3.5 times that of impact parameter determined with PSD1 and PSD2 (see Appendix D). Due to large uncertainties in impact parameter, the analysis was based on large intervals of impact parameter. The response of the detector for this analysis is due to energy deposition from recoil nuclei and electrons. The analysis of the data from the experiments with Fe-only, was based on a relatively uniform detector response at a specific impact parameter. However, for this analysis, the influence of recoil nuclei on energy deposition is not well known for TEPC detectors. Also, for identical trajectories, detector response could be significantly different dependent on whether the nuclear interaction occurred in the front or back wall of the detector. Evaluation of the detector response for trajectories near the cavity/wall interface and wall-only could not be as detailed as in the case of the Fe-only experiments. Because the technique of determining mean impact parameter based on selecting an interval of detector response may provide ambiguous results. Experimental results are for the thin-walled detector simulating 1 μm.

Analysis

1. **Scatter Plot TEPC Response vs. PSD y_1** Figure 4-20 is a plot of energy deposited in PSD y_2, the detector directly downstream of the TEPC. The plot is for events with impact parameter less than 2 mm (as estimated from PSD1 only). From the plot, it is apparent that the most abundant product fragment is manganese (Mn), as expected from experiment (see Appendix C). The mean energy deposited in PSD y_2 was 170.6 MeV, about 60 % of the mean energy deposited by Fe particles.

Figure 4-20. ΔE Y2 for Fragments Produced in the Wall of the TEPC

Impact Parameter < 2 mm
n = 697
μ = 170.6 MeV

Mn
(Z = 25)

Number of Events

ΔE y2 (MeV)
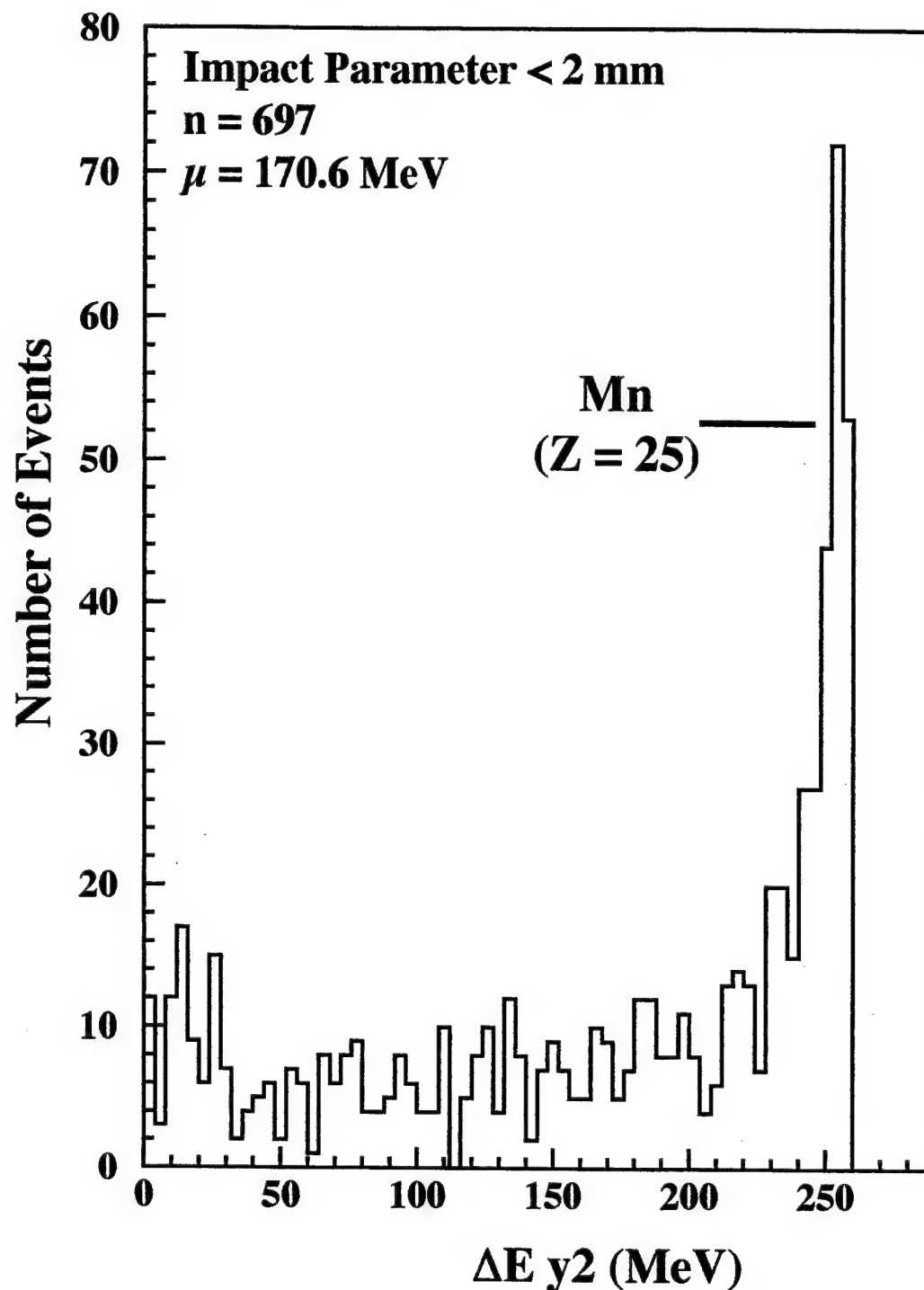
Figure 4-21 is a scatter plot of the detector response vs. energy deposited in PSD y_2, for events with estimated impact parameter less 2 mm. The scatter plot has two obvious characteristics shown by the selected rectangular regions.

The upper rectangular region is characterized by a detector response independent of energy deposited in PSD y_2. This region corresponds to events that enter the detector as Fe, have an energy deposition as expected for Fe particles, but are involved in a charge-changing nuclear interaction in the back wall of the detector. Because target fragments are largely forward directed, recoil nuclei would not be expected to deposit energy in the detector, consistent with the observation made here.

The diagonally oriented rectangle corresponds to events where the response of the detector is generally proportional to the energy deposited in PSD y_2. These events appear to have been involved in a charge-changing interaction before or in the forward wall of the detector. Because the response of the detector is proportional to energy deposited in the downstream silicon detector, it does not appear that significant enhancement of the detector response occurs from recoil nuclei.

There are many particles that generally do not fit into the two rectangular regions of Fig. 4-21. The largest number of particles have $\Delta E\, y_2$ values about 250 MeV, corresponding to Mn. A group of these particles have a detector response (TEPC) < 15 keV μm^{-1}, while another group has a response from 100 to 140 keV μm^{-1}. Because the detector response is less than that expected for Mn or Fe particles traversing the center, it is speculated that these particles traversed the detector near the cavity/wall interface or in the wall-only. These events could be the result of uncertainties in impact parameter. But more likely, these events are the result of nuclear interactions in the downstream portion of PSD x_1 or the air between PSD x_1 and the detector (TEPC). If either of these occurred, the particle would have scattered, possibly causing its true impact parameter to be significantly different from that predicted by the signal in PSD1.

Figure 4-21. Detector Response vs. ΔE y2 for Fragments Produced in the Wall of the TEPC

Impact Parameter < 2 mm
n = 697

Back Wall

Front Wall

y (keV/μm)

ΔE y2 (MeV)
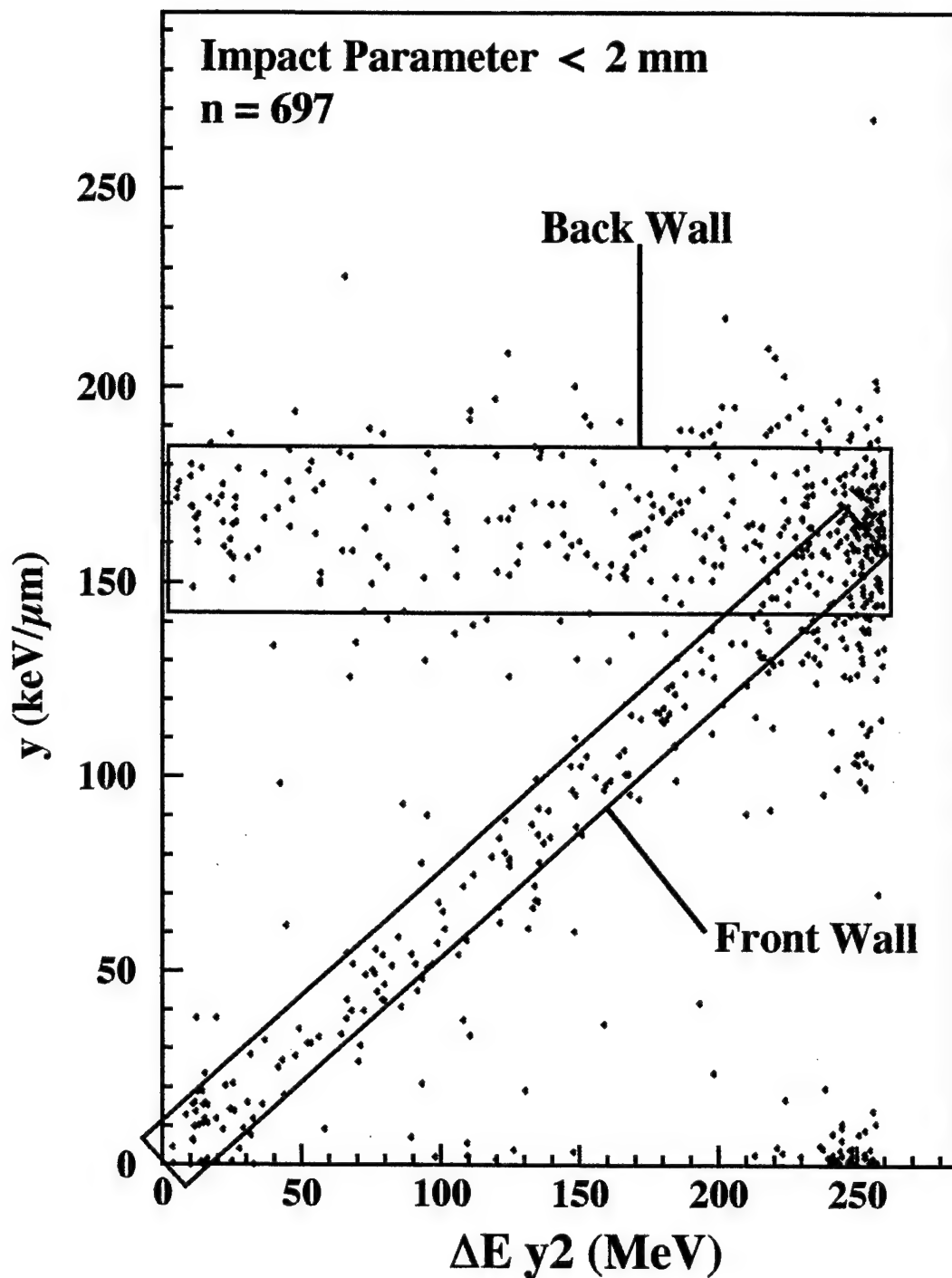
For fragmentation events that have Mn as a product, there is a reasonably probability that an interaction could have occurred in the downstream portion of PSD x_1 without an appreciable decrease in the energy deposited, because the L of Mn is about 92.4 % of Fe. For fragmentation events that have Mn as a product, and occur at a penetration depth at least 53 % of the way through the PSD x_1, they will have an energy deposition that is within 2.5 σ of the mean of the Fe peak (if energy deposition by the Fe and Mn are equal to their expectation values). Forty-seven percent of the thickness of a silicon PSD roughly corresponds to 0.8 mm of A-150 plastic. From Fig. 3-4, the total wall thickness encountered for a trajectory through the center of the detector is 2.54 mm. Thus, for these trajectories, about 25 % of the fragmentation events that have Mn as a product will occur in the downstream portion of PSD x_1 and falsely be attributed to a TEPC wall interaction. For trajectories through cavity/wall interface, about 9 % of the fragmentation events that have Mn as a product will occur in the downstream portion of PSD x_1 instead of the wall of the TEPC. For fragmentation events that have Cr as a product, about 16 and 5 % of the interactions, respectively for trajectories through the center and cavity/wall interface, will occur in the downstream portion of PSD x_1 rather than the wall of the TEPC.

    2. TEPC Response vs. Impact Parameter Distributions of detector response were created for:

        a. events where Fe was identified in PSD1 and PSD2,

        b. events where Fe was identified in PSD1 and but fragment in PSD2, and

        c. events where Fe was identified in PSD1 and but a Mn fragment was identified in PSD2.

The last category was included because Mn fragments were abundant and would be expected to have an energy deposition in the TEPC close to that of Fe (92.4%).

Figure 4-22 contains distributions of detector response for impact parameters less than 2 mm. Figure 4-22a is for Fe events, while Fig. 4-22b is for all charge-changing fragmentation events. The mean detector response for the events that have been involved in

Figure 4-22. Detector Response for Estimated Impact Parameters less than 2 mm [a. Fe and b. All Charge-Changing Fragmentation Events]

81
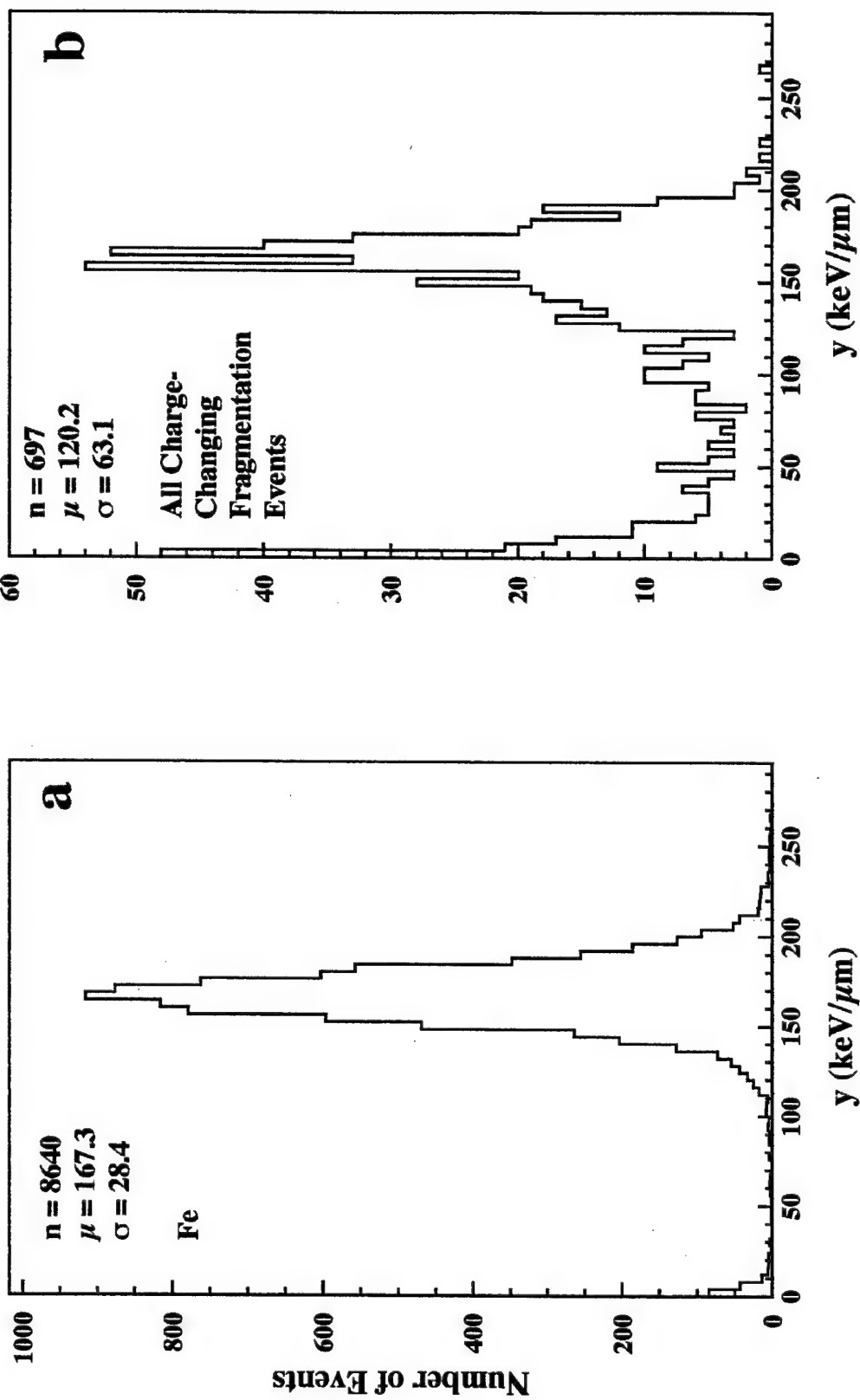
charge-changing fragmentation is about 72 % of the mean for the distribution of Fe events. If 50 % of the charge-changing interactions that occur in the TEPC do so in the back wall and the detector response for these events is the same as Fe events, then the mean response of the detector to events with charge-changing interactions that occur in the forward wall is 44 % of Fe.

Figure 4-23 contains the distribution of detector response for impact parameters between 6 and 7 mm. Figure 4-23a is for Fe events, while Fig. 4-23b is for all charge-changing fragmentation events. The mean detector response for the events that have been involved in a charge-changing fragmentation is about 90 % of the mean for the distribution of Fe events. The ratio of mean lineal energy for these distributions is significantly higher than that of the ratio for events through the center of the detector.

Figure 4-24 is a summary for all distributions of detector response for impact parameters less than 8 mm. The mean detector response to fragmentation events that have Mn as a product was higher than the mean response that included all charge-changing fragmentation products. The detector response to Fe particles was higher than the mean for Mn and all fragments, except for impact parameter intervals near the cavity/wall interface and in the wall-only.

3. Events with TEPC Response Greater than 190 keV μm^{-1}

The mechanism responsible for production of the events with large values of energy deposition was of interest for the experiments were Fe had traversed the detector. It is possible that that these events had unusually high energy deposition due to a contribution from recoil nuclei. The events evaluated here are known to have been involved in fragmentation interactions in the wall of the detector. A comparison of the frequency of production of these high energy deposition events with that for Fe traversals through the detector is provided here. This analysis will assist in determining the possibility that recoil nuclei are responsible for high energy deposition events where Fe traverses the detector. Figure 4-25 is a histogram of the percent of total events with $y > 190$ keV μm^{-1} for Fe

Figure 4-23. Detector Response for Estimated Impact Parameters between 6 and 7 mm [a. Fe and b. All Charge-Changing Fragmentation Events]
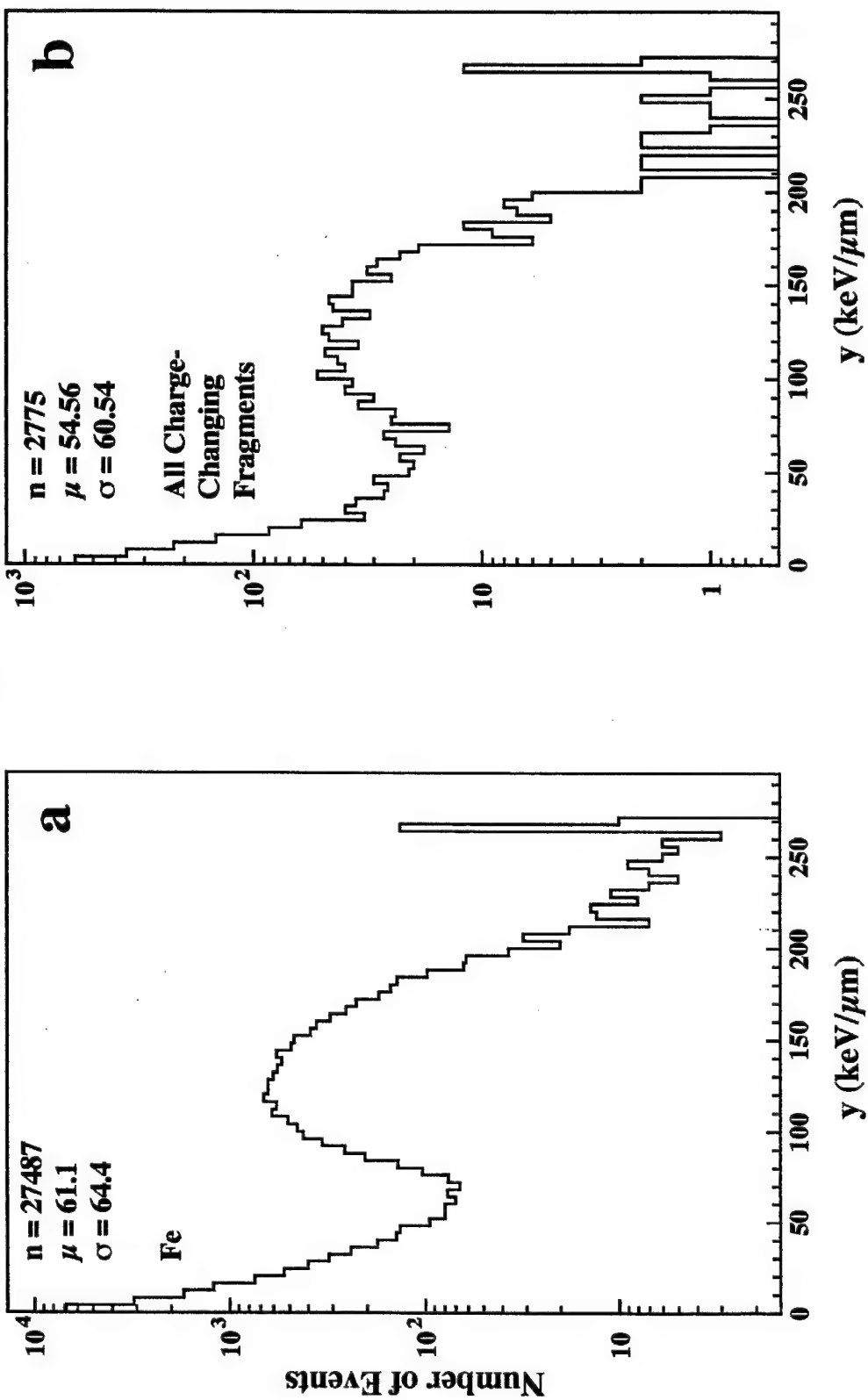
Figure 4-24. Mean Lineal Energy vs. Impact Parameter for Fe Particles through the Detector, All Charge-Changing Fragmentation Events in the Wall, and Fragmentation Events with Mn as a Product
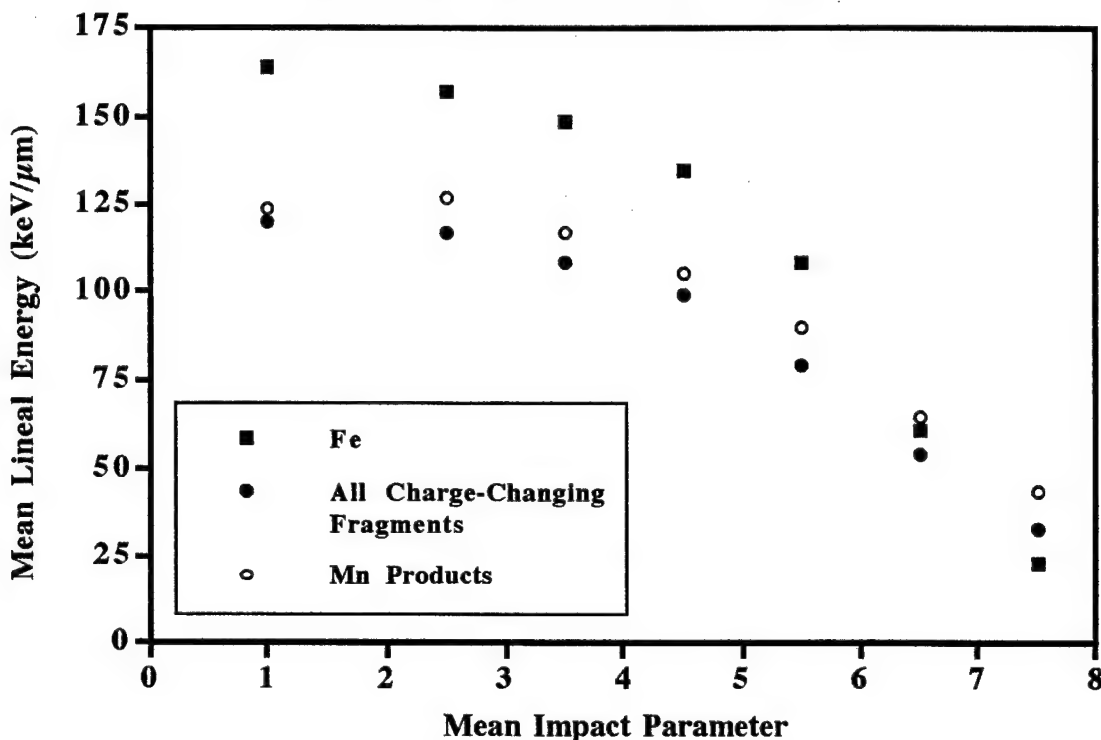
particles through the detector, all charge-changing fragmentation events that occur in the wall of the detector, and fragmentation events that have Mn as a product. Vertical error bars represent an estimate of the 1σ standard error in the estimate of the mean using Poisson statistics.

For events with impact parameters less than 2 mm, the percent of total events for the charge-changing fragmentation events was about half of that for Fe events through the TEPC. This naturally follows from the observations and conclusions drawn from the scatter plot of Fig. 4-21. For the same range of impact parameters, the Mn products had a lower percent of total events with lineal energy greater than 190 keV μm^{-1}, than that for all charge-changing interactions, but uncertainties in this value are high with a sample size of only 6 events and bias introduced by difficulties in interpreting ΔE in PSD x_1 for Mn products.

84

For events near the cavity/wall interface (impact parameters: 5-6 and 6-7 mm), the percent of total events with lineal energy greater than 190 keV μm^{-1} was higher for the Mn fragments than for the Fe events through the detector.

Figure 4-25. Percent of Total Events with Lineal Energy > 190 keV μm^{-1} [Fe Particle through the Detector, All Charge-Changing Fragmentation Events that Occur in the Detector Wall, and Fragmentation Events with Mn Products]
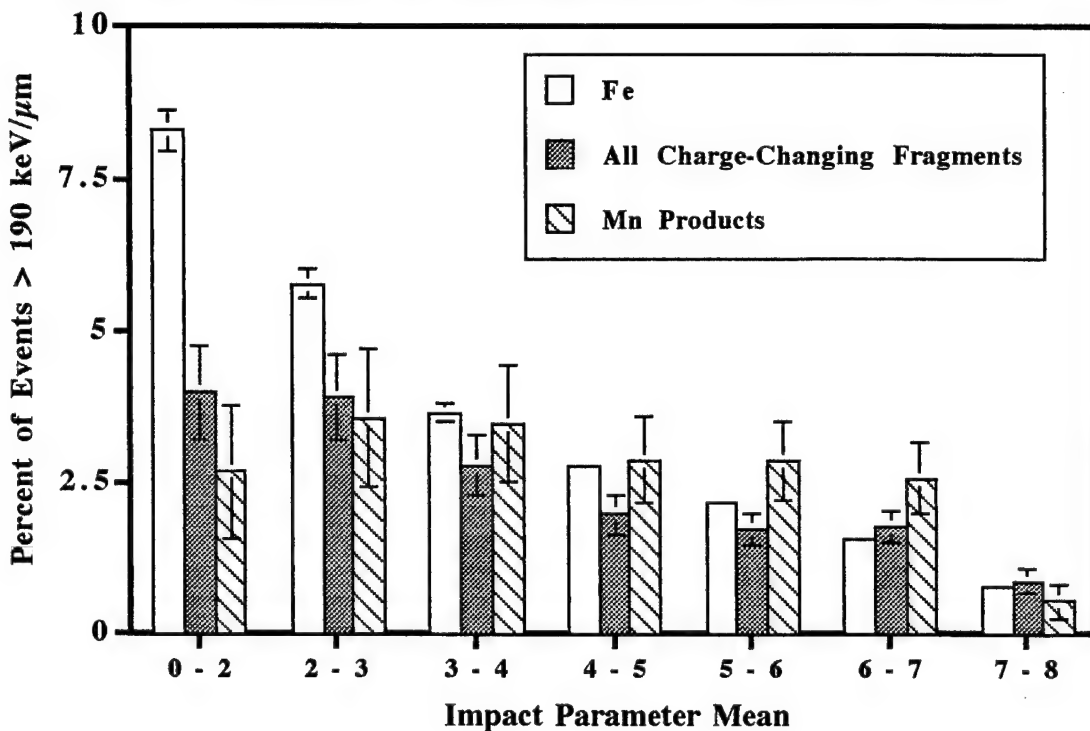
Detector Response to Fragments Produced in the Copper Target

Event Selection

Events with energy deposition in PSD1 2.5σ less than the mean energy deposition for

Fe were selected for analysis. Figure 4-26 is a plot of $\left[\dfrac{\Delta E\, y_2}{\Delta E\, x_1}\right]$ these events. The

distribution has a prominent peak and a broad distribution of events with a ratio of energy deposition lower than the peak. The broad peak is believed to be the result of one of two factors. First, some projectile fragments (within the same event) that penetrate the active volume of PSD x_1 do not penetrate the active volume of PSD y_2. The magnitude of this

Figure 4-26. Quotient (ΔE y2) by (ΔE x1) for Fragmentation Events Produced in the Copper Target [Bars Show Events Selected for Analysis]
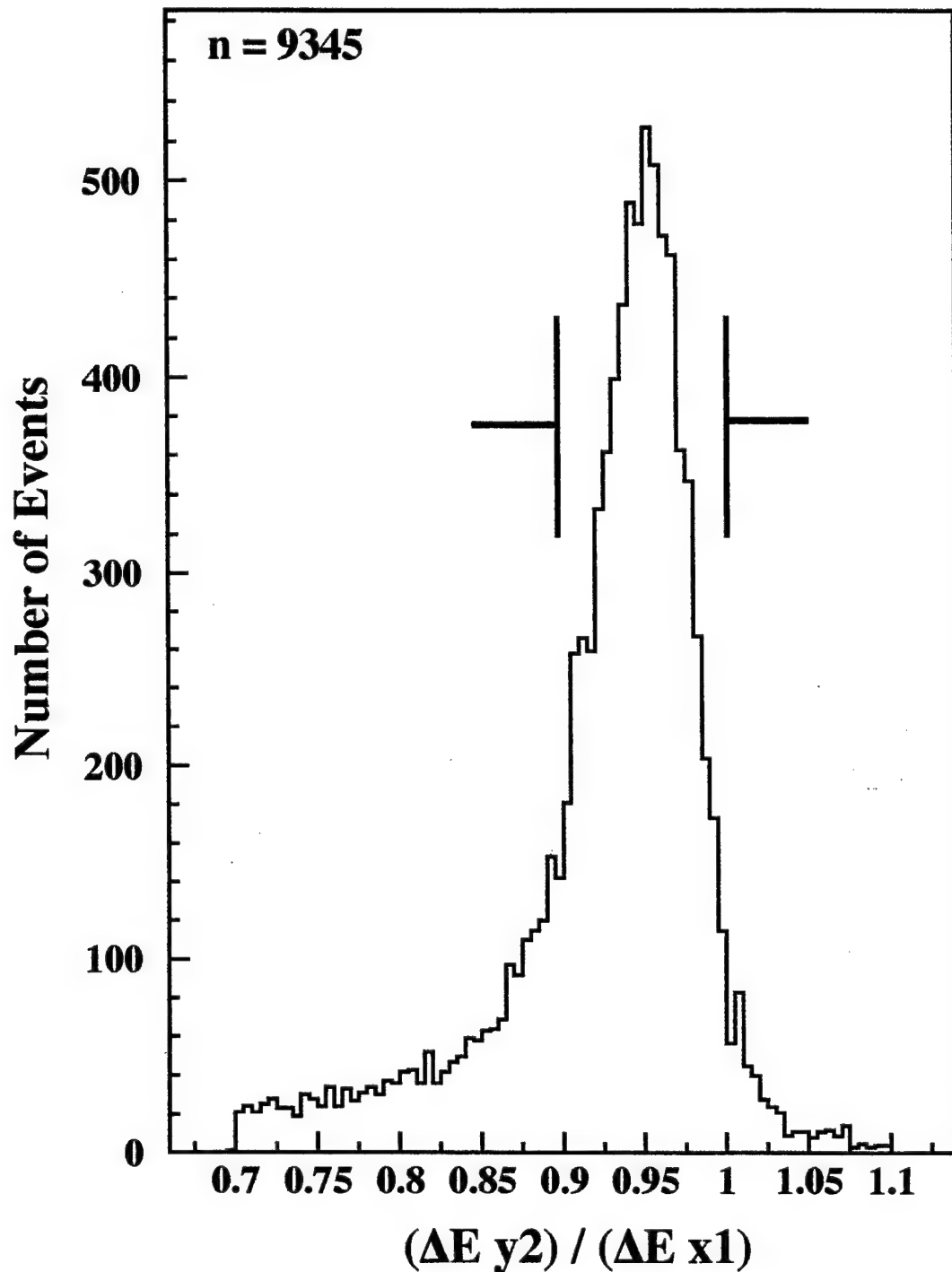
effect is expected to increase as the value of charge-loss in the projectile increases, because there will be an increasing number of projectile fragments. Second, some of the projectile fragments may be involved in additional fragmentation events between PSD x_1 and PSD y_2.

A plot of the same quotient distribution was generated for Fe particles identified in PSD1 and PSD2 (not displayed). This data was normally distributed with mean and standard deviation of 0.957 and 0.024, respectively. The location of the peak in Fig. 4-26 was very close to that observed for Fe particles. The analysis was restricted to events with quotient values between the bars of Fig. 4-26. Because the number of fragments produced in the copper target was small, the analysis of detector response was limited to particles with impact parameter less than 3 mm.

Detector Response

Figure 4-27 is a scatter plot of the detector response vs. the energy deposited in PSD y_2. The data has a linear correlation between the response of the two detectors. One event had an unusually high lineal energy response in the detector (TEPC), near 270 keV μm^{-1} and was assumed to be the result of a wire hit. The plot also contains numerous events with low lineal energy response in the detector. As discussed earlier for evaluation of the response of the thin-walled detector to Fe:

1. these events probably crossed the wall-only of the detector and have low detector response, and

2. were involved in a scattering event that caused the impact parameter to be incorrect.

The number of these events observed in Fig. 4-27 is statistically consistent to the number observed in the analysis of Fe events.

Figure 4-28 is a scatter plot of the quotient of detector (TEPC) response by the energy deposited in PSD y_2. The distribution of events appears to be distributed about the ratio of 0.6, independent of ΔE y_2. A linear regression on the data in this form was not performed because the coefficients would have been dominated by the response of the heavier

87

Figure 4-27. Detector Response vs. (ΔE y2) for Fragments Produced in the Copper Target

Impact Parameter < 3 mm
ΔE y2 > 125 MeV
n = 645

TEPC: $y(keV/\mu m)$

ΔE y2 (MeV)
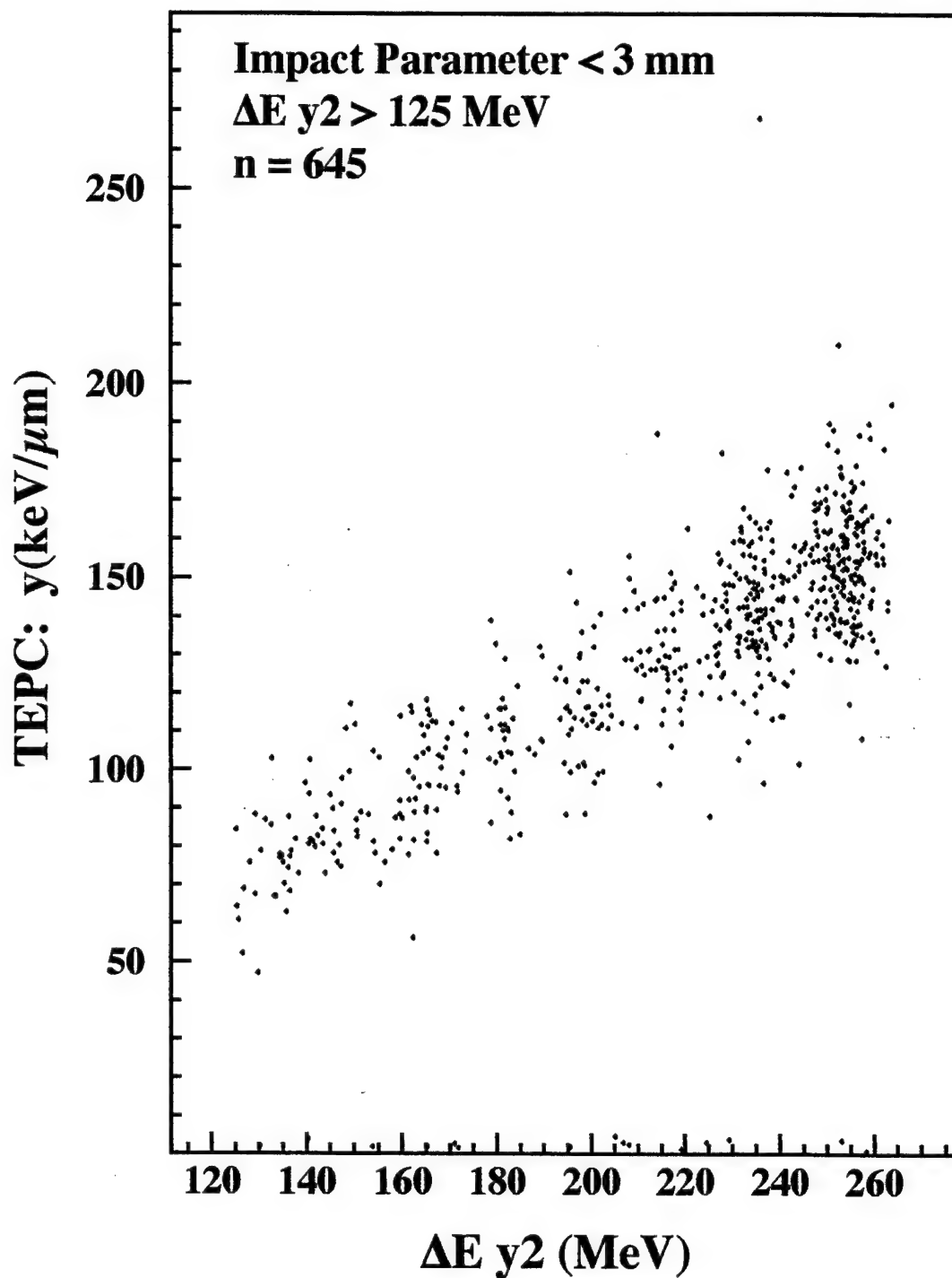
Figure 4-28. Quotient of (Detector Response by ΔE y2) vs. (ΔE y2) for Fragments Produced in the Copper Target

Impact Parameter < 3 mm
ΔE y2 > 125 MeV
n = 645

TEPC / ΔE y2 (per mm)

ΔE y2 (MeV)
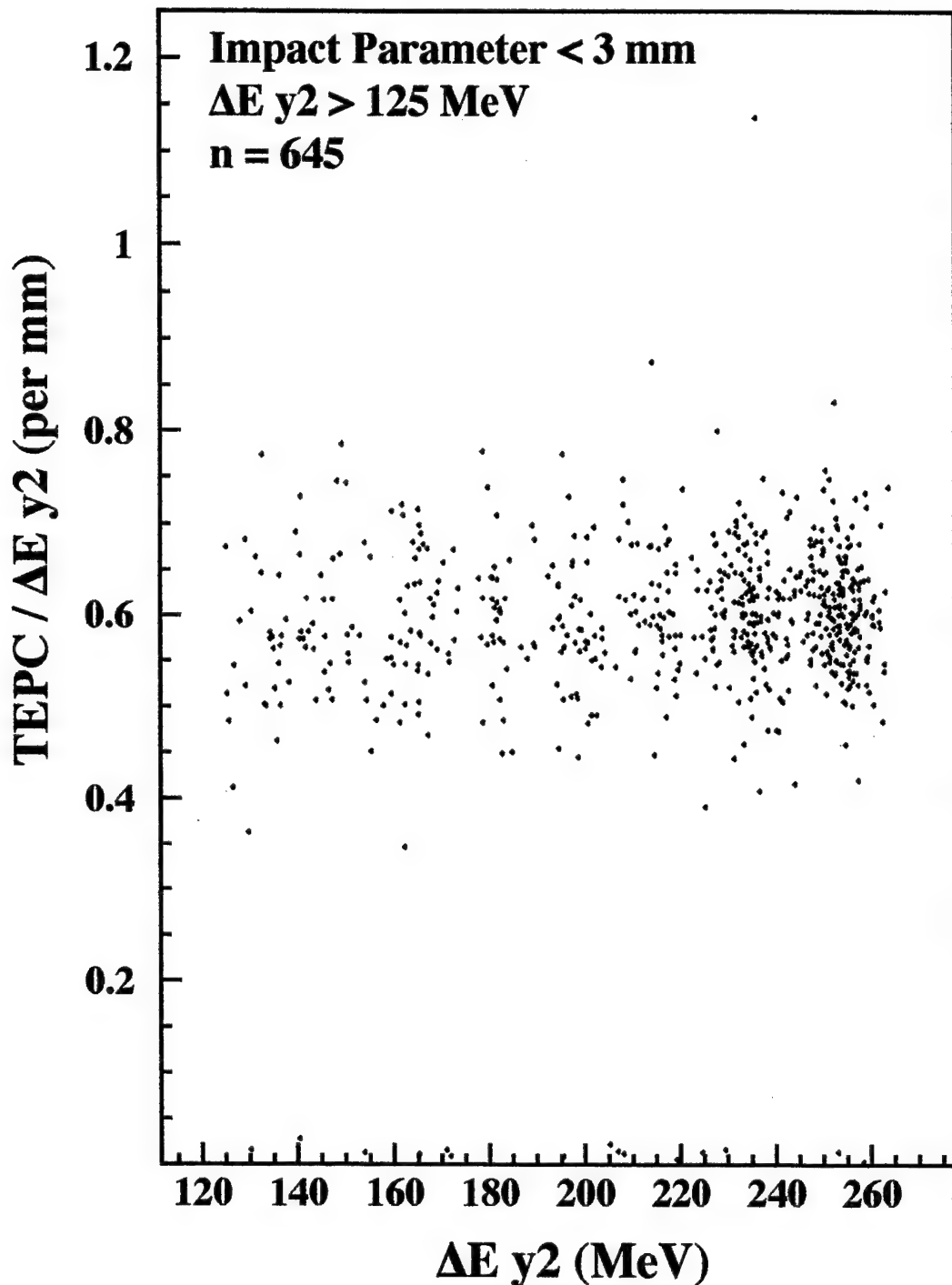
fragments of Mn and Cr. These fragments were greater in number than all others combined.

Since a linear regression of the data in Fig. 4-28 could have produced misleading results. The ratio of detector response to the energy deposited in PSD y_2 was evaluated for groups of fragments. Table 4-6 contains a summary for the fragments and Fe particles through the detector. The events that were postulated to have been involved in scattering events in the detector wall (15) and the one wire hit were omitted from the analysis.

Table 4-6. Quotient of Detector Response by $\Delta E\ y_2$ for Various Groups of Fragments

Particle(s)	Z	TEPC / ΔE y2 (mean)	n
Fe	26	0.6015 ± 0.0006	16605
Mn - Cr	25 - 24	0.604 ± 0.003	372
V - Sc	23 - 21	0.601 ± 0.006	146
Ca - Ar	20 - 18	0.586 ± 0.008	111

T-tests on the mean of the three fragment groupings with that of the Fe data did not demonstrate a difference at a significance level of $\alpha/2 = 0.05$; but at a significance level of $\alpha/2 = 0.025$, the Ca - Ar fragment group was different.

90

Chapter 5: Discussion

Fraction of L Absorbed in the Detector

The mean energy deposited, ε, in the sensitive volume for Fe particle trajectories

through the center of the thin-walled detector was 111.9 ± 0.3 keV ($y = 167.8 \pm 0.4$

keV μm^{-1}) for a 1 μm simulated diameter. This accounts for about 75 % of L for incident

Fe particles. The mean value for the thick-walled detector was 118.1 ± 0.5 keV ($y = 177.1$

± 0.5 keV μm^{-1}) corresponding to about 79 % of L. The model described by Chatterjee

et al. (1976) only describes energy deposition in the radial direction for homogenous

cylinders. These cylinders were superimposed on a spherical geometry with the central

axis of the cylinder corresponding to various impact parameters (see Fig. 4-12). For

trajectories through the center of the detector, the model predicted that 70 % of L would be

deposited in a 1 μm sphere. If one assumes that the model is correct, then 5 % of the

contribution to the measured values of energy deposition is from δ-rays produced for the

thin wall and 9 % from the thick wall.

Metting *et al.* (1986) used a nearly wall-less cylindrical TEPC that simulated a unit

density site of 1.3 μm to collect measurements near the trajectory of 600 MeV/nucleon [56]Fe

ions. The authors reported a loss of about 23 % in L but were not sure if it was due to

δ-ray losses or non-linear response of the detector. The value of energy escaping is close

to that predicted by the Chatterjee model (1976) for 600 MeV/nucleon ions.

Dicello *et al.* (1991) collected microdosimetric spectra with a wall-less cylindrical TEPC

in beams of Fe (535 MeV/nucleon), Ar (570 MeV/nucleon), and Ne (557 MeV/nucleon).

The detector had a mean pathlength of 0.4 μm. The authors reported that for direct traversal primaries, about 20 % of the energy transferred was not absorbed in the detector.

Large Energy Deposition Events

General

The events with the highest energy deposition for Fe particles through the detector did not correspond to those that traversed the center, rather they were due to those that just grazed the cavity/wall interface. It is of interest whether energy deposition for these events is the result of electron ionization or that from both electrons and recoil nuclei.

ICRU (1983) published spectra from walled and wall-less detectors collected by Rodgers *et al.* (1973) for 279 MeV/nucleon nitrogen ions. The ICRU presumed that the very large energy deposition events in the walled counter were either from spallation in the wall of the detector or a contribution from δ-rays at low lineal energies. The experimental set-up used by Rodgers *et al.* did not have the capability to separate the events that traversed the detector unfragmented from those that were involved in fragmentation interactions in the wall of the detector. The analysis presented here allowed separation of the two respective types of events. The data presented below provides convincing evidence for 1 GeV/nucleon Fe, that the mechanism of energy deposition for the events with the highest energy deposition is not dominated by that from recoil nuclei, but rather that from soft collision electrons. Data presented was for the thin-walled detector.

Nuclear Interaction Cross-Sections

The first step in the evaluation of these events is a review of nuclear interaction cross-sections to determine if the probability for nuclear interactions in the wall of the detector is sufficiently high to meet the frequency of these events observed in the experimental data. In the data analysis for Fe ions through the detector, events with nuclear interactions in the wall of the detector could not be rejected from the analysis if the incident Fe particle did not experience a loss of charge. These include: a) elastic scattering (Wilson and Costner, 1975), b) fragmentation of the incident particle with neutron(s) loss-only (Zeitlin *et al.*

92

1997), and c) fragmentation of the target nucleus-only (Heckman *et al.* 1978). An analysis using cross-sections from the listed references determined that the probability of a nuclear interaction in the wall for trajectories near the cavity/wall interface was about 5 %. This analysis assumed that only half of the charged recoils from elastic scattering in the wall could reach the sensitive volume. In the case of target-only fragmentation, the fraction measured for ^{16}O nuclei was applied, because the literature did not have experimental data for ^{56}Fe. This estimate is likely to be higher than that of ^{56}Fe, since ^{16}O ions, of lower Z and doubly-magic, are likely to be more stable (a trend evidenced in the Heckman data, see Appendix C for summary).

From evaluation of Fig. 4-7c, 5 % of the events have $y \geq 190$ keV μm^{-1}. As noted above, the probability of an undetected nuclear interaction along the longest pathlength was about 5 % for those that could direct a recoil nuclei into the cavity. Therefore, based on the nuclear interaction cross-section data alone, it is possible that these large energy deposition events are caused by recoil of target atom nuclei. However, the probability that a significant fraction of the energy deposited for these events is from recoil nuclei is unlikely, because:

1. recoil nuclei produced in the downstream hemisphere of the detector will almost certainly not reach the cavity,

2. many recoil nuclei produced in the wall will be stopped in the wall, and

3. for proton recoils, the maximum energy transfer in a 1 μm diameter site is 98 keV ($y = 147$ keV μm^{-1}), assuming the recoil nuclei traverses the diameter.

Other events in the vicinity of the cavity/wall interface had energy deposition of about 50 keV ($y = 75$ keV μm^{-1}). Energy deposition from these events is believed to be from secondary electrons only. Combining this with the maximum energy deposition from a proton recoil, energy deposition is about 150 keV ($y = 225$ keV μm^{-1}), a value lower than that of over two-thirds of the events with $y \geq 190$ keV μm^{-1} from Fig. 4-7c. Thus, events

with proton recoils alone (elastic scattering) could not be attributed to two-thirds of these events.

Trajectory Analysis

Another method was used to determine if events with high energy deposition were from electrons or the sum of electrons and recoil nuclei. The difference in position, $x_2 - x_1$, using the PSD detectors was plotted for events with $40 \leq y \leq 60$ keV μm^{-1} and $y \geq 240$ keV μm^{-1} when Fe was identified both upstream and downstream of the detector. Events with $y > 240$ keV μm^{-1} were chosen because it limited the number of wire hits events from the analysis. The difference in position was also evaluated when Fe was identified using ΔE in PSD1, but a fragment of Fe was identified using ΔE in PSD2. This data is summarized in Table 5-1.

The standard deviation for the distribution of $(x_2 - x_1)$ was significantly higher in events that were known to have been associated with nuclear interactions between PSD1 and PSD2. The standard deviation increased with the magnitude of charge loss by the incident Fe. For fragmentation events with Mn products, the standard deviation was over twice that of the events with $y > 240$ keV μm^{-1}. Fragmentation events with Mn products on average are the least violent of the charge-changing fragmentation interactions because they have the smallest overlap of projectile and target nuclei. Fragmentation events resulting in neutron(s) loss-only and target-only fragmentation have momentum transfer of nearly the same magnitude as fragmentation events with Mn products. Thus, the standard deviation of the $(x_2 - x_1)$ distribution for these events would be expected to be similar to that of fragmentation events with Mn products. Therefore, it appears unlikely that the majority of events with high energy deposition from Fe through the detector have been involved in nuclear interactions.

Soft Collision Electron Deposition Near the Trajectory of Fe Ions

A simple analysis was performed using the Chatterjee Model (1976) to further assess the mechanism responsible for energy deposition from events with the highest magnitude

Table 5-1. Summary of $(x_2 - x_1)$ Trajectory Analysis as Measured Respectively in PSD2 and PSD1

| Data Analysis | | TEPC Response Range (keV/μm) | $x_2 - x_1$ | |
PSD1	PSD2		μ (mm)	σ (mm)
Fe	Fe	y > 240	- 4.0	1.8
Fe	Fe	40 < y < 60	- 3.9	1.8
Fe	Mn	NA	- 2.9	3.9
Fe	Cr	NA	- 3.3	4.1
Fe	V	NA	- 3.6	3.9
Fe	Ti	NA	- 3.7	3.9
Fe	Sc	NA	- 3.7	4.4
Fe	Ca	NA	- 3.5	4.1
Fe	K	NA	- 3.9	4.4
Fe	Ar	NA	-3.6	4.7
Fe	Cl	NA	- 3.3	5.2

of detector response. From the model (Fig. A-1), the core radius is 9 nm for 1 GeV/ nucleon particles. The model assumes that about 50 % of the energy transferred to matter is from soft collision electrons and the other from δ-rays. The model assumes that the soft collision electrons deposit their kinetic energy in the core region.

Figure 5-1 is a cross-section of the detector cavity and depicts an Fe particle grazing the cavity/wall interface. In the diagram, three distinct segments of the particle trajectory through the wall material have been defined. A and c are respectively, the upstream and downstream segments of the trajectory from the detector midpoint. The length of segment b was limited in length by the criterion that, "every point on the segment had a potion of the core extending into the gas cavity." For a core radius of 9 nm, segment b had a length of 21.5 μm.

Figure 5-1. Fe Grazing the Cavity/Wall Interface of the Detector. [Segment "a" is Upstream Portion of the Trajectory, Segment "b" is Portion of Trajectory with the Core Extending into the Cavity, and Segment "c" is Downstream Portion of the Trajectory]
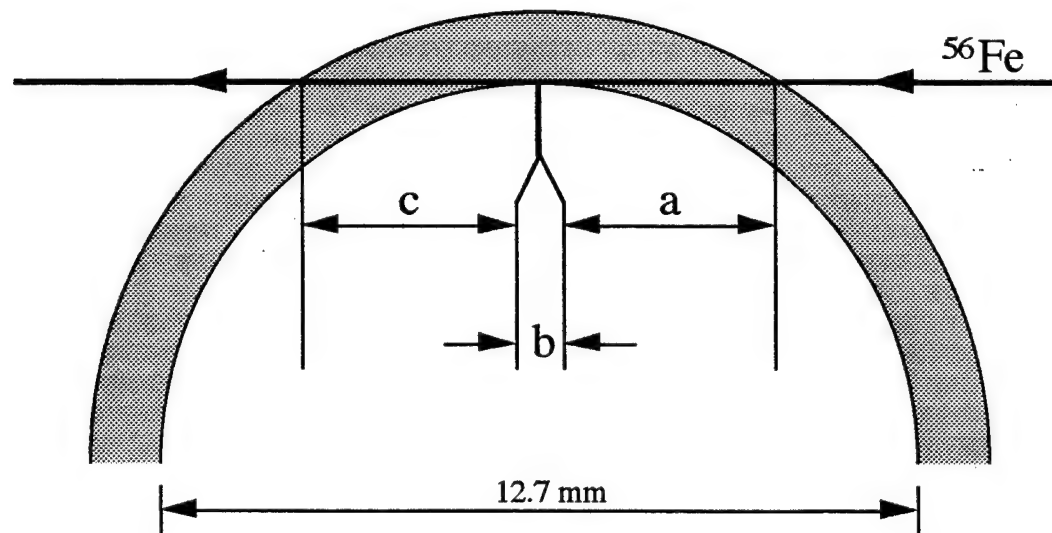
For grazing events, the energy deposited in the detector will be assumed to be comprised of two components: energy deposition from δ-rays produced in segments a and c, and from soft collision electrons in segment b. The contribution from the δ-rays is

assumed to be about 50 keV (75 keV μm^{-1}). This is an energy deposition that is characteristic of Fe events that have trajectories near the cavity/wall interface, but in the wall-only (see Fig. 4-13).

The magnitude of energy deposition with respect to impact parameter is not described by the Chatterjee Model for the core. The model only specifies a mean value of energy deposition. Therefore, accurate estimates of energy deposition in the cavity from soft collision electrons created by a grazing event cannot me made from the model. Other models of energy deposition from heavy ions also suffer large uncertainty in energy deposition for impact parameters very close to the trajectory.

A rough estimate of energy deposition is made with the following assumptions:

1. 75 keV μm^{-1} (one-half of L) is the energy transferred by soft collision electrons,

2. only soft collision electrons generated in segment b are included,

3. 50% of the soft collision electrons are directed away from the cavity, and

4. 75 % of those directed toward the cavity are absorbed in the wall, without any energy deposited in the cavity.

The amount of energy transferred in segment b that is absorbed in the wall (assumption 4) cannot be predicted precisely from the Chatterjee model. In the model, it is assumed that energy deposited in the core is primarily from soft collision electrons and that the energy deposition is uniform. The authors of the model noted that the spatial distribution of energy deposition in the core was not known, but the assumption of a core radius was "introduced mainly for conducting the analytical process." Assumption 4 in the least is conservative to our analysis. Because for segment b, the average distance between the primary ion track and cavity is about one-half the core radius, leading to an average energy deposition of 50 % according to the Chatterjee model. In our analysis, an average energy deposition of only 25 % is assumed. The estimated soft collision electron energy deposition in the cavity is 200 keV (y = 300 keV μm^{-1}).

97

Therefore, from this simple analysis, one may conclude that the high energy deposition events could be the result of energy deposition from electrons alone. Furthermore, for grazing events, soft collision electrons contribute more to energy deposition than δ-rays.

Events with Charge-Changing Interactions in the Detector Wall

1. General Based on the foregoing discussion, it appears unlikely that recoil nuclei are responsible for the high energy deposition events for Fe through the detector. Charge-changing fragmentation's occur with only a few percent of the μ-random Fe particles incident on the detector. The evaluation of these events also reinforce the conclusion that recoil nuclei are not responsible for the majority of high energy deposition events for Fe through the detector.

2. Mn Data

For events near the cavity/wall interface (impact parameters: 5-6 and 6-7 mm), the percent of total events greater than 190 keV μm^{-1} was greater for fragmentation events that had Mn products than for 1) the Fe events through the detector and 2) all charge-changing fragmentation events (see Fig. 4-25). The uncertainty in the percent value for Mn is relatively high compared to the mean since the total number of observations is low. Conclusions about the difference in the mean of the data for Fe events through the detector and that for fragmentation events that have Mn products cannot be made with statistical confidence.

A 99 % confidence interval for the percent of total events greater than 190 keV μm^{-1} was calculated for the Mn data for impact parameters between 6 and 7 mm. The high side value is 4.6 %. As discussed in Chapter 5, about 9 % percent of these events may have occurred upstream of the detector in PSD x_1. Independent of these small errors, it appears inconceivable that a significant fraction of the high energy deposition events for Fe through the detector (that are associated with a non-charge-changing nuclear interaction in the wall) could be due to recoil nuclei, if at best only 5 % of the events that are known to have been associated with fragmentation events that have Mn products had high energy deposition.

98

3. Bias

Some care must be taken in interpreting the data from the charge-changing nuclear interactions in the detector wall. For the Fe particles through the detector, there was a uniform particle fluence. But, for the data collected for charge-changing fragmentation events that occurred in the detector wall, the particle fluence was not uniform because:

1. the pathlength through the wall material of the detector was not uniform (see Fig. 3-4) and

2. probability for a nuclear interaction in the detector is nearly proportional to the pathlength.

Large uncertainties in impact parameter for the data from this experiment prevented resolution of the differences in fluence. Because the longest pathlength through wall material occurred at the cavity/wall interface, the data had a higher particle fluence for these trajectories. This bias would increase the fraction of events with $y > 190$ keV μm^{-1} higher than that for a uniform fluence of particles. Therefore, for the evaluation of these events provided in this section, any bias introduced would be conservative to any conclusions reached.

Summary

Absolute determination of the mechanism responsible for the events with the highest energy deposition for Fe particles through the detector is beyond the scope of this work. But, based on the data and arguments presented, it appears that the majority of high energy deposition events are the result of secondary electrons only.

Implications of Wall Effects on Radiation Protection Dosimetry

General

Walled detectors do not accurately represent single-event energy deposition spectra that would be observed in homogenous media from high velocity ions. Comparison of the experimental data to the Chatterjee model in Fig. 4-12 shows that the experimental data had higher energy deposition than the model for trajectories through the cavity and wall-only of

the detector. The mean lineal energy for the Chatterjee model is not displayed for impact parameters greater than the wall boundary. But, according to the model (Appendix A), energy deposition in the sensitive volume will occur for particle trajectories with impact parameters out to 250 μm. Integration of the energy deposited from these indirect events will account for the energy lost from the direct events due to the escape of energetic δ-rays.

In homogenous media, indirect events will account for a large fraction of the total number of events in a uniform radiation field of high velocity ions, but the magnitude of the energy deposition for individual events will be very low. Many indirect events may involve only a single electron crossing the sensitive volume. Walled detectors compress all of these low energy deposition events into considerably fewer events with higher energy deposition per event. For this reason, application of the ICRU 40 recommendations for determination of mean quality factor may be incorrect for walled detectors.

Mean Q from ICRP 26 and 60 Recommendations

Currently, NASA is applying ICRP recommendations for the determination of $\overline{Q}$ from microdosimetric spectra under the assumption that y = L. On an event-by-event basis, y does not equal L. Based on Fe particles with the same L (see Figs. 4-13, 4-17a, and 4-17b), detector response (y) varied considerably dependent on particle trajectory. For Fe particles through the detector that just grazed the cavity/wall interface, lineal energy values were higher than 300 keV μm^{-1}, though the particles responsible for these events had an L of 150 keV μm^{-1}.

For the experimental data, differences in calculated $\overline{Q}$ values (using ICRP 26 and y = L) from the actual Q are negative but less than 6.2 % (in magnitude). For the same ICRP recommendations, but with y = 8/9 L, the difference in calculated $\overline{Q}$ from the actual Q were all negative, but greater in magnitude than 10 % for all of the ions but He. Thus, at least for these ions, using y = L is more appropriate for calculation of $\overline{Q}$ than using y = 8/9 L. The same general conclusion was reached in application of ICRP 60 recommendations.

For the particles without radial energy loss, differences between calculated $\overline{Q}$ values and the actual Q had magnitudes as high as 9 % for the ions considered under ICRP 26 recommendations with y = L. For the same ICRP recommendations, but with y = 8/9 L, discrepancies were less than 4.1 % for all of the ions considered. For these ions, using y = 8/9 L is more appropriate for calculation of $\overline{Q}$ than using y = L, except for Fe. The same general conclusion was reached in application of ICRP 60 recommendations, again except for Fe.

The recommendation to use y = 8/9L by Ricourt *et al.* (1981) was for lineal energy distributions of detectors irradiated with neutrons of energies less than a few MeV. Recoil nuclei from neutrons of this energy will have low velocity and have little radial energy loss for site diameters in the micron range. Distortions from the wall effect for high velocity ions make the assumption of y = L more appropriate for calculation of $\overline{Q}$ in walled detectors.

Fragments Produced in the Detector Wall

General

The summary of detector response to the charge-changing fragmentation's produced in the detector wall is displayed in Fig. 4-24. As noted earlier, caution should be applied in interpreting the data for intervals of impact parameter near the cavity/wall interface because of uncertainties in impact parameter and a non-uniform particle fluence. For intervals of impact parameter near the center of the detector, these effects introduce less uncertainty. Due to these shortcomings, assessment of the contribution of recoil nuclei to the total energy deposition cannot be made in a concise manner. The discussion and observations will be qualitative in nature only.

Data Analysis

For events with impact parameter less than 2 mm, the mean response of the detector to the fragments produced in the wall was only 72 % of the response to Fe particles through the detector. For events in this interval of impact parameter (see Fig. 4-21), it appeared that

detector response was independent of any recoil nuclei that were produced, but dependent only on whether the nuclear interaction occurred in the front or rear wall of the detector and the degree of charge-reduction in the projectile. Of the 697 events in Fig. 4-21, only one had a detector response greater than 250 keV μm^{-1} (lineal energy) and was likely due to a wire hit. Recoil nuclei are generally scattered in a forward direction. If recoil nuclei had a significant contribution to the energy deposition of these fragmentation events, one would expect that for the fragmentation events that

    1) had Mn or Cr products and

    2) occurred in the front wall of the detector,

energy deposition would be enhanced over Fe particles through the detector. But, it is not. And the fraction of total events greater than 190 keV μm^{-1} is significantly less for the events where fragmentation occurred as compared to Fe through the detector.

Mean detector response for fragmentation events that occurred in the detector wall was lower than that for the Fe events through the detector for all impact parameter intervals in the cavity (Fig. 4-24). It is unknown what fraction of the detector response is due to electron ionization and recoil nuclei for these events. But, the reduction in detector response due to a net reduction in energy deposition from electrons is not fully compensated by energy deposition from recoil nuclei.

Recommendations for Future Work

A more definitive analysis could be accomplished if there were a two PSD pairs upstream of the detector. This was the intention for these experiments, but difficulties were encountered in getting one upstream PSD pair to work. With two pairs of operational upstream PSDs, impact parameter uncertainties could be as low as 0.23 mm. However, detailed plots like those obtained for the Fe events through the detector could not be created. In the case of the Fe data, it was reasonable to assume that the response of the detector was homogenous for particles having the same impact parameter. But, for distributions of detector response where every events is associated with a nuclear

interaction in the wall of the detector, this assumption would be unreasonable because detector response is influenced by the site of the fragmentation.

If two pairs of upstream and downstream PSDs were used, nuclear interaction location could be determined. Due to the uncertainties in the position signals from PSDs, there would be some uncertainty in position, but the ability to determine whether the scattering event occurred in a PSD rather than the TEPC may be valuable. Discrimination of interactions in the PSDs could be made from those in the TEPC. Coincidental scattering in different detectors would complicate this analysis.

Detector Response to Ions of Other Z, but the Same Velocity as Fe

General

The stopping power of high velocity ions of the same velocity is nearly proportional to the Z^2 of the ion because the doubly differential secondary electron spectrum is nearly proportional to Z^2 (ICRU 1996). Subsequently, for ions of different charge but the same velocity, the spatial pattern of energy deposition should be the same and likewise for the fraction of L captured in discrete volumes.

Separate experiments with ions of different charge, but the same velocity, could verify this effect. But, because experiments may be conducted on different days, calibration uncertainties between individual experiments may limit the ability to assess any differences that may exist. The experiments described here were not conducted primarily for the purpose of investigating this effect. However, for the experiment conducted with the Cu target, numerous projectile fragmentation products were created and could be separated based on the energy deposited in the silicon detectors. Evaluation of ions of different charge within a single experiment eliminates calibration uncertainties. However, other uncertainties in the technique exist.

Uncertainties

1. Trajectory

One important consideration in evaluating the fragment data is the potential for introduction of error based on the relative trajectory of projectile particles from the same incident projectile. Figure 5-2 illustrates the trajectory of three fragments of a projectile. Because the evaluation of detector response was for particles through the center of the detector and the heaviest projectile fragment dominates the PSD position signal, particle (a) corresponds to the heaviest fragment. Particles (b) and (c) refer to lighter fragments.

Particle (b) illustrates a fragment that traverses PSD1, but not PSD2. If the energy deposited by fragment (b) comprised a significant fraction of the energy deposited in the PSD1, the event would have been rejected from the analysis because the quotient of $\Delta E\, y_2$ by $\Delta E\, x_1$ would have been outside the acceptance region (see Fig. 4-26). However, for particle (c), it traverses PSD 1 and PSD 2, but doesn't traverse the TEPC. This event would not be rejected through analysis of the quotient of $\Delta E\, y_2$ by $\Delta E\, x_1$, and would have a low quotient of detector response (TEPC) by $\Delta E\, y_2$ as compared to the case where both the heavy and lighter fragments all traverse the TEPC.

The bias introduced by this effect is dependent on the combination of projectile fragments. Figure 5-3 is a bar graph of the stopping power of various heavy projectile fragments and that of a single lighter fragment complement. All values are normalized to the stopping power of Fe. Mn is not displayed, but the difference in ionization between Mn and proton vs. Mn-alone is less than 0.16 %. In the case of a heavy fragment of sulfur ($Z = 16$), the largest lighter fragment has a Z of 10 (neon) and comprises 28 % of the combined stopping power of the two. If the sulfur ion traversed the TEPC and PSD2, but the neon only traverses PSD2, then significant bias would be introduced in evaluation of the detector response.

Figure 5-2. Trajectories of Projectile Fragments (from the Same Incident Projectile) through the Experimental Set-up [a. Traverses PSD1, PSD2, and TEPC, b. Traverses PSD1-Only, c. Traverses PSD1 and PSD2]
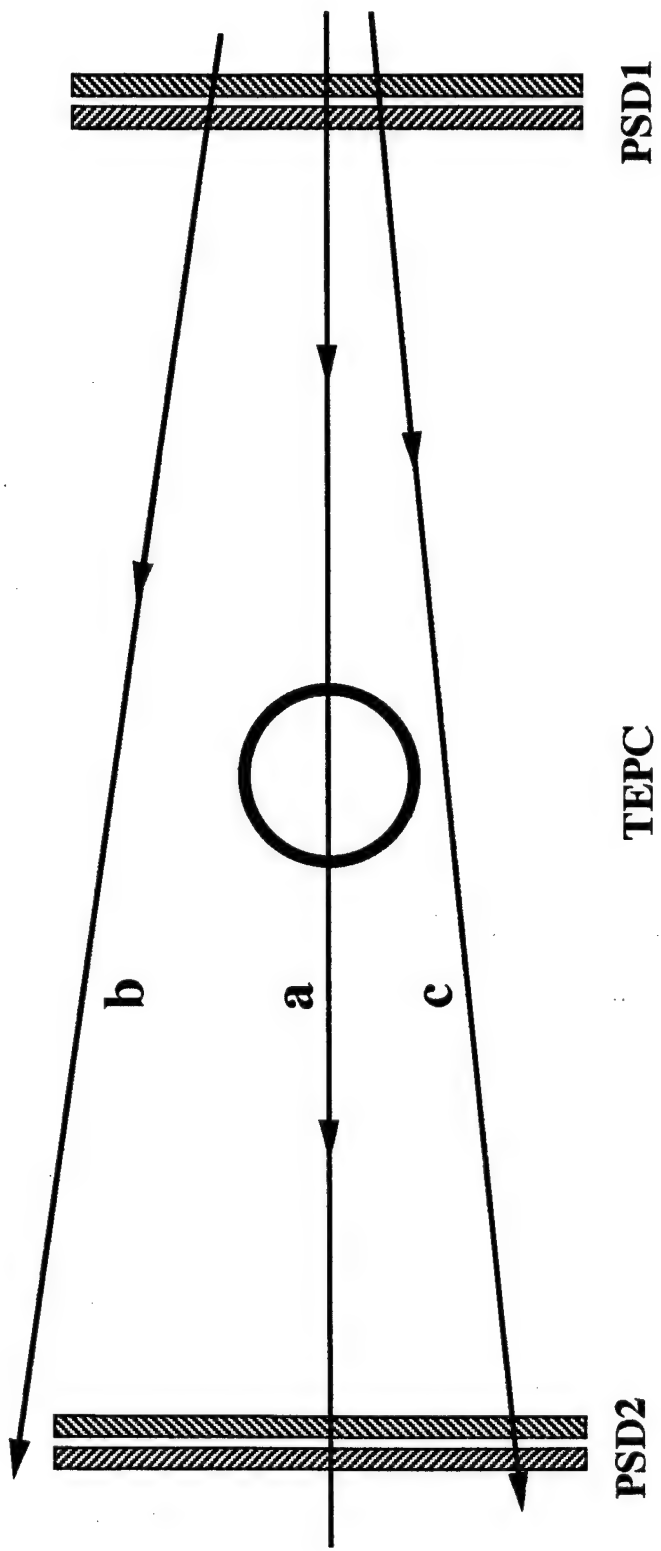
Figure 5-3. Normalized Stopping Power of Heavy and Light Fragment in Select Fragmentation Events
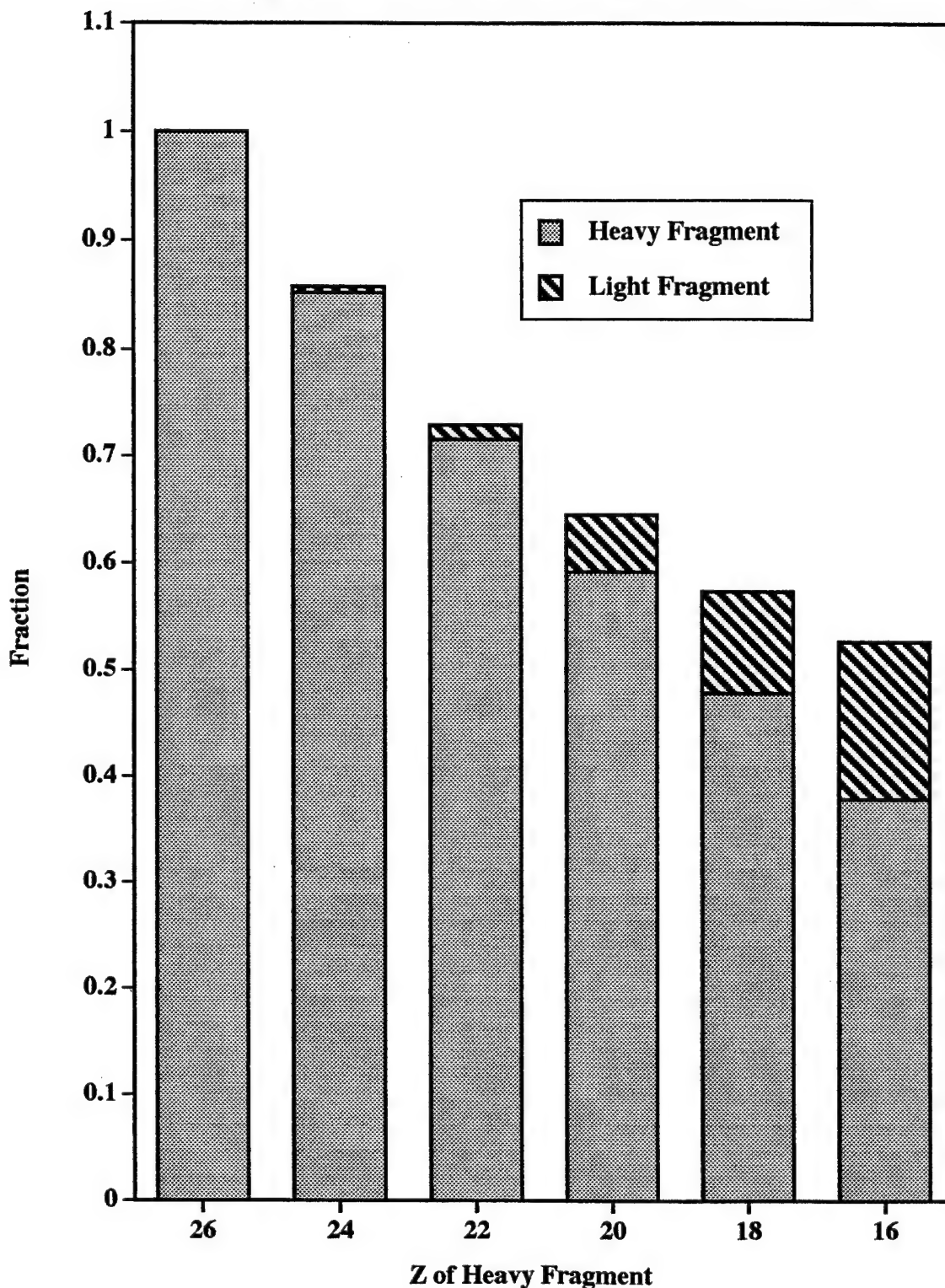
Most fragmentation events with significant reduction in the Z of the projectile, however, will not have only one lighter fragment. Rather, these events are characterized by high multiplicity in fragment number, often numerous doubly and singly charged nuclei. Appendix C contains experimental data for ^{56}Fe fragmentation.

Calculations were performed to determine the angular acceptance of detectors in the experimental set-up for straight projectile trajectories on the centerline of the TEPC and for fragmentation events that occur in the Cu target. The acceptance angles are as follows:

a. TEPC - 0.8°,

b. PSD2 - 1.7°, and

c. PSD1 - 8.3°

The mean emission angle for a proton produced in Fe fragmentation's is 2.78 ± 0.04°, with that of higher Z fragments being lower. The scattering of a proton from the projectile at this angle in the experimental set-up would introduce a lateral separation from the original trajectory of about 22 and 37 mm, respectively at the TEPC and PSD2. This proton would miss both the TEPC and PSD2. Alternatively, the proton could be scattered at an angle of 1.3°, allowing passage through the PSD2, but outside the TEPC.

Even for scattering angles less than 0.8°, where the trajectory of the lighter fragment crosses both the TEPC and PSD2, differences in the trajectory of the heavy and lighter fragments across the cavity will introduce subtle differences in detector response as compared to the particles having the same trajectory.

2. Position Errors

The PSDs determine the location of a particle trajectory based on the relative charge collected on either side of the PSD. For a single charged particle, position uncertainties are due to the finite resolution of the PSD. However, when a combination of charged particles traverse a PSD, the position signal may be ambiguous. The cases for three groups of projectile fragments are illustrated in Fig. 5-4. In Fig. 5-4a, the heavy fragment is Cr ($Z^2 = 576$) and is accompanied by two protons. For this case, the ionization produced by the

Figure 5-4. Combinations of Projectile Fragments from the Same Incident Projectile through a PSD Pair
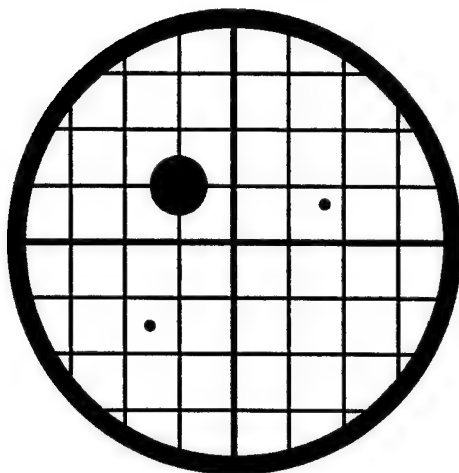
a

Heavy Fragment: Cr (Z = 24)

Light Fragments: 2 - Protons

b

Heavy Fragment: Ca (Z = 20)

Light Fragments: Li (Z = 3),
He, & Proton
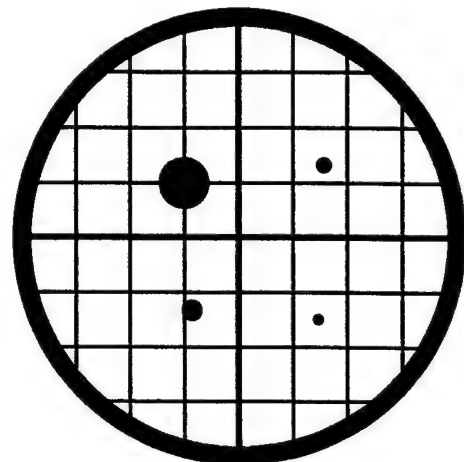
c
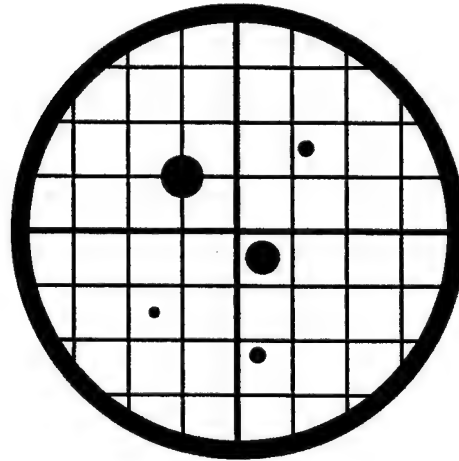
Heavy Fragment: Al (Z = 13)

Light Fragments: O (Z = 8),
2 - He, Proton

protons are insignificant compared to the Cr and the position determination for the Cr should be unaffected. In Fig. 5-4b, the heavy fragment is Ca ($Z^2 = 400$) and is accompanied by Li, He, and a proton. For this case, the ionization produced by the three lighter fragments is 3.5 % of that of the heavy fragment and a minor difference in the assigned and actual position of the heavy particle will be introduced. In Fig. 5-4c, the heavy fragment is Al ($Z^2 = 169$) and is accompanied by O ($Z^2 = 64$), two He, and a proton. The ionization produced for the lighter fragments is over 40 % of that of the Al. For this case, the signal from the device will be ambiguous.

Data

Detector response was analyzed for Fe and projectile fragments down to a heavy fragment Z of 18. Energy deposition in the TEPC and silicon detectors was comprised of that from all projectile fragments traversing the active volumes. Energy deposition for events that had the same heavy fragment may be vary because of the varied number and charge of the lighter fragments. The energy deposited in PSD y_2 should be nearly equal to the combined stopping power of all projectile fragments traversing it because the detector is thick, an approximation to CPE conditions. Therefore, the energy deposited in PSD y_2 provides a reasonable estimate of L for projectile fragments traversing the TEPC. Variance in the trajectory among projectile fragments will bias the TEPC response to lower energy deposition as compared to that in PSD y_2.

The ratio of energy deposited in the detector compared to $\Delta E\ y_2$ was consistent among Fe and projectile fragments with heavy fragment of Z: 21 - 25. For the fragments with heavy fragment of Z: 18 - 20, the mean ratio of energy deposited in the detector compared to that in PSD y_2 compared to that of Fe was 0.974 ± 0.013. For an event with this ratio and an Ar (Z = 18) heavy fragment, the approximate charge that traverses PSD y_2, but misses the TEPC corresponds to Li (Z = 3) or two α-particles.

109

Recommendations for Future Work

A more definitive analysis could be accomplished if there were two PSD pairs upstream of the detector, but downstream of the Cu target. To reduce bias observed in the present work, future experiments should have a silicon device downstream of the detector. This device should be place in close proximity of the detector and have an active area of the same dimensions as that of the detector. This would better insure that the projectile fragments that traverse the downstream silicon detector also traversed the detector.

Chapter 6:   Conclusions

Experiments were performed to measure the response of spherical TEPCs to Fe particles at 1 GeV/nucleon. The objective was to characterize effects caused by the abrupt change in density between the wall of the detector and the cavity gas used to simulate tissue volumes 1, 2, and 3 μm in diameter. The experimental arrangement included a particle spectrometer that determined the species and trajectory of the particles passing through the detector.

The characterization of the wall effect in this work is original and unique. The technique was superior to previous characterizations because the analysis could be performed for a spatially uniform particle fluence and the effect could be observed with respect to particle trajectory.

The data indicated that for Fe particles passing through the center of the detector, only about 75 to 80 % of the energy transferred to the cavity gas based on L was actually measured in the cavity gas (1 μm simulated diameter). A calculation using a model for the radial distribution of energy along a heavy ion track indicated that 30 % of the energy carried by δ-rays would escape the spherical volume. The difference between data and the model was a slight increase in energy deposition by δ-rays produced in the front wall of the detector. However, for this trajectory, the enhanced detector response from δ-rays produced in the wall of the thick-walled detector was not enough to compensate for the radial energy loss from δ-rays created in and escaping the cavity.

The measured value of lineal energy was less than that predicted by L alone for all trajectories with impact parameters less than 5.5 mm from the center of the cavity. At about

111

5.5 mm, the enhancement of detector response from δ-rays created in the wall were about equal to the radial energy loss from δ-rays created in the cavity gas. For particle trajectories approaching the cavity/wall interface, the measured energy deposition increased dramatically. Events with the largest energy deposition (i.e., $y > 250$ keV μm^{-1}) were associated with a very narrow band of impact parameters located at the cavity/wall interface. An analysis of nuclear cross-sections and variations in the trajectory through the detector indicated that the very large energy deposition events were due to enhanced energy deposition by soft collision electrons in the cavity rather than that of recoil nuclei.

The data for energy deposition as a function of impact parameter for the thick-walled TEPC were integrated to determine the absorbed dose measured in the simulated volume of tissue. For a μ-random Fe particles, the absorbed dose corresponded to particles with an L $= 154$ keV μm^{-1} in 1 and 2 μm diameters of tissue. A value of 150 keV μm^{-1} was obtained for the 3 μm simulated diameter. The minor difference in the experimental data from theory was believed to arise from calibration or position uncertainties. Thus, the enhancement of δ-rays to the detector response was sufficient to create CPE in the cavity.

Walled spherical TEPCs can provide accurate determination of absorbed dose, however, the distribution of energy deposition on an event by event basis does not represent that that would be observed in homogenous media.

$\overline{Q}$ was determined for a μ-random irradiation to Fe particles where the detector simulated a 1 μm diameter site. Close approximation of the actual Q was obtained under the assumption that $y = L$ for both ICRP 26 and 60 recommended relationships between Q and L. Similar results were obtained when the data was modified for ions of the same velocity, but lower Z.

For projectile fragments with a heavy fragment of Z between 21 and 25 traversing the center of the detector, the fraction of L absorbed in the detector was the same as that of Fe. For heavy fragments of Z between 18 and 20, the fraction of L absorbed in the detector

112

was about 97 % of that of Fe. Reduced energy deposition was due to inadequacies in the experimental design.

For charge-changing nuclear interactions in the wall of the detector, detector response is lower than that of Fe particles through the detector. Energy deposition from recoil nuclei do not appear to compensate for decreased energy deposition from electrons.

References

Amols, H.I. and Kliauga, P., "Microdosimetry of 10-18 MeV Electrons and Photons Using Walled and Wall-less Detectors," Radiation Protection Dosimetry, Vol. 13 No. 1-4, 365-368, 1985.

Anachkova, E.; Kellerer, A.M.; Roos, H.; "Calibrating and Testing Tissue Equivalent Proportional Counters with ^{37}Ar," Radiation and Environmental Biophysics, 33, 353-364, 1994.

Antonchik, V.A.; Bakaev, V.A.; Bogdanov, S.D.; Vikhrov, A.I.; Dudkin, V.E.; Nefedov, N.A.; Ostroumov, V.I.; Potapov, Yu.V.; "Interaction of ^{56}Fe at 1.8 GeV/nucleon with the Nuclei C, N, and O and with Ag and Br, Soviet Journal of Physics, 33 No. 4, 558-560, 1981.

Attix, F.H., Introduction to Radiological Physics and Radiation Dosimetry, John Wiley and Sons, New York, 1986.

Badhwar, G.D.; Konradi, A.; Hardy, A.; and Braby, L.A.; "Active Dosimetric Measurements on Space Shuttle Flights," Nuclear Tracks and Radiation Measurements, 20, 13-20, 1992.

Bichsel, H., "Review on W-Values," Fourth Symposium on Microdosimetry, Eds. J. Booz and H.G. Ebert, Commission of the European Communities, Luxembourg, 1015-1056, 1973.

Booz, J., "Microdosimetric Spectra and Parameters of Low LET-Radiations," in Proceedings of the Fifth Symposium on Microdosimetry, Eds. H.G. Ebert and J. Booz, Commission of the European Communities, Luxembourg, 311-345, 1975.

Borak, T.B. and Stinchcomb, T.G., "Errors in Estimating Neutron Quality Factor using Lineal Energy Distributions Measured in Tissue-Equivalent Proportional Counters," Health Physics, 43, 219-224, 1982.

Braby, L.A. and Ellett, W.H., "Ionization in Solid- and Grid-Walled Detectors," Radiation Research, 51, 569-580, 1972.

Butts, J.J. and Katz, R., "Theory of RBE for Heavy Ion Bombardment of Dry Enzymes and Viruses," Radiation Research, 30, 855-871, 1967.

Chatterjee, A.; Maccabee, H.D.; Tobias, C.A.; "Radial Cutoff Dose Calculations for Heavy Charged Particles in Water," Radiation Research, 54, 479-494, 1973.

Chatterjee, A. and Schaefer, H.J., "Microdosimetric Structure of Heavy Ion Tracks in Tissue," Radiation and Environmental Biophysics, 13, 215-227, 1976.

Chatterjee, A., "Penetration of Heavy Charged Particles through Matter," Lecture Presented at Department of Radiological Health Sciences, Colorado State University, Colorado, Spring 1993.

Chunxiang, Z.; Dunn, D.E.; Katz, R.; "Radial Distribution of Dose and Cross-Sections for the Inactiviation of Dry Enzymes and Viruses," Radiation Protection Dosimetry, Vol 13 No. 1-4, 215-218, 1985.

Cox, R., Thacker, J., and Goodhead, D.T.; "Inactivation and Mutation of Cultured Mammalian Cells by Aluminum Characteristic Ultra-soft X-rays. II. Dose Response of Chinese Hamster and Human Diploid Cells to Aluminum X-rays and Radiations of Different LET," International Journal of Radiation Biology, 31, 561-576, 1977.

Cucinotta, F.A.; Katz, R.; Wilson, J.W.; Townsend, L.W.; Nealy, J.E.; Shinn, J.L.; "Cellular Track Model of Biological Damage to Mammalian Cell Cultures from Galactic Cosmic Rays," NASA Technical Paper 3055, National Aeronautics and Space Administration, NASA Langley Research Center, Hampton VA, 1991.

Cucinotta, F.A.; Katz, R.; Wilson, J.W.; Dubey, Rajendra, R.; "Heavy Ion Track-Structure Calculations for Radial Dose in Arbitrary Materials," NASA Technical Paper 3497, National Aeronautics and Space Administration, NASA Langley Research Center, Hampton VA, 1995.

Curtis, S.B. and Schimmerling, W., "Nuclear Physics of Accelerated Heavy Ions," in Biological and Medical Research with Accelerated Heavy Ions at the Bevalac: 1974 - 1977, eds. Sheryl Elam, Lawrence Berkeley Laboratory, University of California, Report LBL-5610, April 1977.

Dicello, J.F.; Wasliolek, M.; and Zaider, M.; "Measured Microdosimetric Spectra of Energetic Ion Beams of Fe, Ar, Ne, and C: Limitations of LET Distributions and Quality Factors in Space Research and Radiation Effects," IEEE Transactions on Nuclear Science, 38, 1203-1209, 1991.

Dietze, G.; Menzel, H.G.; and Buhler, G.; "Calibration of Tissue-Equivalent Proportional Counters used As Radiation Protection Dosemeters," Radiation Protection Dosimetry, 9 No. 3, 245-249, 1984.

Dudkin, V.E.; Kovalev, E.E.; Nefedov, N.A.; Antonchik, V.A.; Bogdanov, S.D.; Ostoumov, V.I.; Crawford, H.J.; and Benton, E.V.; "Multiplicities of Secondaries in Interactions of 1.8 GeV/Nucleon ^{56}Fe Nuclei with Photoemulsion and the Cascade Evaporation Model," Nuclear Physics, A509, 783-799, 1990.

Dudkin, V.E.; Kovalev, E.E.; Nefedov, N.A.; Antonchik, V.A.; Bogdanov, S.D.; Ostoumov; V.I., Benton, E.V.; and Crawford, H.J.; "Target Fragments in Collisions of 1.8 GeV/Nucleon ^{56}Fe Nuclei with Photoemulsion Nuclei and the Cascade- Evaporation Model," Nuclear Physics, A530, 759-769, 1991.

Dudkin, V.E.; Kovalev, E.E.; Nefedov, N.A.; Antonchik, V.A.; Bogdanov, S.D.; Kosmach, V.F.; Likhachev, A.Yu.; Benton, E.V.; and Crawford, H.J.; "Dependence of the Multiplicities of Secondary Particles on the Impact Parameter in Collisions of High Energy Neon and Iron Nuclei with Photoemulsion Nuclei," Nuclear Physics, A551, 723 - 733, 1993.

Dudkin, V.E.; Kovalev, E.E.; Nefedov, N.A.; Antonchik, V.A.; Bogdanov, S.D.; Kosmach, V.F.; Likhachev, A.Yu.; Hassan, J.; Benton, E.V.; and Crawford, H.J.; "Multiplicities in Nuclear Interactions Induced by ^{20}Ne, ^{40}Ar, and ^{56}Fe Nuclei at 0.1 - 0.5 GeV/nucleon," Nuclear Physics, A568, 906 - 1006, 1994.

Eickel, R. and Booz, J., "The Influence of the Counter Wall and the Counter Shape on the Spectral Energy Deposition in Small Volumes by ^{60}Co Gamma-Rays and 200 kV X-Rays," Radiation and Environmental Biophysics, 13, 145-165, 1976.

Failla, Patricia McClement and Failla, Gioacchino, "Measurement of the Dose in Small Tissue Volumes Surrounding 'Point' Sources of Radioisotopes," Radiation Research, 13, 61-91, 1960.

Failla, G., "The Distribution of Energy Imparted to a Homogenous Medium Nonuniformly Irradiated," Radiation Research, 5, 205-215, 1956.

Failla, G., "The Flux of Secondary Ionizing Particles in a Uniformly Irradiated Homogenous Medium of Varying Density: Application to Walled Ionization Chambers," Radiation Research, 4, 102-109, 1956.

Fain, J.; Monnin, M.; Montret, M.; "Energy Density Deposited by a Heavy Ion Around its Path," in Proceedings of the Fourth Symposium on Microdosimetry, Eds. J. Booz, H.G. Ebert, R. Eickel, A. Waker, Commission of the European Communities, Luxembourg, 1974.

Glass, W.A. and Gross, W.A., "Wall-less Detectors in Microdosimetry," in Topics in Radiation Dosimetry, Radiation Dosimetry Supplement 1, Ed. Frank J. Attix, Academic Press, NY, 221.

Glass, W.A. and Braby, L.A., "A Wall-less Detector for Measuring Energy Deposition Spectra," Radiation Research, 39, 230-240, 1969.

Goodhead, D.T., Thacker, J., and Cox, R.; "Effectiveness of 0.3 keV Ultrasoft X-rays for the Inactivation and Mutation of Cultured Mammalian Cells," International Journal of Radiation Biology, 36, 101-114, 1978.

Goodman, L.J. and Colvett, R.D., "Biophysical Studies with High-Energy Argon Ions - I. Depth Dose Measurements in Tissue-Equivalent Liquid and in Water," Radiation Research, 70, 455-468, 1977.

Goodman, L.J. and Coyne, J.J., "W_n and Neutron Kerma for Methane-Based Tissue-Equivalent Gas," Radiation Research, 82, 13-26, 1980.

Gross, William; Biavati, B.J.; Rossi, H.H.; "Microdosimetry of Directly Ionizing Particles with Wall-less Proportional Counters," in Proceedings of the Second Symposium on Microdosimetry, Eds. H.G. Ebert and J. Booz, Commission of the European Communities, Luxembourg, 249-267, 1970.

Haque, A.K.M.M. and Saq'an, S.A., "Microdosimetric Study with Cylindrical Walled and Wall-less Proportional Counters," in Proceedings of the Sixth Symposium on Microdosimetry, Eds. H.G. Ebert and J. Booz, Harwood Academic Publishers Ltd., London, 1185-1201, 1978.

116

Heckman, H.H.; Greiner, D.E.; Lindstrom, P.J.; Shwe, H.; "Fragmentation of ^{4}He, ^{12}C, ^{14}N, and ^{16}O Nuclei in Nuclear Emulsion at 2.1 GeV/nucleon," Physical Review C, 17 No. 5, 1735-1747, 1978.

Hilbert, Jerald W. and Baily, Norman A., "Energy Deposition in Microscopic Volumes by High-Energy Protons," Radiation Research, 39, 1-14, 1969.

International Commission on Radiological Units and Measurements, ICRU Report 10a, Radiation Units Quantities and Units, National Bureau of Standards Handbook 84, Washington, 1962.

International Commission on Radiation Units and Measurements, ICRU Report 16, Linear Energy Transfer, International Commission on Radiation Units and Measurements, Washington, 15 June 1970.

International Commission on Radiation Units and Measurements, ICRU Report 31, Average Energy Required to Produce an Ion Pair, International Commission on Radiation Units and Measurements, Washington, 1979.

International Commission on Radiation Units and Measurements, ICRU Report 33, Radiation Quantities and Units, International Commission on Radiation Units and Measurements, Washington, 15 April 1980.

International Commission on Radiation Units and Measurements, ICRU Report 36, Microdosimetry, International Commission on Radiation Units and Measurements, Bethesda Md, 31 December 1983.

International Commission on Radiation Units and Measurements, ICRU Report 40, The Quality Factor in Radiation Protection, International Commission on Radiation Units and Measurements, Bethesda Md, 4 April 1986.

International Commission on Radiation Units and Measurements, ICRU Report 49, Stopping Powers and Ranges for Protons and Alpha Particles, International Commission on Radiation Units and Measurements, Bethesda Md, 15 May 1993.

International Commission on Radiation Units and Measurements, ICRU Report 55, Secondary Electron Spectra from Charged Particle Interactions, International Commission on Radiation Units and Measurements, Bethesda Md, 20 March 1996.

International Commission on Radiological Protection, ICRP Report 26, Recommendations of the ICRP, Annals of the ICRP 1, No. 3, Pergamon Press, New York, 1977.

International Commission on Radiological Protection, ICRP Report 60, 1990 Recommedations of the ICRP, Annals of the ICRP 21 (1-3), Pergamon Press, New York, 1991.

Katz, R.; Ackerson, B.; Homayoonfar, M.; Sharma, S.C.; "Inactivation of Cells by Heavy Ion Bombardment," Radiation Research, 47, 402-425, 1971.

Kellerer, A.M., "An Algorithm for LET Analysis," Physics in Medicine and Biology, 17, 232-238, 1972.

Kellerer, A.M. and Rossi, H.H., "The Theory of Dual Radiation Action," Current Topics in Radiation Research, 8, 85-158, 1972.

Kellerer, A.M., "Event Simultaneity in Cavities," Radiation Research, 48, 216-233, 1971.

Kellerer, A.M., "An Assessment of Wall Effects in Microdosimetric Measurements," Radiation Research, 47, 377-386, 1971.

Kliauga, P.; Colvett, R.D.; Goodman, L.J.; Lam, Y.M.; "Microdosimetry of 400 MeV/AMU ^{12}C and 450 MeV/AMU ^{40}Ar Beams," in Proceedings of the Sixth Symposium on Microdosimetry, Eds. H.G. Ebert and J. Booz, Harwood Academic Publishers Ltd., London, 1173-1183, 1978.

Kliauga, P., "Measurement of Single-event Energt Deposition Spectra at 5 nm to 250 nm Simulated Site Sizes," Radiation Protection Dosimetry, 31, 119-123, 1990.

Kliauga, P., "Microdosimetry at Middle Ages: Some Old Experimental Problems and New Aspirations," Radiation Research, 124, S5-S15, 1990.

Kliauga, P., "Risk Assessment for HZE Particles: The Importance of Wall Effects in Experimental   Measurements," in Radiation Physics, Biophysics, and Radiation Biology, Eds. E.J. Hall and M. Zaider, Center for Radiological Research, Department of Radiation Oncology, College of Physicians and Surgeons of Columbia University, Progress Report, 15-23, May 1994. Available through National Technical Information Center (DE94 015657).

Kliauga, P., "Nanodosimetry of Heavy Ions Using a Miniature Cylindrical Counter of Wall-less Design," Radiation Protection Dosimetry, 52 Nos. 1-4, 317-321, 1994.

Kraft, G.; Kramer, M.; and; Scholz, M.; " LET, Track Structure and Models," Radiation and Environmental Biophysics, 31, 161-180, 1992.

Leonard, B.E. and Boring, J.W., "The Average Energy per Ion Pair, W, for Hydrogen and Oxygen Ions in Tissue Equivalent Gas," Radiation Research, 55, 1-9, 1973.

Luxton, G. and Fessenden, P., "Microdosimetric Measurements of Pretherapeutic Heavy Ion Beams," Radiation Research, 79, 256-272, 1979.

Metting, N.F.; Braby, L.A.; Rossi, H.H.; Kliauga, P.J.; Howard, J.; Schimmerling, W.; Wong, M.; Rapkin, M.; "Measurement of Energy Depositions Near High Energy, Heavy Ion Tracks," Pacific Norwest Laboratory Report No. 5950, December 1986, Available through National Technical Information Center (DE86 015818).

Metting, N.F.; Rossi, H.H.; Braby, L.A.; Kliauga, P.J.; Howard, J.; Zaider, M.; Schimmerling, W.; Wong, M.; Rapkin, M.; "Microdosimetry near the Trajectory of High-Energy Heavy Ions," Radiation Research, 116, 183-195, 1988.

Meyers, I.T., "Ionization," in Radiation Dosimetry, 2nd Ed, Vol 1, Eds. Attix, Frank H.; Roesch, W.C.; and Tochlin, W.E.; Academic Press, NY, 1968.

Mood, A.M., Graybill, F.A., and Boes, D.C.; Introduction to the Theory of Statistics, 3rd Ed, McGraw-Hill, N.Y., 1974.

National Council on Radiation Protection and Measurements, NCRP Report 98, Guidance on Radiation Received in Space Activities, National Council on Radiation Protection and Measurements, Bethesda Md, 31 Jul 89.

Oldenburg, U. and Booz, J., "Wall Effects of Spherical Proportional Counters," in <u>Proceedins of the Second Symposium on Microdosimetry</u>, Eds. H.G. Ebert and J. Booz, Commission of the European Communities, Luxembourg, 269-281, 1970.

Ottolenghi, A.; Merzagora, M.; Tallone, L.; Durante, M.; Paretzke, H.G.; and Wilson, W.E.; "The Quality of DNA Double-Strand Breaks: a Monte Carlo Simulation of the End-Structure of Strand Breaks Produced by Protons and Alpha Particles," Radiation and Environmental Biophysics," 34, 239-244, 1995.

Ricourt, A; Posny, F.; Soulie, R.; Chemtob, M.; and Ngugen, V.D.; "Possibilities d'Utilization des Techniques Microdosimetriques pour la Determination de L' equivalent de dose," <u>Proceedings of the Seventh Symposium on Microdosimetry</u>, Eds. H.G. Ebert, J. Booz, and H.D. Hartfiel, Harwood Academic Publishers Ltd., London, 1173-1183, 1980.

Rodgers, R.C.; Dicello, J.F.; and Gross, W.; "The Biophysical Properties of 3.9 GeV Nitrogen Ions II. Microdosimetry," Radiation Research, 54, 12-23, 1973.

Rossi, Harald H. and Rosenzweig, Walter; "Measurements of Neutron Dose as a Function of Linear Energy Transfer," Radiation Research, 2, 417-425, 1955.

Rossi, Harald H. and Rosenzweig, "A Device for the Measurement of Dose as a Function of Specific Ionization," Radiology, 64, 404-411, 1955.

Rossi, Harald H., "Microscopic Energy Distribution in Irradiated Matter," in <u>Radiation Dosimetry</u>, 2nd Ed, Vol 1, Eds. Attix, Frank H. and Roesch, William C., Academic Press, NY, 1968.

Rossi, H.H. and Zaider, M., <u>Microdismetry and its Applications</u>, Springer-Verlag, Berlin, 1996.

Savitzky, A. and Golay, M.J.E., "Smoothing and Differentiation of Data by Simplified Least Squares Procedures," Analytical Chemistry, 36 No. 8, 1627-1637, 1964.

Schimmerling, W.; Kaplan, S.; Subramanian, T.S.; McDonald, W.J.; Gabor, G.; Sadoff, A.; Alpen, E.; "Measurements of W for High Energy Ions," Eighth Symposium on Microdosimetry, Eds. J. Booz and H.G. Ebert, Luxembourg, 311-320, 1982.

Schrewe, U.J.; Brede, H.J.; Pihet, P.; Menzel, H.G.; "On the Calibration of Proportional Counters with Built-In α-Particle Sources," Radiation Protection Dosimetry, 23 No. 1/4, 249-252, 1988.

Simmons, J.A., "Comments on Measurements of W-Values in Tissue-Equivalent Gas for Alpha Particles," Physics in Medicine and Biology, 31 No. 3, 275-279, 1986.

Stinchcomb, T.G. and Borak, T.B.; "Neutron Quality Parameters vs Energy Below 4 MeV from Microdismetric Calculations," Radiation Research, 93, 1-18, 1983.

Thomas, R.H.; Lyman, J.T.; de Castro, T.M.; "A Measurement of the Average Energy Required to Create an Ion Pair in Nitrogen by High-Energy Ions," Radiation Research, 82, 1-12, 1980.

Toburen, L.H.; Braby, L.A.; Metting, N.F.; Kraft, G.; Scholz, M.; Kraske, F.; Schmidt-Bocking, H.; Dorner, R.; Seip, R.; "Radial Distributions of Energy Deposited Along Charged Particle Tracks," Radiation Protection Dosimetry, Vol 31 No. 1/4, 199-203, 1990.

Townsend, L.W.; Wilson, J.; and Cucinotta, F.A.; "A Simple Parameterization as a Function of Linear Energy Transfer," Health Physics, 53 No. 5, 531-532, 1987.

Turner, J.E., "Atoms, Radiation, and Radiation Protection," McGraw-Hill Inc., New York, 1992.

Varma, M.N.; Baum, J.W.; and Kuehner, A.V.; "Energy Deposition in Tissue Equivalent Gas," Radiation Research, 62, 1-11, 1975.

Varma, M.N.; Paretzke, H.G.; Baum, J.W.; Lyman, J.T.; Howard, J, "Dose as a Function of Radial Distance from a 930 MeV ^{4}He Ion Beam," in Proceedings of the Fifth Symposium on Microdosimetry, Eds. J. Booz, H.G. Ebert, and B.G.R. Smith, Commission of the European Communities, Luxembourg, 1976.

Varma, M.N. and Baum, J.W., "Energy Deposition in Nanometer Regions by 377 MeV/nucleon ^{20}Ne Ions," Radiation Research, 81, 355-363, 1980.

Varma, M.N.; Baum, J.W.; Kliauga, P.; Bond, V.P., "Microdosimetric Parameters for Photons as a Function of Depth in Water using Wall-less and Walled Counters, Radiation Research, 88, 466-475, 1981.

Westfall, G.D.; Wilson, L.W.; Lindstrom, P.J.; Crawford, H.J.; Greiner, D.E.; Heckman, H.H.; "Fragmentation of Relativistic ^{56}Fe," Physical Review C, 19 No.4, 1309-1323, 1979.

Wilson, J.W. and Costner, C.M., "Nucleon and Heavy-Ion Total and Absorption Cross Section for Selected Nuclei," NASA Technical Note D-8107, National Aeronautics and Space Administration, Washington DC, 1975.

Wilson, J.W.; Townsend, L.W.; Schimmerling, W.; Khandelwal, G.S.; Khan, F.; Nealy, J.E.; Cucinotta, F.A.; Simonsen, L.C.; Shinn, J.L.; Norbury, J.W.; "Transport Methods and Interactions for Space Radiations," NASA Reference Publication 1257, National Aeronautics and Space Administration, Washington, 1991.

Wilson, J.W.; Kim, M.; Schimmerling, W.; Badavi, F.F,; Thibeault, S.A.; Cucinotta, F.A.; Shinn, J.L.; Kiefer, R.; "Issues in Space Radiation Protection: Galactic Cosmic Rays," Health Physics, 68 No. 1, 50-58, 1995.

Wilson, W.E. and Paretzke, H.G., "A Stochastic Model of Ion Track Structure," Radiation Protection Dosimetry, 52 No. 1-4, 249-253, 1994.

Wong, M.; Schimmerling, W.; Phillips, M.H.; Ludewigt, B.A.; Landis, D.A.; Walton, J.T.; Curtis, S.B.; "The Multiple Coulomb Scattering of Very Heavy Charged Particles," Medical Physics, 17 No. 2, 163-171, 1990.

Zeitlin, Cary, Lawrence Berkeley Laboratory, Personal Communication, 1996.

Zeitlin, Cary, Lawrence Berkeley Laboratory, Personal Communication, 1997.

120

Zirkle, R. E.; Marchbank, D.F.; Kuck, K.D.; "Exponential and Sigmoid Survival Curves Resulting from Alpha and X-irradiation of *Aspergillus* spores," Journal of Cellular Comparative Physiology, 39 Supplement 1, 1952.

Appendix A: Chatterjee Track Structure Model

The Chatterjee model (1973, 1976, and 1993) defines energy density around the trajectory of heavy charged particles. The energy deposition is defined for two distinct regions: the core and penumbra. The energy deposited in the core is defined by equation A-1:

$$\rho_{core} = \frac{L\,[\,2\,+\,2\ln\,(^{r_p}\!/_{r_c})\,]}{2\,\pi\,r_c^2\,[\,1\,+\,2\ln\,(^{r_p}\!/_{r_c})\,]}, \qquad (A-1)$$

where r_p, r_c, L are the penumbra radius, core radius, and the stopping power, respectively. The energy deposited in the penumbra is defined by equation A-2:

$$\rho_{penumbra} = \frac{L}{2\,\pi\,r^2\,[\,1\,+\,2\ln\,(^{r_p}\!/_{r_c})\,]}, \qquad (A-2)$$

where r is the radial distance from the particle trajectory. The plot in Fig. A-1 provides core and penumbra radii.

Figure A-2 provides a plot of dose (keV μm^{-3}) versus radial distance from the trajectory of a 1 GeV/nucleon ^{56}Fe in homogenous unit density media. Although it is agreed that there is no clear demarcation between a core region and the penumbra portion of the track, it is treated as such in the model. For both regions of the track, it is assumed that energy deposition is homogenous. From the graph, it is apparent that beyond the core region, dose is a function of the reciprocal of the radial distance squared.

Figure A-1. Core and Penumbra Radii for Chatterjee Model (1993)
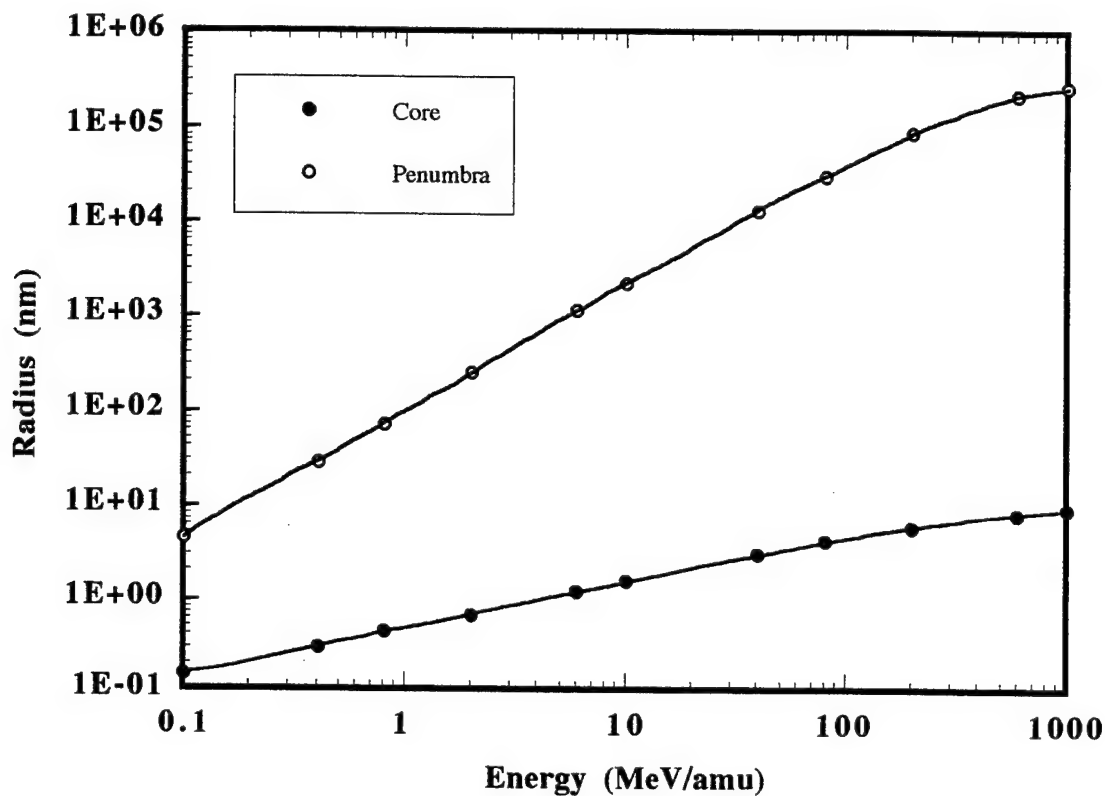
Figure A-2. Dose vs. Radial Distance from Trajectory For 1 GeV/nucleon
^{56}Fe Particle, Chatterjee Model (1993)
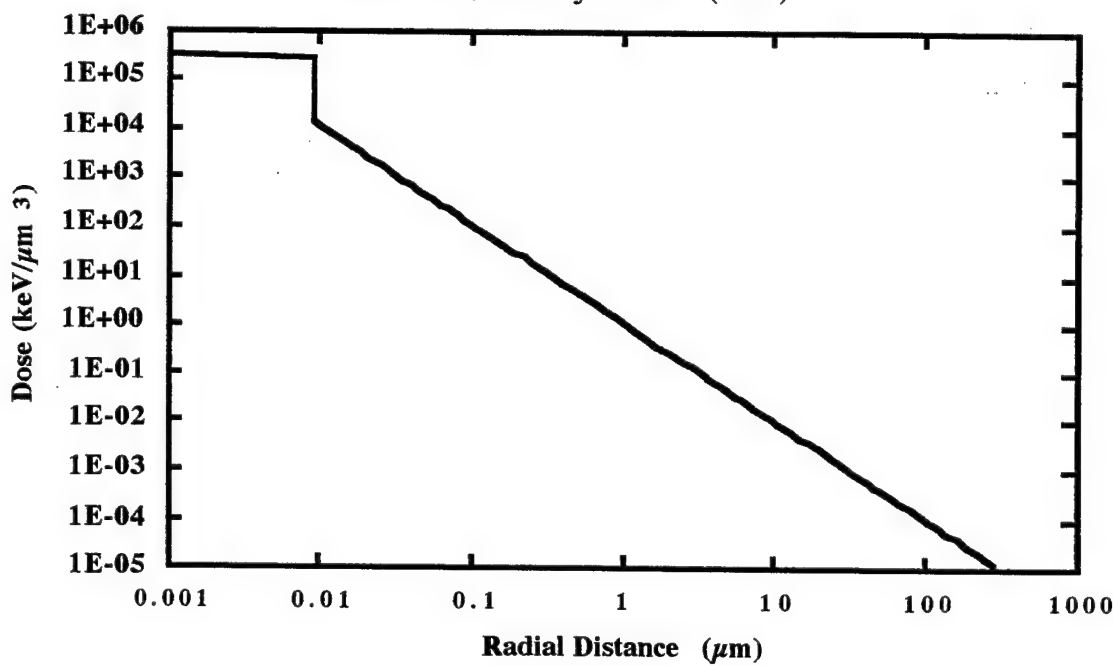
The model can be used to calculate energy absorbed is volumes of any size in the

vicinity of heavy ion trajectories as illustrated in Figure A-3 for a sphere. In the Figure, the

trajectory is perpendicular to the page, dense ionization in vicinity of the core is simulated

by black and dark shading, while δ-rays are extending radially from the trajectory. Three

trajectories are illustrated: one where the trajectory is penetrating the sphere in the center

Figure A-3. Trajectories of Heavy Ion in Vicinity of Spherical Volume.
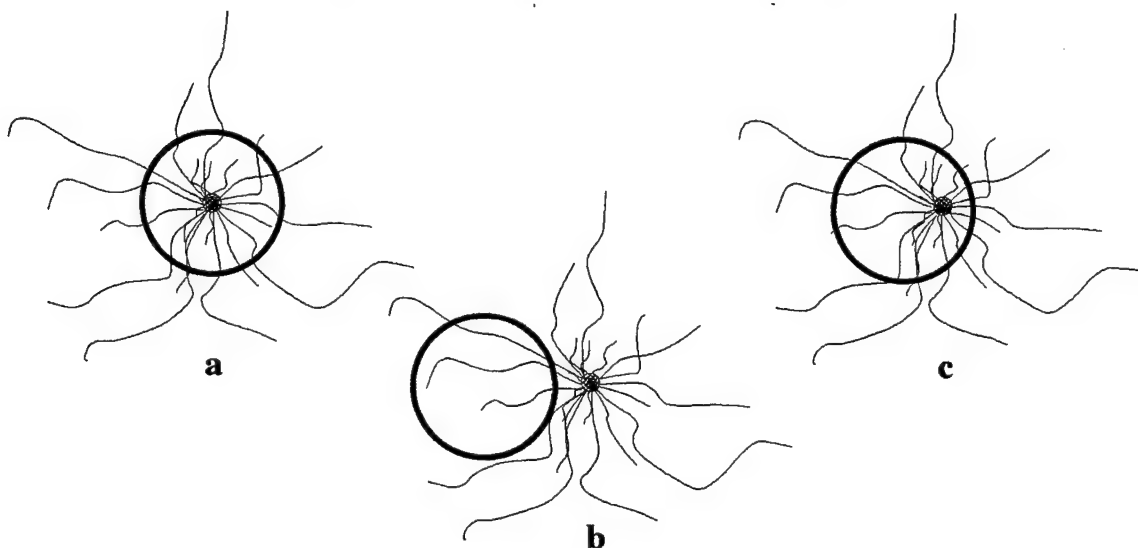
where the chord length through the volume is maximum (a), another where the trajectory is

outside of the sphere (b), and the last where the trajectory is through the sphere, but near

the edge (c). For volumes with diameters on the order of microns that are applicable to

microdosimetry (and illustrated in Fig. A-3), virtually all soft collision electrons produced

along the ion trajectory in the sensitive volume will be absorbed. For trajectories where

the ion does not intersect the volume (Fig. A-3b), soft collision electrons will not contribute

to absorbed energy in the volume and energy deposition will be from energetic δ-rays

generated outside the sensitive volume. For the model, provided the radial distance of the

ion trajectory to the volume is less the penumbra radius, ionization from δ-rays will contribute to the absorbed energy in the volume.

Figure A-4 illustrates the approach taken to calculate the energy absorbed in sensitive volumes in the vicinity of ion trajectories. The volume of the detector was divided into

Figure A-4. Voxelized Detector Volume in Vicinity of Ion Trajectory.

Radial Distance
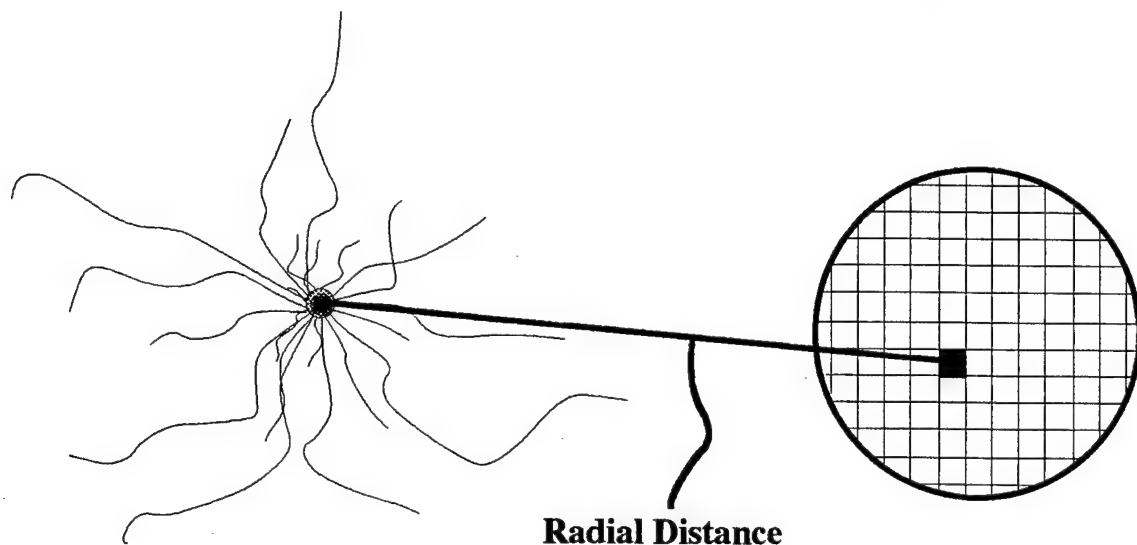
many smaller discrete volumes (voxels) as illustrated in the Figure. The energy deposited in each volume was the product of the radial dose and the volume of the voxel. The voxel volume was the product of the cross-sectional area of each voxel and the voxel length. Voxel length was calculated from geometrical dimensions of a sphere. For calculations, detector volumes were broken into 4280 voxels of cross-sectional voxel area dependent on the radius of the sphere simulated. Absorbed energy in the vicinity of 1 GeV/amu ^{56}Fe was calculated for spheres of varying radii. Figure A-5 provides a summary of the calculations for a 0.5 μm radius sphere in terms of the mean lineal energy.

Figure A-5. Mean Lineal Energy vs. Distance from Detector Center
of Ion Trajectory for a 0.5 μm Radius Sphere
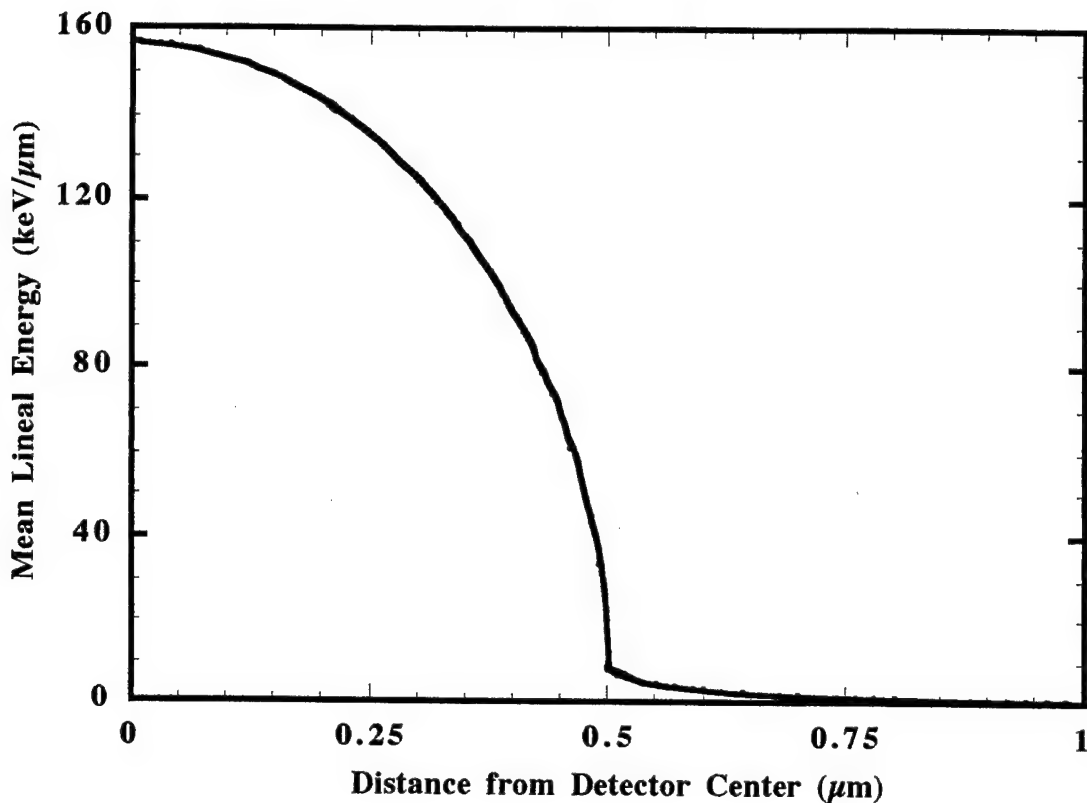
The fraction of the L absorbed in volumes directly traversed by ions is a parameter

of interest. Chatterjee's model (1993) provides a formula that relates the fraction of L

absorbed in an infinite cylinder around the trajectory of an ion for cylinders of various

radii. The formula is a simple integration of Eqs. A-1 and -2 from the center of the cylinder

to the radius of interest. Figure A-6 provides a plot of the fraction of L absorbed in infinite

cylindrical and bound spherical volumes for 1 GeV/nucleon ions at various radii. As

expected, the infinite cylinders will have higher absorbed fraction of L than the spheres.

Figure A-6. Fraction of L Absorbed in Cylindrical and Spherical
Volumes for 1 GeV/Nucleon Ions, Based on Chatterjee Model (1993)
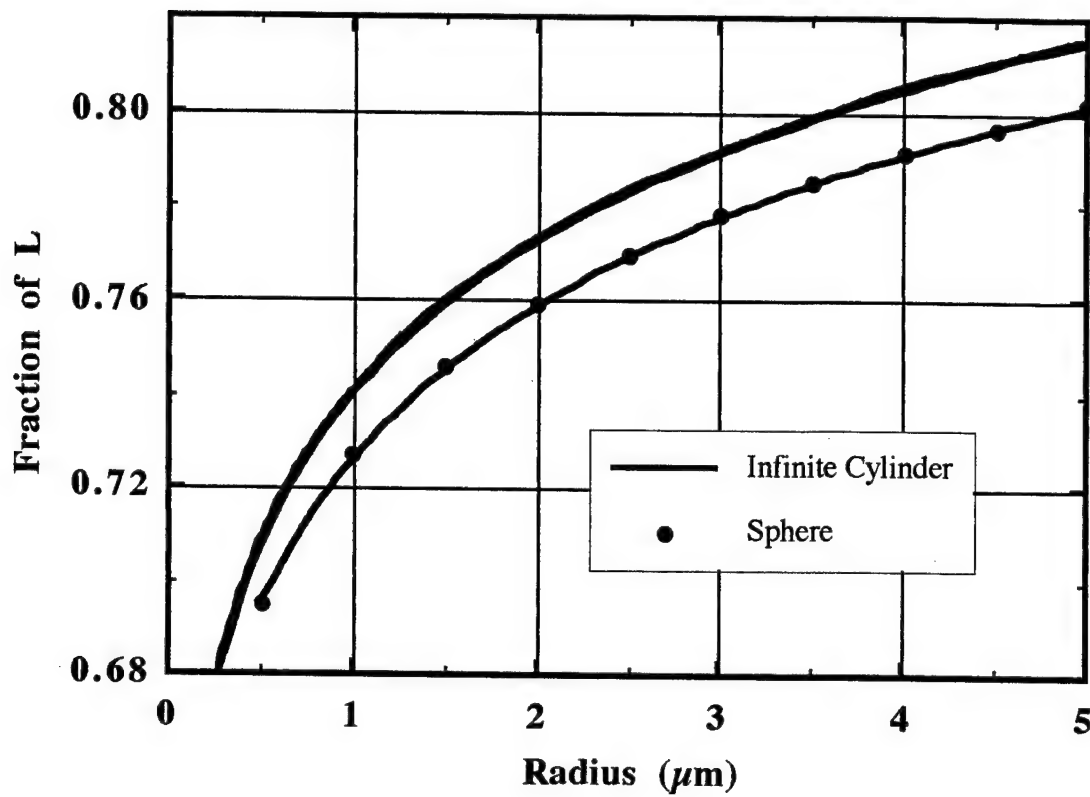
Appendix B: Calibration

General

The objective of microdosimetry is to measure the energy deposited in a sensitive volume, while TEPCs measures the charge collected per event that is proportional to the number of ion pairs formed within the simulated volume (cavity). The two parameters are related to each other by W, the mean energy expended per ion pair formed. W-values vary considerably among radiation types, proportional counter fill gases, energy of the incident radiation, and the energy deposited by the radiation.

Energy calibrations must be carried out by irradiating the counter with a radiation that deposits a known amount of energy. Generally, α-particle, neutron, or x-ray sources are used. K-line aluminum (1.49 keV), ^{55}Fe, and ^{37}Ar x-ray sources are used, with the aluminum and argon more appropriate for counters that simulate diameters less than a micron. Additionally, x-ray calibration sources are more appropriate for low-LET radiation measurements since the energy range and W-values of the two are more closely matched. For x-ray sources, the range of the secondaries are considerably lower than a few microns (ICRU 1983), dimensions typical of traditional microdosimeters. Thus, the geometry does not limit the ionization produced. For walled proportional counters constructed of A-150 plastic, over time and under continuous vacuum, the plastic shrinks and becomes dimensionally unstable leading to errors in the actual size of the cavity (Kliauga 1990). These errors can invalidate a calibration. Another problem with some x-ray sources is that they do not sample the entire detector volume; ^{37}Ar sources avoid this problem because they are mixed with the counting gas (Anachkova *et al.* 1991). Built-in α-particle calibration

128

sources of [241]Am and [244]Cm are commonly used in commercially available microdosimeters (Schrewe *et al.* 1988). The sources are commonly mounted on the outside of the wall of the detector. A small hole drilled in the wall allows penetration and collimation of the α-particles. A dominant peak in the spectrum is caused by α-particles that cross the cavity along the full chord length for spherical counters and normally to the height for cylindrical counters. The spherical TEPCs used in these experiments have built-in [244]Cm sources that are gravity controlled. External fast neutron sources are another method of calibration and use recoil protons as the radiation source. In contrast to built-in α-calibration sources, these sources do not provide recoil protons of a single energy or single pathlength in the cavity. Calibration is made by evaluation of the proton-edge of the collected spectrum - a position in the spectrum where protons have both maximum stopping power and maximum chord length. Calibration of cylindrical counters with neutron sources requires special procedures due to the chord length distribution (Anachkova *et al.* 1994).

W-values

ICRU Report 31 (1979) provided a comprehensive review of W-values. ICRU defines W as the quotient of E by N, where N is the mean number of ion pairs formed when the initial kinetic energy, E, of a charged particle is completely dissipated in the gas:

$$W = \frac{E}{N}.$$

(B-1)

The differential value, w, of the mean energy required to produce an ion pair is the quotient of dE by dN, where dE is the mean energy lost by a charged particle of energy E in traversing an absorber of thickness dx, and dN is the mean number of ion pairs produced when dE is completely dissipated in the gas:

$$w = \frac{dE}{dN}.$$

(B-2)

129

The relationship between W and w is defined by:

$$W(E) = \frac{E}{\int_I^E d\varepsilon/w(\varepsilon)},\tag{B-3}$$

where I is the lowest ionization potential of the medium and ε is the instantaneous energy of the particle while slowing down. Numerous measurements of W have been performed, many of which are summarized in ICRU Report 31, but very few have been made on w (Bichsel 1972).

ICRU (1979) and Goodman and Coyne (1980) have summarized W values for protons, α-particles, and heavy ions in tissue-equivalent (TE) gas. Goodman and Coyne performed least-squares evaluations of experimental data. Empirical functions for protons and α-particles from their work are:

$$W(\text{protons}) = 29.28\,(\ln E)^{-2} + 29.99\,(\text{eV ion pair}^{-1})\text{ and}\tag{B-4}$$

$$W(\alpha\text{-particles}) = 49.96\,(\ln E)^{-0.2418}\,(\text{eV ion pair}^{-1}),\tag{B-5}$$

where E is initial particle energy in keV/nucleon. Figure B-1 provides a plot of the Goodman and Coyne empirical functions for protons, α-particles, and oxygen ion. Three noticeable features of the functions are apparent. First, W values for all three particles increase significantly for low initial energy particles and is due to a larger fraction of the energy transferred to atoms or molecules in the form of excitation rather than ionization. Second, for low energy particles, W values are higher for particles of higher Z-number. And lastly, at higher velocities, W values become relatively independent of energy. Myers (1968) noted that W values, in general, should exhibit little dependence on energy above:

$$E_0 = \frac{1}{2}\,M\,v_0^2,\tag{B-6}$$

130

where M is the projectile mass and v_0 is the velocity of an electron in the first Bohr orbit.

Figure B-1. Empirical Functions of W for Protons, α-Particles, and Oxygen Ions (Goodman and Coyne 1980).
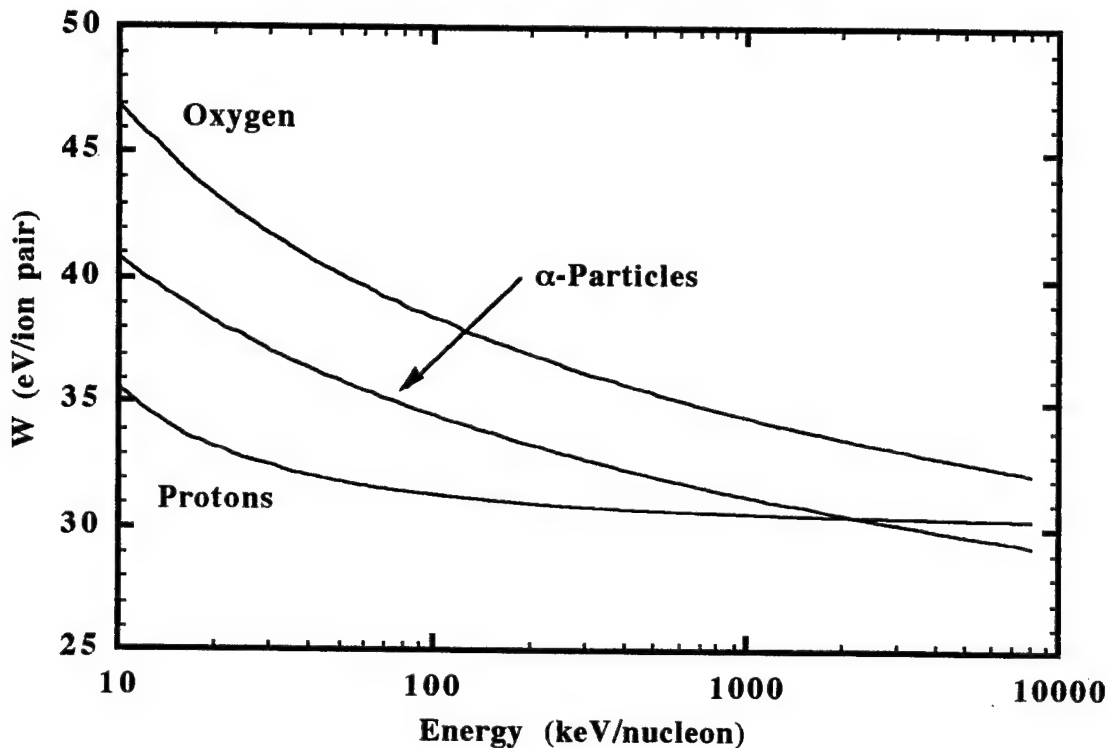
Very little experimental work on W- and w-values determination have been accomplished for high-energy heavy ions. Goodman and Colvett (1977) reported that the value of $w(\varepsilon)$ in TE gas for 429 MeV/amu Ar^{18+} ions to be similar to that of ^{137}Cs photons, under the assumption that the $w(\varepsilon)$ of ^{60}Co, 29.2 ± 0.6 eV ion pair^{-1} from Leonard and Boring (1973), is the same as that for ^{137}Cs. This value is reasonably close to the W of 31.0 eV ion pair^{-1} for 5.3 MeV using the Goodman and Coyne empirical formula. Thomas *et al.* (1980) measured $w(\varepsilon)$ values for 250 MeV/nucleon C^{6+}, 375 MeV/nucleon Ne^{10+}, and 479 MeV/nucleon Ar^{18+} ions in nitrogen gas. Respectively, the reported values along with percent fractional errors (% FE) were: 36.4 ± 0.6 (% FE = 1.7 %), 35.4 ± 0.8 (%FE = 2.3 %), 34.7 ± 0.5 (% FE = 1.4 %) eV ion pair^{-1}. From the experimental data, the authors

131

could not conclude that there was a Z dependence of $w(\varepsilon)$ nor any significant difference between the three values. Schimmerling *et al.* (1982) measured $w(\varepsilon)$ for Ne^{10+}, Al^{13+}, Si^{14+} in nitrogen and P-7 gas over particle energy range of 100 - 700 MeV/nucleon. The mean value reported for nitrogen gas was 33.0 ± 2.3 eV ion pair^{-1}, with % FE of 7.0 %. The values of Thomas *et al.* are close to the recommended W value, 36.39 ± 0.23 eV ion pair^{-1}, reported in ICRU Report 31 for α-particles of approximate energy 5.3 MeV in nitrogen. The value reported by Schimmerling *et al.* is lower than the ICRU value, but may not be different considering the relatively large % FE.

Calibration Comparisons with Far-West Technologies 1/2" LET TEPC

Calibration was performed by three separate techniques for the thin-walled TEPC used in these experiments:

1. single-event peak of unscattered α-particles from the built-in ^{244}Cm source,

2. proton-edge from irradiation with ^{239}Pu:Be unmoderated neutron source, and

3. α-particle-edge from α-particles that are scattered in the borehole of the detector wall as described by Schrewe *et al.* (1988).

The first and third technique were performed for the thick-walled detector.

In the comparison, stopping power values for protons and α-particles were taken from ICRU Report 49 (1993) for propane-based TE gas. Mean energy deposited by particles was calculated with these stopping power values and the continuous stopping distance approximation (CSDA). Because the particles used for the calibrations do not completely stop in the cavity of the detector, W-values were determined from the empirical formulas of

Goodman and Coyne and Equation B-2, where dE is difference in the initial, E_i, and final, E_f, energy of the particle, and

$$dN = (E_i / W_i) - (E_f / W_f), \qquad (B\text{-}7)$$

where W_i and W_f are the W-values respectively for particles of energy equal to the initial and final energy of the particle. The classical definition of W-value infers an integration of $w(\varepsilon)$ from the initial particle energy to that of the lowest ionization potential. To avoid confusion, W-values calculated in this manner will be referred to as integral w-values. Initial α-particle energy from the [244]Cm source was assumed to be 5.789 MeV, the frequency-weighted mean of the energy of the two alpha particles emitted. Also, separate calculations of energy transferred were performed for the single-event peak of unscattered α-particles from the built-in [244]Cm source for the thin- and thick-walled detectors. This is necessary since the initial and final energy of the α-particle will be different for the two detectors because there is a difference in the energy lost by α-particles in the wall region. Table B-1 summarizes factors used in the calibrations and comparison among techniques. From the energy transferred values listed in the Table, it is apparent that there are significant differences dependent on simulated diameter. For the α-peak values, there is a 1.7 and 1.9 percent difference between the energy transferred for the 0.5 and 3 μm simulated diameters, respectively for the thin and thick walled cavities. However, for the α– and proton-edge values, the differences are greater, 3.3 % and 15.8 %, respectively. In comparison of the integral w-values from 0.5 to 3 μm for each of the techniques, the maximum difference was 0.7 % and deemed trivial. However, the difference between the integral w-values of the α-edge technique and the other two is as high as 7.4 %. This

133

difference is very close to that reported by Schrewe *et al.* (1988) for a similar comparison of calibration techniques.

Table B-1. Calibration Factors

Technique	Simulated Diameter (μm)	Energy Transferred (keV μm^{-1})	Initial Particle Energy (MeV)	Final Particle Energy (MeV)	Integral *w*-Value (eV ion pair^{-1})
α-peak	0.5	83.79	5.785	5.743	29.93
thin	1	84.06	5.781	5.697	29.93
walled	2	84.62	5.772	5.603	29.94
detector	3	85.19	5.764	5.508	29.95
α-peak	0.5	83.83	5.781	5.739	29.93
thick	1	84.15	5.772	5.688	29.93
walled	2	84.80	5.756	5.568	29.94
detector	3	85.48	5.739	5.482	29.95
proton	0.5	100.8	0.107	0.057	30.83
edge	1	97.75	0.139	0.041	30.82
(max.	2	91.21	0.206	0.024	30.79
energy)	3	86.06	0.270	0.015	30.76
alpha	0.5	259.3	0.694	0.564	32.22
edge	1	257.8	0.765	0.507	32.21
(max.	2	255.2	0.926	0.416	32.17
energy)	3	250.9	1.111	0.357	32.10

Comparison of Thin-Walled Detector

The spectrum collected for the internal α-calibration source is displayed in Figure B-2. The prominent peak near channel 60 corresponds to unscattered α-particles, while the point of maximum energy deposition of scattered α-particles occurs near channel 150 and is called the α-edge. Events with magnitude significantly higher than that of the α-edge are

134

few in number and are likely attributable to α-particle coincidences. The peak to the left of

that for unscattered α-particles, has a peak frequency about 5 % of the peak for unscattered

α-particles. The lower energy deposition peak has a mean energy deposition about half

that of the prominent peak and is due to α-particles that are absorbed by the helix or anode

wires after passing part of the way through the cavity.

Figure B-2. Internal α-Particle Calibration Source Spectrum
(Serial Number = 1373, HV = 600 volts, Simulated Diameter = 1 μm)
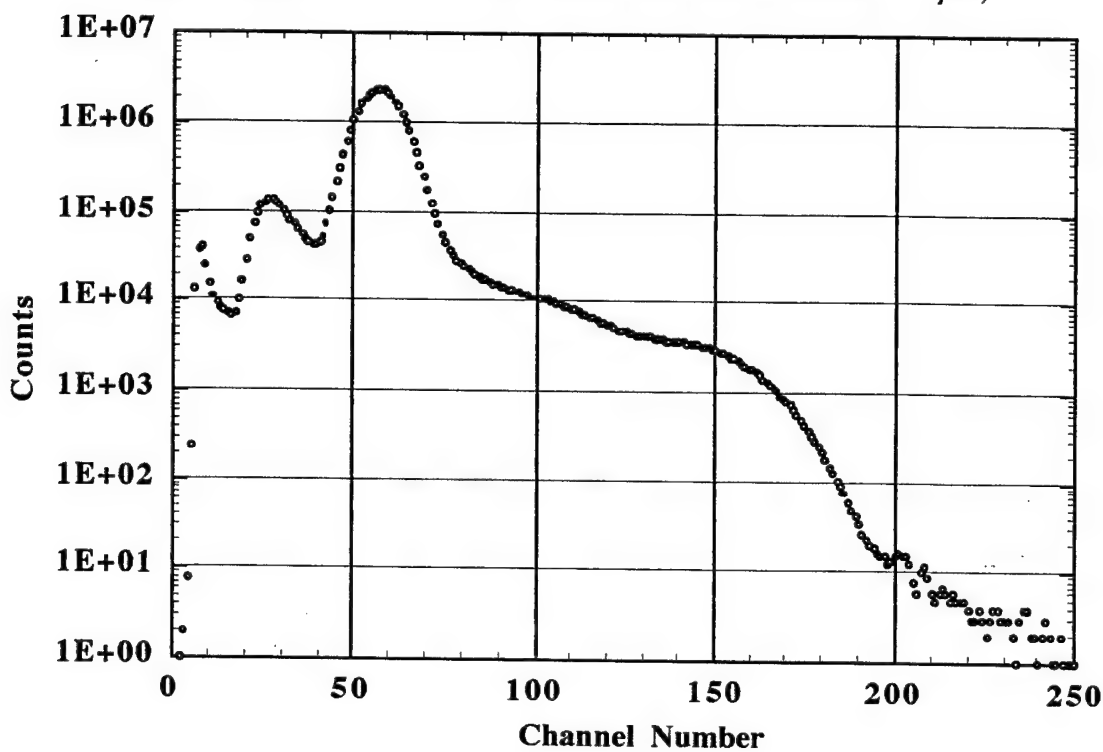
The peak corresponding to unscattered α-particles appears asymmetric and would result

in a difference between the mean and most probable value (Schrewe *et al.* 1988). Schrewe

et al. (1988) calculated the distribution functions for various simulated diameters of

spherical TEPCs and determined that energy loss straggling follows a Vavilov distribution

for diameters up to 2 μm and that the relative difference in the mean and most probable

energy deposition are small at 1 and 0.6 %, respectively for 1 and 2 μm. Because the

difference is small for simulated diameters greater 1 μm, and 1 μm was the smallest

diameter used in our experiments, energy deposition corresponding to the most probable

value will be assumed to be equal to the mean. To evaluate the magnitudes corresponding

to the most probable energy and α-edge, the first derivative of the frequency distribution

was calculated by a numerical technique of Savitzky and Golay (1964).

Figure B-3 is the first derivative of the calibration data of Fig. B-2, truncated for data

channels in the vicinity of the most probable value. Interpolation of the data points

provides an approximate "zero" crossing-point at channel 56$\frac{2}{3}$.

Figure B-3. First Derivative of Data from Fig. B-2 (Most Probable Value Region).
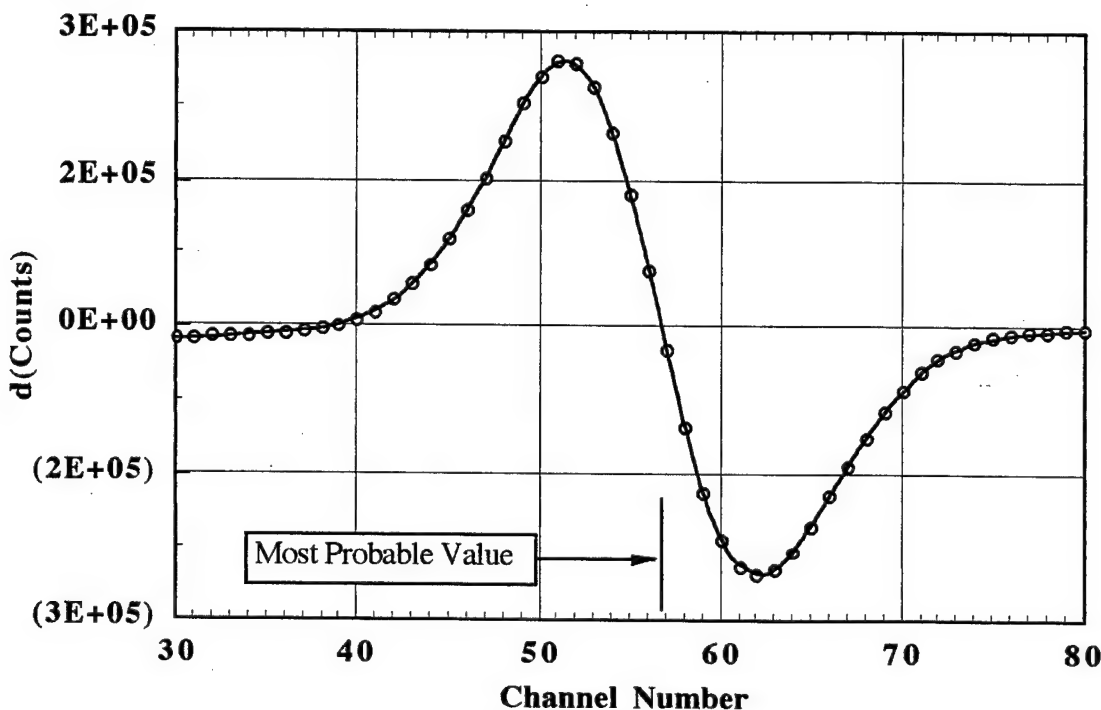
Figure B-4 is the first derivative of the same data in the vicinity of the α-edge. Precise

evaluation of the α-edge is complicated and would require a detailed simulation of the

energy loss and straggling outside and inside of the detector according to Schrewe *et al.*

136

(1988). From inspection of the plot, there is a broad minimum in the distribution with the center near channel 157.

Figure B-4. First Derivative of Data from Fig. B-2 (α-Edge Region)
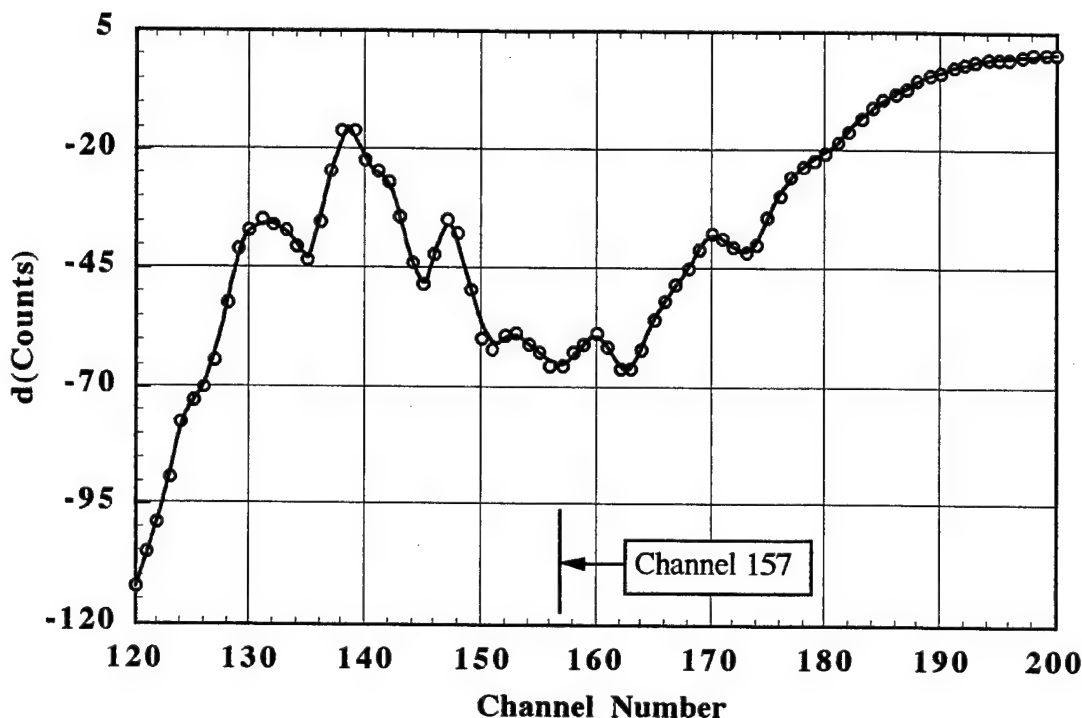
For neutron spectra collection, α-particle calibrations were performed before and after the neutron spectrum was collected to insure constant gas pressure in the TEPC existed throughout the measurements. Before and after α-calibration spectra are displayed in Fig. B-5 truncated in the region of the most probable value. Figure B-6 contains the first derivative spectra of the data in Fig. B-5. Most probable value constancy, ~ channel 80.6, indicates constant gas pressure throughout the measurements.

Figure B-7 is a plot of the neutron spectrum collected over a 14-hour period. Apparent from the spectrum is the proton-edge near channel 100. Figure B-8 contains the first derivative spectrum of the neutron data truncated for the channels in the vicinity of the proton-edge. As used for evaluation of the α-edge, the local minimum in the derivative is

137

Figure B-5. Before and After α-Calibration Spectra for Neutron Measurements.
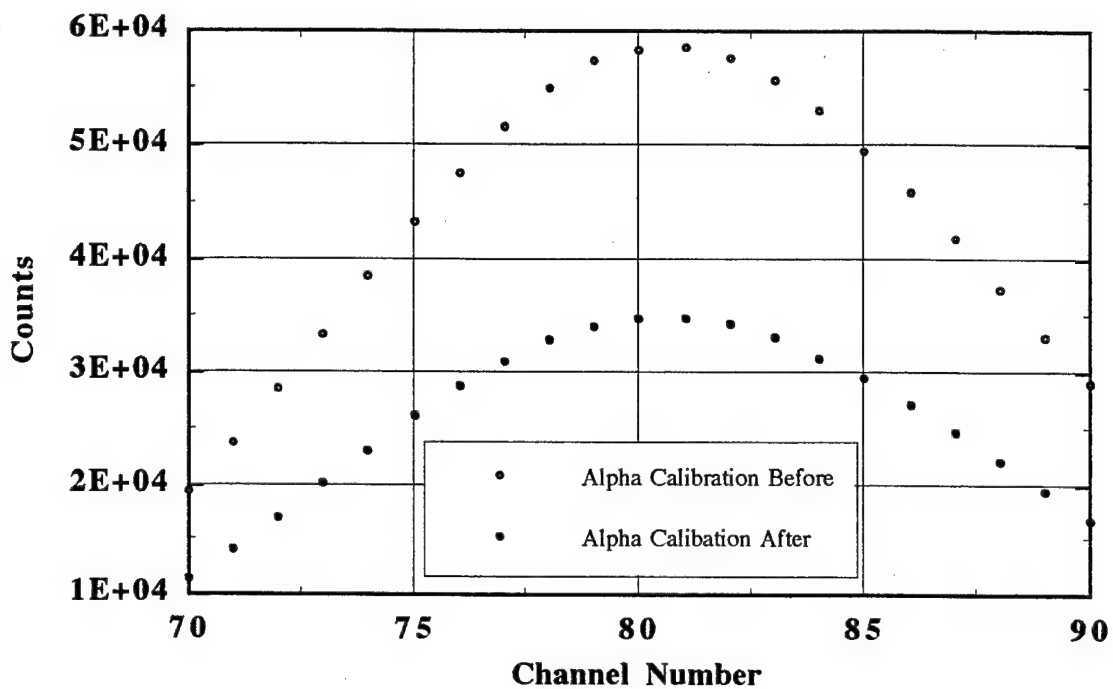
Figure B-6. First Derivative of Data from Fig. B-5.

138
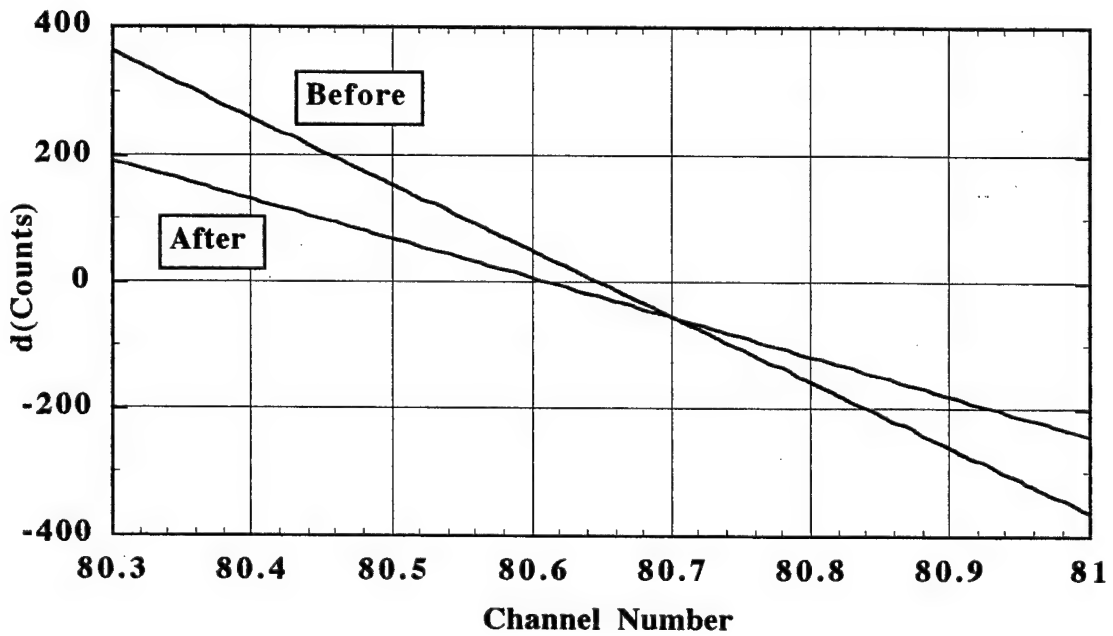
Figure B-7. Neutron Spectrum (Serial Number = 1373, HV = 600 volts, Simulated Diameter = 1 μm)
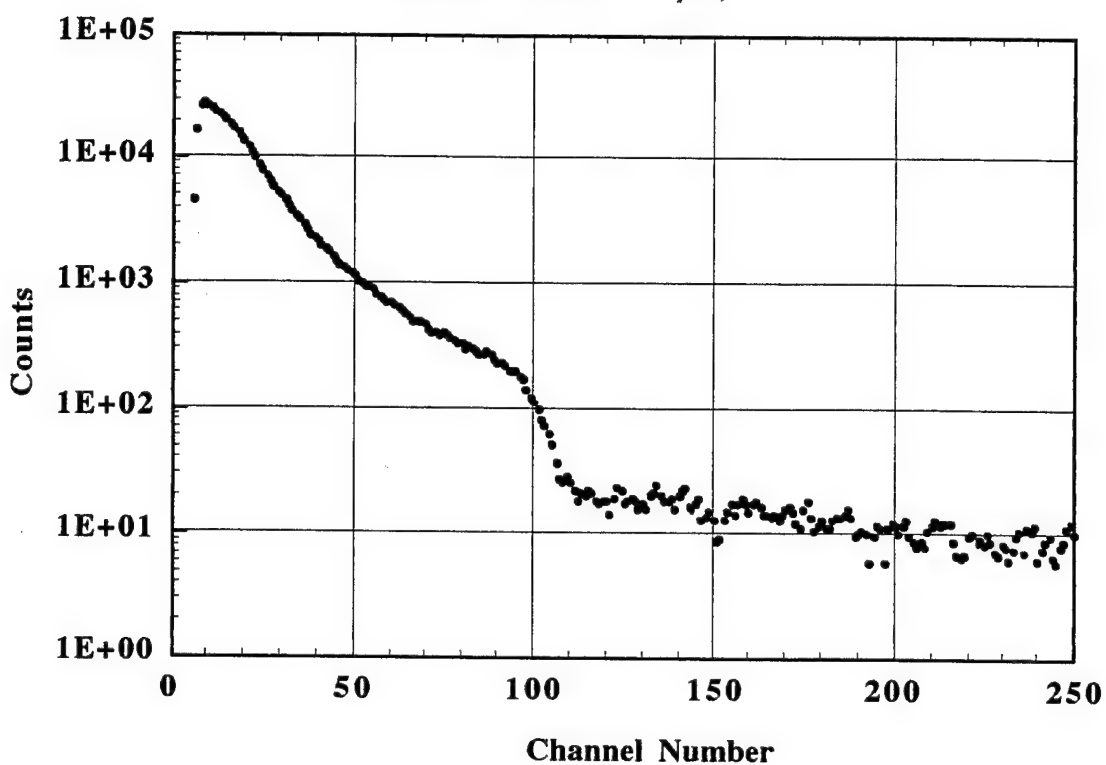
Figure B-8. First Derivative of Data from Fig. B-7.

139
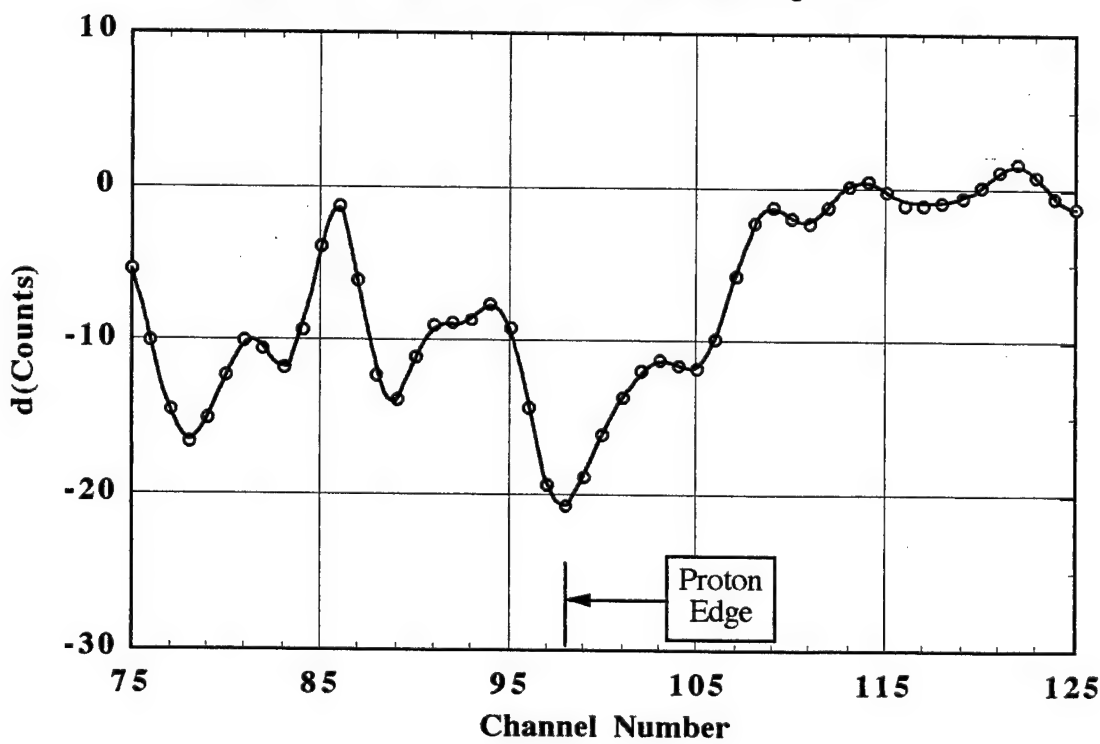
the point where the frequency spectrum has its steepest negative slope and is designated the proton-edge. For this data set, channel 98 possesses the lowest value in the derivative spectrum in this region. From inspection of Fig. B-7, this criterion seems reasonable.

To provide accurate comparison of the three techniques, a research pulser calibration of the multichannel analyzer was performed. Table B-2 provides pulser settings for analyzer channels 5 through 254.

The relative location of the three features are compared. Pulser settings are related to relative energy deposited from Table 2.

1. The ratio of the pulser settings determines the relative ratio of ion pairs created by two techniques being compared.

2. The ratio of the number of ion pairs expected between two techniques being compared is calculated from energy transferred values and integral w-values from Table 1. Finally, the two ratios from 1. and 2. above are compared. Equation B-8 is a summary of the calculations for comparison of the α-peak and proton-edge:

$$\text{Ratio} = \frac{\text{P.S.(test)}}{\text{P.S.}(\alpha\text{-peak})} * \frac{E_t(\alpha\text{-peak})}{E_t(\text{test})} * \frac{w(\text{test})}{w(\alpha\text{-peak})}, \qquad (B-8)$$

where P.S. is the relative pulser setting and E_t is the energy transferred. For comparison of the α-edge to α-peak, the ratio is:

$$\text{Ratio} = \frac{605.88}{207.66} * \frac{84.06}{257.8} * \frac{32.21}{29.93} = 1.024. \qquad (B-9)$$

Equation B-10 summarizes the calculation of the ratio of the expected number of ion pairs between the proton-edge to those produced by the mean of the α-peak.

$$\text{Ratio} = \frac{367.44}{325.38} * \frac{84.06}{97.75} * \frac{30.82}{29.93} = 1.000. \qquad (B-10)$$

140

Table 2. Relationship of Research Pulser Settings to Multichannel
Analyzer Channel Number for Conversion Gain = 256

Channel Number	Pulser Setting	Channel Number	Pulser Setting	Channel Number	Pulser Setting	Channel Number	Pulser Setting	Channel Number	Pulser Setting
5	10.08	55	201.11	105	398.14	155	597.88	205	797.07
6	13.82	56	205.00	106	402.12	156	601.88	206	801.03
7	17.56	57	208.90	107	406.10	157	605.88	207	804.98
8	21.31	58	212.80	108	410.08	158	609.88	208	808.93
9	25.06	59	216.70	109	414.06	159	613.88	209	812.88
10	28.82	60	220.60	110	418.05	160	617.88	210	816.83
11	32.58	61	224.50	111	422.03	161	621.88	211	820.78
12	36.34	62	228.41	112	426.01	162	625.88	212	824.72
13	40.10	63	232.32	113	430.00	163	629.88	213	828.67
14	43.87	64	236.23	114	433.99	164	633.87	214	832.61
15	47.65	65	240.14	115	437.98	165	637.87	215	836.55
16	51.42	66	244.06	116	441.96	166	641.87	216	840.49
17	55.20	67	247.97	117	445.95	167	645.86	217	844.43
18	58.99	68	251.89	118	449.94	168	649.86	218	848.36
19	62.77	69	255.82	119	453.93	169	653.85	219	852.30
20	66.56	70	259.74	120	457.93	170	657.85	220	856.23
21	70.36	71	263.66	121	461.92	171	661.84	221	860.16
22	74.15	72	267.59	122	465.91	172	665.83	222	864.08
23	77.95	73	271.52	123	469.91	173	669.83	223	868.01
24	81.76	74	275.45	124	473.90	174	673.82	224	871.93
25	85.56	75	279.39	125	477.89	175	677.81	225	875.85
26	89.37	76	283.32	126	481.89	176	681.80	226	879.77
27	93.18	77	287.26	127	485.89	177	685.79	227	883.69
28	97.00	78	291.20	128	489.88	178	689.78	228	887.60
29	100.82	79	295.14	129	493.88	179	693.77	229	891.52
30	104.64	80	299.08	130	497.88	180	697.75	230	895.43
31	108.46	81	303.02	131	501.87	181	701.74	231	899.34
32	112.29	82	306.97	132	505.87	182	705.72	232	903.24
33	116.12	83	310.92	133	509.87	183	709.71	233	907.15
34	119.96	84	314.87	134	513.87	184	713.69	234	911.05
35	123.79	85	318.82	135	517.87	185	717.67	235	914.95
36	127.63	86	322.77	136	521.87	186	721.65	236	918.85
37	131.48	87	326.72	137	525.87	187	725.63	237	922.74
38	135.32	88	330.68	138	529.87	188	729.61	238	926.63
39	139.17	89	334.64	139	533.87	189	733.59	239	930.52
40	143.02	90	338.60	140	537.87	190	737.57	240	934.41
41	146.88	91	342.56	141	541.87	191	741.54	241	938.30
42	150.73	92	346.52	142	545.87	192	745.52	242	942.18
43	154.59	93	350.48	143	549.87	193	749.49	243	946.06
44	158.45	94	354.45	144	553.87	194	753.46	244	949.94
45	162.32	95	358.41	145	557.88	195	757.43	245	953.81
46	166.19	96	362.38	146	561.88	196	761.40	246	957.68
47	170.06	97	366.35	147	565.88	197	765.37	247	961.55
48	173.93	98	370.32	148	569.88	198	769.34	248	965.42
49	177.81	99	374.29	149	573.88	199	773.31	249	969.29
50	181.68	100	378.26	150	577.88	200	777.27	250	973.15
51	185.56	101	382.23	151	581.88	201	781.23	251	977.01
52	189.45	102	386.21	152	585.88	202	785.19	252	980.86
53	193.33	103	390.18	153	589.88	203	789.15	253	984.72
54	197.22	104	394.16	154	593.88	204	793.11	254	988.57

142

From the ratios, it is apparent that, within the uncertainties of:

1. selection of an appropriate position of the α- and proton-edges,

2. integral w-values, and

3. energy transferred calculations,

that the three techniques provide similar results for this detector.

Comparison of Thick-Walled Detector

The spectrum collected for the internal α-calibration source is displayed in Fig. B-9. The prominent peak of the spectrum is similar to that of the thin-walled detector. But, some notable differences exist. The peak to the left of the prominent peak, that is caused by absorption of α-particles in the helix and anode wires, is of greater magnitude than that of the thin-walled detector. This is due to a higher degree of collimation and a higher fraction of unscattered particles being absorbed by the wires. Also, the scattered contribution to the spectrum is greater with a more prominent plateau than for that of the thin-walled detector. Figure B-10 is the first derivative of the spectrum contained in Fig. B-9 truncated for the region of the most probable value that is located at channel 65. Figure B-11 is the first derivative of the spectrum in the vicinity of the α-edge. The location of the α-edge (channel 181) is more apparent than was the case of the thin-walled detector that had a broader distribution at the minimum. This is reasonable since the thick-walled detector had a higher proportion of scattered particles. Using Equation B-8, the ratio of the expected number of ion pairs produced by the α-edge and α-peak is calculated:

$$\text{Ratio} = \frac{701.74}{240.14} * \frac{84.15}{257.8} * \frac{32.21}{29.93} = 1.027. \qquad \text{(B-11)}$$

143

Figure B-9. Internal α-Particle Calibration Source Spectrum
(Serial Number = 1376, HV = 600 volts, Simulated Diameter = 1 μm)
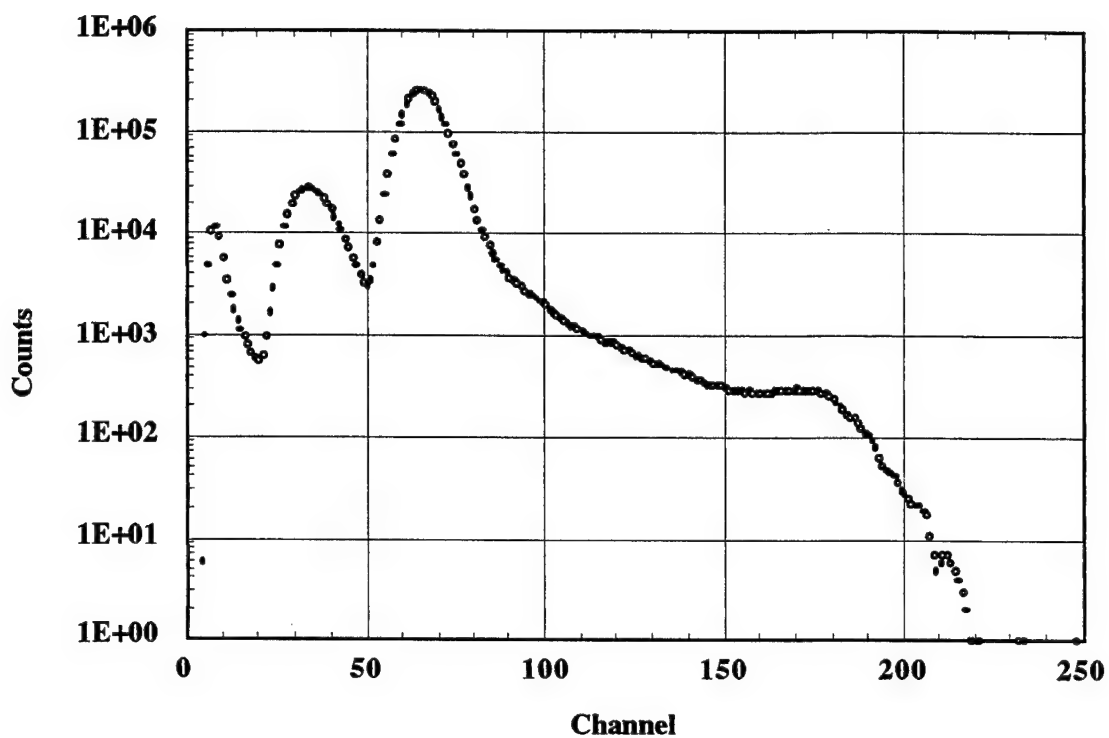
Figure B-10. First Derivative of Data from Fig. B-9 (Most Probable Value Region)

144
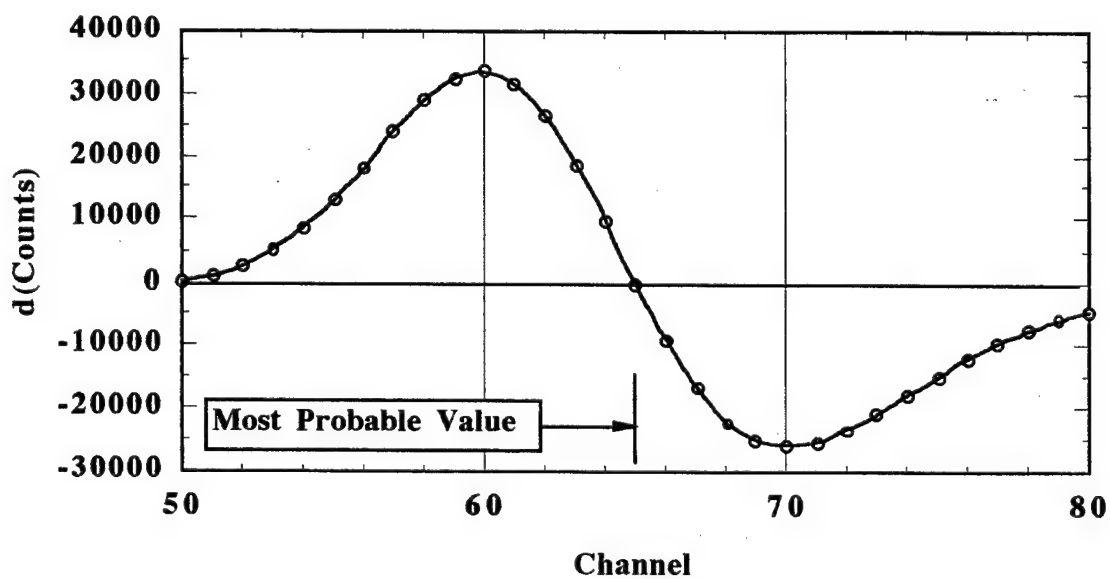
Figure B-11 First Derivative of Data from Fig. B-9 (α-Edge Region)
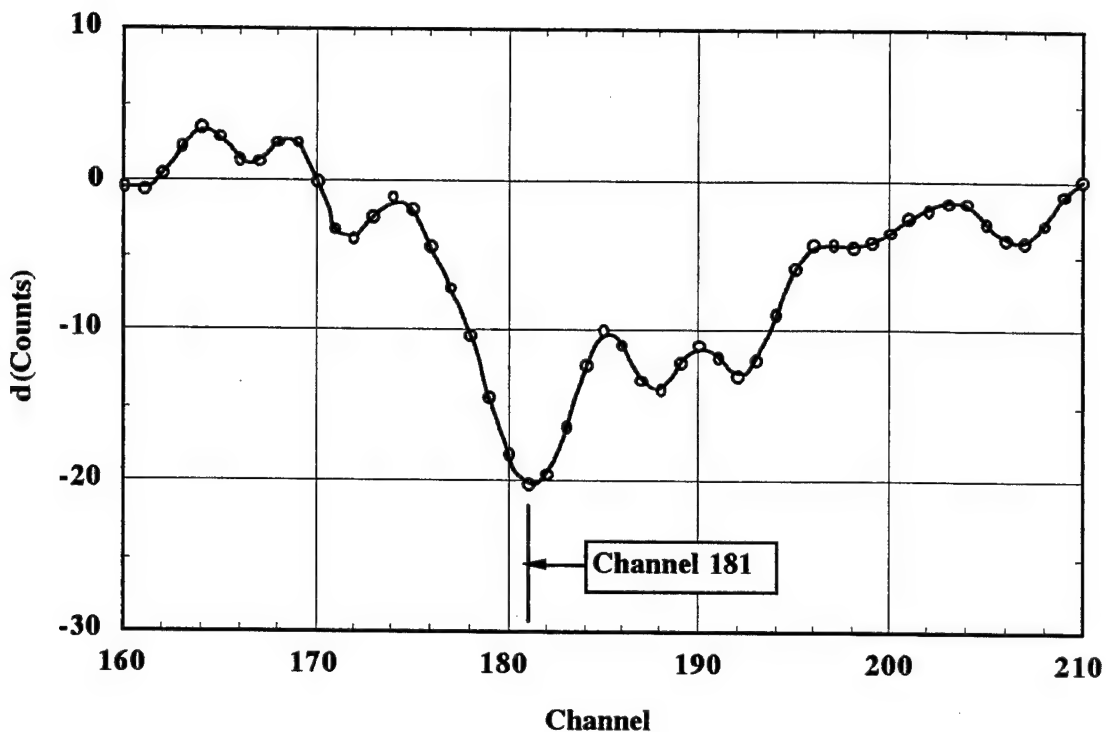
Thus, for the thick-walled detector, as was the case for the thin, there is close agreement between the two techniques.

Calibration for ^{56}Ions

Based on the comparison of calibration techniques, best available literature on w-values, it is reasonable to apply the most probable value of the internal α-calibration source spectra directly to ^{56}Fe ions without any correction for w-values.

Appendix C: Nuclear Interactions

General

Considerable interest and effort to model nuclear interaction cross-sections of high-velocity ions have been performed by NASA and others over the last 40 years. Details on current models used by NASA are in NASA Reference Publication 1257 (Wilson *et al.* 1991). Heavy charged particles traversing matter lose energy primarily through ionization and excitation of atoms, except at very low velocities where nuclear interactions become an important form of energy loss. While nuclear interactions are responsible for relatively small energy transfer in high-velocity ions, the interactions alters energy deposition at the interaction site and the characteristics of the radiation field from fragmentation interactions (Wilson *et al.* 1991). Nuclear interactions between projectile and target nuclei involve electromagnetic forces, also referred to as the Coulombic force. Nuclear forces are also involved when the impact parameter between the two nuclei is less than the sum of the respective nuclear radii. In interactions of this type, the nuclear forces typically dominate the interaction. For nuclear interactions that occur at impact parameters greater than the sum of the nuclear radii, electromagnetic interactions are only important. These interactions contribute to a phenomenon called multiple Coulomb scattering, have a negligible contribution to energy loss, have negligible interaction cross-sections as compared to that of collisions (Wilson *et al.* 1991), and are ignored in discussion of nuclear cross-sections in the remainder of this appendix. The total nuclear interaction cross-section, σ_{TOT}, is the sum of the elastic interaction cross-section, σ_S, and the absorption (inelastic) interaction cross-section, σ_{ABS}.

146

Elastic Scattering

Elastic scattering is a nuclear interaction process where there is conservation of momentum and kinetic energy and the two nuclei remain intact. Figure C-1 provides an example of elastic scattering. The example illustrates an interaction between a high-velocity ^{56}Fe projectile nucleus and a target ^{12}C nucleus. In the interaction, the path and velocity of the iron nucleus remains relatively unchanged and neither of the nuclei have a change in nucleon number, A or charge, Z. Particles from these interactions are scattered primarily in the forward direction (ICRU 1993).

Figure C-1. Elastic Scattering.
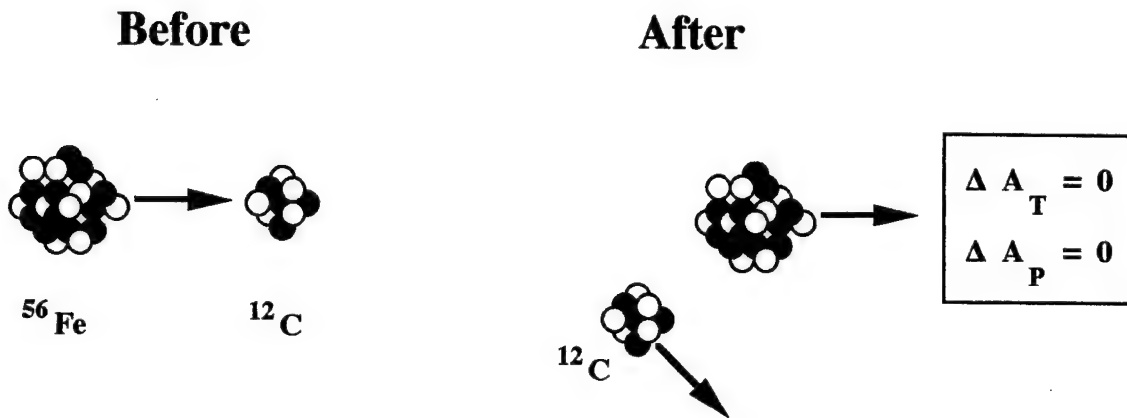
Wilson and Costner (1975) applied the coherent wave as an approximation to the elastic channel and found good agreement with available experimental data. NASA uses these approximations in their nuclear transport calculations (Wilson *et al.* 1991). For measurements collected in this experiment, production of scattered nuclei in the wall of the TEPC could influence the response in the cavity if these particles have sufficient penetration range. Equation B-1 defines the maximum energy transfer from a projectile to target particle at rest (Turner 1992).

$$Q_{max} = \frac{2\gamma^2 M_1 V^2}{1 + 2\gamma \, M_1/M_2 + M_1^2/M_2^2},$$
(C-1)

where Q_{max} is the maximum kinetic energy transfer, M_1 is the rest mass of the target nuclei, M_2 is the rest mass of the projectile, $\gamma = 1/\sqrt{1-\beta^2}$, $\beta = V/c$, and c is the speed of light.

For 1 GeV/amu ^{56}Fe ions, the maximum kinetic energy transfer to is 5800 and 3200 MeV/nucleon to proton and carbon nuclei, respectively, the two primary components of the TEPC wall. Figure C-2 is a plot of particle penetration range in water versus kinetic energy based on ICRU 49 (ICRU 1993) and Equation 4.25 of Turner (1992). From the plot, it is apparent that carbon or hydrogen recoil nuclei of maximum energy from 1 GeV/nucleon Fe ions will have a penetration range in excess of 10^6 μm (1 m). But, the majority of recoils will have considerably less energy, where the penetration range is greatly reduced.

Absorption (Inelastic) Interactions

In general, products of absorption nuclear interactions, are fragments of the projectile nucleus, fragments of the target nucleus, and nucleons (or groups of them like α-particles) produced in the interaction region where the two nuclei overlap in the collision (Curtis and Schimmerling 1977). Projectile fragments emerge from the interaction in a direction very close to the initial particle direction and with little or no change in velocity. Target fragments, however, have a broad angular distribution, low-energies, and high multiplicity in particle number. Central or "head on" collisions are unique where products are formed from projectile and target nucleons, and have intermediate particle kinetic energies between that described above for projectile and target fragments. According to Curtis and Schimmerling (1977), projectile fragmentation, target fragmentation, and central collisions have the following additional characteristics.

148

Figure C-2. Range of Proton and Carbon Nuclei in Water (unit density).
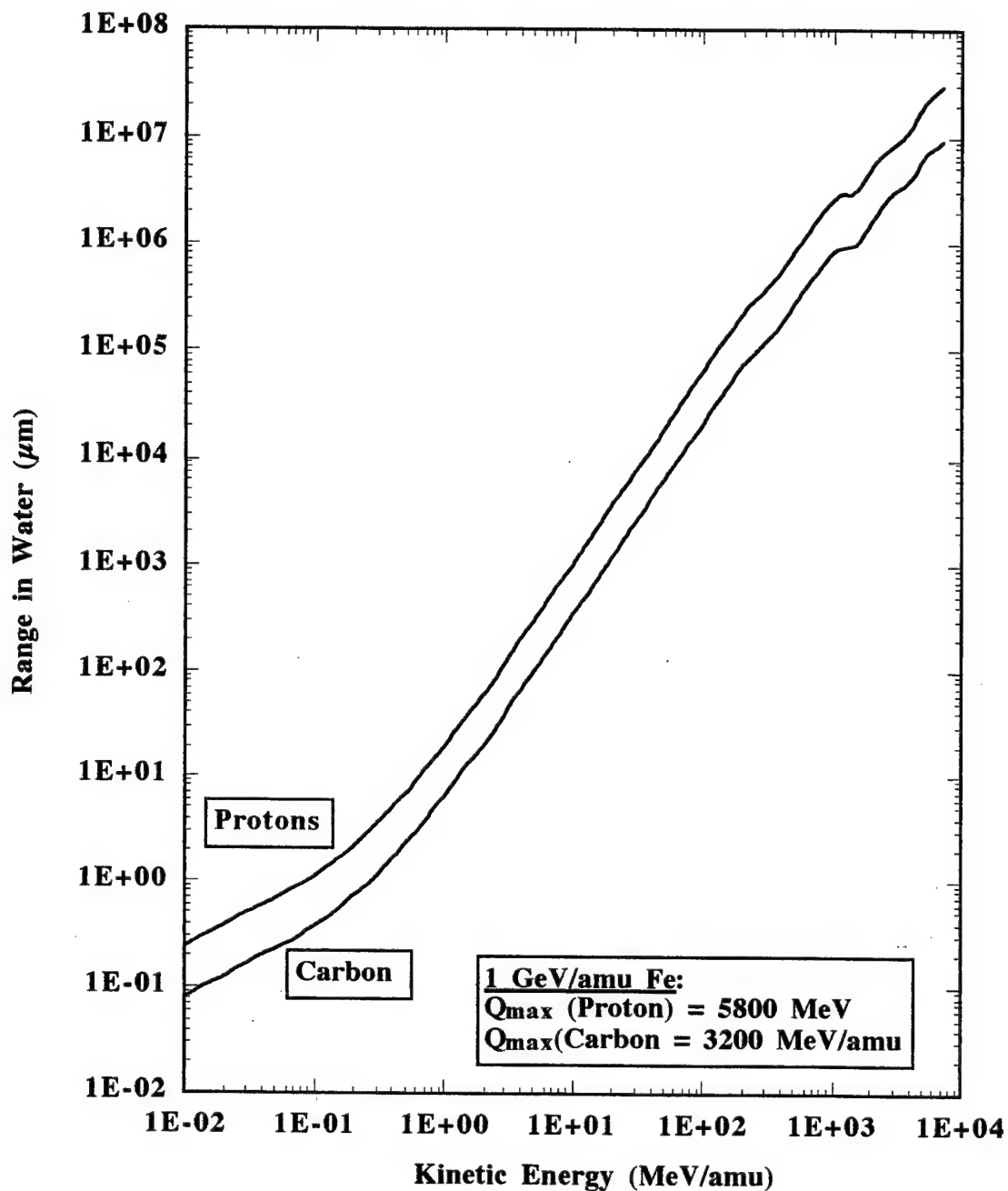
Projectile Fragmentation

1. The reactions resulting in projectile fragments are due to grazing collisions.

2. Total reaction cross-sections are generally independent of energy for projectiles of energy greater than 300 MeV/nucleon.

3. Fragment velocity and trajectory is close to that incident projectile.

4. The probability of producing a fragment is related to the target mass only through a geometric scale factor.

5. The interaction cross-sections have been approximated by considering the overlap of two black discs, that represent the area of the projectile and fragment nuclei. Examples of projectile-only fragmentation are provided in Figure C-3. By a convention used by Heckman *et al.* (1978), these events are referred to as "Type 1." In example **a**, ^{56}Fe is fragmented into ^{52}Cr and ^4He. While in example s **b** and **c**, only one nucleon is stripped off, respectively a neutron and proton. Reactions of the type described in examples **b** and **c** present difficulties in experiments designed to evaluate inelastic cross-sections. For both solid-state detectors and photographic nuclear emulsions, lack of charge in neutrons prevents detection of neutron loss-only fragments. While in the case of proton loss-only fragmentation, the ionization can be too low to be detected in some photographic nuclear emulsion experiments (Heckman *et al.* 1978).

Target Fragmentation

1. The distribution of reaction products is not significantly dependent on heavy-ion energy between 0.3 and 2 GeV/nucleon.

2. Target fragmentation reaction products are nearly independent of projectile mass except for interaction cross-section scaling factors. Examples of target-only fragmentation are provided in Figure C-4. Heckman *et al.* (1978) referred to these as "Type 4." Example **a** is typical in that it contains multiplicity, with three fragments. The other examples are less typical but possible, and contain single nucleon-loss fragmentation of a proton and neutron, that normally are difficult to interpret by photographic film techniques.

150

Figure C-3. Projectile-Only Fragmentation (Type 1).

Before   **After**
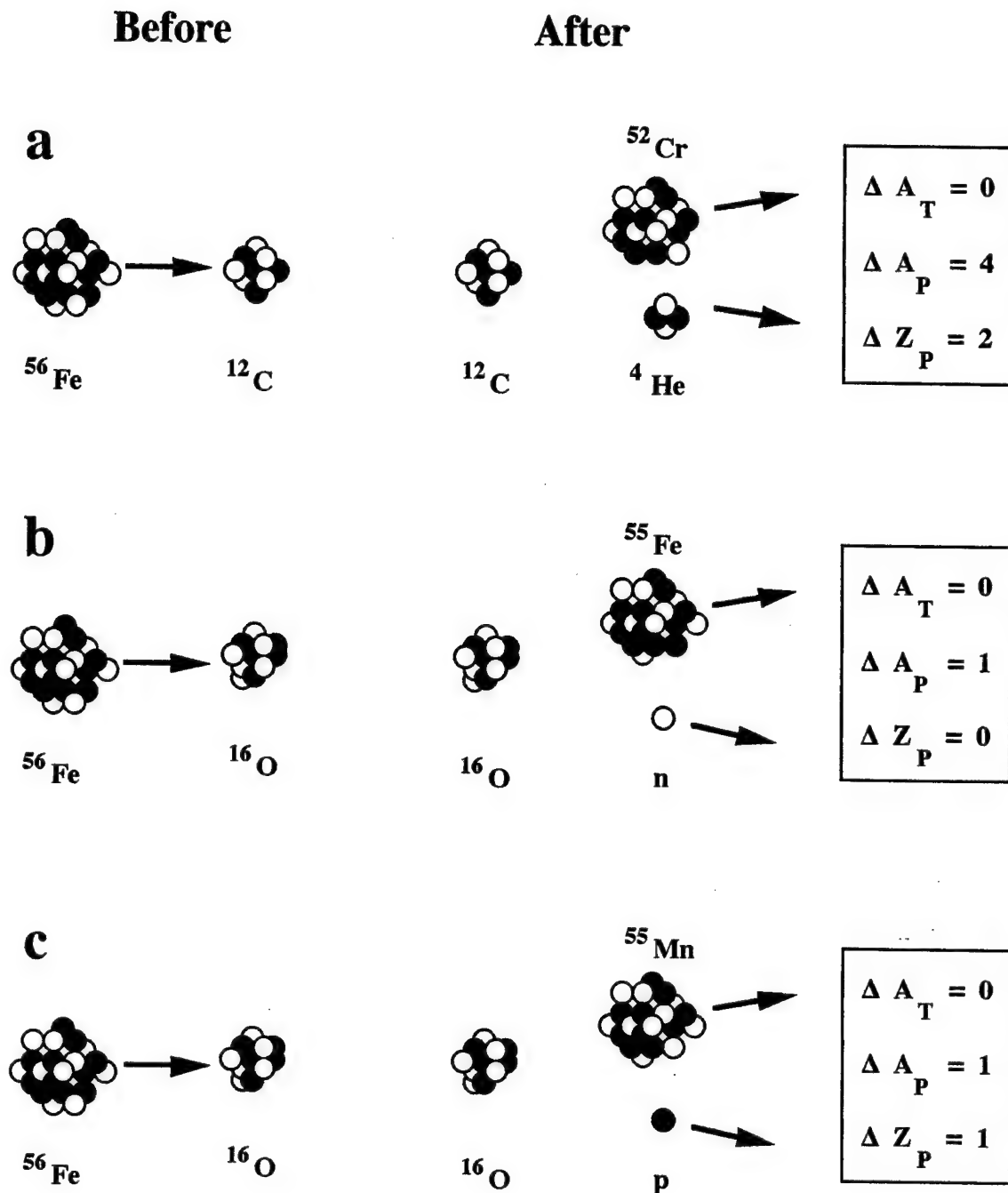
Figure C-4. Target-Only Fragmentation (Type 4)
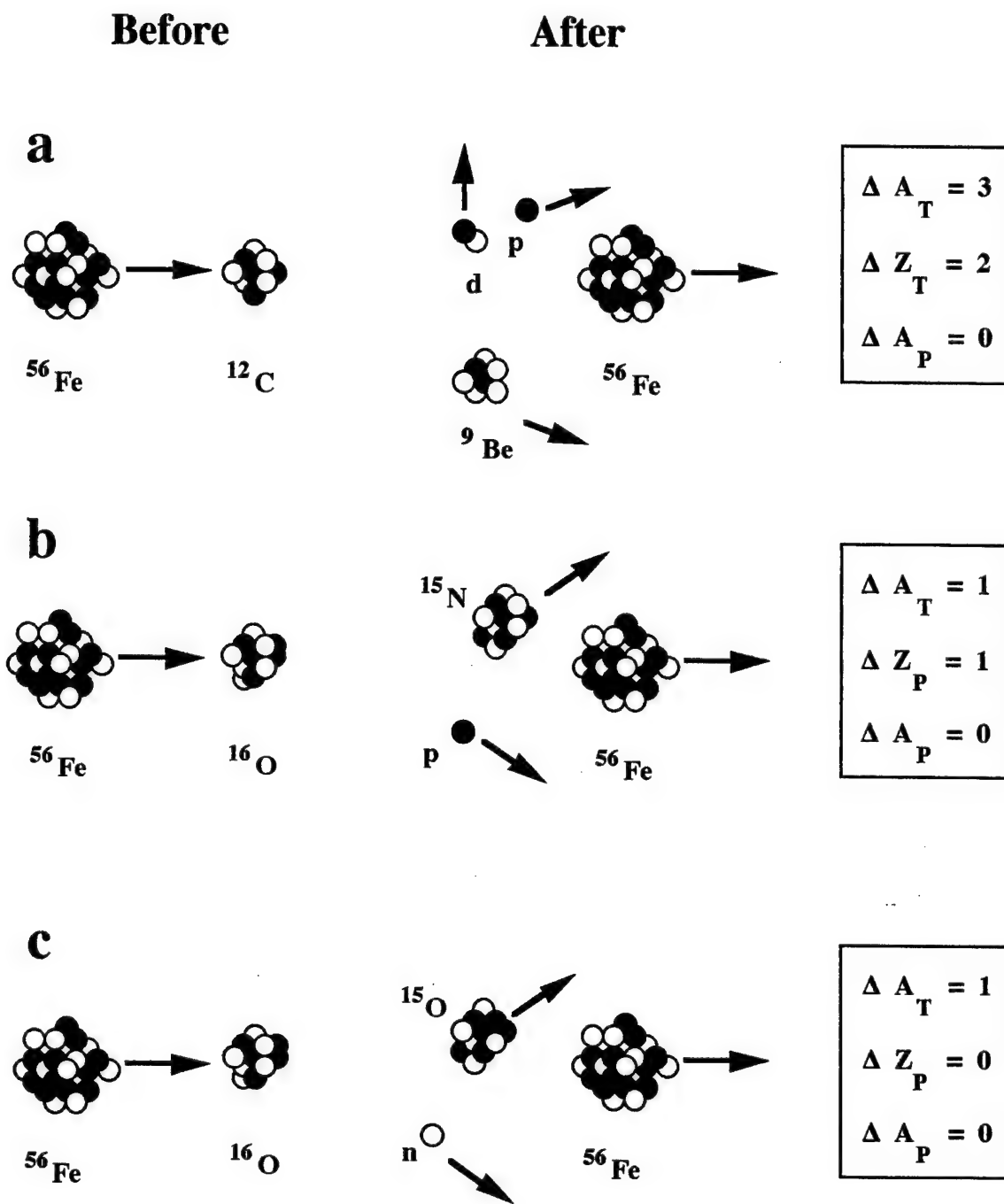
Projectile and Target Fragmentation

Nuclear absorption interactions of heavy projectiles more commonly are involved in fragmentation of both the target and projectile. Interactions of this type are referred to as "Type 3." Figure C-5 provides examples. The characteristics of the reaction products, respectively, are similar to those noted for projectile- and target-only fragmentation.

Figure C-5. Target and Projectile Fragmentation (Type 2).

Before

After

a

^{56}Fe → ^{12}C

^{3}He

^{9}Be → ^{4}He

^{52}Cr

$\Delta A_T = 3$

$\Delta Z_T = 2$

$\Delta A_P = 4$

$\Delta Z_P = 2$

b

^{56}Fe → ^{16}O

^{4}He

^{12}C

^{42}Ca

^{12}C

n

n

$\Delta A_T = 4$

$\Delta Z_T = 2$

$\Delta A_P = 14$

$\Delta Z_P = 6$

153
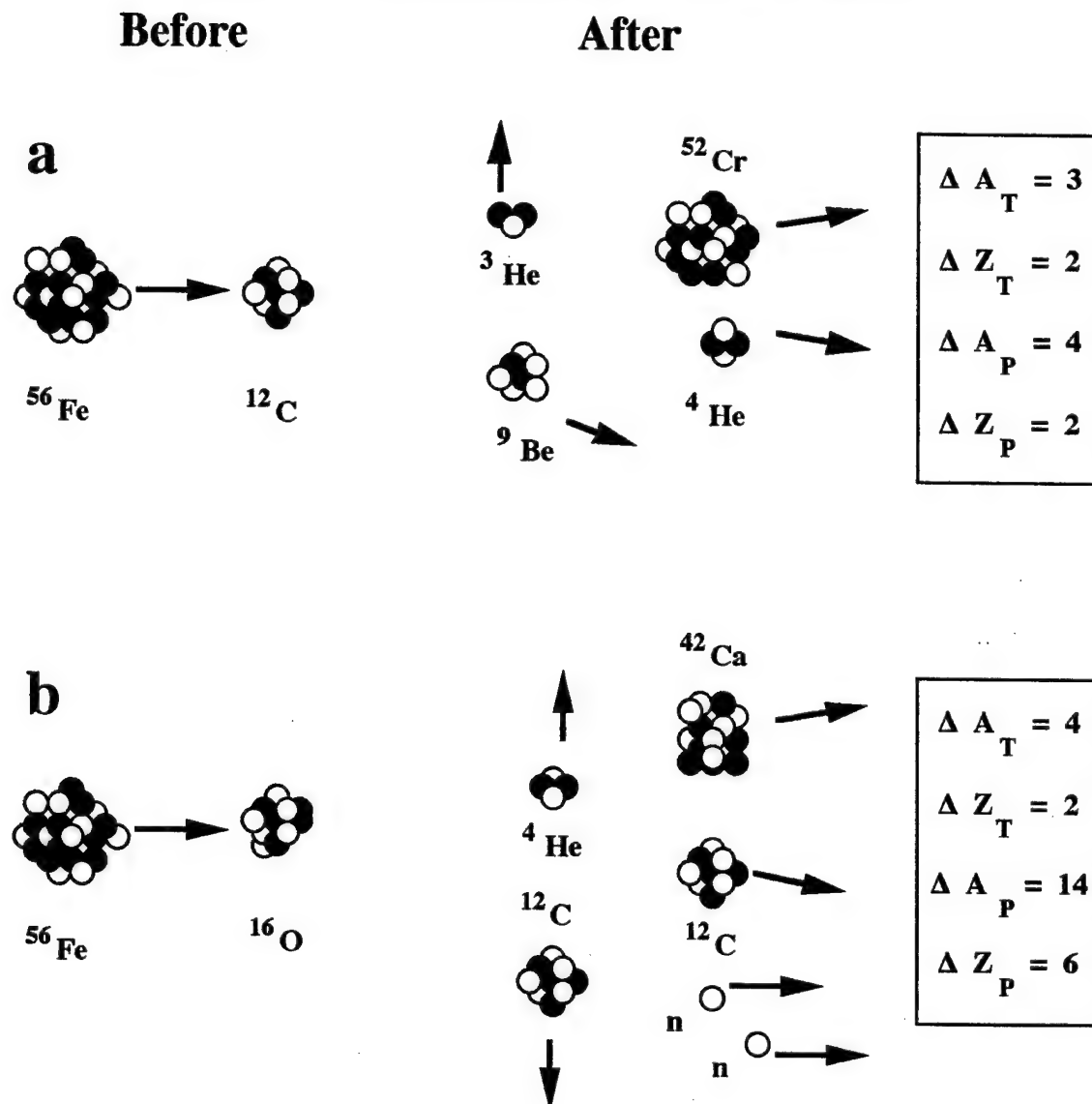
Absent from the two cases in Figure C-5 are target or projectile fragments with a single nucleon-only removal fragment. Single nucleon-only removal is more common with grazing collisions that have small target-projectile nuclear overlap whereas collisions of this type have greater nuclear overlap and thus higher multiplicity in projectile fragments.

Central Collisions

Central collisions involve head on collisions resulting in both target and projectile fragmentation that result in large amounts of energy transferred to the target. Some researchers have postulated that nuclear shock waves are produced by these interactions (Curtis and Schimmerling 1977). The end result of these interactions is illustrated in Fig. C-6 where there is a catastrophic destruction of both target and projectile, and no forward fragments from the projectile.

Figure C-6. Central Collision (Type 3).

Before   **After**

^{56}Fe ^{12}C

$$\Delta Z_T \geq 2$$
$$\Delta Z_P \geq 2$$
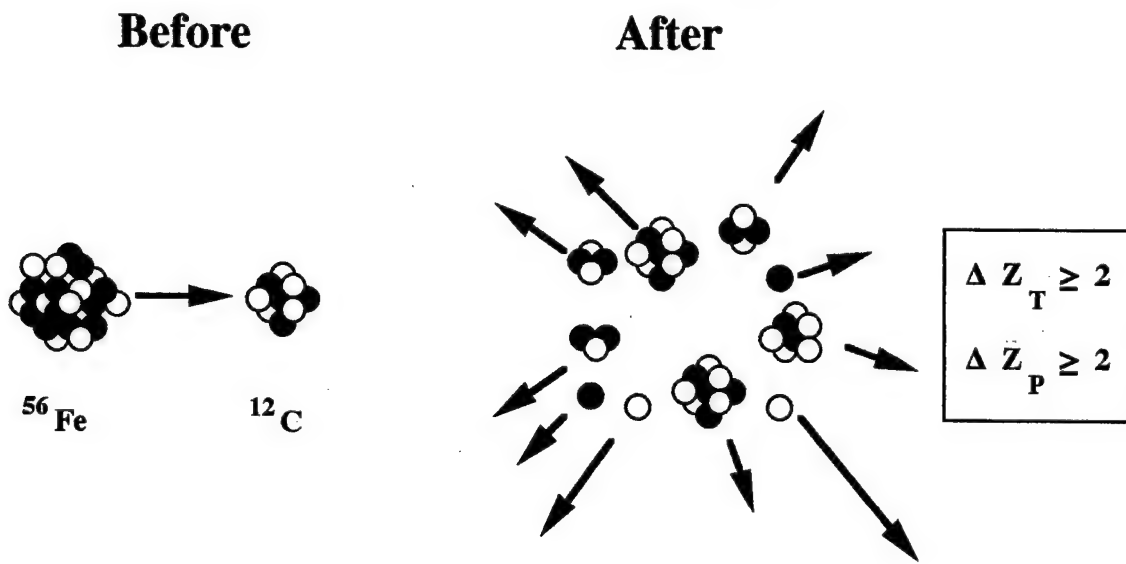
Model Predictions and Experimental Data

Wilson and Costner Theoretical Data on Cross-Sections

Wilson and Costner (1975) presented a high-energy heavy-ion reaction model that provided both total and absorption nuclear interaction cross-sections. The model was compared to experimental data with close agreement. Figure C-7 provides cross-sections for iron projectiles on carbon from the model. A recent measurement from Dudkin *et al.*

154

(1990) of iron on carbon is noted on the graph with reasonable agreement with the model. The ratio of absorption cross-section to total cross-section, about 55 %, is reasonably independent of energy.

Figure C-7. Total and Absorption Nuclear Interaction
Cross-Sections for Fe Projectiles on Carbon
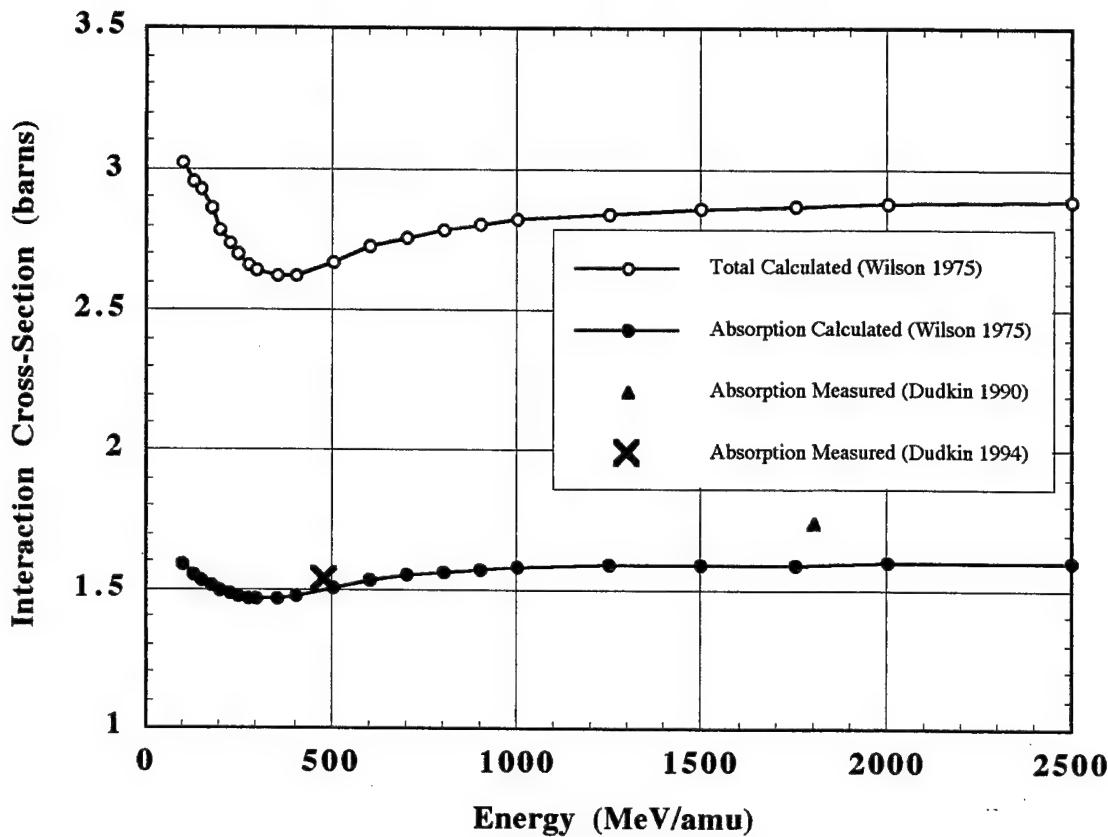
Dudkin et al. (1990 and 1994) respectively found for 0.48 and 1.8 GeV/nucleon Fe projectiles, close agreement in measured and theoretically calculated inelastic cross-sections using the Brant-Peters formula:

$$\sigma_{abs} = \pi\, r_0^2\, [\, A_P^{1/3} + A_T^{1/3} - B\, (\, A_P^{-1/3} + A_T^{-1/3}\,)\,]^2, \qquad \text{(C-2)}$$

where A_P and A_T are the respective masses of projectile and target nuclei, $r_0 = 1.32$ fm, and $B = 0.85$.

Westfall Experimental Data on Fragmentation

Westfall *et al.* (1979) measured the element production cross-section of ^{56}Fe on many targets with a solid-state detector transmission system. The results of the carbon target are shown in Fig. C-8. From the graph, it is obvious that small number nucleon losses (ΔZ: 1 - 4) account for over half of the projectile fragmentation events, excluding central collisions that could not be evaluated. Total charge-changing cross-section, $\sigma_{\Delta Z \geq 1}$, and mass-changing cross-section, $\sigma_{\Delta A \geq 1}$, for the carbon target were 1.56 ± 0.05 and 1.66 ± 0.06 barns, respectively. Neutron-only removal cross-sections could not be measured and were estimated at 100 millibarns (mb).

Figure C-8. Element Production Cross-Sections from ^{56}Fe Projectiles on Carbon at 1.88 GeV/nucleon (Westfall *et al.* 1979).
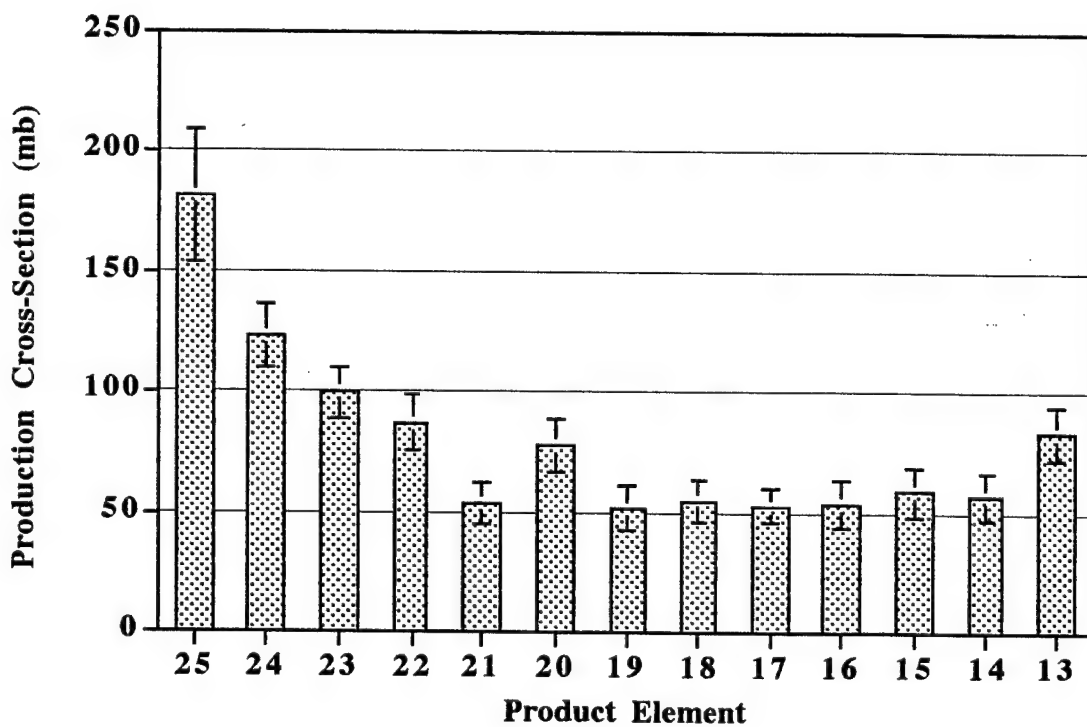
Dudkin Experimental Data on Fragmentation

Dudkin *et al*. (1990, 1991, 1993 and 1994) evaluated target and projectile fragment characteristics from 1.8 GeV/nucleon ^{56}Fe incident on nuclei of photographic nuclear emulsion. They separated interactions into one of three categories based on the target nuclei: Ag or Br; H; and C, N, or O. Only a summary of the CNO data will be presented here since it is most applicable to secondaries created in A-150 plastic.

In the 1990 work, fragments of interactions were separated into one of five types:

1. black (b) - $E_P \leq 26$ MeV,

2. gray (g) - $26 < E_P \leq 400$ MeV,

3. stream (s) - $E_P > 400$ MeV,

4. stream (s') - $E_p > 400$ MeV (singly charged projectile particles),

5. heavily ionizing (h) particles from target breakup, and

6. fragments of the projectile nuclei.

Total charge of the non-interacting fragments of the projectile nucleus $Q = \Sigma_i \, n_i Z_i$ was determined for each interaction, where n_i is the number of fragments and Z_i is the charge of all relativistic single-charged fragments within 5° of the projectile trajectory.

They determined the fragmentation cross-section for different projectile products as follows: 0.49 ± 0.06 barns ($20 \leq Z \leq 26$), 0.50 ± 0.08 barns ($10 \leq Z \leq 19$),), 0.38 ± 0.06 barns ($6 \leq Z \leq 9$),), 0.36 ± 0.06 barns ($3 \leq Z \leq 5$),), 3.38 ± 0.31 barns (α-particles), 7.02 ± 0.57 barns (protons). They found the mean emission angle of the fragments in each group to be: $1.03 \pm 0.08°$ ($20 \leq Z \leq 26$), $1.16 \pm 0.08°$ ($10 \leq Z \leq 19$), $1.44 \pm 0.13°$ ($6 \leq Z \leq 9$), $2.00 \pm 0.15°$ ($3 \leq Z \leq 5$), $2.50 \pm 0.08°$ (α-particles), and $2.78 \pm 0.04°$ (protons). Thus, for increasing fragment size, the mean angle of emission decreases. They determined the relative percent probabilities of definite number of projectile fragments of ^{56}Fe from interactions with CNO target nuclei. Figure C-9 is adapted from the data.

Graph C-9. Relative Percent Probabilities of Definite Number of ^{56}Fe Fragments [Adapted From Dudkin etal (1990)].
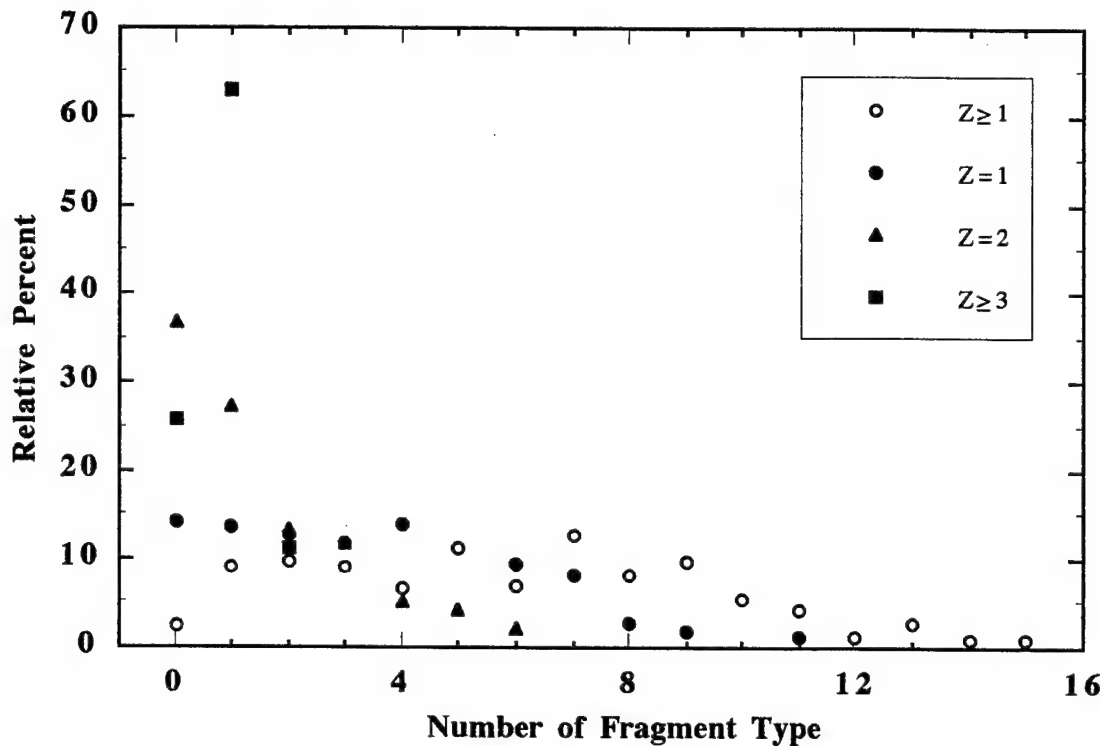
From the Figure, about 2 % of the interactions did not have any relativistic charged particles emitted along the initial trajectory of the projectile. These interactions are categorized as central collisions (type 3). The complexity of the projectile fragmentation interactions is apparent from the data. For example, about 63 % of the interactions have one projectile fragment with $Z \geq 3$ and 10.9 % have two projectiles with $Z \geq 3$. Combined, these interactions are predominately grazing collisions that leave a large portion of the projectile intact. On the other hand, about 25 % of the interactions had no projectile fragments of $Z \geq 3$ and were dominated by collisions with large overlap of target and projectile nuclei. One-third of the interactions produced five or more proton fragments, at least 70 % produced at least two protons, and over one-third had two or more α-particles.

Studies were conducted on CNO target fragments produced by ^{56}Fe projectiles. Per the classification system given above, the means were as follows: 1.77 ± 0.10 (n_b),

$2.87 \pm 0.14 \ (n_g)$, $4.64 \pm 0.13 \ (n_h)$, $8.12 \pm 0.50 \ (n_s)$, $3.90 \pm 0.18 \ (n_{s'})$, and

$20.05 \pm 0.35 \ (Q)$. Figure C-10 provides correlations of the mean Q "$\langle Q \rangle$", $\langle n_b \rangle$, $\langle n_h \rangle$,

and $\langle n_s \rangle$ with respect to n_g, the number of gray particles.

Figure C-10. Correlations of $\langle Q \rangle$, $\langle n_b \rangle$, $\langle n_h \rangle$, and $\langle n_s \rangle$ with n_g from ^{56}Fe on CNO [Adapted from Dudkin *et al.* (1990)].
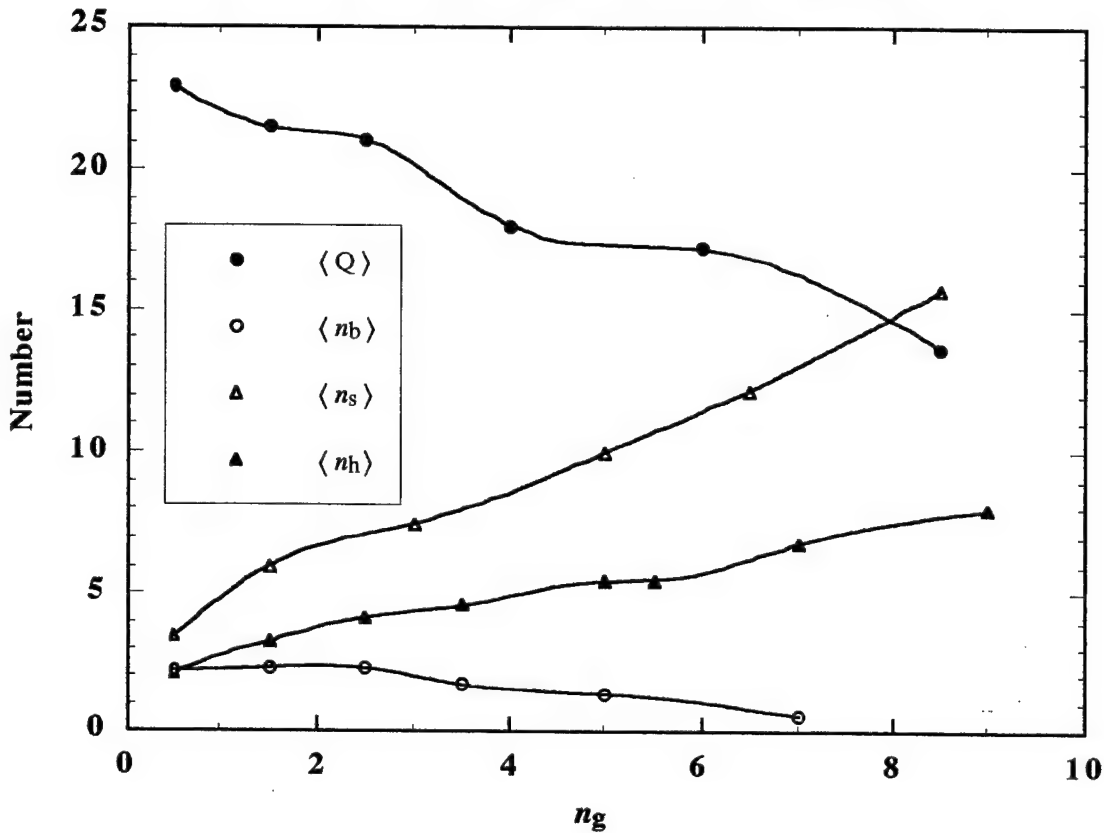
From the figure, $\langle Q \rangle$ and $\langle n_b \rangle$ are negatively correlated to n_g, while $\langle n_h \rangle$ and $\langle n_s \rangle$ are

positively correlated. Independent of n_g, the mean number of black particles, $\langle n_b \rangle$, is less

than the shower particles, $\langle n_s \rangle$, or the heavily ionizing particles, $\langle n_h \rangle$. Dudkin *et al.*

(1993) later determined the correlation between $\langle Q \rangle$, $\langle n_s \rangle$, and $\langle n_g \rangle$ with impact

parameter for various projectile and target nuclei combinations. Figure C-11 provides

values of $\langle Q \rangle$ and $\langle n_g \rangle$ and vs. impact parameters for ^{56}Fe projectiles on CNO.

Figure C-11. $\langle Q \rangle$ and $\langle n_g \rangle$ vs. Impact Parameter Range of ^{56}Fe on CNO (Dudkin *et al.* 1993).
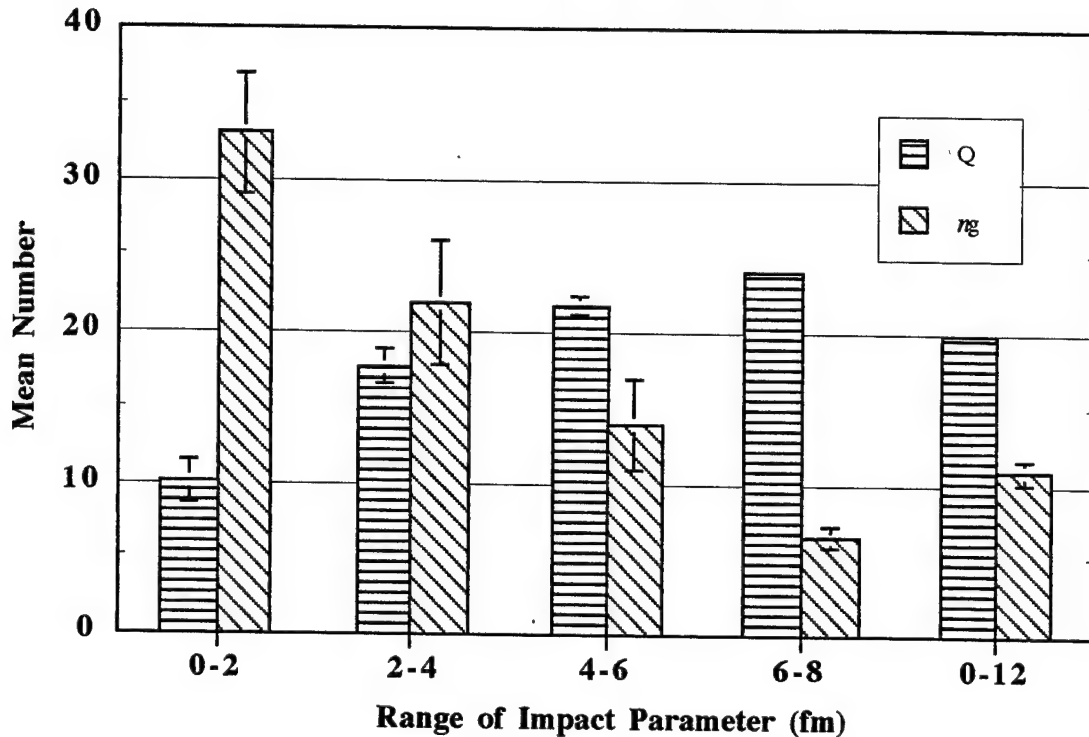
As expected, for grazing interactions that have little nuclei overlap, high conservation of mean projectile charge and a decrease in the number of gray particles. Another point of interest from the mean values of Q and n_g, is that the sum is less than 23.95, less than the Z of iron. Thus, for some interactions, conservation of charge would not exist along the particle trajectory.

Dudkin *et al.* (1991) analyzed characteristics of target fragment protons and α-particles. Table C-1 lists characteristics ^{56}Fe projectiles interacting on CNO for events that had almost complete target breakup. Particles were separated into: protons of energy 30 - 400 MeV, protons $\leq$ 30 MeV, and α-particles less than 40 MeV. For each category, mean

160

values of multiplicity $\langle n \rangle$, emission angle $\langle \Theta \rangle$, energy $\langle E \rangle$, transverse momentum $\langle P_\perp \rangle$,

and longitudinal momentum $\langle P_\parallel \rangle$ or forward/backward ratio of the secondaries ($_{\bar{n} / \bar{n}}$) are

provided.

Table C-1. Characteristics of Proton and α-Particle Secondaries from Fragmentation of 1.8 GeV/nucleon ^{56}Fe on CNO of Photographic Nuclear Emulsion (Dudkin *et al.* 1991).

Secondary Particle	Range (MeV)	$\langle n \rangle$	$\langle \Theta \rangle$ (degree)	$\langle E \rangle$ (MeV)	$\langle P_\perp \rangle$ (MeV/c)	$\langle P_\parallel \rangle$ (MeV/c)	$\bar{n} / \bar{n}$
proton	30 - 400	2.46 ± 0.13	48 ± 1	198 ± 5	359 ± 8	394 ± 14	—
proton	≤ 30	1.66 ± 0.10	84 ± 2	9.1 ± 0.4	91 ± 3	—	1.3 ± 0.2
α-particle	≤ 40	0.18 ± 0.03	79 ± 6	17.2 ± 1.2	264 ± 19	—	2.2 ± 0.5

Simple observations can be drawn from the data. First, for the high-energy protons: 30 - 400 MeV, the transverse and longitudinal momenta are similar, and the particles are directed primarily in the forward direction. For the low-energy protons and α-particles, there is a considerably higher fraction of the secondaries emitted in the backward direction with about 43 and 24 %, respectively.

Dudkin *et al.* (1994) analyzed 0.1 - 0.5 GeV/nucleon ^{56}Fe interactions in photographic emulsion. The range of velocity of these projectiles: 0.43 - 0.76c was significantly less than the 0.94c velocity of the 1.8 GeV/nucleon projectiles of their other work. The following mean multiplicities were reported for CNO target nuclei: 2.43 ± 0.14 (n_b), 2.26 ± 0.17 (n_g), 4.64 ± 0.13 (n_h), 3.04 ± 0.24 (n_s), 3.46 ± 0.21 ($n_{s'}$), 22.18 ± 0.29 (Q), . In comparison to the 1.8 GeV/amu data:

1. the sum of the mean Q and n_s. is 25.64, 7% higher than the 1.8 GeV/amu data,

2. there was a decrease in the total inelastic cross-section, and

3. there was a lower degree of destruction of the colliding nuclei.

161

Antonchik *et al.* (1982) also evaluated mean multiplicities of target fragments from high-velocity heavy ions. They compared 1.2 GeV/nucleon ^{14}N to 3.6 GeV/nucleon ^{12}C and found no appreciable change in multiplicities of any category of target fragment. Thus, the energy dependence of target fragment multiplicities is apparent only in the low-energy region.

Heckman Experimental Data on Fragmentation

Using photographic nuclear emulsion detectors, Heckman *et al.* (1978) measured the absorption interaction cross-sections of 2.1 GeV/nucleon ^{4}He, ^{12}C, ^{14}N, and ^{16}O projectiles. By examination of the films, they were able to categorize fragmentation events by type as used here already in this appendix. Figure C-12 lists the percent interaction of each type of the total for each projectile. One notable feature from initial inspection of the data is that for each projectile, about 50 % of the interactions involved a change in mass of both the projectile and target. Also, for heavy ion projectiles involved in interactions of this type, rarely are mass changes of the neutron-only type. Another notable feature of the data is the relatively constant proportion of interaction type, independent of projectile. One difficulty in interpretation of nuclear films is proper correction of the data for neutron(s)-only removals. The authors estimated that about 5.3, 6.0, 5.4, and 4.8 % of the interaction events had neutron(s)-only removal, respectively in order from lower to higher mass projectile. Also, for the three heavy projectiles, $\Delta Z = 1$ removals from the target and projectiles were difficult to assess because the ionization produced by singly charged ions was too low. Corrections for $\Delta Z = 0, 1$ were calculated and determined to belong to type 1 and 4 interactions. The maximum correction possible for each type is represented by a small line bar above the data.

Figure C-12. Classification of Interaction Types of 2.1 GeV/nucleon ^{4}He, ^{12}C, ^{14}N, and ^{16}O on Photographic Nuclear Emulsion (Heckman etal 1978).
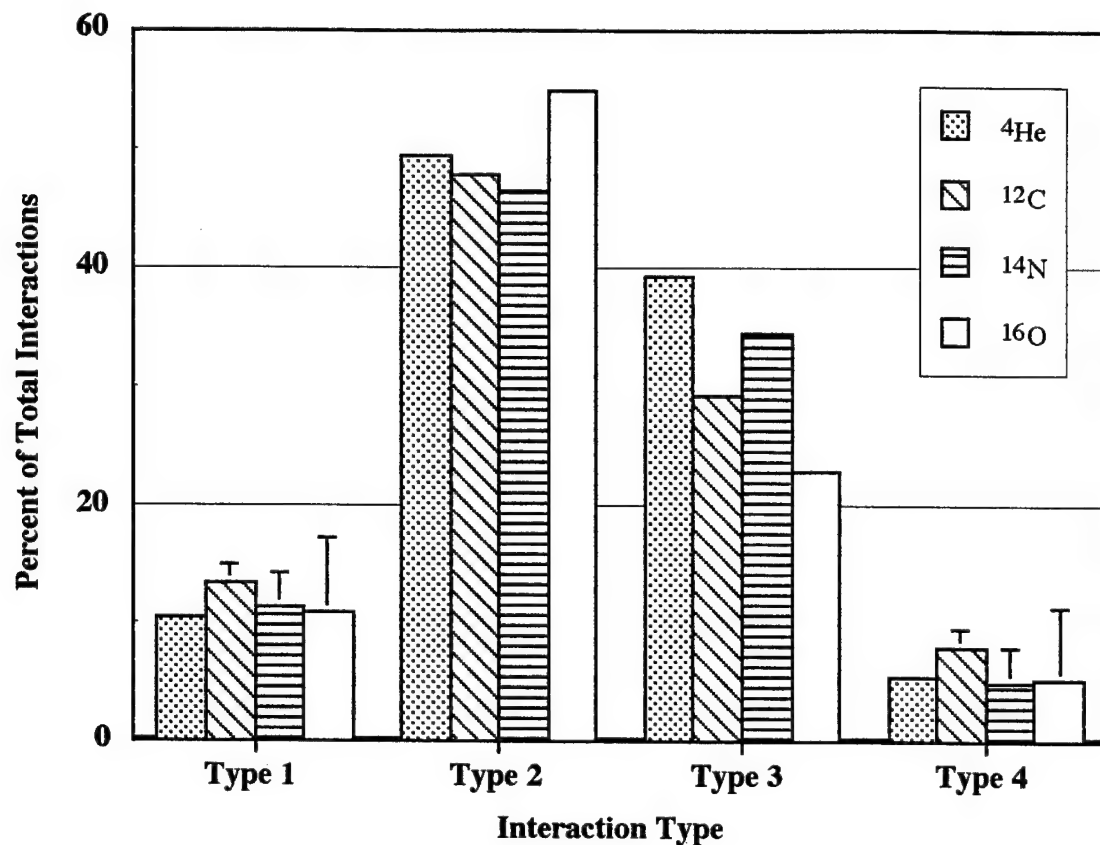
Appendix D: Position Determinations

General Description

Figure D-1 illustrates the arrangement of the position-sensitive detectors (PSD1 and PSD2) with respect to the TEPC in a three coordinate system. Each PSD consists of two devices, one oriented to determine relative position in the x-direction and the other in the y-direction.

Figure D-1. Arrangement of Position-Sensitive Detectors in
Relationship to TEPC in a Three-Dimension Frame
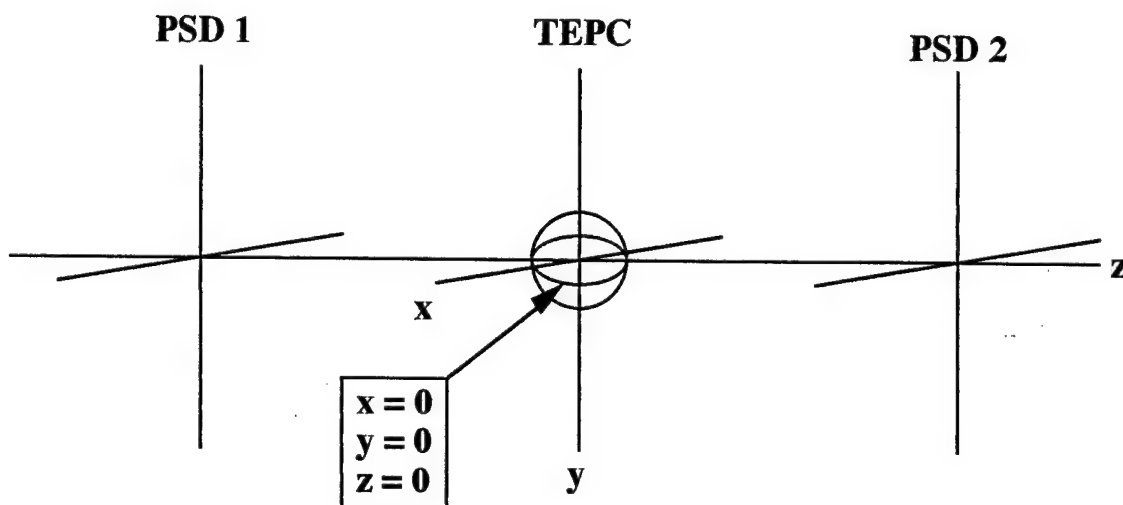
Each device in the PSD has an active silicon thickness of about 1000 μm (1 mm). The two devices were placed in contact and assumed to have the same z-position. The z-position for each PSD pair relative to the center of the TEPC was measured. All x- and y-position values were normalized to the line traversing the three detectors, with x, y, and z = 0 for the TEPC center. This was necessary since the position-sensitive devices had a small x and y offset from the center of the TEPC.

164

Position Calculation Equations

FORTRAN code was written to calculate the perpendicular distance of the heavy ion trajectory from the detector center and is referred to as the impact parameter. For particles traversing the cavity of the detector, chord length, l, of the trajectory in the cavity was calculated, with the maximum being 12.7 mm, the diameter.

For the calculations, particle trajectories were assumed to be on a straight line and defined by Equation D-1:

$$\frac{x - x_1}{x_2 - x_1} = \frac{y - y_1}{y_2 - y_1} = \frac{z - z_1}{z_2 - z_1}, \qquad \text{(D-1)}$$

where x_1, x_2, y_1, and y_2 are the normalized position values determined by the PSDs and z_1 and z_2 are the measured locations of the PSDs relative to the center of the TEPC. The direction cosines are defined as u, v, and w:

$$u = \cos\alpha = \frac{x_2 - x_1}{d}, \qquad \text{(D-2)}$$

$$v = \cos\beta = \frac{y_2 - y_1}{d}, \text{ and} \qquad \text{(D-3)}$$

$$w = \cos\gamma = \frac{z_2 - z_1}{d}, \qquad \text{(D-4)}$$

where d is the distance between the two points and α, β, and γ are the angles formed between the particle trajectory and the respective axes x, y, and z. The following relationship exists among the direction cosines:

$$u^2 + v^2 + w^2 = 1. \qquad \text{(D-5)}$$

For simplicity of presentation, ℓ, m, and n are defined as:

165

$$\ell = x_2 - x_1, \qquad \text{(D-6)}$$

$$m = y_2 - y_1, \text{ and} \qquad \text{(D-7)}$$

$$n = z_2 - z_1. \qquad \text{(D-8)}$$

Rearranging terms, the following relationships exist:

$$y = x\left(\frac{m}{\ell}\right) + \left(y_1 + \frac{x_1}{\ell}\right), \qquad \text{(D-9)}$$

$$z = x\left(\frac{n}{\ell}\right) + \left(z_1 + \frac{x_1}{\ell}\right), \text{ and} \qquad \text{(D-10)}$$

$$z = y\left(\frac{n}{m}\right) + \left(z_1 + \frac{y_1}{m}\right). \qquad \text{(D-11)}$$

Similar equations can be formulated for a line from the detector center perpendicular to the particle trajectory. The direction cosines of this line are defined as u', v', and w':

$$u' = \cos\alpha' = \frac{x - 0}{b}, \qquad \text{(D-12)}$$

$$v' = \cos\beta' = \frac{y - 0}{b}, \text{ and} \qquad \text{(D-13)}$$

$$w' = \cos\gamma' = \frac{z - 0}{b} \qquad \text{(D-14)}$$

where b is the impact parameter and α', β', and γ' are the angles formed between the line and the respective axes x, y, and z. Like the other set of direction cosines, the sum of the direction cosines-squared equals one. Because the two lines are perpendicular, the following relationship exists among the six direction cosines:

$$uu' + vv' + ww' = 0. \qquad \text{(D-15)}$$

Then by substitution,

$$\frac{x}{b}\frac{\ell}{d} + \frac{y}{b}\frac{m}{d} + \frac{z}{b}\frac{n}{d} = 0 \text{ and} \qquad \text{(D-16)}$$

$$\ell x + my + nz = 0. \qquad \text{(D-17)}$$

Substitution of the line equation (Eq. D-1) into this equation for each of the three axes, the coordinates of the intercept points x_I, y_I, and z_I can be determined:

$$x_I = \frac{(m^2 + n^2)x_1 - m\ell y_1 - n\ell z_1}{d^2}, \qquad \text{(D-18)}$$

$$y_I = \frac{(\ell^2 + n^2)y_1 - m\ell x_1 - nm z_1}{d^2}, \text{ and} \qquad \text{(D-19)}$$

$$z_I = \frac{(\ell^2 + m^2)z_1 - n\ell x_1 - nm y_1}{d^2} \qquad \text{(D-20)}$$

where

$$d^2 = \ell^2 + m^2 + n^2. \qquad \text{(D-21)}$$

It follows that the impact parameter, b, and the chord length, l, can be calculated:

$$b = \sqrt{x_I^2 + y_I^2 + z_I^2} \text{ and} \qquad \text{(D-22)}$$

$$l = 2\sqrt{r^2 - b^2}, \qquad \text{(D-23)}$$

where r is the detector radius (6.35 mm). To provide an ability to determine the trajectory of individual particles in the detector plane, the angle of incidence, θ, was calculated for each trajectory. Because, the particle trajectories had a limited angle of acceptance in the z-dimension, θ was calculated from the x_I and y_I intercept values:

$$\theta = \tan^{-1}\left(\frac{y_I}{x_I}\right). \qquad\qquad (D\text{-}24)$$

Sign corrections were made with the final output angle conforming to the convention illustrated in Fig. D-2, where the cross-section of the detector is shown in the x-y plane.

Figure D-2. Angle Convention Used for Data Analysis.
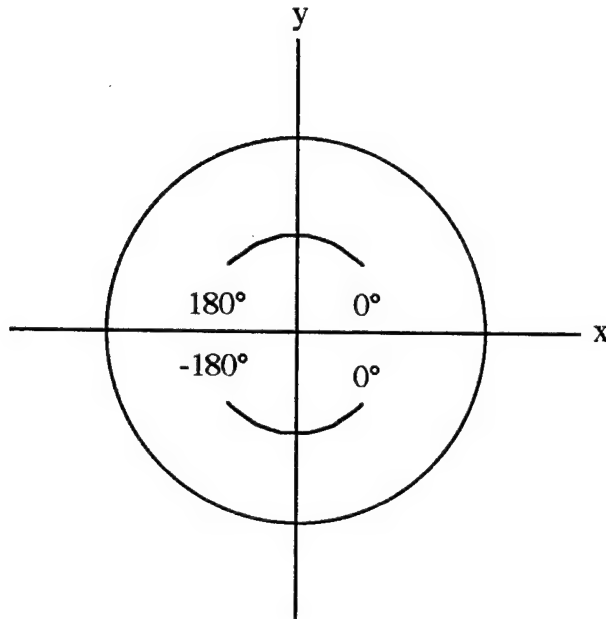
Position Uncertainty Estimations

Figure D-3 is a histogram of impact parameter for events with energy deposition greater than 170 keV ($y = 255$ keV μm^{-1}) in the thin-walled detector. Over 85 % of the events are distributed about the cavity/wall interface (impact parameter = 6.35 mm). For events with impact parameter between 5.7 and 7.0 mm (140 events), the mean was 6.356 ± 0.017 mm with a standard deviation of the data about the mean of 0.23 mm. The standard deviation value for this distribution of events is a reasonable estimate of the uncertainty in impact parameter at the cavity/wall interface, provided the impact parameter interval that gives rise to these events is small compared to the uncertainties in impact parameter.

Figure D-3. Distribution of Impact Parameter for Fe Events with High Lineal Energy in the Thin-Walled Detector [Simulated Diameter = 1 μm]

n = 175
TEPC: y > 255
1 μm

Impact Parameter
Range: 5.7 - 7.0 mm
Mean = 6.356 +/- 0.017
S. D. = 0.23
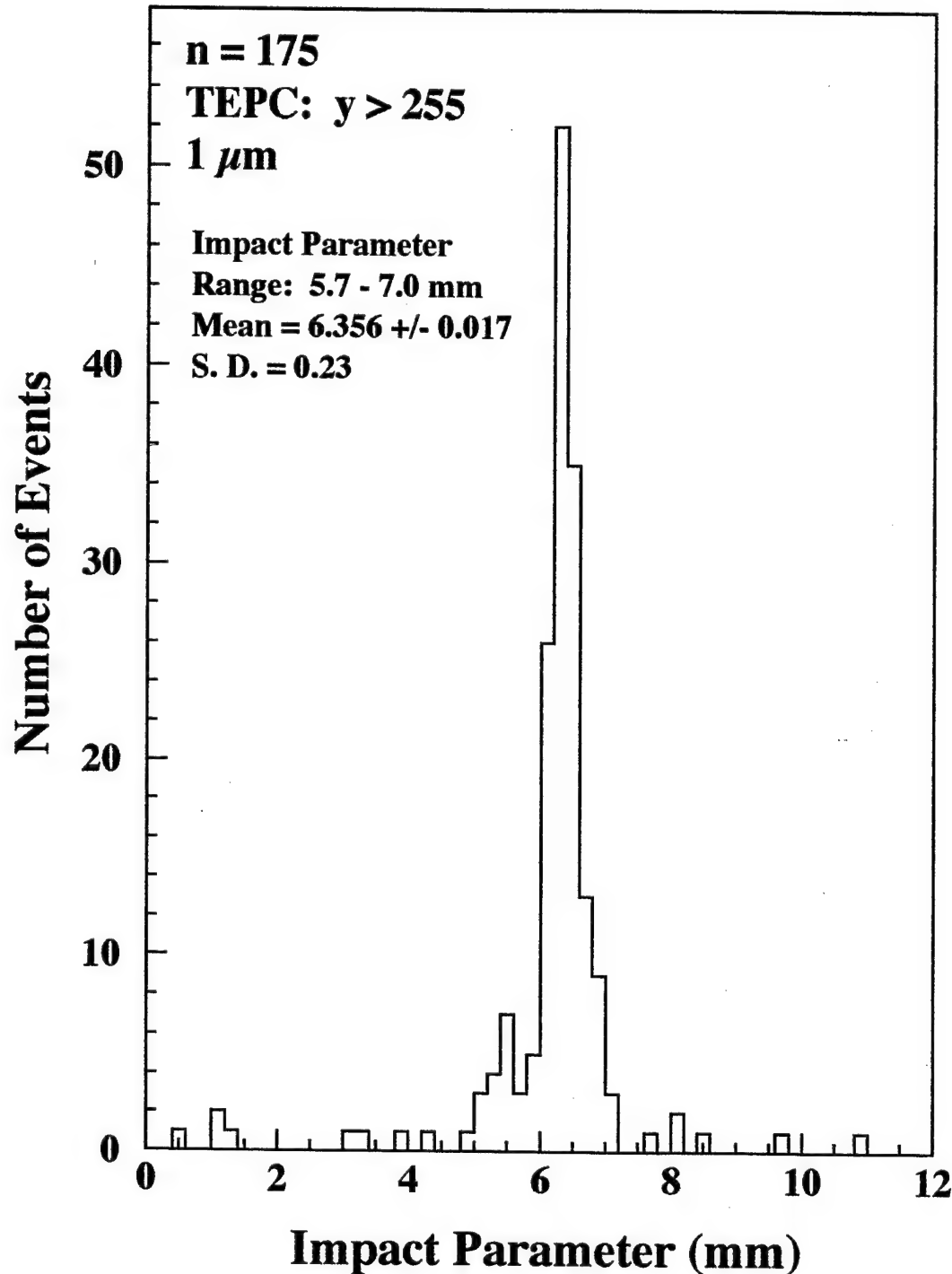
At the cavity/wall interface, about 12,000 particles per mm of impact parameter interval were observed from plots of detector response from selection on impact parameter. For the 140 particles (the number of particles between 5.7 and 7.0 mm given in Fig. D-3), the impact parameter interval would be 0.0125 mm, based on 12,000 particles per mm. This value is much lower than the estimated uncertainty in impact parameter, 0.23 mm. Thus, 0.23 mm will be used as an estimate of uncertainty in impact parameter at the cavity/wall interface.

Many factors may contribute to the uncertainty in impact parameter. Most important is the uncertainty in the signals from the PSD. Other contributions may be from distortions in the shape of the detector wall, multiple coulomb scattering, and errors in measured distances between components in the experimental set-up. Errors in measured distances between components in the experimental set-up are assumed to be negligible. The contribution from wall distortions is difficult to assess, but no distortions were observed in x-ray photographs of the wall. Calculations were made to assess the impact of multiple coulomb scattering on position uncertainties. The effect had a small contribution to position uncertainties compared to that estimated for the PSD devices alone.

Estimation of PSD Uncertainty

The estimated uncertainty in impact parameter at the cavity/wall interface is based on the combined uncertainty of all four PSD devices. An analysis was performed to estimate the uncertainty in the individual PSD under the assumptions that:

1. uncertainties were based only on uncertainties in PSD devices and

2. the uncertainty among the devices was equal.

A computer analysis was performed on an $Excell_{TM}$[1] spreadsheet with Crystal $Ball_{TM}$[2] Monte Carlo-based software. The analysis was based on parallel particle trajectories with true impact parameter of 6.35 mm randomly located around the detector.

---

[1] Microsoft Corporation, 1993-1994.

[2] Decisioneering Inc., 1988-1996.

An initial guess of the PSD uncertainty was input into the spreadsheet. A Monte Carlo simulation was performed with an output distribution of impact parameter. The standard deviation of the calculated distribution of impact parameter was the estimate of uncertainty in impact parameter. The input value of PSD uncertainty was modified until the simulated distributions of impact parameter yielded an estimate of uncertainty in impact parameter reasonably close to 0.23 mm. A PSD uncertainty of 0.325 mm in 30,000 Monte Carlo simulations yielded a standard deviation in the distribution of impact parameter equal to 0.228 mm, within one percent of the target value.

Monte Carlo simulations were performed for other impact parameters using a PSD uncertainty of 0.325 mm. Estimated uncertainties in impact parameter ranged from a low of 0.214 mm (impact parameter = 0.5 mm) to a high of 0.231 mm (impact parameter = 4.25 mm) for 30,000 trials each. Thus, uncertainties in impact parameter are relatively constant, independent of impact parameter.

Impact Parameter Bias Estimates

Impact parameters were calculated from the combined signals from the four PSD devices. In the calculations, position signals were squared. As a result, uncertainties in PSD signals will introduce a bias in the calculated impact parameter.

Analyses were carried out to determine bias in calculation of impact parameter. The calculations were performed with the same spreadsheet described above. PSD uncertainty was set equal to 0.325 mm, 10 different true values of impact parameter were evaluated, and 30,000 simulations were performed. Fig. D-4 contains the results expressed in terms of percent bias vs. impact parameter. For all impact parameters evaluated, impact parameter was positively biased compared to true impact parameter. Bias was highest for small impact parameters and very small for large values. A power function fit to the data is shown as a solid line in the Figure. One standard deviation (1σ) errors were not displayed because they were on the order of the size of the data symbols or less. The data was replotted with the abscissa on a power function scale to weight the errors with respect to a

171

Fig. D-4. Bias in Impact Parameter Determination Expressed as Percent Bias.
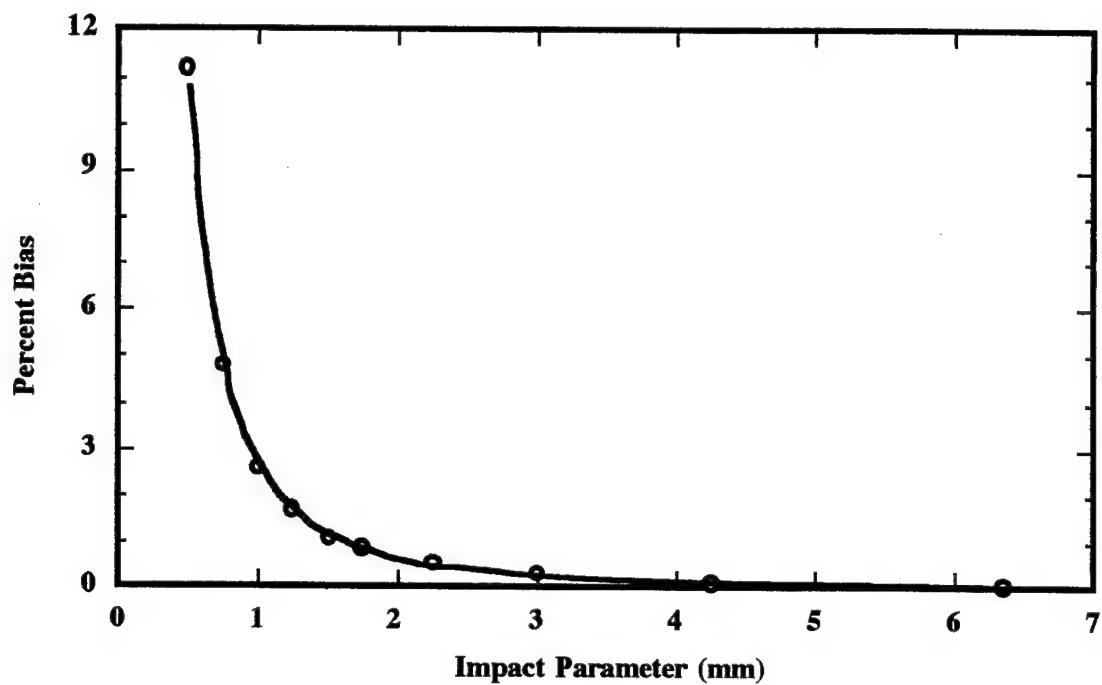
Fig. D-5. Bias in Impact Parameter Determination (Fluence Weighted).
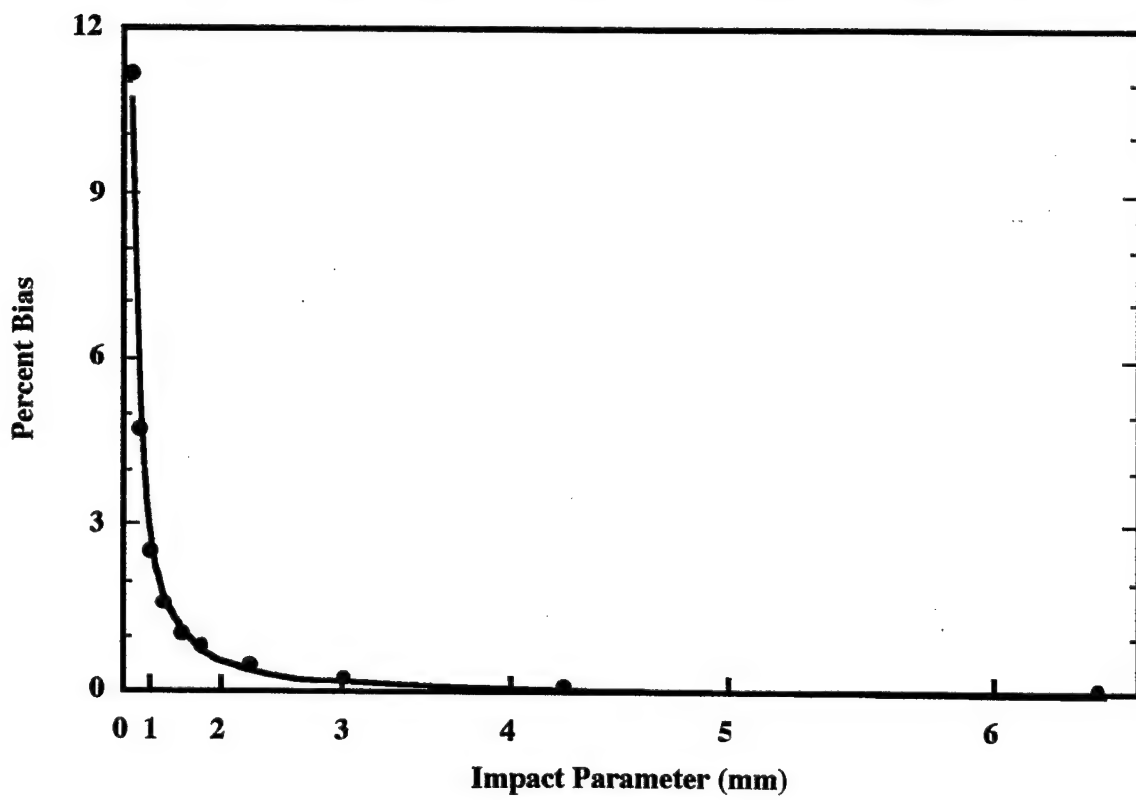
μ-random irradiated detector. From the Fig. D-5, it is apparent that a relatively low fraction of particles have significant bias.

Impact Parameter Determinations: PSD1 vs. Both Pairs

In analysis of the data where charge-changing fragmentation events occurred in the wall of the detector, impact parameters would be incorrect if calculated with both pairs of PSDs. This data was evaluated with impact parameter estimated from PSD1-only. Impact parameter estimates from PSD1-only will have greater uncertainty than those determined with both set of PSDs because the beam did not contain particles that were perfectly parallel in trajectory. This analysis estimated the uncertainty in impact parameter for PSD1-only.

The analysis of uncertainty was based in part on experimental data and Monte Carlo simulations. Uncertainty in impact parameter is based on the uncertainty in PSD x_1, PSD y_1, and that from the uncertainty in particle trajectory. The latter effect is due to the non-parallel beam. Earlier in this appendix, uncertainty in PSD response was estimated at 0.325 mm. Particle trajectory can be evaluated from the distributions of $(x_2 - x_1)$ and $(y_2 - y_1)$. Figure D-6 contains the distribution of $(x_2 - x_1)$ for Fe particles through the detector with the copper target. The data is normally distributed with a mean and standard deviation of -3.47 and 1.84 mm, respectively. One standard deviation in the trajectory angle of these particles in the x-dimension is 0.17°, based on a distance between the PSDs of 622 mm and the standard deviation of 1.84 mm in the distribution of $(x_2 - x_1)$.

1. True Impact Parameter = 5.5 mm

A Monte Carlo simulation was performed for an impact parameter of 5.5 mm in PSD1. The standard deviation of 1.8 mm was used for $(x_2 - x_1)$ and $(y_2 - y_1)$. PSD uncertainties of 0.325 mm were used. The output of the Monte Carlo simulation was impact parameter.

For 40,000 trials, the mean of the distribution was 5.567 ± 0.004, with a CV of 14.8 %. The ratio of the mean to the true impact parameter was 1.01. The kurtosis and skewness of the distribution were 3.03 and -0.002, respectively, indicating normality.

Figure D-6. Distribution of (X2 - X1) for Fe Particles through the Detector with Copper Target [Simulated Diameter = 1 μm]

μ = -3.47 mm
σ = 1.84 mm
n = 174,839

Number of Events

x2 - x1 (mm)
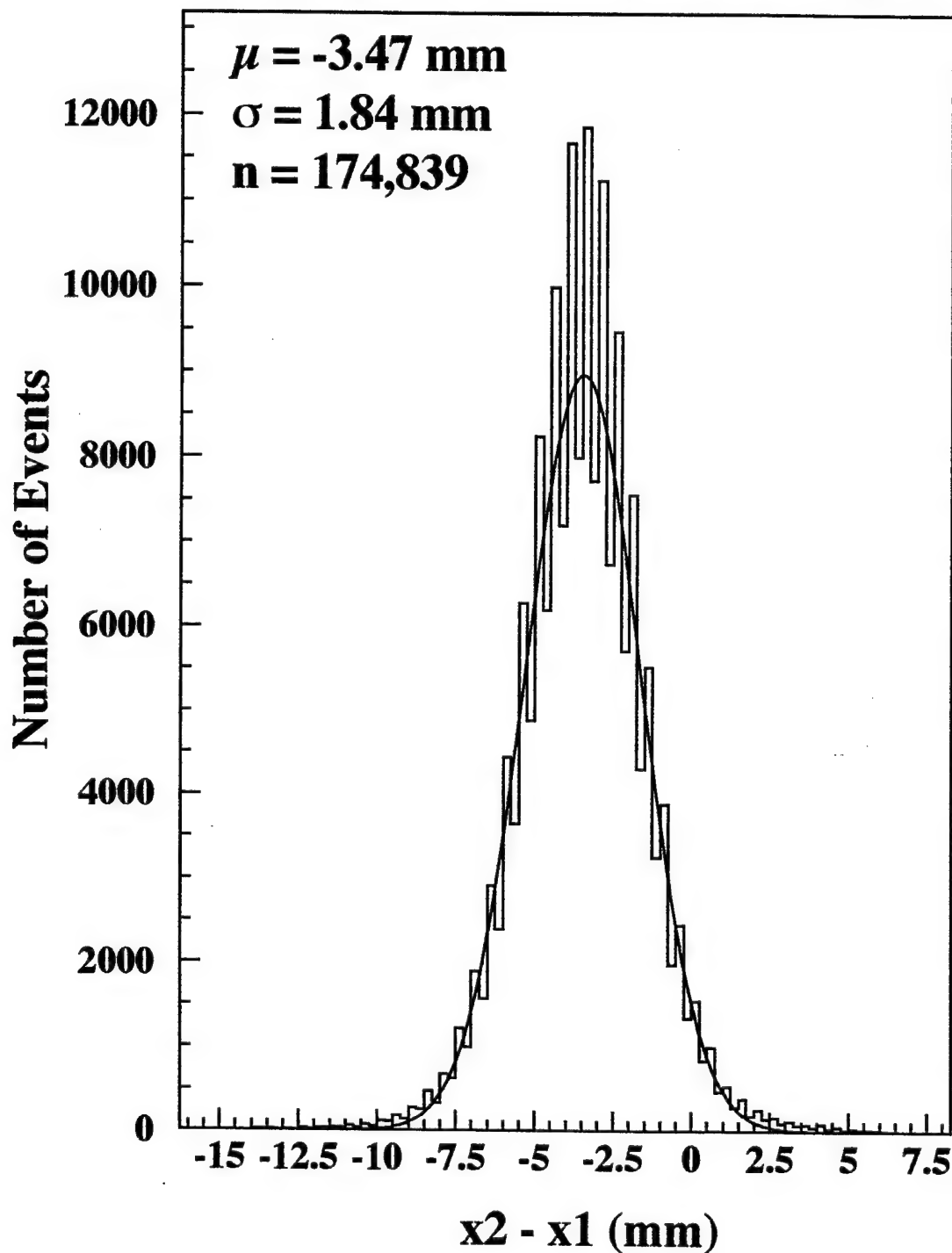
An evaluation of experimental data was performed to confirm the results and assumption used in the Monte Carlo simulation. For Fe events through the detector, impact parameter was calculated with both PSD pairs and PSD1-only. Fig. D-7 contains the distribution of the ratio of impact parameter from PSD1-only to that calculated from both PSDs. The distribution was created for Fe events through the detector, the copper target in place, and impact parameters between 5 and 6 mm (as determined by both PSDs). The data follows a normal distribution and has a mean of 1.007 and CV of 14.6%.

The data is closely approximated by the Monte Carlo simulated distribution. At 5.5 mm, impact parameter based on PSD1-only had a slight positive bias compared to impact parameter based on both PSDs. The 1σ uncertainty in impact parameter at 5.5 mm was estimated at 0.84 mm by the Monte Carlo calculations.

2. Uncertainty in Impact Parameter

Uncertainties in impact parameter were estimated by Monte Carlo calculations for other impact parameters. Distributions of the ratio of the impact parameter from PSD1-only to that from both pairs were created. A summary of the analysis of the experimental data and paired estimates of uncertainties by Monte Carlo calculations are in Table C-1.

Figure D-7. Impact Parameter Ratio: (PSD1-Only) to (PSD1 & PSD2) for Fe Particles through the Detector with Impact Parameters between 5 and 6 mm
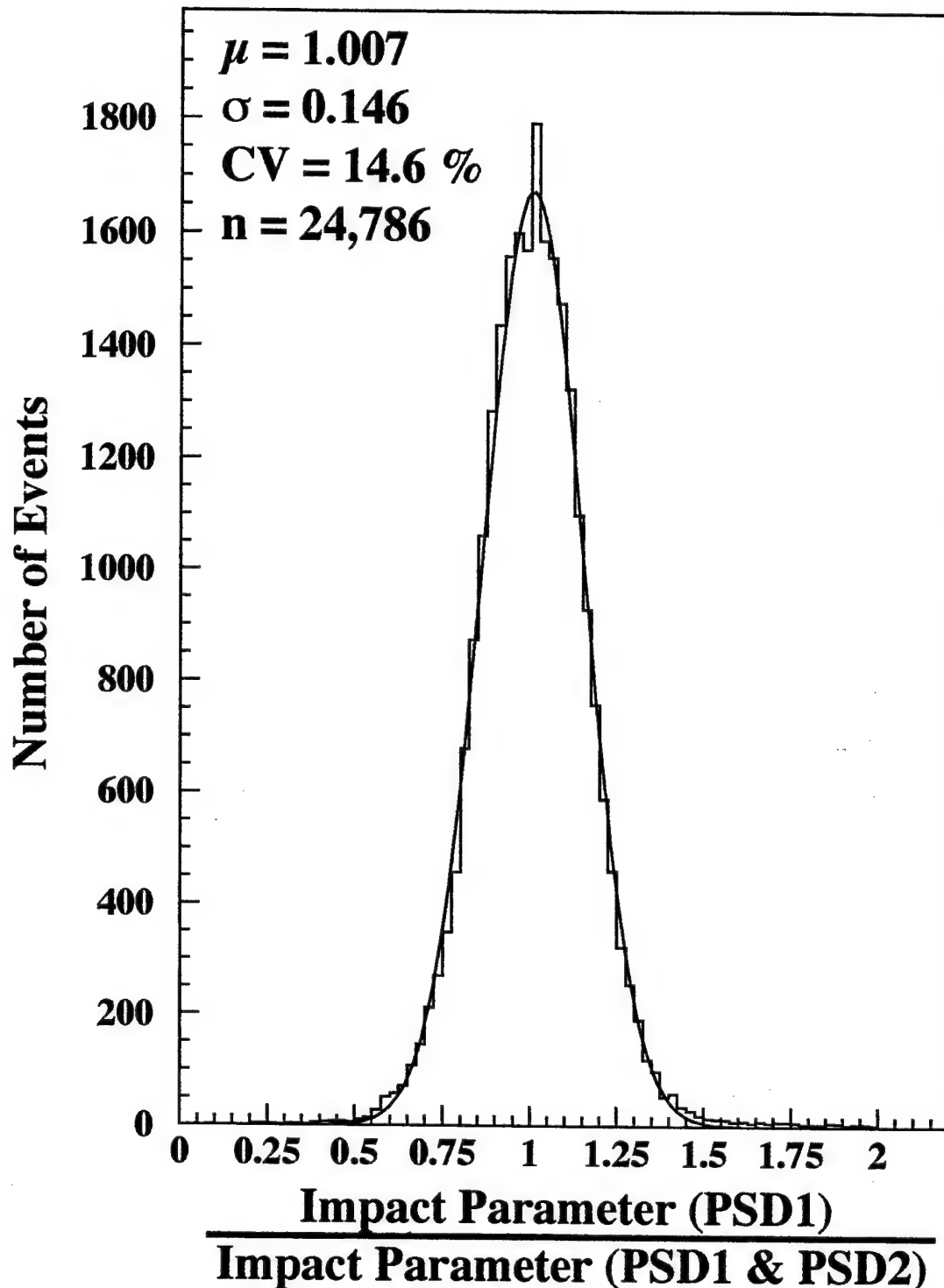
Table D-1. Ratios of Impact Parameter from (PSD1-Only) to that with Both PSD Pairs, and Estimated Uncertainties in Impact Parameter by Monte Carlo Calculations [Experimental Data with Fe Particles through the Detector with Cu Target in Place]

Impact Parameter Range (mm)	Experimental Data $\frac{(PSD1)}{(PSD1 \& PSD2)}$			Estimated Uncertainty Monte Carlo
	Mean	Standard Deviation	Event Number	(1σ) (mm)
2 - 3	1.067 ± 0.003	0.337 ± 0.003	10,467	0.81
3 - 4	1.054 ± 0.002	0.239 ± 0.002	15,321	0.84
4 - 5	1.029 ± 0.001	0.180 ± 0.001	20,519	0.82
5 - 6	1.007 ± 0.001	0.146 ± 0.001	24,786	0.84
6 - 7	0.995 ± 0.001	0.124 ± 0.001	26,275	0.85
7 - 8	0.988 ± 0.001	0.112 ± 0.001	26,429	0.89
8 - 9	0.983 ± 0.001	0.100 ± 0.001	24,977	0.90

Appendix E: Calculations for Random Variables

General

The energy deposition, ΔE, in the PSDs was dependent on many factors. As noted in Chapter 4, these factors are stochastic in nature and can be treated as random variables, X_i. The "average" or expected value, $E[X]$, for the random variable, X_i, is one measure of central tendency. Another property of random variables is the variance, $\text{Var}[X_i]$, and provides some indication of how the distribution is spread. The variance of a random variable is defined as:

$$\text{Var}[X] = E[\{X - E[X]\}^2],\qquad\qquad (\text{E-1})$$

where X is the random variable and $E[X]$ is the expected value of the random variable.

More commonly the expectation value is given the symbol, μ, and the variance, σ^2.

The square root of the variance, σ, is the standard deviation and is more commonly used to describe dispersion. The coefficient of variation (CV) is the quotient: σ/μ.

Quotient of Two Random Variables

A function of two random variables is their quotient. Let X and Y be two random variables with respective expectation values, μ_X and μ_Y, and variances, σ^2_X and σ^2_Y. The covariance between the two random variables is defined as $\text{Cov}[X, Y]$ or simply $\sigma^2_{X,Y}$. In general, no exact solutions exist for the expectation and variance of the quotient of two random variables (Mood *et al.* 1974). Approximate solutions given by Mood *et al.* (1974) are given in Eqs. E-2 and -3.

$$\mu_{\left[\frac{X}{Y}\right]} \approx \frac{\mu_X}{\mu_Y} - \frac{1}{\mu_Y^2}\sigma_{X,Y}^2 + \frac{\mu_X}{\mu_Y^3}\sigma_Y^2 \tag{E-2}$$

$$\sigma_{\left[\frac{X}{Y}\right]}^2 \approx \left(\frac{\mu_X}{\mu_Y}\right)^2 \left(\frac{\sigma_X^2}{\mu_X^2} + \frac{\sigma_Y^2}{\mu_Y^2} - \frac{2\sigma_{X,Y}^2}{\mu_X\mu_Y}\right) \tag{E-3}$$

Equation E-4 was produced by substitution, rearrangement, and under the simplification:

$$\mu_{\left[\frac{X}{Y}\right]} \approx \frac{\mu_X}{\mu_Y} \text{ from Eq. E-2.}$$

$$\frac{\sigma_{X,Y}^2}{\mu_X\mu_Y} \approx \frac{\left[CV^2(X) + CV^2(Y) - CV^2\left(X/Y\right)\right]}{2} \tag{E-4}$$

Estimation of the CV for the Covariant Term between $\Delta E\ y_1$ and $\Delta E\ x_1$

Distributions of $\Delta E\ y_1$, $\Delta E\ x_1$, and $\left[\dfrac{\Delta E\ y_1}{\Delta E\ x_1}\right]$ were displayed in Figs. 4-2 and -3.

Using the statistics of the distributions tabulated in Table E-1, an estimation of the covariance between $\Delta E\ y_1$ and $\Delta E\ x_1$ was made using Eq. E-4. The covariance was estimated at 3.1 MeV^2 ($\sigma = 1.8$ MeV). Percent CV's for the distributions are listed in Table E-1 and the estimated CV of the covariant term between $\Delta E\ y_1$ and $\Delta E\ x_1$ is listed as well. For $\Delta E\ y_1$ and $\Delta E\ x_1$, the covariant term represents 22 and 16 % of the total variance, respectively.

179

The mean of the quotient distribution, $\mu_{\left[\frac{\Delta E\, y_1}{\Delta E\, x_1}\right]}$, is very close to the quotient of the

mean of the distribution of energy in each PSD, $\left(\dfrac{\mu_{\Delta E\, y_1}}{\mu_{\Delta E\, x_1}}\right)$. Thus, the assumption made in

forming equation E-4 was appropriate in this case.

Table E-1. Summary Statistics and Estimated Percent CV
of the Covariant Term between $\Delta E\, y_1$ and $\Delta E\, x_1$

Distribution	(MeV)		Percent Coefficient of Variation	
	μ	σ	Total	Covariant Term
$\Delta E\, y_1$	258	3.75	1.45	0.68
$\Delta E\, x_1$	279	4.40	1.58	0.63
$\Delta E \left[\dfrac{y_1}{x_1}\right]$	0.925	0.0179	NA	NA

Appendix F: Summary of Miscellaneous Calculations

Charged Particle Equilibrium

Calculations were performed for the detector based on response to a μ-random incident beam of Fe particles. The response was compared to that of an equivalent homogenous site irradiated to an equivalent spatially infinite beam. For the homogenous case, dose is defined by Eq. F-1:

$$DOSE = \frac{\phi \cdot L}{\rho}, \qquad\qquad (F\text{-}1)$$

where ϕ is the particle fluence, L is the stopping power, and ρ is the density of the medium.

Dose to the cavity of the detector is based on the integral of Eq. F-2:

$$DOSE = \sum_{b_{min}}^{b_{max}} \frac{\phi \cdot \varepsilon(b)}{m} \Delta A , \qquad\qquad (F\text{-}2)$$

where as shown in Fig. F-1, b_{min} is the center of the detector, b_{max} is the outer boundary of the wall of the detector, ΔA is the incremental area as shown by the annulus, and m is the mass of the cavity fill gas. In the figure, the cavity defines the detector cross-section area, A_d. Based on $dA = 2\pi \cdot b \cdot \Delta b$; $y = \frac{\varepsilon}{l}$; and $m = V \cdot \rho$, where V is the cavity volume; Eq. F-2 can be redefined.

$$DOSE = \phi \sum_{b_{min}}^{b_{max}} \frac{\bar{l} \cdot y(b)}{\rho \cdot V} 2\pi \cdot b \cdot \Delta b. \qquad\qquad (F\text{-}3)$$

With $V = \frac{\pi}{6} D^3$, $A_D = \frac{\pi}{4} D^2$, and substituting the expression for dose from

Eq. F-1, the following equivalence should exist if CPE has been achieved.

$$\frac{\phi \cdot L}{\rho} \equiv \frac{\phi}{\rho \cdot A_D} \sum_{b_{min}}^{b_{max}} y(b) \cdot 2\pi \cdot b \cdot \Delta b. \qquad (F-4)$$

Simplifying, Eq. F-4 is solved for L.

$$L \equiv \frac{\sum\limits_{b_{min}}^{b_{max}} y(b) \cdot 2\pi \cdot b \cdot \Delta b}{A_D}. \qquad (F-5)$$

For the calculations, $\bar{y}(b)$ was substituted for $y(b)$.

Figure F-1. Illustration of Parameters Used to
Determine Absorbed Dose in the Detector

182
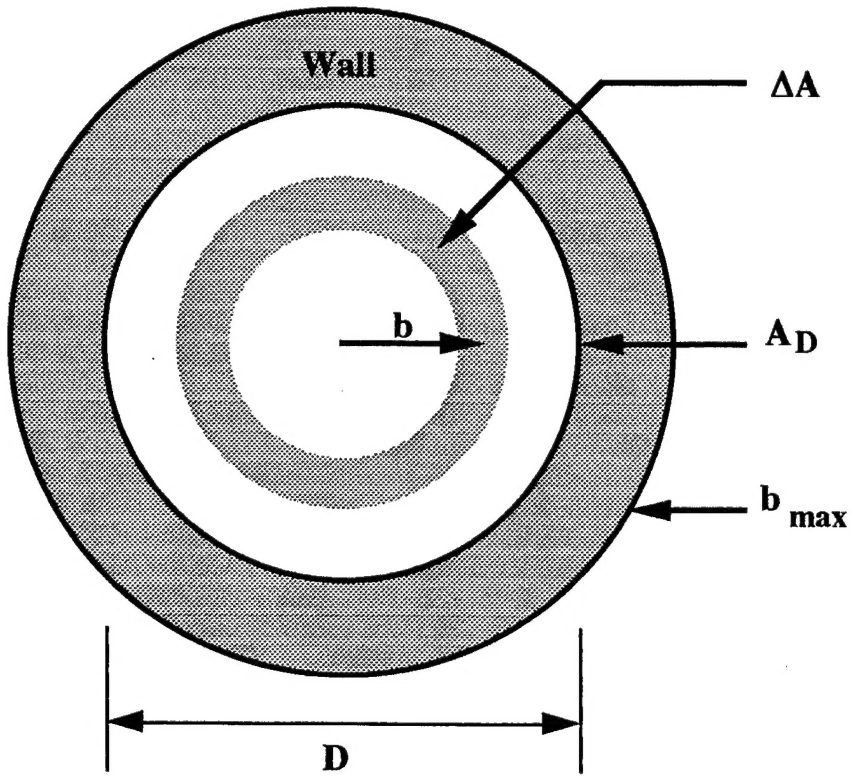
Frequency Mean and Dose Mean Lineal Energy

Frequency mean lineal energy, $\bar{y}_F$ was calculated with Eq. F-6.

$$\bar{y}_F = \frac{\sum\limits_{b_{min}}^{b_{max}} \bar{y}(b) \bullet b \bullet \Delta b}{\sum\limits_{b_{min}}^{b_{max}} b \bullet \Delta b}. \qquad \text{(F-6)}$$

Dose mean lineal energy, $\bar{y}_D$, was calculated with Eq. F-7.

$$\bar{y}_D = \frac{\sum\limits_{b_{min}}^{b_{max}} \bar{y}(b)^2 \bullet b \bullet \Delta b}{\bar{y}_F}. \qquad \text{(F-7)}$$

Mean Quality Factor

Mean quality factor, $\bar{Q}$, was determined for the distributions of $\bar{y}$ vs. impact parameter, b, with Eq. F-8.

$$\bar{Q} = \frac{\sum\limits_{b_{min}}^{b_{max}} Q(\bar{y}) \bullet \bar{y}(b) \bullet b \bullet \Delta b}{\sum\limits_{b_{min}}^{b_{max}} \bar{y}(b) \bullet b \bullet \Delta b}. \qquad \text{(F-8)}$$